Diss. ETH no. 28595

CROSS-LAMINATED TIMBER RIB PANELS IN FIRE

A thesis submitted to attain the degree of

DOCTOR OF SCIENCES of ETH ZURICH
(Dr. sc. ETH Zurich)

presented by

MIRIAM KLEINHENZ

Dipl.-Ing., Karlsruhe Institute of Technology
born on 30.03.1987
citizen of Germany

accepted on the recommendation of

Prof. Dr. Andrea Frangi (ETH Zurich)
Prof. Dr. Alar Just (Tallinn University of Technology)
Univ.-Prof. Dr.-Ing. Stefan Winter (Technical University of Munich)
Prof. Dr. Ingo Burgert (ETH Zurich)

2022

Acknowledgements

I gratefully acknowledge the financial support from Stora Enso Wood Products GmbH. A very special thank you to Thomas Demschner, Niko Kumer, and Julien Lapere, for supporting and motivating me in our many discussions and meetings.

I would like to warmly thank Prof. Dr. Andrea Frangi for giving me the opportunity to pursue my PhD at ETH Zurich and welcoming me at the Chair of Timber Structures of the Institute of Structural Engineering (IBK). I thank him for his committed support and trust, which allowed me to extend my research to many interesting topics, and for his guidance and encouragement throughout the years.

I would also like to thank Prof. Dr. Alar Just, from the Tallinn University of Technology, for co-supervising me since the beginning and for welcoming me into his research group. Being part of his team has been a great honour and joy.

My thanks go to Univ.-Prof. Dr.-Ing. Stefan Winter, from the Technical University of Munich, for supervising me for many years and for being part of my doctoral examination committee.

Last but not least, I would like to thank Prof. Dr. Ingo Burgert, from the ETH Zurich, for being part of my doctoral examination committee.

Of irreplaceable value to me were the technical discussions with Katrin Nele Mäger and Pedro Palma, who wholeheartedly supported me. The experimental work would not have been possible without the support of Magdalena Sterley, from RISE Research Institutes of Sweden in Stockholm, with whom I had the privilege to work.

It was a pleasure being a part of the Chair of Timber Structures at ETH Zurich. I am fortunate that many of my colleagues became good friends. I apologise for not listing you all. My thanks go to Jelena Ogrizovic, Katharina Müller, Dominik Bissig, Jonas Wydler, Stephan Schilling, Charles Binck, Alex Cao, Johanna Saladin-Michel, Marcel Muster, Nadja Manser, Julian Brogli, Philippe Grönquist, Konstantinos Voulpiotis and everyone else in *Gruppe Frangi*, whose friendship and support made my time at ETH about much more than just this thesis. My special thanks go to the *fire group* Reto Fahrni, Joachim Schmid, Michael Klippel, and Chamith Karannagodage. The experimental work had the unsurpassable assistance of Martin Viertel, Dominik Werne, Christoph Gisler, Thomas Jaggi, Oliver Zgraggen, Paul Fischlin, Thomas Meierhans, and Thomas Schnider.

A very special thank you to Yasmin Lemcherreq and Salma Mozaffari for the coffee breaks, laughs, and motivation boosts. A very special thank you to the colleagues as well as to Veronika Hofmann and Sylvia Franz who proof-read individual parts of this thesis.

Most of all, I am thankful beyond words to my family, especially my parents, and my loved one. Everything I have achieved is thanks to you.

Zurich, May 2022 Miriam Kleinhenz

Abstract

Cross-laminated timber rib panels are floor systems consisting of cross-laminated timber plates rigidly bonded to glued-laminated timber ribs. The composite action is achieved by screw-press gluing using a one-component polyurethane adhesive. The structural behaviour, fire behaviour, and fire resistance were studied using experimental, numerical, and analytical investigations. The overall aim of the thesis was the development of design rules for cross-laminated timber rib panels in fire.

The experimental investigations cover ultimate-load tests at normal temperature as reference tests, and fire resistance tests under standard fire exposure on four cross-section types. In addition, shear tests of the glue line between cross-laminated timber plate and glued-laminated timber rib were performed at normal and elevated temperatures for analysis of the cross-sections' composite action. The results of the reference tests show good agreement with results based on the method of rigidly bonded components and the effective width according to the final European draft of cross-laminated timber design prEN 1995-1-1. The shear tests and the fire resistance tests confirm the assumptions that the glue line remains intact and the effect of the composite action is maintained in fire. The screws remaining after screw-press gluing have negligible influence on the fire behaviour of the floor system. The fire resistance tests show results on the safe side compared to predictions of the fire behaviour according to EN 1995-1-2 and its final draft prEN 1995-1-2. However, the fire resistance is underestimated due to the conservative assumption that the effective width is limited to the rib width in case of fire.

The numerical investigations cover thermal, mechanical, and thermo-mechanical simulations using finite-element models. All finite-element models are validated against the experimental results. A new set of temperature-dependent thermal properties for timber exposed to standard fire is proposed to take into account the post-fall-off behaviour in fire. The thermo-mechanical models give good approximations of the cross-sections' structural behaviour in fire and their fire resistance. A parametric study analyses the structural behaviour in fire, and thus the effective width in fire for a parameter range expected in practice.

Design rules are presented for the design of cross-laminated timber rib panels in fire. The effective width in fire is defined depending on the effective width at normal temperature according to prEN 1995-1-1. The analytical investigations are discussed in comparison to the experimental and numerical results using the method of rigidly bonded components for the design in fire. The developed design rules are shown to give safe estimates of the fire resistance.

Zusammenfassung

Brettsperrholz-Rippendecken sind Deckensysteme, deren Flansch aus Brettsperrholz mithilfe eines Einkomponenten-Polyurethan-Klebstoffs durch Schraubpressverklebung schubsteif mit Rippen aus Brettschichtholz verbunden wird. Das Tragverhalten, das Brandverhalten und der Feuerwiderstand der massiven Holzrippendecke wurden anhand von experimentellen, numerischen und analytischen Untersuchungen diskutiert. Übergeordnetes Ziel der Arbeit war die Entwicklung von Bemessungsregeln für Brettsperrholz-Rippendecken im Brandfall.

Die experimentellen Untersuchungen umfassten Traglastversuche bei Normaltemperatur als Referenzversuche und Feuerwiderstandsversuche unter Normbrandkurve an vier Querschnittstypen. Zusätzlich wurden Scherversuche an der Klebefuge zwischen Brettsperrholzplatte und Brettschichtholzrippe bei Normaltemperatur und erhöhten Temperaturen zur Analyse der Verbundwirkung durchgeführt. Die Ergebnisse der Referenzversuche zeigen eine gute Übereinstimmung mit den Ergebnissen, die auf der Verbundtheorie mit starrem Verbund und der effektiven Breite gemäß dem europäischen Entwurfsdokument für die Bemessung von Brettsperrholz beruhen (prEN 1995-1-1). Die Scherversuche und die Feuerwiderstandsprüfungen bestätigen die Annahme, dass die Klebefuge intakt und die Wirkung des Verbundes im Brandfall erhalten bleibt. Die nach der Schraubpressverklebung verbleibenden Schrauben haben einen vernachlässigbaren Einfluss auf das Brandverhalten des Deckenystems. Die Feuerwiderstandsprüfungen zeigen Ergebnisse auf der sicheren Seite im Vergleich zu den Vorhersagen des Brandverhaltens nach EN 1995-1-2 und dessen Entwurfsdokument prEN 1995-1-2. Allerdings wird der Feuerwiderstand aufgrund der konservativen Annahme, dass die effektive Breite im Brandfall auf die Rippenbreite begrenzt ist, unterschätzt.

Die numerischen Untersuchungen umfassen thermische, mechanische und thermomechanische Simulationen mit Finite-Elemente-Modellen. Alle Finite-Elemente-Modelle werden anhand der experimentellen Ergebnisse validiert. Es wird ein neuer Satz temperaturabhängiger thermischer Eigenschaften für Holz, das einem ISO-Normbrand ausgesetzt ist, vorgeschlagen, um das Verhalten nach einem Lamellenabfall zu berücksichtigen. Der Vergleich mit weiteren experimentellen Ergebnissen zeigt, dass die thermischen Modelle gute Ergebnisse des Brandverhaltens der Probekörper liefern. Die thermomechanischen Modelle liefern gute Ergebnisse des Tragverhaltens und der Feuerwiderstände der Querschnitte. Eine Parameterstudie analysiert das Tragverhalten im Brandfall und damit die effektive Breite im Brandfall für einen in der Praxis zu erwartenden Parameterbereich.

Bemessungsregeln werden für Brettsperrholz-Rippendecken im Brandfall abgeleitet. Hierbei wird die effektive Breite im Brandfall in Abhängigkeit von der effektiven Breite unter Normaltemperatur gemäss prEN 1995-1-1 definiert. Die analytischen Untersuchungen werden im Vergleich zu den experimentellen und numerischen Ergebnissen unter Verwendung der Verbundtheorie mit starrem Verbund für die Bemessung im Brandfall diskutiert. Die hergeleiteten Bemessungsregeln führen zu Ergebnissen der Feuerwiderstände auf der sicheren Seite.

Contents

1. Introduction

1.1 Background

In construction, long-span floor systems are required for building types such as commercial office buildings, residential buildings, schools, and industrial buildings. In timber construction, long-span floor systems with increased bending stiffness can be achieved by timber-timber composite structures. Case studies from the literature confirmed the efficiency of geometric shapes, such as T-beams and boxed girders, and gave recommendations concerning design and application. In the field of timber bridges, stress-laminated deck sections were combined with glued-laminated timber beams by Davalos and Salim (1993). The composite action was developed through friction by stressing the section with high-strength steel bars through the decks and beams, leading to slip between deck and beams (Taylor et al. 2001; Gilun and Meronk 2006). In the field of multi-storey timber construction, Jacquier and Girhammar (2015) combined cross-laminated timber plates of 0.50 m width with glued-laminated timber beams using double-sided punched metal plate fasteners and inclined screws. Chen and Lam (2013) and Gu (2017) combined cross-laminated timber plates of 0.60 m and 0.70 m width with glued-laminated timber beams using inclined self-tapping screws. Masoudnia, Hashemi, and Quenneville (2018) combined cross-laminated timber plates of 2.00 m width with laminated veneer lumber beams using inclined self-tapping screws and proposed design rules for the non-rigid floor system (Masoudnia, Hashemi, and Quenneville 2017). In all studies, slip was recorded between the mechanically connected plates and beams, indicating sufficiently high levels but no full levels of composite action. The shear stiffness of the flexible connections affected the structural behaviour of the floor systems.

A rigid connection can be achieved using an adhesive as connector between plates and beams or ribs. Cross-laminated timber rib panels represent a timber-timber composite structure consisting of cross-laminated timber plates rigidly bonded to glued-laminated timber ribs. The full composite action between the composite components is provided by means of screw-press gluing (Ebner 2018; Blomgren et al. 2021). Gundelwein, Grosse, and Rautenstrauch (2002) investigated the design of the ribbed floor system. For high loads and large rib distances, the introduction of an effective width of the cross-section was emphasised to take into account the phenomenon of the so-called shear lag.

In collaboration with Stora Enso Wood Products GmbH, Graz University of Technology provided recommendations concerning design and application of the screw-press gluing technique using a polyurethane adhesive (Purbond HB S709), and the determination of the effective width of

cross-laminated timber rib panels at normal temperature (Bratulic, Augustin, and Schickhofer 2019; Bogensperger 2013). The structural behaviour of the floor system in fire had not been studied, yet. The thermal stability of the rigid connection's adhesive was unknown, which might deteriorate under fire or elevated temperatures (Gu 2017).

1.2 Objectives and scope

The aim of the research project presented in this dissertation was to study the fire behaviour and fire resistance of cross-laminated timber rib panels, and to extend current design rules in fire for cross-laminated timber rib panels. The fire resistance behaviour should be described based on current design rules in fire of the European design standard for timber structures, the so-called Eurocode 5 (EN 1995-1-2), and the final draft of the Eurocode 5-1-2 revision (prEN 1995-1-2). The objectives of the experimental investigations were to assess failure modes, structural behaviour, and the stiffness at normal temperature. In fire, the investigation focused on the fire behaviour of the composite cross-section, in particular the influence of the screws remaining after screw-press gluing, the thermal stability of the glue line between the composite components, and the fire resistance of the floor system. The objectives of the numerical investigations were to model the fire behaviour, and structural behaviour in fire based on the conclusions obtained in the experimental investigations, and extend the range of studied cross-sections to support the investigation of the effective width in fire.

The fire resistance tests were based on the standard time-temperature curve (ISO 834-1) according to test standard EN 1363-1. The standard time-temperature curve represents a normative testing curve used as an international reference system, rather than a real fire. Thus, for some applications (e.g. buildings of higher consequence classes) authorities may require a performance-based design including the verification of burnout. In this case, the influence of exposed timber surfaces on the fire dynamics in compartments needs to be considered (Mindeguia et al. 2020; McNamee et al. 2021; Schmid and Frangi 2021; Garcia-Castillo, Paya-Zaforteza, and Hospitaler 2021).

The focus was made on the structural behaviour of cross-laminated timber rib panels at normal temperature and under standard fire exposure. The analysis was restricted to uniformly distributed loads. The layup of cross-laminated timber plates was investigated as 3-layered or 5-layered with layer thicknesses of 20, 30, and 40 mm. The fire behaviour of the composite cross-section was investigated without insulation material in the cavities. The design was limited to a simply supported system under a positive moment and a parameter range expected in practice.

1.3 Overview

This dissertation starts with a review of modelling approaches, and design rules for cross-laminated timber, glued-laminated timber, and cross-laminated timber rib panels at normal temperature and in fire (chapter 2).
The experimental investigations are presented. The main outcomes are analysed, focusing on the composite action, and the behaviour of the glue line between the composite components. The structural behaviour, and the fire behaviour are investigated and compared to estimated results according to prEN 1995-1-1 and prEN 1995-1-2 (chapter 3).
The developed framework to model cross-laminated timber rib panels in fire is presented. The results of the numerical investigations are compared to experimental data. The results of a parametric study are used to give conclusions for the effective width in fire (chapter 4).
Design rules for cross-laminated timber rib panels are proposed, focusing on the composite action and the effective width in fire. The analytical results of the proposed models are compared to results of the experimental and numerical investigations (chapter 5).

2. State of the art

2.1 Overview

The state of the art of the individual cross-section's components, and the composite cross-section is presented, mostly related to European standardization. Material properties are modelled as linear-elastic orthotropic. The existing design rules are reviewed for cross-laminated timber rib panels at normal temperature and in fire. The thermal stability of adhesives is addressed focusing on the glue line between cross-laminated timber plate and glued-laminated timber rib.

2.2 Cross-laminated timber

2.2.1 Overview

According to EN 16351, cross-laminated timber (CLT) is a structural timber element consisting of at least three face-bonded layers out of solid timber laminations with at least one transversal layer orthogonally oriented to the two longitudinal layers. For this thesis, the longitudinal layers are oriented parallel to the system's axis in x-direction. The single CLT layers consist of edge-bonded laminations. The grading and production were conducted by Stora Enso Wood Products GmbH in Ybbs, Austria (Stora Enso 2020). The laminations are graded with suitable visual and machine procedures, and assigned to the strength class of softwood C24 according to EN 338. The European Technical Assessment ETA-14/0349 provides information on the performance of the CLT plates. Currently, the design of cross-laminated timber is not covered by the European design standard for timber structures, Eurocode 5 (EN 1995-1-1; EN 1995-1-2)[1].

2.2.2 Mechanical properties

Nine engineering constants are necessary for the definition of the orthotropic material model: three moduli of elasticity E, three shear moduli G, and three Poisson's ratios v. The ratio between passive deformation ε_{j} (perpendicular to the direction of the applied force) and active deformation ε_{i} (in direction of the applied force) is defined as Poisson's ratio v_{ij} (Kumpenza et al. 2018). For the symmetric compliance matrix of the orthotropic material model, the

[1] Amendments were published in 2008 and 2014 (EN 1995-1-1:2004/A1:2008; EN 1995-1-1:2004/A2:2014).

Poisson's ratios are taken as average values from each corresponding off-diagonal term according to Formulae 2.1 and 2.2

$$v_{xy} = v_{xz} = \frac{v_{xy} + v_{xz}}{2} \tag{2.1}$$

$$v_{yz} = v_{zy} = \frac{v_{yz} + v_{zy}}{2} \tag{2.2}$$

where the deformations in y-direction and z-direction are equalised (Neuhaus 1981; Bodig and Jayne 1993; Kumpenza et al. 2018).
Table 2.1 lists the material properties in accordance with the consolidated draft of Eurocode 5 for the informal enquiry (prEN 1995-1-1). The values of the Poisson's ratios are based on Bodig and Jayne (1993) and calculated as average values (Formulae 2.1 and 2.2). Table 2.2 lists the material strength values. The characteristic strength values are given according to the consolidated draft of Eurocode 5 for the informal enquiry (prEN 1995-1-1). For the determination of the mean strength values, probabilistic models were used according to the JCSS guidelines for structural timber (JCSS 2006).

Table 2.1. Cross-laminated timber - Material properties according to prEN 1995-1-1 (unless otherwise stated).

Material	E_x [1)]	E_y	E_z	G_{xy}	G_{xz}	G_r	v_{xy} [2)]	v_{xz} [2)]	v_{yz} [2)]
CLT24	[N/mm^2]	[N/mm^2]	[N/mm^2]	[N/mm^2]	[N/mm^2]	[N/mm^2]	[-]	[-]	[-]
	12500	450	450	Formula 2.3	650	Formula 2.4	0.395	0.395	0.410

[1)] Values given by Stora Enso.

[2)] Values based on Bodig and Jayne (1993).

Table 2.2. Cross-laminated timber - Material strength values according to prEN 1995-1-1 (unless otherwise stated).

Material	$f_{m,x}$	$f_{c,x}$	$f_{t,x}$	$f_{v,x}$	f_r	ρ [1)]	b_l [1)]
CL24	[N/mm^2]	[N/mm^2]	[N/mm^2]	[N/mm^2]	[N/mm^2]	[kg/m^3]	[mm]
k	24	24	16	3.5	Formula 2.5	-	
mean	37.1	33.9	27.1	5.4	1.5$\cdot$ $f_{r,k}$	465	150

[1)] Values taken from Stora Enso.

The shear modulus in-plane of the gross cross-section G_{xy} is determined according to Formula 2.3

$$G_{xy} = \min\left(\frac{650}{1 + 2.6 \cdot (\frac{t_l}{b_l})^{1.2}}; 450\right) \tag{2.3}$$

where t_l is the thickness of the lamination, and b_l is either the width of the lamination, the distance between the edge and a groove or the spacing between grooves within the lamination. If the layer thicknesses are different in longitudinal and transversal direction, t_l is determined as the mean value of the layer thicknesses (Silly 2010). In this thesis, b_l is the average distance between grooves of the edge-bonded laminations, declared as 150 mm by Stora Enso. Non edge-bonded laminations of CLT layers have a roll-over tendency. Thus, the shear stiffness in-plane is decreased for short boards with high t_l/b_l-ratios (Winter, Kreuzinger, and Mestek

2008). Parametric studies have shown that the reduction in shear stiffness is up to 25% for relevant ratios in practice between 0.10 and 0.25 (Silly 2010). For edge-bonded laminations, the shear stiffness in-plane is usually higher but can be overestimated due to grooves within the laminations (Brandner et al. 2015). Formula 2.3 gives a limitation of 450 N/mm^2 for ratios $t_\mathrm{l}/b_\mathrm{l} \leq 0.25$. In the prEN 1995-1-1 first draft, parameter and exponent in Formula 2.3 depended on the number of layers, and therefore on the shear flexibility of the CLT plate resulting from the shear-soft transversal layers. The formula has been simplified by taking the factor '2.6' and the exponent '1.2' for a 7-layered CLT plate as approach on the safe side.
The rolling shear modulus G_r and the characteristic value of the rolling shear strength $f_\mathrm{r,k}$ are determined according to Formulae 2.4 and 2.5

$$G_\mathrm{r} = \min(30 + 17.5 \cdot (\frac{b_\mathrm{l}}{t_\mathrm{l}}); 100) \tag{2.4}$$

$$f_\mathrm{r,k} = \min(0.2 + 0.3 \cdot (\frac{b_\mathrm{l}}{t_\mathrm{l}}); 1.40) \tag{2.5}$$

where b_l is the spacing between grooves within the lamination, declared as 150 mm by Stora Enso, and t_l is the mean value of the layer thicknesses. Again, the stiffness and strength values for rolling shear significantly depend on the $b_\mathrm{l}/t_\mathrm{l}$-ratio (Brandner et al. 2016). The formulae taken from Ehrhart et al. (2015) give limitations for ratios $b_\mathrm{l}/t_\mathrm{l} > 4$.

2.2.3 Calculation methods

Due to the crosswise orientation of the CLT layers, the assumption of a homogeneous cross-section is not entirely accurate as for solid or glulam timber. The simple beam theory according to Euler-Bernoulli underestimates the shear flexibility of the transversal layers. An overview of calculation methods for the design of CLT plates loaded out-of-plane was given in Bogensperger et al. (2012), in parallel to the revision process of Eurocode 5. There, the different methods for the determination of stresses and deflections are presented, explained in detail and compared to each other. The accuracy of the different methods was of interest, especially in comparison to a flexible-in-shear multi-layered FE model. Methods of mechanically or flexibly connected bending beams are the shear analogy and the gamma-method. The shear analogy method was defined as most accurate method. The gamma-method was identified as less accurate but with less computational effort. As modified gamma-method, it also takes into account the shear deformations of the transversal layers, especially of interest for the determination of deflections (Wallner-Novak, Koppelhuber, and Pock 2014). For CLT plates of certain slenderness, the determination of stresses and deflections are determined with sufficient accuracy with the following two methods.

Method of rigidly bonded components (Bernoulli-beam)

The method of rigidly bonded components follows the approach of the simple beam theory according to Euler-Bernoulli. Shear deformations are not considered and, therefore have no influence on the internal forces of the composite cross-section or the deflection (Wallner-Novak,

Koppelhuber, and Pock 2014). Compared to a method of flexibly connected components, the method gives good results for slenderness conditions between span and CLT thickness of $l/t_{\mathrm{CL}} > 30$ (Schickhofer et al. 2010; Mestek 2011).

Method of shear-flexible beam (Timoshenko-beam)

The method of shear-flexible beam according to Timoshenko is an extension of the Bernoulli-beam (Timoshenko and Goodier 1951; Altenbach, Altenbach, and Rikards 1996). The cross-section remains plane but does not remain perpendicular to the longitudinal axis. The influence of shear deformations on the internal forces of the composite cross-section is not taken into account, as in the case of the Bernoulli-beam. However, the deflection caused by shear deformations is added to the deflection caused by bending deformations. Shear deflection can account for 30% of the bending deflection or rather 23% of the deflection, depending on lay-up, slenderness, and load pattern (Wallner-Novak, Koppelhuber, and Pock 2014). Compared to a method of flexibly connected components, the method gives good results for slenderness conditions between span and CLT thickness of $15 < l/t_{\mathrm{CL}} < 30$ (Schickhofer et al. 2010).
The shear deflection depends on the shear stiffness. The effective shear stiffness out-of-plane of the cross-section $(GA)_{\mathrm{ef}}$ is determined according to Formula 2.6

$$(GA)_{\mathrm{ef}} = \kappa \cdot \sum (GA) \tag{2.6}$$

with

$$\kappa = \frac{5}{6} \cdot \frac{1}{\frac{1}{26^2} \cdot (2 + \frac{G_{\mathrm{r}}}{G_{\mathrm{xz}}}) \cdot (120 \cdot \frac{G_{\mathrm{xz}}}{G_{\mathrm{r}}} + 102)} \tag{2.7}$$

where κ is the shear correction factor on the basis of a corrected shear distortion over the height. The value depends on the type of cross-section (in case of a rectangular beam: $\kappa = 5/6$). Formula 2.7 applies for a 3-layered CLT with layers of equal thickness (Schickhofer et al. 2010).

2.3 Glued-laminated timber

2.3.1 Overview

According to EN 14080, glued-laminated timber (glulam) is a structural timber element consisting of at least two parallel, face-bonded layers out of solid timber laminations. In this thesis, the strength class GL 24h is assigned according to EN 14080. The design of glued-laminated timber is covered by the European design standard for timber structures, Eurocode 5 (EN 1995-1-1; EN 1995-1-2).

2.3.2 Mechanical properties

Nine engineering constants are necessary for the definition of the orthotropic material model: three moduli of elasticity E, three shear moduli G, and three Poisson's ratios v. Table 2.3 lists the material properties according to EN 14080. The values of the Poisson's ratios are based on Bodig and Jayne (1993) and calculated as average values (Formulae 2.1 and 2.2). Table 2.4

Table 2.3. Glued-laminated timber - Material properties according to EN 14080 (unless otherwise stated).

Material GL 24h	E_x [N/mm^2]	E_y [N/mm^2]	E_z [N/mm^2]	G_{xy} [N/mm^2]	G_{xz} [N/mm^2]	G_{yz} [N/mm^2]	v_{xy} [1)] [-]	v_{xz} [1)] [-]	v_{yz} [1)] [-]
	11500	300	300	650	650	65	0.395	0.395	0.410

[1)] Values based on Bodig and Jayne (1993).

Table 2.4. Glued-laminated timber - Material strength values according to EN 14080.

Material GL 24h	f_m [N/mm^2]	$f_{c,0}$ [N/mm^2]	$f_{t,0}$ [N/mm^2]	f_v [N/mm^2]	ρ [kg/m^3]
k	24	24	19.2	3.5	-
mean	31	29.4	26.2	4.5	420

lists the material strength values. The characteristic strength values are given according to EN 14080. For the determination of the mean strength values, probabilistic models were used according to the JCSS guidelines for glued-laminated timber (JCSS 2006).

2.4 Cross-laminated timber rib panels at normal temperature

2.4.1 Overview

The composite structure of cross-laminated timber rib panels consists of CLT plates connected to glulam ribs. The distinction is made between one CLT plate as top flange (T-section) and CLT plates as top and bottom flanges (box-section), see Figure 2.1. Based on ETA-20/0893 and Stora Enso 2022, typical span lengths are between 5 m and 16.50 m. The width is maximum 3.50 m and the height minimum 160 mm. The thickness of the CLT plate varies between 60 mm and 200 mm. The geometry of the glulam rib is rectangular with minimum cross-section dimensions of 60 mm width and 100 mm height. Full composite action is provided by a rigid connection between the composite components by means of screw-press gluing (SPG) using a one-component polyurethane adhesive (Purbond HB S709) according to EN 15425. Screw-press gluing is an alternative to hydraulic pressure to attach the CLT panels to the ribs (Kairi et al. 1999). In the case of cross-laminated timber rib panels, the needed contact pressure in the glue line between the composite components is induced by using partially threaded screws with

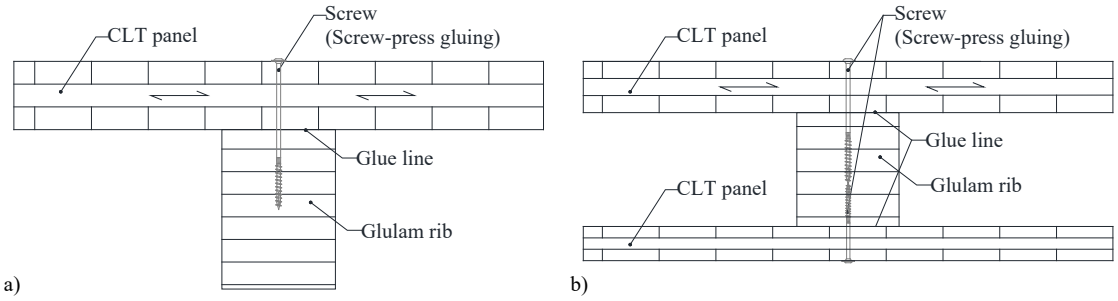

Figure 2.1. Types of cross-section of cross-laminated timber rib panel: a) T-section; b) Box-section.

large washer head and counter threaded tip according to ETA-11/0190, which remain in the cross-section after the curing time of the adhesive. The minimum required pressure for SPG – declared as 0.10 N/mm^2 - is applied to guarantee the glue line thickness of 0.3 mm (Bratulic and Augustin 2016). In Bratulic et al. (2019), a proposal is made of a simplified analytical approach for an optimised SPG-design by determination of the maximum screw spacing, taking into account the required pressure over the rib's width and the minimum screw clamping capacity. The self-weight of the CLT plates is not taken into account.

2.4.2 Effective width

For ribbed cross-sections, the assumption that the cross-section remains plane is incorrect. The simple beam theory according to Euler-Bernoulli is not applicable because the strains in the flange vary depending on the distance from the rib due to the in-plane shear flexibility of the flange. The strains are higher in the part of the flange above the rib than in the parts far from the rib. This phenomenon is termed shear lag. The cross-section is not equally stiff over the entire flange width. The stiffer part above the rib shows higher longitudinal strains, while parts far from the rib experience higher shear strains. This leads to a non-uniform distribution of the longitudinal strains along the flange width. For simplified design methods, it is proposed to introduce an effective width or effective plate width (Chwalla 1936; Timoshenko 1940). The effective width defines an equivalent cross-section that provides the same maximum bending stress and effective bending stiffness as the actual cross-section. The non-uniform stress distribution over the flange width can be replaced by a uniform stress distribution over an effective width. As a result, constant strain distributions over the effective width can be assumed without overestimating the system's structural behaviour (Timoshenko 1940; Masoudnia, Hashemi, and Quenneville 2018). Based on the concept used for steel-concrete composite systems (Ahn et al. 2004; Chiewanichakorn et al. 2004; Chen et al. 2007), Formula 2.8 shall apply

$$\sigma_{\mathrm{x,max}}(z) \cdot b_{\mathrm{ef}} = \int \sigma_{\mathrm{x}}(y,z)\, dy\, dz \tag{2.8}$$

where $\sigma_{\mathrm{x,max}}(z)$ is the maximum bending stress distribution along the thickness of the CLT plate t_{CL} at rib centre, b_{ef} is the effective width, and $\int \sigma_{\mathrm{x}}(y,z)\, dy\, dz$ is the integral of all bending stresses along the thickness t_{CL} and along the width b of the CLT plate, as illustrated in Figure 2.2.

Current structural design methods for timber structures do not contain a determination method of the effective width for timber composite structures, much less for massive timber rib panels. In the first generation of Eurocodes, information is given on an effective width or effective flange width for steel structures (EN 1993-1-5), concrete structures (EN 1992-1-1), and steel-concrete composite structures (EN 1994-1-1). Timber-concrete composite structures follow in practice the procedure for steel-concrete composite structures (Dias, Schänzlin, and Dietsch 2018; Schänzlin 2018). No design rules can be found for timber constructions, except for maximum values for the design of glued thin-flanged beams. In EN 1995-1-1, the non-uniform distribution of stresses in the flanges of glued thin-flanged beams is taken into account due to not only shear lag but

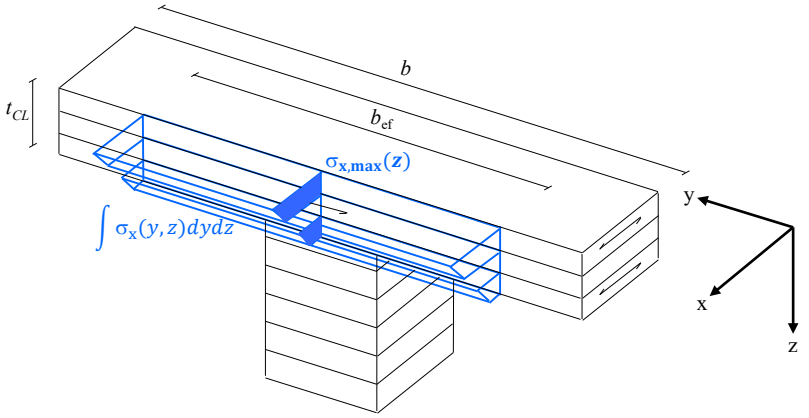

Figure 2.2. Determination of the effective width at normal temperature.

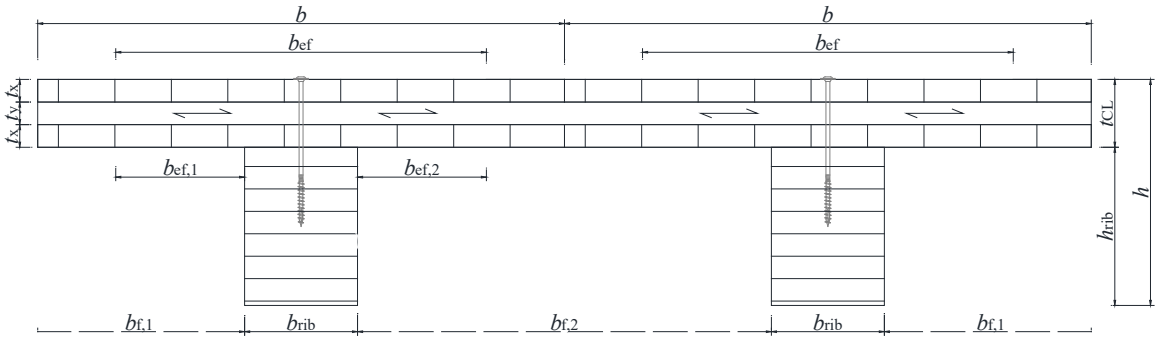

Figure 2.3. Geometry of the cross-section of cross-laminated timber rib panels.

also buckling of the flanges. Plywood, oriented strand board, and particleboard or fibreboard are considered as flange material. EN 1995-1-1 proposes values based on span, thickness of the flange, and rib width of the cross-section. The distinction is made between beams with one top flange (I-beams) and beams with top and bottom flanges (U-beams), and between flanges in compressive or tensile zone.

Bogensperger (2013) conducted analytical and numerical analyses on the effective width of cross-laminated timber rib panels under bending. By setting up a differential equation system to determine the bending stress distribution in the CLT plate, the maximum bending stress was calculated and used to determine the effective width by equalising it with the maximum bending stress calculated by simple beam theory. Data fitting to FE solutions led to formulae for a parameter range expected in practice (Augustin and Thiel 2017). The analyses were limited to a simply supported system under a positive moment, and to cross-sections with rigid composite action and one CLT plate as top flange. The possibility is mentioned that the shear flexibility of the structure increases in case of a non-rigid connection between CLT plate and rib (Bogensperger 2013). The simplified formulae serve as the basis for the consolidated draft of Eurocode 5 for the informal enquiry (prEN 1995-1-1). The effective width of ribbed plates built up from cross-laminated timber plates at normal temperature b_{ef} is determined by Formula 2.9

$$b_{ef} = b_{rib} + \sum b_{ef,i} \tag{2.9}$$

where b_{rib} is the rib width, and $b_{\mathrm{ef,i}}$ is the effective width at either side of the rib (Figure 2.3). For the verification of stresses of uniformly distributed loads and the verification of serviceability limit states for uniformly distributed and single loads, $b_{\mathrm{ef,i}}$ may be calculated according to Formula 2.10.[2]

$$b_{\mathrm{ef,i}} = b_{\mathrm{f,i}} \cdot (0.5 - 0.35 \cdot (\frac{b_{\mathrm{f,i}}}{l})^{0.9} \cdot (\frac{(EA)_{\mathrm{x}}}{(GA)_{\mathrm{xy}}})^{0.45}) \tag{2.10}$$

For the verification of stresses of single loads, $b_{\mathrm{ef,i}}$ may be calculated according to Formula 2.11 for $h_{\mathrm{rib}}/t_{\mathrm{CL}} \leq 2$ or Formula 2.12 for $h_{\mathrm{rib}}/t_{\mathrm{CL}} > 2$

$$b_{\mathrm{ef,i}} = b_{\mathrm{f,i}} \cdot (0.5 - 0.40 \cdot (\frac{b_{\mathrm{f,i}}}{l})^{0.25} \cdot (\frac{(EA)_{\mathrm{x}}}{(GA)_{\mathrm{xy}}})^{0.1}) \tag{2.11}$$

$$b_{\mathrm{ef,i}} = b_{\mathrm{f,i}} \cdot (0.5 - 0.28 \cdot (\frac{b_{\mathrm{f,i}}}{l})^{0.3} \cdot (\frac{(EA)_{\mathrm{x}}}{(GA)_{\mathrm{xy}}})^{0.3}) \tag{2.12}$$

where $h_{\mathrm{rib}}/t_{\mathrm{CL}}$ is the ratio of rib height to thickness of the CLT plate. Following steel and concrete design, the effective width b_{ef} depends mainly on the type of loading and on the ratio of clear rib distance to span $b_{\mathrm{f,i}}/l$. In addition, the effective width b_{ef} depends on the orthotropy of the flange, expressed by the in-plane stiffness of the longitudinal CLT layers per meter width $(EA)_{\mathrm{x}}$ and the shear stiffness in-plane of the gross CLT cross-section per meter width $(GA)_{\mathrm{xy}}$. The modulus of elasticity E_{x} and the shear modulus in-plane of the gross cross-section G_{xy} are determined according to section 2.2.2. The units of the parameters are mm and N/m. Stiffness properties are used as mean values without reduction by the partial safety factor for materials. For the effective width at normal temperature b_{ef}, no distinction is made in prEN 1995-1-1 between CLT plates in compressive and tensile zones.
The maximum effective width b_{ef} occurs in the centre of the field at midspan for uniformly distributed loads or at the position of the single load and decreases towards the supports (Girkmann 1963; Bogensperger 2013). For the verification of stresses at the support, the assumption of an effective width b_{ef} as at midspan would be on the unsafe side. Here, the effective width at either side of the rib $b_{\mathrm{ef,i}}$ may be calculated as for single loads according to Formulae 2.11 and 2.12 or taking half of the rib width b_{rib} (Augustin and Thiel 2017). Bogensperger (2013) limited the analyses to one CLT plate as top flange. For the box-sections of this thesis, the effective width b_{ef} is calculated separately for the top and the bottom CLT plates.

2.4.3 Design at normal temperature

The design of cross-laminated timber rib panels at normal temperature is in accordance with EN 1990 and EN 1995-1-1. The composite section's shear lag is taken into account by using the effective width b_{ef} according to prEN 1995-1-1 (section 2.4.2). Thus, the design is limited to a simply supported system under a positive moment and applicable for the following parameter range expected in practice:

[2]The original formula takes the minimum from the value of 0.5 and Formula 2.10. However, Formula 2.10 is always less than the value of 0.5. The same applies to Formulae 2.11 and 2.12

- $0.02 \leq b_{\mathrm{f,i}}/l \leq 0.25$, for the ratio of clear rib distance to span
- $5 \leq (EA)_{\mathrm{x}}/(GA)_{\mathrm{xy}} \leq 22$, for the ratio of in-plane stiffness of the longitudinal CLT layers per meter width to shear stiffness of the gross cross-section of the CLT plate per meter width
- $14 \leq l/h \leq 22$, for the ratio of span to overall height.

The influence of the shear flexibility of CLT based on its shear-soft transversal layers is negligible due to the slenderness of the CLT plates of the long-span floor system; i.e. $l/t_{\mathrm{CL}} > 30$. The influence on the distribution of internal forces and moments can be disregarded (section 2.2.3). According to prEN 1995-1-1, this assumption is applicable for ultimate and serviceability limit states.

Method of rigidly bonded components

The calculation method of rigidly bonded components (Bernoulli-beam) is applied. The method is based on the assumption of full composite action between CLT plate and glulam rib. Full composite action is achieved when no horizontal slip is observed at the material interface between CLT plate and glulam rib. The perfect transfer of strains between the components results in a continuous strain distribution over the total height of the cross-section h. Its curvature depends on the stiffness of each component i. The bending stiffness of the transversal CLT layers is taken as zero. The effect of the glue line on the elastic properties is negligible. The continuous strain distribution results in one global neutral axis for the composite cross-section. The neutral axis is located in the centre of gravity of the composite cross-section z_{s}, determined by Formula 2.13

$$z_{\mathrm{s}} = \frac{\sum(E_{\mathrm{i}} \cdot A_{\mathrm{i}} \cdot a_{\mathrm{i}})}{\sum(E_{\mathrm{i}} \cdot A_{\mathrm{i}})} \tag{2.13}$$

where E_{i} is the mean value of the individual component's modulus of elasticity, A_{i} is its cross-section area, and a_{i} is the distance to its centroid from a selected origin.
The effective bending stiffness of the composite cross-section about the y-axis $(EI)_{\mathrm{ef}}$ is defined by Formula 2.14

$$(EI)_{\mathrm{ef}} = \sum_{i=1}^{n+1}(EI)_{\mathrm{i}} = \sum_{i=1}^{n+1}(\frac{E_{\mathrm{i}} \cdot b_{\mathrm{i}} \cdot h_{\mathrm{i}}^3}{12} + E_{\mathrm{i}} \cdot b_{\mathrm{i}} \cdot h_{\mathrm{i}} \cdot z_{\mathrm{i}}^2) \tag{2.14}$$

where $(EI)_{\mathrm{i}}$ is the bending stiffness of component i, E_{i} is the mean value of its modulus of elasticity, b_{i} is its width, h_{i} is its height, and z_{i} is the distance of its centroid to the global centre of gravity z_{s}. The effective width b_{ef} defines the width b_{i} of n-longitudinal CLT layers ($n = 1$ for top CLT layer, $n = 2$ for second CLT layer etc.). Therefore, it is involved in both the determination of the global centre of gravity z_{s}, and the effective bending stiffness of the composite cross-section $(EI)_{\mathrm{ef}}$. The rib is considered as (n+1)-component.

Ultimate limit state design

For the ultimate limit state, the fundamental combination is used for the calculation of the design value of the sum of actions p_d of the floor system based on Formula 2.15 according to EN 1990

$$p_\mathrm{d} = g_\mathrm{d} + q_\mathrm{d} = \gamma_\mathrm{g} \cdot g_\mathrm{k} + \gamma_\mathrm{q} \cdot q_\mathrm{k} \tag{2.15}$$

with

$$g_\mathrm{k} = g_\mathrm{k,SW} + g_\mathrm{k,S} \tag{2.16}$$

where g_d and g_k are the design and characteristic values of the permanent actions, q_d and q_k are the design and characteristic values of the variable action of the floor system, γ_g is the partial factor for permanent actions, γ_q is the partial factor for variable actions, $g_\mathrm{k,SW}$ is the characteristic value of the self-weight of the floor system, and $g_\mathrm{k,S}$ is the characteristic value of the superimposed action on the floor system.
Design normal stresses $\sigma_\mathrm{i,d}(x,z)$ and design shear stresses $\tau_\mathrm{i,d}(x,z)$ of component i are calculated at certain coordinates x and z according to Formula 2.17 and Formula 2.18

$$\sigma_\mathrm{i,d}(x,z) = \frac{M_\mathrm{y,d}(x) \cdot E_\mathrm{i} \cdot z}{(EI)_\mathrm{ef}(x)} \tag{2.17}$$

$$\tau_\mathrm{i,d}(x,z) = \frac{V_\mathrm{z,d}(x) \cdot \sum ES_\mathrm{y}(z)}{(EI)_\mathrm{ef}(x) \cdot b(z)} \tag{2.18}$$

where $M_\mathrm{y,d}(x)$ is the design bending moment about y-direction at the coordinate x, $V_\mathrm{z,d}(x)$ is the design shear force in z-direction at the coordinate x, E_i is the individual components' modulus of elasticity, $(EI)_\mathrm{ef}(x)$ is the effective bending stiffness of the composite cross-section at the coordinate x, $\sum ES_\mathrm{y}(z)$ is the sum of the static moment at the coordinate z of the composite cross-section, and $b(z)$ is the tributary width for shear at the coordinate z.

For the verification of normal stresses, Figure 2.4 summarizes the relevant cases of the T-section at midspan $x = l/2$ of the simply supported system under a positive moment. The effective width b_ef is calculated at midspan according to Formula 2.9. The maximum normal stress at the top edge of the CLT plate $\sigma_\mathrm{1,d}(z_\mathrm{top})$ is calculated according to Formula 2.19

$$\sigma_\mathrm{1,d}(z_\mathrm{top}) = \sigma_\mathrm{N,1,d} + \sigma_\mathrm{M,1,d} = \frac{M_\mathrm{y,d} \cdot E_1}{(EI)_\mathrm{ef}} \cdot z_\mathrm{top} \tag{2.19}$$

with

$$\sigma_\mathrm{N,1,d} = \frac{M_\mathrm{y,d} \cdot E_1}{(EI)_\mathrm{ef}} \cdot z_1 \tag{2.20}$$

$$\sigma_\mathrm{M,1,d} = \frac{M_\mathrm{y,d} \cdot E_1}{(EI)_\mathrm{ef}} \cdot \frac{h_1}{2} \tag{2.21}$$

where $M_\mathrm{y,d}$ is the design bending moment about y-direction, $(EI)_\mathrm{ef}$ is the effective bending stiffness of the composite cross-section at midspan, E_1 is the modulus of elasticity of the first CLT layer, z_1 is the distance of its centroid to the global centre of gravity, and h_1 is its height.

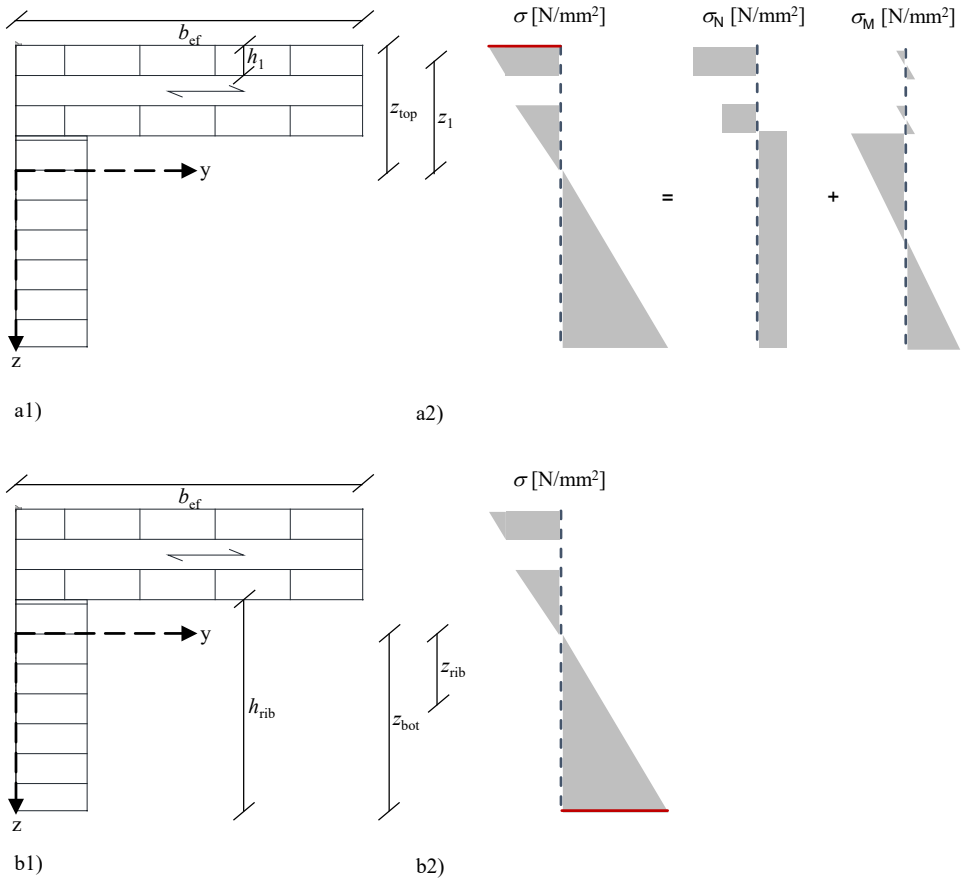

Figure 2.4. Maximum design normal stresses at midspan (coordinate $x = l/2$): a) Normal stress at the top edge of the cross-laminated timber plate (z_{top}); b) Normal stress at the bottom edge of the glulam rib (z_{bot}).

The normal stresses out of bending $\sigma_{\mathrm{i,d}}$ can be divided into a part out of internal normal force $\sigma_{\mathrm{N,i,d}}$ and a part out of internal bending moment $\sigma_{\mathrm{M,i,d}}$. In the case of full composite action, the largest possible pair of internal normal forces occurs, while the internal bending moments of the cross-section's components are small. Thus, the verification of normal stresses can be separated into the verification of normal stresses out of bending $\sigma_{\mathrm{i,d}}$, of normal stresses out of internal normal force $\sigma_{\mathrm{N,i,d}}$, and of normal stresses as combination of internal normal force $\sigma_{\mathrm{N,i,d}}$ and internal bending moment $\sigma_{\mathrm{M,i,d}}$.

For the top CLT layer, the stress gradient is very small. The verification of normal stresses out of bending is decisive at the top edge. The verification of the normal stresses out of internal compressive force in its centroid might be decisive, if the compressive strength value in-plane is not limited to the bending strength value out-of-plane as defined in prEN 1995-1-1. The interaction of normal stresses out of internal bending moment and internal compressive force is not required (Winter, Kreuzinger, and Mestek 2008). The expressions according to Formulae 2.22 and Formulae 2.23 shall be satisfied for the maximum normal stress at the top edge of the CLT plate $\sigma_{1,\mathrm{d}}(z_{\mathrm{top}})$, and its stress part out of internal normal force $\sigma_{\mathrm{N},1,\mathrm{d}}$

$$\sigma_{1,\mathrm{d}}(z_{\mathrm{top}}) \leq f_{\mathrm{m,x,d}} \tag{2.22}$$

$$\sigma_{\mathrm{N,1,d}} \leq f_{\mathrm{c,x,d}} \tag{2.23}$$

with

$$f_{\mathrm{m,x,d}} = k_{\mathrm{mod}} \cdot \frac{f_{\mathrm{m,x,k}}}{\gamma_{\mathrm{M}}} \tag{2.24}$$

$$f_{\mathrm{c,x,d}} = k_{\mathrm{mod}} \cdot \frac{f_{\mathrm{c,x,k}}}{\gamma_{\mathrm{M}}} \tag{2.25}$$

where $f_{\mathrm{m,x,d}}$ and $f_{\mathrm{m,x,k}}$ are the design and the characteristic bending strengths out-of-plane of cross-laminated timber, and $f_{\mathrm{c,x,d}}$ and $f_{\mathrm{c,x,k}}$ are the design and characteristic compressive strengths in-plane of cross-laminated timber (section 2.2.2). According to prEN 1995-1-1, k_{mod} is the modification factor taking into account the effect of the duration of load and moisture content (e.g. for medium term action and service class 1 taken as 0.80), and γ_{M} is the partial safety factor for cross-laminated timber taken as 1.25. System factors are not to be taken into account if strength values are determined according to prEN 1995-1-1 (Dietsch et al. 2018).
The maximum normal stress at the bottom edge of the glulam rib $\sigma_{\mathrm{rib,d}}(z_{\mathrm{bot}})$ is calculated according to Formula 2.26

$$\sigma_{\mathrm{rib,d}}(z_{\mathrm{bot}}) = \sigma_{\mathrm{N,rib,d}} + \sigma_{\mathrm{M,rib,d}} = \frac{M_{\mathrm{y,d}} \cdot E_{\mathrm{rib}}}{(EI)_{\mathrm{ef}}} \cdot z_{\mathrm{bot}} \tag{2.26}$$

with

$$\sigma_{\mathrm{N,rib,d}} = \frac{M_{\mathrm{y,d}} \cdot E_{\mathrm{rib}}}{(EI)_{\mathrm{ef}}} \cdot z_{\mathrm{rib}} \tag{2.27}$$

$$\sigma_{\mathrm{M,rib,d}} = \frac{M_{\mathrm{y,d}} \cdot E_{\mathrm{rib}}}{(EI)_{\mathrm{ef}}} \cdot \frac{h_{\mathrm{rib}}}{2} \tag{2.28}$$

where $M_{\mathrm{y,d}}$ is the design bending moment about y-direction, $(EI)_{\mathrm{ef}}$ is the effective bending stiffness of the composite cross-section at midspan, E_{rib} is the rib's modulus of elasticity, z_{rib} is the distance of its centroid to the global centre of gravity, and h_{rib} is its height.
For the glulam rib, the interaction of normal stresses out of internal bending moment $\sigma_{\mathrm{M,rib,d}}$ and internal tensile force $\sigma_{\mathrm{N,rib,d}}$ is decisive. The expression according to Formula 2.29 shall be satisfied

$$\frac{\sigma_{\mathrm{N,rib,d}}}{f_{\mathrm{t,0,d}}} + \frac{\sigma_{\mathrm{M,rib,d}}}{f_{\mathrm{m,d}}} \leq 1 \tag{2.29}$$

with

$$f_{\mathrm{t,0,d}} = k_{\mathrm{mod}} \cdot k_{\mathrm{h}} \cdot \frac{f_{\mathrm{t,0,k}}}{\gamma_{\mathrm{M}}} \tag{2.30}$$

$$f_{\mathrm{m,d}} = k_{\mathrm{mod}} \cdot k_{\mathrm{h}} \cdot \frac{f_{\mathrm{m,k}}}{\gamma_{\mathrm{M}}} \tag{2.31}$$

with

$$k_{\mathrm{h}} = min((\frac{600}{h_{\mathrm{M}}})^{0.1}; 1.1) \tag{2.32}$$

where $f_{\mathrm{t,0,d}}$ and $f_{\mathrm{t,0,k}}$ are the design and characteristic tensile strength parallel to the grain of glued-laminated timber, and $f_{\mathrm{m,d}}$ and $f_{\mathrm{m,k}}$ are the design and characteristic bending strength

of glued-laminated timber (section 2.3.2). According to EN 1995-1-1, k_{mod} is the modification factor taking into account the effect of the duration of load and moisture content (e.g. for medium term action and service class 1 taken as 0.80), k_{h} is the depth factor taking into account the effect of member size on bending or tensile strength of glued-laminated timber for the rib heights less than 600 mm, and γ_{M} is the partial safety factor for glued-laminated timber taken as 1.25. In the case of box-sections, the verification of normal stresses out of bending at the bottom edge of the lowest CLT layer i of the bottom CLT plate $\sigma_{\mathrm{i,d}}(z_{\mathrm{bot}})$ is decisive. The characteristic bending strength value for bending out-of-plane $f_{\mathrm{m,x,k}}$ according to prEN 1995-1-1 takes into account the effects of combined bending and tensile stresses.

For the verification of shear stresses, Figure 2.5 summarizes the relevant cases of the T-section at the supports $x = 0$ or $x = l$. In this thesis, the effective width at either side of the rib $b_{\mathrm{ef,i}}$ at the supports is calculated as for single loads according to Formulae 2.11 or 2.12. The verification of rolling shear $\tau_{\mathrm{r,d}}(z_{\mathrm{r}})$ can be decisive within the transversal CLT layer exhibiting the highest shear stress, calculated according to Formula 2.33

$$\tau_{\mathrm{r,d}}(z_{\mathrm{r}}) = \frac{V_{\mathrm{z,d}} \cdot E_1 \cdot S_{\mathrm{y}}(z_{\mathrm{r}})}{(EI)_{\mathrm{ef}} \cdot b(z_{\mathrm{r}})} \tag{2.33}$$

with

$$S_{\mathrm{y}}(z_{\mathrm{r}}) = b_{\mathrm{ef}} \cdot h_1 \cdot (h - z_{\mathrm{s}} - h_1/2) \tag{2.34}$$

$$b(z_{\mathrm{r}}) = b_{\mathrm{rib}} + 2t_{\mathrm{x}} \tag{2.35}$$

where $V_{\mathrm{z,d}}$ is the design shear force in z-direction, E_1 is the modulus of elasticity of the first CLT layer, $(EI)_{\mathrm{ef}}$ is the effective bending stiffness of the composite cross-section at the support, h_1 is the height of the first CLT layer, h is the total height of the composite cross-section, and z_{s} is the centre of gravity of the composite cross-section. For the static moment $S_{\mathrm{y}}(z)$ only parts are of interest contributing to the stiffness of the cross-section. Thus, the static moment within the transversal layer $S_{\mathrm{y}}(z_{\mathrm{r}})$ corresponds with the static moment at the end of the longitudinal layer. The tributary width $b(z_{\mathrm{r}})$ within the transversal (second) layer can be extended by the thickness of the longitudinal (first) CLT layer t_{x} on each side of the rib's width b_{rib} based on a force propagation at an angle of 45 degrees. This assumes that the CLT layers are edge-bonded between the laminations, thus that no gap occurs at the edge line of the glulam rib in the bottom CLT layer (Augustin and Thiel 2017).
The expression according to Formula 2.36 shall be satisfied

$$\tau_{\mathrm{r,d}}(z_{\mathrm{r}}) \leq f_{\mathrm{r,d}} \tag{2.36}$$

with

$$f_{\mathrm{r,d}} = k_{\mathrm{mod}} \cdot \frac{f_{\mathrm{r,k}}}{\gamma_{\mathrm{M}}} \tag{2.37}$$

where $f_{\mathrm{r,d}}$ and $f_{\mathrm{r,k}}$ are the design and the characteristic strengths for rolling shear out-of-plane of cross-laminated timber (section 2.2.2). According to prEN 1995-1-1, k_{mod} is the modification factor taking into account the effect of the duration of load and moisture content

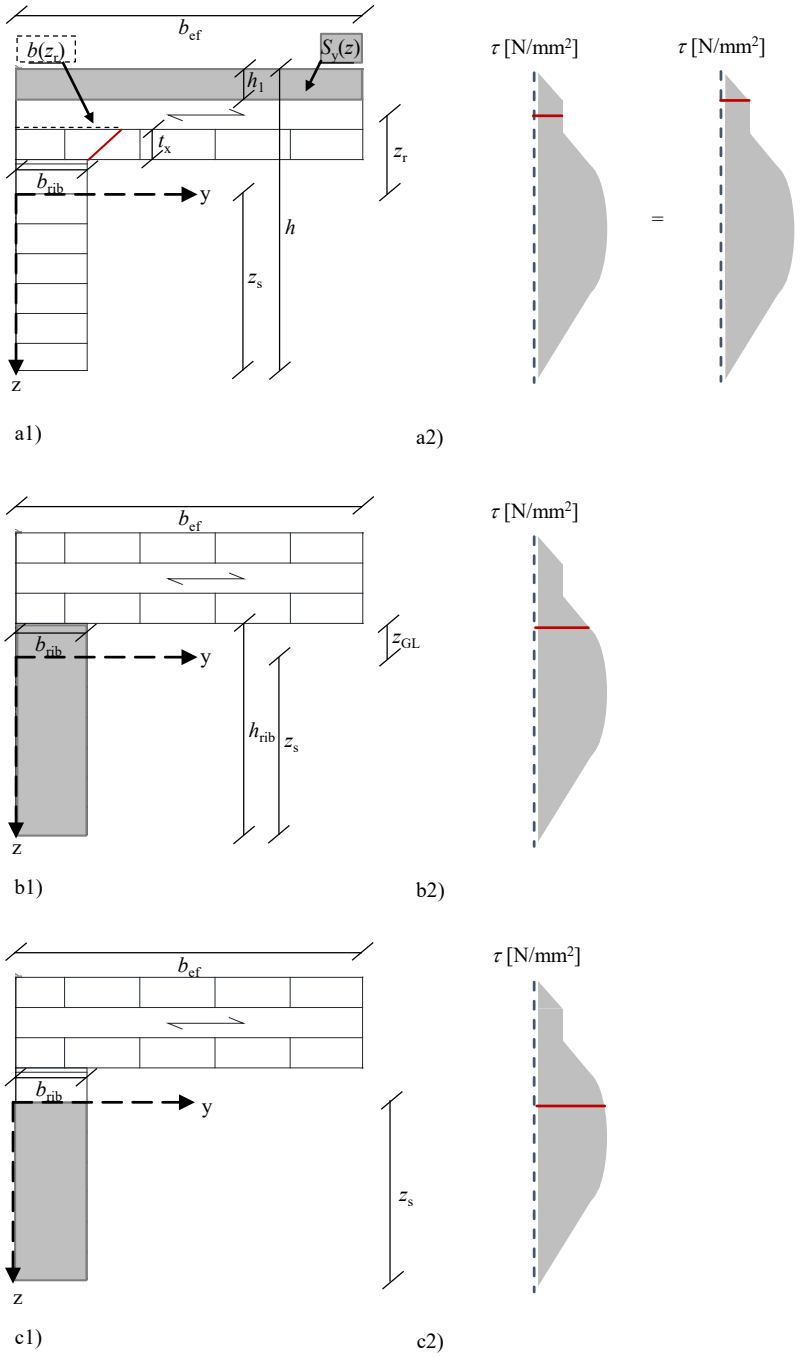

Figure 2.5. Maximum design shear stresses at the support (coordinate $x = 0$): a) Rolling shear (z_r); b) Shear in the glue line (z_{GL}); c) Shear at the centre of gravity (z_s).

(e.g. for medium term action and service class 1 taken as 0.80), and γ_{M} is the partial safety factor for cross-laminated timber taken as 1.25.
The verification of shear in the glue line $\tau_{\mathrm{GL,d}}(z_{\mathrm{GL}})$ can be decisive, calculated according to Formula 2.38

$$\tau_{\mathrm{GL,d}}(z_{\mathrm{GL}}) = \frac{V_{\mathrm{z,d}} \cdot E_{\mathrm{rib}} \cdot S_{\mathrm{y}}(z_{\mathrm{GL}})}{(EI)_{\mathrm{ef}} \cdot b(z_{\mathrm{GL}})} \tag{2.38}$$

with

$$S_{\mathrm{y}}(z_{\mathrm{GL}}) = b_{\mathrm{rib}} \cdot h_{\mathrm{rib}} \cdot (z_{\mathrm{s}} - h_{\mathrm{rib}}/2) \tag{2.39}$$

$$b(z_{\mathrm{GL}}) = b_{\mathrm{rib}} \tag{2.40}$$

where $V_{\mathrm{z,d}}$ is the design shear force in z-direction, E_{rib} is the rib's modulus of elasticity, $S_{\mathrm{y}}(z_{\mathrm{GL}})$ and $b(z_{\mathrm{GL}})$ are the static moment and the tributary width at the height of the glue line, $(EI)_{\mathrm{ef}}$ is the effective bending stiffness of the composite cross-section at the support, b_{rib} and h_{rib} are the rib's width and height, and z_{s} is the centre of gravity of the composite cross-section.
The rigid glue line exhibits high stiffness and shear capacity. In the case of a perfectly rigid glue line, it is assumed that the shear strength of the glue line is higher than the shear strength parallel to the grain of the longitudinal CLT layer. The expression according to Formula 2.41 shall be satisfied

$$\tau_{\mathrm{GL,d}}(z_{\mathrm{GL}}) \leq f_{\mathrm{v,x,d}} \tag{2.41}$$

with

$$f_{\mathrm{v,x,d}} = k_{\mathrm{mod}} \cdot \frac{f_{\mathrm{v,x,k}}}{\gamma_{\mathrm{M}}} \tag{2.42}$$

where $f_{\mathrm{v,x,d}}$ and $f_{\mathrm{v,x,k}}$ are the design and the characteristic strengths for longitudinal shear out-of-plane of cross-laminated timber (section 2.2.2). According to prEN 1995-1-1, k_{mod} is the modification factor taking into account the effect of the duration of load and moisture content (e.g. for medium term action and service class 1 taken as 0.80), and γ_{M} is the partial safety factor for cross-laminated timber taken as 1.25.
Finally, the verification of the maximum shear parallel to the grain $\tau_{\mathrm{COG,d}}(z_{\mathrm{s}})$ can be decisive at the centre of gravity (probably in the glulam rib), calculated according to Formula 2.43

$$\tau_{\mathrm{COG,d}}(z_{\mathrm{s}}) = \frac{V_{\mathrm{z,d}} \cdot E_{\mathrm{rib}} \cdot S_{\mathrm{y}}(z_{\mathrm{s}})}{(EI)_{\mathrm{ef}} \cdot b(z_{\mathrm{s}})} \tag{2.43}$$

with

$$S_{\mathrm{y}}(z_{\mathrm{s}}) = b_{\mathrm{rib}} \cdot z_{\mathrm{s}} \cdot z_{\mathrm{s}}/2 \tag{2.44}$$

$$b(z_{\mathrm{s}}) = b_{\mathrm{rib}} \tag{2.45}$$

where $V_{\mathrm{z,d}}$ is the design shear force in z-direction, E_{rib} is the rib's modulus of elasticity, $S_{\mathrm{y}}(z_{\mathrm{s}})$ and $b(z_{\mathrm{s}})$ are the static moment and the tributary width at the centre of gravity, $(EI)_{\mathrm{ef}}$ is the effective bending stiffness of the composite cross-section at the support, b_{rib} is the rib's width, and z_{s} is the centre of gravity of the composite cross-section.

The expression according to Formula 2.46 shall be satisfied

$$\tau_{\mathrm{COG,d}}(z_{\mathrm{s}}) \leq f_{\mathrm{v,d}} \tag{2.46}$$

with

$$f_{\mathrm{v,d}} = k_{\mathrm{mod}} \cdot k_{\mathrm{cr}} \cdot \frac{f_{\mathrm{v,k}}}{\gamma_{\mathrm{M}}} \tag{2.47}$$

where $f_{\mathrm{v,d}}$ and $f_{\mathrm{v,k}}$ are the design and the characteristic shear strengths of glued-laminated timber (section 2.3.2). According to EN 1995-1-1, k_{mod} is the modification factor taking into account the effect of the duration of load and moisture content (e.g. for medium term action and service class 1 taken as 0.80), k_{cr} is the crack factor taking into account the influence of cracks (for glued-laminated timber), and γ_{M} is the partial safety factor for glued-laminated timber taken as 1.25. In the case of box-sections, the verification of rolling shear, and shear in the glue line have to be checked for the bottom CLT plate, as well.

Serviceability limit state design

For the serviceability limit state, instantaneous and final deflection considering long-term effects should be calculated based on characteristic and quasi-permanent combinations of actions according to EN 1990. Creep deformations and deflection limits would be taken from EN 1995-1-1 and the applicable national annex. In this thesis, only instantaneous deflections are investigated. Therefore, the characteristic combination is used for the calculation of the characteristic value of the sum of actions of the floor system p_{k} based on Formula 2.48

$$p_{\mathrm{k}} = g_{\mathrm{k}} + q_{\mathrm{k}} \tag{2.48}$$

where g_{k} is the characteristic value of the permanent action of the floor system based on Formula 2.16, and q_{k} is the characteristic value of the variable action of the floor system.
Bogensperger (2013) and Thiel et al. (2014) demonstrated the importance of the shear deformations of cross-laminated timber rib panels. Based on the calculation method of the shear-flexible beam (Timoshenko-beam) as extension of the Bernoulli-beam, the shear deflection is added to the bending deflection (section 2.2.3). For a simply supported system with uniform load distribution, the deflection w is calculated according to Formula 2.49

$$w = w_{\mathrm{m}} + w_{\mathrm{v}} \tag{2.49}$$

with

$$w_{\mathrm{m}} = \frac{5 \cdot p_{\mathrm{k}} \cdot l^4}{384 \cdot (EI)_{\mathrm{ef}}} \tag{2.50}$$

$$w_{\mathrm{v}} = \frac{p_{\mathrm{k}} \cdot l^2}{8 \cdot (GA)_{\mathrm{ef}}} \tag{2.51}$$

with

$$(GA)_{\mathrm{ef}} = \kappa \cdot \sum (GA)_{\mathrm{i}} = \kappa \cdot \sum (G_{\mathrm{i}} \cdot b_{\mathrm{i}} \cdot h_{\mathrm{i}}) \tag{2.52}$$

where w_{m} is the bending deflection, w_{v} is the shear deflection, p_{k} is the characteristic value of

the sum of actions (Formula 2.48), l is the span, $(EI)_{\mathrm{ef}}$ is the effective bending stiffness of the composite cross-section at midspan (Formula 2.14), and $(GA)_{\mathrm{ef}}$ is the effective shear stiffness out-of-plane of the composite cross-section. The latter takes into account the shear correction factor κ depending on the type of cross-section. $(GA)_{\mathrm{i}}$ is the individual component's shear stiffness out-of-plane, G_{i} is its shear modulus out-of-plane, b_{i} is its width, and h_{i} is its height. The shear modulus out-of-plane G_{xz} is taken from Table 2.1 and 2.3. For the transversal CLT layers, the shear modulus out-of-plane G_{i} can be taken as zero or as the rolling shear modulus of cross-laminated timber G_{r} according to section 2.2.2. The effective width b_{ef} defines the width b_{i} of both the longitudinal and the transversal CLT layers. The effective width at either side of the rib $b_{\mathrm{ef,i}}$ is calculated according to Formula 2.10.
Using the shear correction factor κ for ribbed plates according to prEN 1995-1-1, the shear flexibility caused by the effect of shear lag of the composite cross-section is taken into account. The shear correction factor κ may be used according to Formula 2.53

$$\kappa = \frac{5}{6} - \frac{1}{4}\frac{(\frac{b_{\mathrm{ef}}}{b_{\mathrm{rib}}})^{0.7}}{(\frac{h_{\mathrm{rib}}}{t_{\mathrm{CL}}})^{0.5}} \tag{2.53}$$

where b_{ef} is the effective width, b_{rib} is the rib width, h_{rib} is the rib height, and t_{CL} is the thickness of the CLT plate.
In Bogensperger (2013), the analyses were limited to T-sections. For the box-sections of this thesis, the shear correction factor is determined according to Formula 2.53 taking the mean value of the top and the bottom CLT plates' effective widths b_{ef} and heights t_{CL}.

2.5 Cross-laminated timber rib panels in fire

2.5.1 Overview

The fire behaviour of timber is characterized by the process of charring. After heating of the wood and evaporation of the water, degradation of the wood begins at approximately 200°C, accompanied by the release of combustible gases (Roberts 1970). This process is called pyrolysis and transforms wood into char coal. The temperature at which timber is considered to be transformed into char is set as 300°C according to EN 1995-1-2. As described in section 2.4.1, the composite components of cross-laminated timber rib panels are rigidly connected by means of screw-press gluing (SPG). The behaviour of this glue line, and the structural behaviour of the system in fire depend on the fire behaviour of the cross-section, and the thermal stability of the polyurethane adhesive of the glue line (Purbond HB S709). The fire behaviour of the cross-section depends on the fire behaviour of the individual cross-section's components, and hence on the thermal stability of the face-bonds between their layers.

2.5.2 Thermal stability of adhesives

Face-bonds between layers

The thermal stability of the face-bonds between the CLT layers is defined as bond line integrity. Depending on whether the integrity of the bond line is maintained or not, the fall-off of charred CLT layers during fire exposure needs to be taken into account for the fire behaviour of the CLT plates (Frangi et al. 2008; Frangi et al. 2009; Mindeguia et al. 2020). The bond line integrity is assumed to be not maintained, unless the thermal resistance of the adhesive has been confirmed (Brandon and Dagenais 2018; Dagenais et al. 2021; Fahrni, Klippel, and Frangi 2021). Requirements and test methods for the assessment of the bond line integrity in fire and the fire performance of CLT are under investigation for inclusion into standards (ANSI/APA PRG 320; prEN 1995-1-2). The possibility of not maintained bond line integrity for the face-bonded glulam layers has not been investigated, yet.

Glue line between cross-laminated timber plate and glued-laminated timber rib

The shear transfer through the glue line of the composite components must be ensured in fire. The behaviour of the glue line's polyurethane adhesive (Purbond HB S709) is unknown for elevated temperatures. Further knowledge of the glue line's behaviour for temperatures up to 200°C can be used to draw conclusions for the thermal stability of the adhesive before the pyrolysis of wood and thus the composite action in fire. The literature study shows that strength properties of glue lines were investigated by small-scale tests at constant elevated temperatures, as being a simple test method for the evaluation of the thermal stability of adhesives.
Frangi, Fontana, and Mischler (2004) performed shear tests of glued timber specimens at elevated temperatures for analysis of the fire behaviour of timber-concrete composite floors. The target temperatures ranged between 20°C and 170°C. Different adhesives were tested including two types of one-component polyurethane (PUR). Linear functions per tested adhesive were determined for the temperature-dependent reduction of the shear strength as approach on the safe side. Possible failure modes were wood failure and adhesive failure in accordance with Schmid (2001). The hypothesis was confirmed that above a certain temperature the failure mode of the adhesive changed from adhesion failure (failure between wood and adhesive) to cohesion failure (adhesive failure in the bond line). Such a change was observed around 70°C for one and around 160°C for the other tested PUR adhesive. The results showed a dependency of the fire behaviour of PUR adhesives on their chemical composition. This outcome was confirmed by Clauss (2011), where the thermal stability of new developed PUR adhesives was significantly increased for temperatures up to 220°C, near the ignition temperature of wood.
The US standard ASTM D7247 describes a standard test method for evaluating the shear strength of adhesive bonds in laminated wood products at elevated temperatures up to 232°C. The adhesive is considered acceptable if the ratio of the mean residual shear strength between 21°C (70°F) and 232°C (450°F) is equal to or higher than the lower 95% confidence interval on the ratio of the mean residual shear strength for the solid timber specimens. Since no requirement for the adhesive shear strength at elevated temperatures higher than 90°C was given in a

European standard, the European test standard EN 17224 recommends the performance criteria according to ASTM D7247. Background information on the establishment of this standard and the development of small-scale shear tests is given by Yeh and Brooks (2006). There, the assumption was pointed out that the adhesives used in timber products do not lose strength more than solid timber when exposed to elevated temperatures.

Figure 2.6 shows the relative shear strength determined from the shear test results given by Frangi, Fontana, and Mischler (2004), Clauss (2011), and Yeh and Brooks (2006). All test specimens were stored under standard climate (temperature 20ºC and relative humidity 65%), were oven-dried to an almost uniform temperature distribution and were loaded until failure at constant temperatures. All test results confirmed the temperature-dependent strength reduction with increasing temperatures for up to 232°C. Different types of PUR adhesives were tested showing different amount of relative shear strength in comparison to the solid timber results (spruce, beech and Douglas fir). Test results by Clauss (2011), and Yeh and Brooks (2006) showed significant reductions in shear strength only at temperatures above 180°C. According to the US performance criteria given in ASTM D7247, the PUR adhesives tested by Yeh and Brooks (2006) performed poorly at 232°C, but two out of three acceptably at 204°C.

Further research investigated strength and stiffness properties under elevated temperatures. Small-scale tests were performed to measure the shear strength of adhesives at elevated temperatures up to 260°C for analysis of the premature delamination behaviour of not fully charred CLT layers (Zelinka et al. 2018; Zelinka et al. 2019). Different adhesives were tested including PUR adhesives. Shear tests at normal temperature were not conducted. A temperature-dependent reduction in shear strength was observed for all specimens, only that the results for the PUR adhesives resulted below solid timber throughout the range of temperatures. The results showed relatively high timber strength. Klippel (2014) investigated the fire behaviour of different adhesives both in small-scale tests at elevated temperatures as well as in fire tests. Finger-jointed small-scale timber members were tested at target temperatures up to 220°C. The work reported by Frangi et al. (2012) was thus extended by one temperature level higher than 140°C. Different adhesives were tested including PUR adhesives. The comparison between tests at elevated temperatures and fire tests did not produce congruent results in terms of adhesive performance, as there was no significant difference in the fire resistance of the tested adhesives. Mäger et al. (2021) performed small-scale tests under cone heater with static loading. Finger-jointed small-scale timber members were tested in tension as indication of the adhesive behaviour. Investigations are ongoing to draw conclusions on the correlation of test methods at elevated temperatures to full-scale fire tests.

The literature study summarises tests for PUR adhesives tested at elevated temperatures close to the ignition temperature. With increasing temperatures, the strength properties decreased for both solid timber and the glue line. The difficulty was addressed in how to implement those results from steady-state heating condition to fire tests under fire exposure.

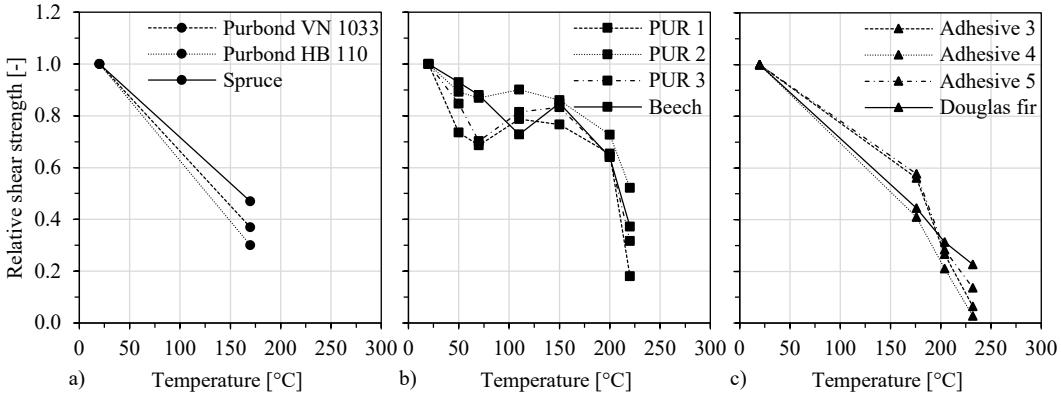

Figure 2.6. Relative shear strength of glue lines at elevated temperatures according to: a) Frangi, Fontana, and Mischler (2004); b) Clauss (2011); c) Yeh and Brooks (2006).

2.5.3 Design in fire

The design of cross-laminated timber rib panels in fire is currently not covered in standards. In this thesis, the fire behaviour and fire resistance are described using the terminology of Eurocode 5 (EN 1995-1-2) and the final draft of the Eurocode 5 part 1-2 revision (prEN 1995-1-2).

Residual cross-section

Figure 2.7 illustrates how the residual cross-section is calculated reducing the initial cross-section from each fire exposed side by the charred depth d_{char}, determined by Formula 2.54

$$d_{\text{char}} = \sum_{Phases} (\beta \cdot t) \tag{2.54}$$

where β is the design charring rate in mm/min of different phases and t is the time in min. Despite the charring process, the rib gains height in the area of transition to the CLT plate, defined as transition zone. The bending stiffness of the transversal CLT layers is taken as zero.

Normal charring

The rectangular residual cross-sections of the glulam rib and the CLT plate are calculated applying to the CLT plates the basic charring rate β_0 for timber members made of softwood of 0.65 mm/min due to one-dimensional charring of the plate ($k_{\text{n}} = 1.0$) and to the ribs the notional charring rate $\beta_{\text{n}} = k_{\text{n}} \cdot \beta_0 = 1.08 \cdot 0.65 = 0.70$ for glulam including the effect of corner rounding.

Stepwise bi-linear charring

In the final draft of the Eurocode 5 part 1-2 revision (prEN 1995-1-2), the charred depth of CLT is modelled using a simplified model, which takes into account two different scenarios: linear charring when the bond line integrity is maintained and stepwise bi-linear charring when

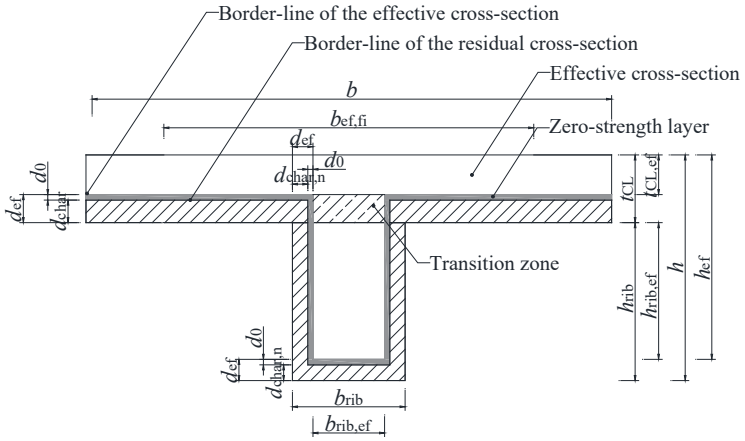

Figure 2.7. Effective cross-section method according to prEN 1995-1-2.

the bond line integrity is not maintained. It means that the fall-off of charred CLT layers is considered when the bond line integrity is not maintained during fire exposure (section 2.5.2). In this thesis, the charred depth d_{char} of the CLT plate is modelled using the stepwise bi-linear model including fall-off of charred CLT layers; the so-called step model (Klippel and Schmid 2017) or European charring model (prEN 1995-1-2). After the fall-off of the first charred CLT layer, the charring rate β_0 for solid wood of 0.65 mm/min is doubled to 1.30 mm/min (post-protected charring) until the charred layer reaches a thickness of 25 mm. Then the charring rate decreases again to the basic value of the charring rate β_0 (consolidated charring). For CLT layers thinner than 25 mm, the doubled charring rate does not decrease until the next layer.

Protected charring

In the case of an initially protected cross-section, encapsulated phases (no charring) and protected charring phases (decreased charring) are defined by the start time of charring t_{ch} and the failure time of the fire protection system (= fall-off time) t_{f}, calculated according to prEN 1995-1-2. For gypsum plasterboards type F, the start time of charring t_{ch} and the failure time t_{f} are determined according to Formulae 2.55-2.58

$$t_{\mathrm{ch}} = min(\sum t_{\mathrm{prot}}; t_{\mathrm{f}}) \tag{2.55}$$

with

$$\sum t_{\mathrm{prot}} = t_{\mathrm{prot},0} = 30 \cdot (\frac{h_{\mathrm{i}}}{15})^{1.2} \tag{2.56}$$

for 1 layer

$$t_{\mathrm{f}} = (1.3 \cdot h_{\mathrm{p}} + 9) \cdot 1.10 \tag{2.57}$$

for 2 layers

$$t_{\mathrm{f}} = (1.5 \cdot h_{\mathrm{p}} + 15) \cdot 1.10 \tag{2.58}$$

where $\sum t_{\mathrm{prot}}$ is the sum of protection times of the gypsum plasterboards, $t_{\mathrm{prot},0}$ is the basic protection time for gypsum plasterboards, and h_{p} is the thickness of the single gypsum

plasterboard panel or the total thickness of multiple panels. For one layer of gypsum plasterboard, h_i is equal to the thickness of the single gypsum plasterboard panel h_1, and for two layers replaced by $h_\mathrm{i} = h_1 + 0.8 \cdot h_2$. Since the gypsum plasterboards are applied to linear or plane timber members, the failure time t_f is increased in Formulae 2.57-2.58 by 10%. After the start of charring, the charring rate is decreased to the protected charring rate according to Formula 2.59

$$\beta = k_2 \cdot k_\mathrm{n} \cdot \beta_0 \tag{2.59}$$

with

$$k_2 = 1 - \frac{h_\mathrm{p}}{55} \tag{2.60}$$

where k_2 is the protection factor for gypsum plasterboards, k_n is the conversion factor, β_0 is the basic charring rate, and h_p is the thickness of the single gypsum plasterboard panel or the total thickness of multiple panels. After the fall-off of the fire protection system, the basic charring rate β_0 for CLT of 0.65 mm/min and the notional charring rate β_n for glulam of 0.70 mm/min are doubled to 1.30 mm/min and 1.40 mm/min (post-protected charring) until the charred layer reaches a thickness of 25 mm. Then the charring rate decreases again to the value of normal charring rate β_0 and β_n (consolidated charring). In the case of an initially protected T-section with void cavities, the start time of charring of the lateral sides of the glulam rib facing the cavity corresponds with the failure time of the fire protection system (post-protected charring).

Effective cross-section

In Eurocode 5, the effective cross-section method determines the part of the cross-section which strength and stiffness properties are assumed to be unaffected for a certain fire resistance time (effective cross-section). Figure 2.7 illustrates how the effective cross-section is calculated adding the zero-strength layer d_0 to the charred depth d_char to reduce the initial cross-section from each fire exposed side by the effective charred depth d_ef, determined by Formula 2.61

$$d_\mathrm{ef} = d_\mathrm{char} + d_0 \tag{2.61}$$

where the zero-strength layer d_0 accounts for the reduction in stiffness and strength of timber under standard fire exposure. The zero-strength layer d_0 for glulam in bending is taken as 10 mm according to prEN 1995-1-2. Depending on the stress distribution along the height of the cross-section, the zero-strength layer d_0 is taken as 12 mm for the CLT plate loaded under tensile bending and as 16 mm for the CLT plate being loaded under compressive bending in accordance with prEN 1995-1-2. If the calculated effective charred depth d_ef is within a transversal layer, it is increased to the end of the transversal layer and supplemented by 2 mm for the CLT plate loaded under tensile bending, by 4 mm for the CLT plate loaded under compressive bending.

Method of flexibly connected bending beams

According to the former Stora Enso European technical approval for cross-laminated timber rib panels ETA-17/0911, the rigid composite action of the cross-section should not have been taken into account in the fire situation. The concern was that the thermal stability of the glue line's polyurethane adhesive (Purbond HB S709) would not be maintained in fire. Therefore, the former Stora Enso structural design manual (Stora Enso 2018) did not guarantee the shear transfer through the rigid connection between CLT plate and glulam rib in fire. Instead, the SPG-screws were activated for the shear transfer. Based on the effective cross-section, the centre of gravity of the composite cross-section in fire $z_{\mathrm{s,fi}}$, the effective bending stiffness of the composite cross-section about the y-axis in fire $(EI)_{\mathrm{ef,fi}}$, and the design stresses in fire $\sigma_{\mathrm{i,d,fi}}(x,z)$ and $\tau_{\mathrm{i,d,fi}}(x,z)$ of component i would have been calculated using the gamma-method of flexibly connected bending beams(EN 1995-1-1; Bogensperger, Silly, and Schickhofer 2012). Here, the bending stiffness of the composite cross-section is decreased by a gamma-value based on the slip modulus for mechanical connections in case of fire due to the flexibility of the composite connection.

Effective width in fire

Current structural design methods for timber structures do not contain a determination method of an effective width in fire. The effective width is unknown and thus limited to the rib width in fire $b_{\mathrm{ef,fi}} = b_{\mathrm{rib,ef}}$.

Verification of stresses in fire

The verification of stresses is carried out in accordance with the design at normal temperature (section 2.4.3). Stiffness properties are used as mean values, without reduction by partial safety factors or reduction factors for stiffness properties. The combination of actions for accidental design situations is used for the calculation of the design value of the sum of actions in fire $p_{\mathrm{d,fi}}$ of the floor system based on Formula 2.62 according to EN 1990

$$p_{\mathrm{d,fi}} = g_{\mathrm{k}} + \psi_1 \cdot q_{\mathrm{k}} \tag{2.62}$$

where g_{k} is the characteristic value of the permanent action of the floor system based on Formula 2.16, ψ_1 is the factor for frequent value of a variable action, and q_{k} is the characteristic value of the variable action of the floor system. Here, ψ_1 is 0.5 according to EN 1990 for Category B: office areas.
The relevant design strength value in fire $f_{\mathrm{d,fi}}$ is determined by Formula 2.63

$$f_{\mathrm{d,fi}} = k_{\mathrm{mod,fi}} \cdot \frac{f_{20}}{\gamma_{\mathrm{M,fi}}} = k_{\mathrm{mod,fi}} \cdot k_{\mathrm{fi}} \cdot \frac{f_{\mathrm{k}}}{\gamma_{\mathrm{M,fi}}} \tag{2.63}$$

where f_{k} is the characteristic strength value of the corresponding material (section 2.2.2 and 2.3.2). According to prEN 1995-1-2, $k_{\mathrm{mod,fi}}$ is the modification factor for fire taken as 1.0, k_{fi} is the modification factor for strength and stiffness property for the fire situation taken as 1.15

for glued-laminated timber and cross-laminated timber, and $\gamma_{M,fi}$ is the partial safety factor for the fire situation taken as 1.0. Depth factor, system factors, or crack factor are not taken into account.

2.5.4 Conclusions

Design rules for cross-laminated timber rib panels at normal temperature are given in EN 1995-1-1 and prEN 1995-1-1. The calculation method of rigidly bonded components is used for the glued composite cross-section. The existing design rules in fire are applied according to EN 1995-1-2 and prEN 1995-1-2. Unless the thermal resistance of the adhesive between the face-bonded CLT layers is confirmed, the integrity of the bond line is assumed to be not maintained and the fall-off of charred CLT layers during fire exposure is taken into account. Due to the uncertain thermal stability of the glue line between CLT plate and glulam rib, the method of flexibly connected bending beams would have been used for the design in fire. The effective width in fire is limited to the rib width in fire $b_{ef,fi} = b_{rib,ef}$.

3. Experimental investigations

3.1 Overview

In this chapter, the design approach and the cross-sections of the experimental program are presented. The experimental investigations cover ultimate-load tests at normal temperature as reference tests, and fire resistance tests exposed to standard fire. In addition to the reference tests, shear tests of the glue line between CLT plate and glulam rib were performed at normal and elevated temperatures for analysis of the cross-sections' composite action. In the reference tests, particular attention is given to the effective bending stiffness, and accordingly to the effective width at midspan. In the full-scale fire tests, particular attention is given to the influence of the screws remaining after screw-press gluing, the fire behaviour, and the composite action of the cross-section. At the end, experimental results are compared and related to each other. The experimental results of the shear tests at normal temperature are compared to the shear tests at 20°C of the shear tests at elevated temperatures. Furthermore, the relative shear strength at elevated temperatures is used to draw conclusions for the glue line's performance under standard fire exposure.
Some results presented in this chapter have been published in Kleinhenz, Just, and Frangi (2021), and Kleinhenz et al. (2021).

3.2 Design approach and cross-section types

Four different cross-sections are evaluated, including two T-sections (one CLT plate as top flange) and two box-sections (CLT plates as top and bottom flanges). One of each cross-section type has been designed as initially protected cross-section. In these tests, no insulation material was used in the cavity. An overview and the geometry of the different cross-sections (A, B, C, and D) of the experimental program are presented in Figure 3.1. The rigid composite action between the cross-sections' components was secured through screw-press gluing (SPG) using the one-component polyurethane adhesive Purbond HB S709 (section 2.4.1). Gypsum plasterboards type F according to EN 520 were installed at the bottom of cross-sections B and D.
The design assumptions were based on Stora Enso reference data. A simply supported system was defined with a span l of 9 m and a CLT width b of 0.933 m. The target bending moment was calculated using a uniformly distributed load ($g_{\mathrm{k}} = g_{\mathrm{k,self\text{-}weight}} + 1.50$ kN/m^2; $q_{\mathrm{k}} = 4.50$ kN/m^2) and the combination of loads for accidental design situations (EN 1990). The effective cross-section method was used for fire resistance times of 60 min (A, C) and 90 min (B, D) taking into

account the encapsulated phase and protected charring phase for initially protected sides of cross-sections B and D, as described in section 2.5.3. Contrary to prEN 1995-1-2, the zero-strength layer for glulam d_0 of 7 mm was used according to EN 1995-1-2 and applied as zero-strength layer for CLT. The verification of normal stresses as combined bending and tension parallel to the grain was decisive at the bottom of the cross-sections at midspan. The verification of normal stresses out of bending $\sigma_{\mathrm{i,d}}$ was not divided into a part out of internal normal force $\sigma_{\mathrm{N,i,d}}$ and a part out of internal bending moment $\sigma_{\mathrm{M,i,d}}$. Contrary to the approach in Stora Enso 2018, the composite action was assumed to maintain rigid. Thus, the calculation method of rigidly bonded components could be applied for the effective cross-section, as described in section 2.4.3. For the design of the four cross-sections, the effective width was limited to the rib width in fire $b_{\mathrm{ef}} = b_{\mathrm{rib,fi}}$. However, the cross-sections were chosen in such a way that the degree of utilisation of the tensile bending capacity was exceeded by up to 20%.
Based on Bratulic and Augustin 2016, a simplified analytical approach was used by TU Graz for an optimised SPG-design. A maximum screw spacing was determined taking into account the required pressure over the rib's width and the minimum screw clamping capacity. The self-weight of the CLT plates was not taken into account. Screw types including screw head diameter d_{head} and screw spacings a are presented in Figure 3.1.
After the design of the cross-sections, the decision was made to conduct the fire resistance tests on a horizontal furnace of 5.20 m length and 3.00 m width (Figure 3.18). Therefore, the test load was recalculated to match the target bending moment of the design using the test length of 5.20 m. The failure mode on tensile bending was still decisive. The experimental program and further investigations are governed by the bending moment to shear force ratio of the furnace.

3.3 Ultimate-load tests under normal temperature

3.3.1 Test setup and procedure

Ultimate-load tests at normal temperature were performed as reference tests for the fire resistance tests at the laboratory of the Institute of Structural Engineering of ETH Zurich between April and June 2019. Twelve test specimens were tested using three replicates per cross-section type of Figure 3.1 (A1-A3, B1-B3, C1-C3, and D1-D3). From arrival to the day of the test, the mean moisture content of the CLT plates dropped from 10% to 9.5% and of the glulam ribs from 13% to 11%. After arrival, the mean density of the plates was 465 kg/m^3 (CoV = 2%) and of the ribs 443 kg/m^3 (CoV = 4%). In advance to the ultimate-load tests, the bending stiffness of the single CLT plates and glulam ribs were determined in bending at two points according to EN 408. The bending stiffness as local modulus of elasticity and the material properties are given in Table 3.1. The local modulus of elasticity of the CLT plates was calculated based on the net cross-section of the longitudinal CLT layers according to EN 16351. The mean value of the local modulus of elasticity of the plates was 13,5 kN/mm^2 (CoV = 4%), of the ribs of test specimens A2 to B3 11,4 kN/mm^2 (CoV = 4%) and of the ribs of test specimens C1 to D3 10.4 kN/mm^2 (CoV = 18%). The above-average value of 15.2 kN/mm^2 of the rib of test specimen A1 is striking. Since also the loadbearing capacity resulted above average for a

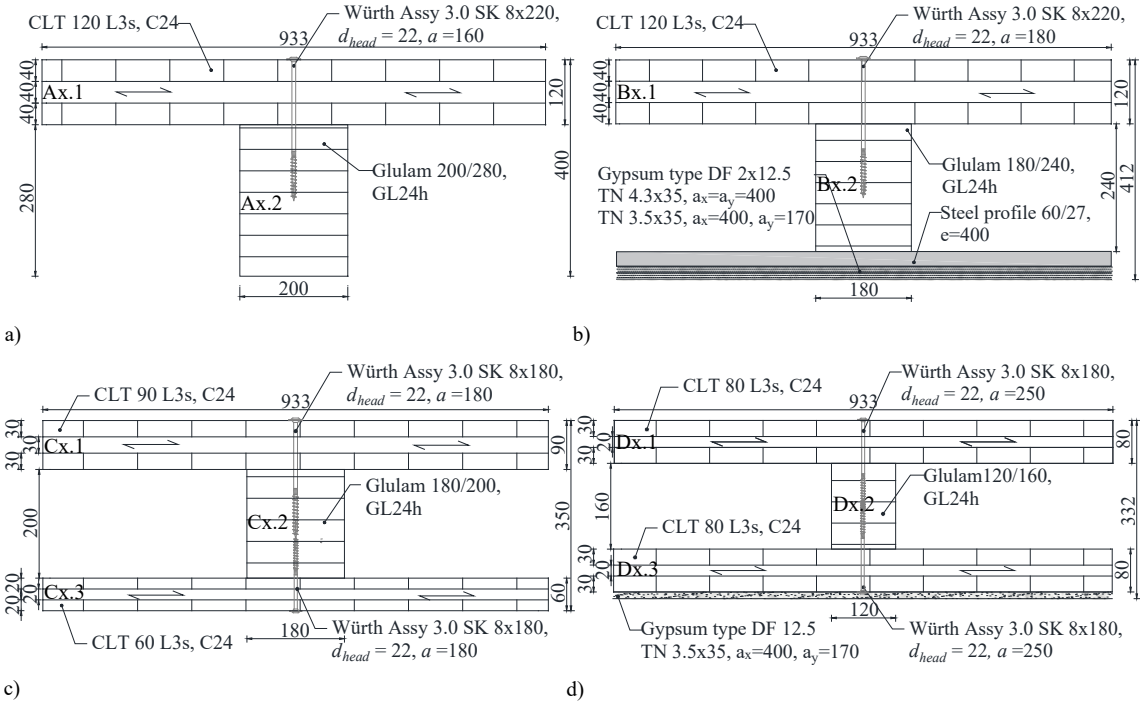

Figure 3.1. Cross-section types of the experimental program including the nomenclature of the components (x = number of replicate per cross-section type), in [mm]: a) T-section (A); b) T-section initially protected (B); c) Box-section (C); d) Box-section initially protected (D).

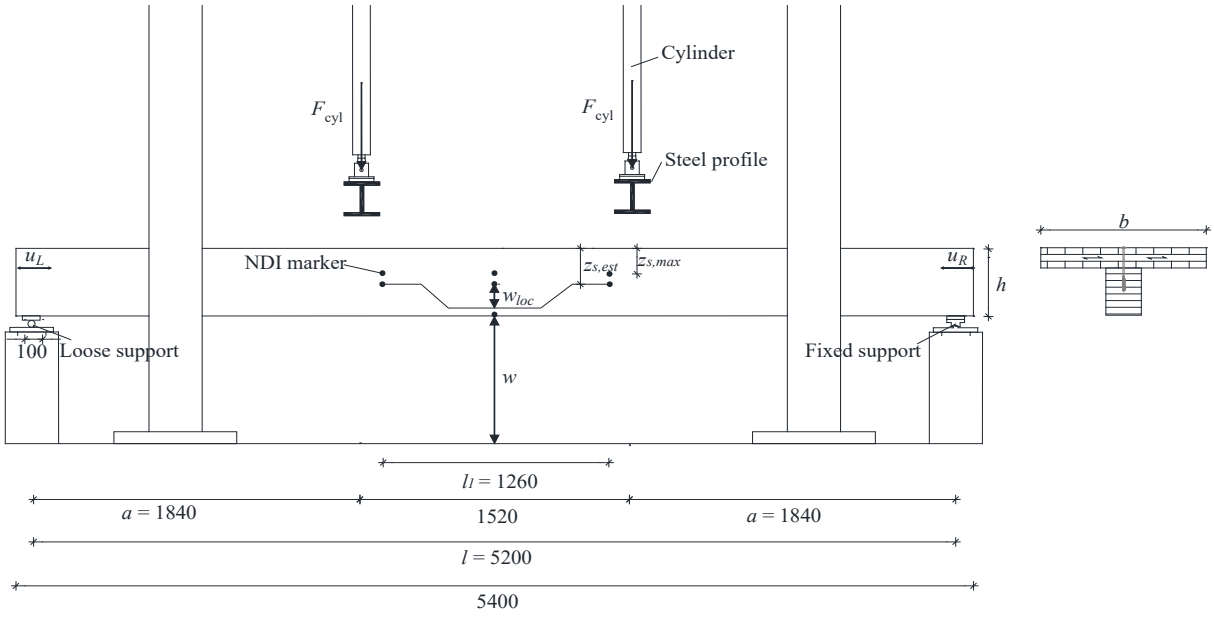

Figure 3.2. Reference tests - Test setup in accordance with EN 408, in [mm].

Figure 3.3. Reference tests - Screw-press gluing at ETH Zurich: a) Application of Purbond HB S709; b) Preparation of large washer head screws; c) Assembly of composite components; d) Assembled test specimen (minimum curing time: 175 min).

rib quality of GL 24h according to EN 14080, test specimen A1 is included in the results but excluded from average values of the analysis.

Subsequently, the single CLT plates and glulam ribs were glued together by Stora Enso by means of screw-press gluing at ETH Zurich (Figure 3.3), using the one-component polyurethane adhesive Purbond HB S709. In the case of box-sections, the rib was prepared upside down for screw-press gluing of the bottom CLT plate on the bottom of the glulam rib. Then, the system was flipped after 240 min for screw-press gluing of the top CLT plate on the top of the glulam rib (minimum curing time: 175 min). An amount of adhesive of around 160 g/m^2 was applied evenly over the sanded surface of the glulam rib. The lab environment was documented as dry climate with a temperature of 23°C and 29% air humidity.

The ultimate-load tests were performed as bending tests in accordance with EN 408. The layers of the ribs exhibited tensile stresses, as in the previous stiffness tests. The test setup had a span l of 5.20 m in accordance with the furnace size (Figure 3.18). The test specimens were simply supported and had one rib with a cross-laminated timber width b of 0.933 m. Cross-sections B and D were tested without gypsum plasterboards. For bending at two points, two hydraulic cylinders applied the mechanical load uniformly with steel profiles of 200 mm depths along the test specimen's width as presented in Figure 3.2. The measurement system included the load cells for the applied cylinder forces F_{cyl}, load cells at the fixed support as control measurement,

Table 3.1. Reference tests - Material properties of each component (cross-laminated timber plates and glued-laminated timber ribs) per test specimen (nomenclature explained in Figure 3.1): Dimensions and moisture content measured at three points over the length.

Component	Type	Strength class	h [mm]	b [mm]	mc [%]	m [kg]	ρ [kg/m^3]	$E_{m,l}$ [MN/m^2]
A1.1	CLT 120 L3s	C24	120	928	9.3	279	463	13008
A2.1	CLT 120 L3s	C24	120	932	9.3	277	458	12936
A3.1	CLT 120 L3s	C24	120	933	8.6	281	464	13000
B1.1	CLT 120 L3s	C24	120	933	10.0	283	467	14008
B2.1	CLT 120 L3s	C24	120	932	9.8	283	469	12906
B3.1	CLT 120 L3s	C24	120	933	9.3	277	457	12509
C1.1	CLT 90 L3s	C24	90	933	7.2	210	463	13563
C2.1	CLT 90 L3s	C24	90	933	9.4	208	459	13772
C3.1	CLT 90 L3s	C24	89	931	8.6	207	462	13582
C1.3	CLT 60 L3s	C24	60	933	9.3	141	465	14076
C2.3	CLT 60 L3s	C24	60	933	7.5	143	473	14336
C3.3	CLT 60 L3s	C24	60	932	7.3	136	449	13329
D1.1	CLT 80 L3s	C24	80	933	10.4	192	475	12761
D2.1	CLT 80 L3s	C24	80	933	8.3	189	469	14058
D3.1	CLT 80 L3s	C24	80	933	8.5	190	471	12664
D1.3	CLT 80 L3s	C24	80	933	9.6	191	473	14095
D2.3	CLT 80 L3s	C24	80	933	10.0	189	468	13918
D3.3	CLT 80 L3s	C24	80	932	10.8	189	468	13600
MEAN					9.1		465	13451
SD					1.0		6.5	558
CoV					0.11		0.01	0.04
A1.2	GLT 200/280	GL24h	278	197	12	144	485	15198
A2.2	GLT 200/280	GL24h	277	198	13.4	133	449	11879
A3.2	GLT 200/280	GL24h	277	198	13.5	128	431	11963
B1.2	GLT 180/240	GL24h	237	178	11.7	99	432	10754
B2.2	GLT 180/240	GL24h	238	177	11.8	100	441	11184
B3.2	GLT 180/240	GL24h	238	178	11.8	101	441	11099
C1.2	GLT 180/200	GL24h	198	178	10.3	79	415	8918
C2.2	GLT 180/200	GL24h	198	177	10.5	80	419	8388
C3.2	GLT 180/200	GL24h	197	178	10.6	85	451	12228
D1.2	GLT 120/160	GL24h	160	120	9.8	48	460	13346
D2.2	GLT 120/160	GL24h	159	120	10.5	45	433	8641
D3.2	GLT 120/160	GL24h	160	120	9.8	48	460	11066
MEAN					11.3		443	11222
SD					1.2		18.8	1884
CoV					0.11		0.04	0.17

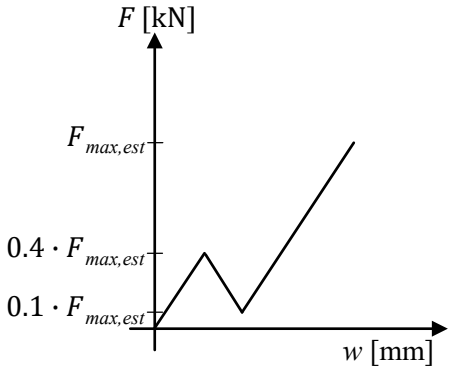

Figure 3.4. Reference tests - Load cycles.

a linear variable differential transformer (LVDT) at midspan for the deflection w, and LVDTs at the supports to measure the horizontal slip u_{R} und u_{L} as relative displacements between CLT plate and glulam rib. An Optotrak Certus position sensor (NDI) was installed to record the local deflection on the front of the specimen. The distance between the test specimen and the position sensor was approximately 3 m. NDI markers were fixed on the surface of the test specimen, which allowed for a 3D tracking of these markers throughout the testing. Their locations are shown in Figure 3.2. One NDI marker was located at the bottom edge of the test specimen at midspan. The LVDT at midspan confirmed the accuracy of the NDI measurement. To determine the local effective bending stiffness in the shear-free zone of the composite cross-section, further markers were placed on the front side of the test specimen at midspan and below the force application points at a distance l_1 of 1.26 m according to EN 408. Over the height of the specimen, these markers were located at two estimated positions of the neutral axis (= global centre of gravity): at $z_{\mathrm{s,max}}$ for the maximum system (width b), and at $z_{\mathrm{s,est}}$ for the estimated system according to prEN 1995-1-1 (width b_{ef}). As the actual position can be assumed to be within these limits, the mean on both cases was calculated as local deflection w_{local}.
The tests were performed under displacement control at a constant rate of 0.2 mm/s, reaching in two load cycles the ultimate load within 500 s (Figure 3.4). In the first load cycle, the load was increased up to 40% of the estimated failure load $F_{\mathrm{max,est}}$ and released again to 10%. In the second load cycle, the test showing linear-elastic load-deflection behaviour was continued until a failure led to a significant load drop.

3.3.2 Static system

Experimental effective bending stiffness

In accordance with EN 408, the experimental effective bending stiffness is calculated as global and local effective bending stiffness $(EI)_{\mathrm{ef,g}}$ and $(EI)_{\mathrm{ef,l}}$ according to Formulae 3.1 and 3.2

$$(EI)_{\mathrm{ef,g}} = \frac{(3 \cdot a \cdot l^2 - 4 \cdot a^2)}{48} \frac{\Delta F}{\Delta w} \tag{3.1}$$

$$(EI)_{\mathrm{ef,l}} = \frac{a \cdot l_1^2}{16} \frac{\Delta F}{\Delta w_{\mathrm{loc}}} \tag{3.2}$$

with

$$\Delta F = 2 \cdot \Delta F_{\mathrm{cyl}} \tag{3.3}$$

where a linear regression is used to determine the slope of the load-deflection curve $\Delta F/\Delta w$ and $\Delta F/\Delta w_{\mathrm{local}}$ of the first load cycle. l is the span, and a is the distance between support and force application, as shown in Figure 3.2.

Experimental and estimated effective width

For a composite cross-section, the effective bending stiffness $(EI)_{\mathrm{ef}}$ is determined by Formula 2.14. Due to the correlation between effective bending stiffness $(EI)_{\mathrm{ef}}$ and effective width b_{ef} (section 2.4.3), the experimental effective widths $b_{\mathrm{ef,test}}$ per test specimen are calculated by equating Formula 2.14 to the local effective bending stiffness $(EI)_{\mathrm{ef,l}}$ according to Formula 3.2. A solve-function of nonlinear equations is used.
The estimated effective width b_{ef} is determined according to prEN 1995-1-1 (section 2.4.2). Since no formula is given for loading in bending at two points, the formula for uniformly distributed loads is used.

Experimental and estimated stresses

In accordance with section 2.4.3, normal stresses at the bottom edge of the glulam rib or the bottom CLT plate (z_{bot}) are calculated according to Formula 3.4

$$\sigma_{\mathrm{i}}(z_{\mathrm{bot}}) = \sigma_{\mathrm{N,i}} + \sigma_{\mathrm{M,i}} = \frac{M_{\max} \cdot E_{\mathrm{i}}}{(EI)_{\mathrm{ef}}} \cdot z_{\mathrm{bot}} \tag{3.4}$$

with

$$\sigma_{\mathrm{N,i}} = \frac{M_{\max} \cdot E_{\mathrm{i}}}{(EI)_{\mathrm{ef}}} \cdot z_{\mathrm{i}} \tag{3.5}$$

$$\sigma_{\mathrm{M,i}} = \frac{M_{\max} \cdot E_{\mathrm{i}}}{(EI)_{\mathrm{ef}}} \cdot \frac{h_{\mathrm{i}}}{2} \tag{3.6}$$

Shear stresses at the centre of gravity (z_{s}), and in the glue line (z_{GL}) are calculated according to Formulae 3.7 - 3.8

$$\tau_{\mathrm{COG}}(z_{\mathrm{s}}) = \frac{\frac{F_{\max}}{2} \cdot \sum ES_{\mathrm{y}}(z_{\mathrm{s}})}{(EI)_{\mathrm{ef}} \cdot b(z_{\mathrm{s}})} \tag{3.7}$$

$$\tau_{\mathrm{GL}}(z_{\mathrm{GL}}) = \frac{\frac{F_{\max}}{2} \cdot \sum ES_{\mathrm{y}}(z_{\mathrm{GL}})}{(EI)_{\mathrm{ef}} \cdot b(z_{\mathrm{GL}})} \tag{3.8}$$

where $(EI)_{\mathrm{ef}}$ is the effective bending stiffness, $\sum ES_{\mathrm{y}}(z)$ is the sum of the static moment at the coordinate z of the composite cross-section, and $b(z)$ is the width at the individual

coordinate z. Maximum force $F_{\max}$ and bending moment $M_{\max}$ include self-weight of the test specimen. Furthermore, the formulae consider the modulus of elasticity E_{i}, the height h_{i}, and the distance to the global centre of gravity z_{i} of the individual component i; i.e. glulam rib or bottom CLT plate. The bending stiffness as local modulus of elasticity and the dimensions of the single CLT plates and glulam ribs are taken from Table 3.1. For the calculation of the shear stresses, the effective bending stiffness at the support is considered as equal to the effective bending stiffness at midspan.
The stresses can be calculated as experimental or estimated stresses. Therefore, the effective bending stiffness is taken either as local effective bending stiffness $(EI)_{\mathrm{ef,l}}$ according to Formula 3.2 or as estimated effective bending stiffness $(EI)_{\mathrm{ef}}$ according to Formula 2.14. Either the experimental result or the estimated result according to prEN 1995-1-1 is taken as effective width b_{ef} of the cross-section.

Estimated bending and shear ratio

For the investigation of the influence of the effective width b_{ef} on the stresses, normalized ratios are defined as bending ratio r_{m} and shear ratio r_{v} according to Formulae 3.9 and 3.10

$$r_{\mathrm{m}} = \frac{(EI)_{\mathrm{ef}}}{E_{\mathrm{i}} \cdot z_{\mathrm{i}}} \tag{3.9}$$

$$r_{\mathrm{v}} = \frac{(EI)_{\mathrm{ef}}}{\sum ES_{\mathrm{y}}(z_{\mathrm{i}})} \tag{3.10}$$

where $(EI)_{\mathrm{ef}}$ is the effective bending stiffness of the composite cross-section according to Formula 2.14, $\sum ES_{\mathrm{y}}(z_{\mathrm{i}})$ is the sum of the static moment at the coordinate z_{i} of the composite cross-section, and E_{i} is the modulus of elasticity of component i. The ratios depend on the effective width b_{ef} of the system.

Experimental and estimated deflection

The experimental bending deflection $w_{\mathrm{m,test}}$ is subtracted from the experimental deflection w to obtain the experimental shear deflection $w_{\mathrm{v,test}}$, as shown in Formula 3.11

$$w_{\mathrm{v,test}} = w - w_{\mathrm{m,test}} \tag{3.11}$$

with

$$w_{\mathrm{m,test}} = \frac{F_{\mathrm{cyl,max}} \cdot a \cdot (3l^2 - 4a^2)}{24 \cdot (EI)_{\mathrm{ef,l}}} \tag{3.12}$$

where $F_{\mathrm{cyl,max}}$ is the maximum load per cylinder, $(EI)_{\mathrm{ef,l}}$ is the local effective bending stiffness according to Formula 3.2, l is the span, and a is the distance between support and force application, as shown in Figure 3.2.
For the simply supported system loaded in bending at two points, the deflection w_{est} is estimated as sum of the estimated bending deflection $w_{\mathrm{m,est}}$ and the estimated shear deflection $w_{\mathrm{v,est}}$.

according to Formula 3.13

$$w_{\text{est}} = w_{\text{m,est}} + w_{\text{v,est}} \tag{3.13}$$

with

$$w_{\text{m,est}} = \frac{F_{\text{cyl,max}} \cdot a \cdot (3l^2 - 4a^2)}{24 \cdot (EI)_{\text{ef}}} \tag{3.14}$$

$$w_{\text{v,est}} = \frac{F_{\text{cyl,max}} \cdot a}{(GA)_{\text{ef}}} \tag{3.15}$$

with

$$(GA)_{\text{ef}} = \kappa \cdot \sum (GA)_{\text{i}} = \kappa \cdot \sum (G_{\text{i}} \cdot b_{\text{i}} \cdot h_{\text{i}}) \tag{3.16}$$

where $F_{\text{cyl,max}}$ is the maximum load per cylinder, l is the span, and a is the distance between support and force application, as shown in Figure 3.2. The effective width b_{ef} of the system is estimated according to prEN 1995-1-1. $(EI)_{\text{ef}}$ is the effective bending stiffness according to Formula 2.14, and $(GA)_{\text{ef}}$ is the effective shear stiffness. The latter takes into account the shear correction factor κ depending on the type of cross-section. $(GA)_{\text{i}}$ is the individual component's shear stiffness out-of-plane, G_{i} is its shear modulus out-of-plane, b_{i} is its width, and h_{i} is its height. The shear modulus out-of-plane G_{xz} is taken from Table 2.1 and 2.3. For the transversal CLT layers, the shear modulus out-of-plane G_{i} is taken as the rolling shear modulus of cross-laminated timber G_{r}, according to section 2.2.2. The modulus of elasticity and the dimensions of the single CLT plates and glulam ribs are taken from Table 3.1.
For the single CLT plates, the shear correction factors κ are determined according to Formula 2.7, resulting in a uniform value of 0.30. For the single glulam ribs, the shear correction factor κ is taken for a rectangular beam, $\kappa = 5/6 = 0.83$. For the test specimens assembled as cross-laminated timber rib panels, the shear flexibility caused by the composite section's shear lag is taken into account by using the shear correction factor κ according to prEN 1995-1-1. The shear correction factors κ are determined according to Formula 2.53. Even though, the analyses were limited to one CLT plate as top flange, Formula 2.53 is used for the determination of the shear correction factors κ of the box-sections, taking the mean value of the top and the bottom CLT plates' effective widths b_{ef} and heights t_{CL}. The shear correction factor κ results on average in a value of 0.42 for all test specimens (CoV = 19%).

3.3.3 Results

Measurements and observations

Table 3.2 lists the measurements, and the observed failure modes per test specimen. The test specimens assembled as T-section exhibited brittle failure under tensile bending stresses at the bottom of the rib at midspan in expected stress ranges. Test specimen C1 exhibited brittle shear failure in the rib at the right support. It is worth noticing that test specimen C1 exhibited a low-modulus of elasticity of 8.9 kN/mm^2 for a rib quality of GL 24h according to EN 14080 and the lowest density of 415 kg/m^3 compared to all ribs (Table 3.1). The shear verification results in a maximum shear stress in the rib of 2.2 N/mm^2. Test specimens C2 to D3 exhibited shear failure in the glue line between CLT plate and glulam rib at the supports. The shear failures in

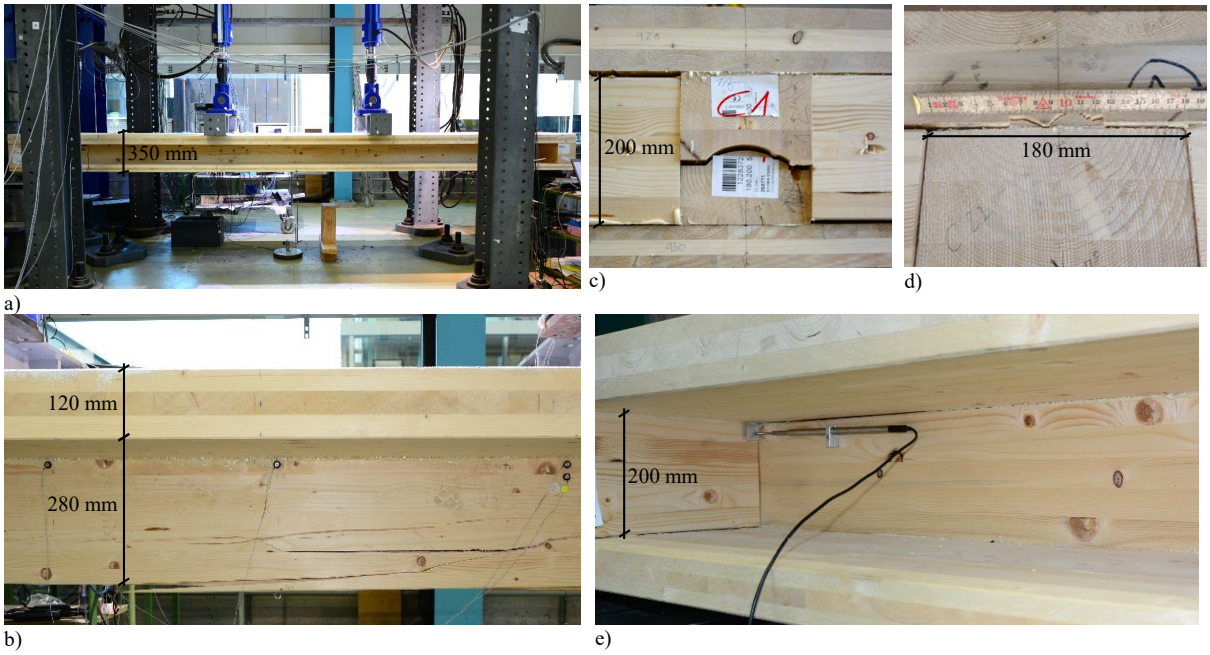

Figure 3.5. Reference tests - a) Front view of test specimen in the test setup (test specimen C1); b) Front view of tensile bending failure at the bottom of the rib at midspan (test specimen A2); c) Side view of shear failure in 2/5 rib height at the right / fixed support (test specimen C1); d) Front view + e) Side view of shear failure in the top glue line at the left / loose support (test specimen C2).

the glue line were located directly in the glue line and not in the wood of the longitudinal CLT layer. They were observed at both specimen ends and in both glue lines: C2, C3, and D3 failed in the top glue line, while D1 and D2 failed in the bottom glue line. Rolling shear failure in the cross layers of the CLT was not observed. The different failure types are shown in Figure 3.5. Figure 3.5 shows that the test specimens were assembled as done in practice, including blocking ends framing the ribs at both specimen ends. The blocking ends were screw-press glued to the CLT plates and unfixed to the ribs, to which they were about 1 mm less in height. In order to exclude their influence on the failure behaviour, the blocking ends were cut horizontally at mid height before testing test specimen D1, which failed in the glue line, as well.

Figure 3.6 presents the force-deflection-curve of the deflection w for all test specimens. Test specimens B1-B3 exhibited high deflections in combination with the lowest forces, indicating the lowest stiffness. The other test specimens show similar force-deflection behaviour. The mean value of all test specimens is 41 mm for the deflection w, and 2.20 mm for the local deflection w_{loc}. The experimental shear deflection $w_{\mathrm{v,test}}$ was determined in average to 10 mm, thus 24% of the deflection w, respectively 32% of the bending deflection $w_{\mathrm{m,test}}$. Figure 3.7 presents the force-deformation-curve of the horizontal slip u as mean value of the measurements at the right and left support for all test specimens. The difference between both positions is negligible. In the case of the box-sections, the horizontal slip is shown for the failed glue line, except for test specimen C3. The maximum horizontal slip of all glue lines is 0.80 mm for test specimen C2. The mean value of all unfailed glue lines is 0.24 mm, while 0.45 mm for all failed glue lines. The glue lines deformed less than 1.00 mm. The failure behaviour is brittle.

Table 3.2. Reference tests - Maximum load per cylinder, ultimate load including self-weight, and corresponding deflections and horizontal slip per test specimen including the observed failure modes.

Test specimen	Cross-section type	Failure			$F_{\mathrm{cyl,max}}$	F_{max}	w	$w_{\mathrm{v,test}}$	w_{loc}	u_{mean}
		Type	Position	Location						
					[kN]	[kN]	[mm]	[mm]	[mm]	[mm]
A1	T	Tensile bending	Midspan	Bottom edge of rib	176	356	53	16	2.7	0.36
A2					88	181	31	9	1.5	0.20
A3					106	216	38	9	2.1	0.23
B1					93	190	46	8	2.9	0.35
B2					78	160	42	9	2.5	0.17
B3					76	156	38	5	2.3	0.25
C1	Box	Shear	Support	Rib	102	208	34	9	1.8	0.19
C2	Box	Shear in glue line	Support	Top glue line	147	298	52	15	2.7	0.80
C3				Top glue line	110	224	38	9	2.1	0.17[2)]
D1[1)]				Bottom glue line	112	228	43	12	2.2	0.33
D2				Bottom glue line	99	202	38	10	2.0	0.31
D3				Top glue line	98	200	37	9	2.0	0.36
Mean					107	219	41	10	2.2	0.31

[1)] Blocking ends at the supports were horizontally cut.

[2)] Horizontal slip was measured in the unfailed glue line.

Experimental effective bending stiffness

The experimental effective bending stiffness are presented in Table 3.3. The global and local effective bending stiffness according to Formulae 3.1 and 3.2 show homogeneous results per cross-section type, except for A due to test specimen A1 (see section 3.3.1).

Experimental effective width

The experimental effective widths $b_{\mathrm{ef,test}}$ are presented in Table 3.3. The high differences per cross-section type indicate the sensitivity of the determination of the effective width $b_{\mathrm{ef,test}}$ with regard to the measurement accuracy.

Experimental stresses

In Table 3.3, the experimental stresses (Formulae 3.4 - 3.8) are compared to mean strength values determined according to JCSS based on 5% fractile strength values of EN 14080 and prEN 1995-1-1. The effect of the glulam member size on the bending or tensile strengths, and the influence of cracks of the glulam ribs are not taken into account. The determined mean strength values are the following: mean tensile strength $f_{\mathrm{t,mean}}$ of the glulam rib (parallel to the

grain) or the bottom CLT plate (in-plane), mean bending strength $f_{\mathrm{m,mean}}$ of the glulam rib or the bottom CLT plate (out-of-plane), mean shear strength of the glulam rib $f_{\mathrm{v,mean}}$ and mean strength for longitudinal shear out-of-plane of the longitudinal CLT layer $f_{\mathrm{v,x,mean}}$. The results confirm that the tensile bending capacity was decisive or even exceeded for the test specimens of cross-section type A, B, and C. The results indicate that bending capacity and shear capacity in the centre of gravity were equally decisive for the test specimens of cross-section type D.

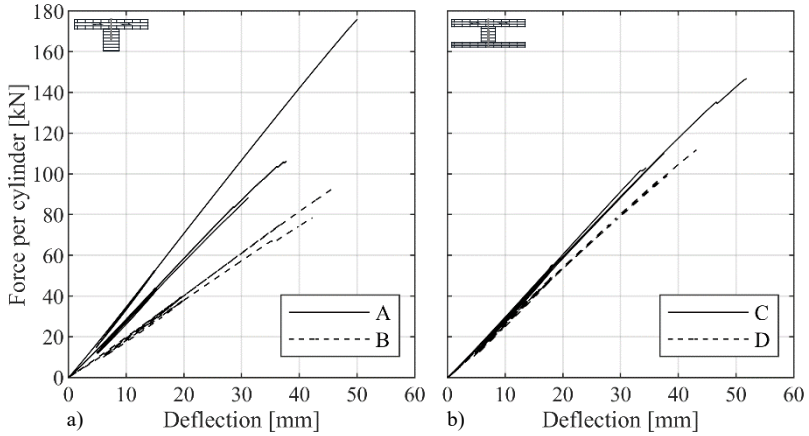

Figure 3.6. Reference tests - Deflection at midspan of all test specimens: a) T-sections; b) Box-sections.

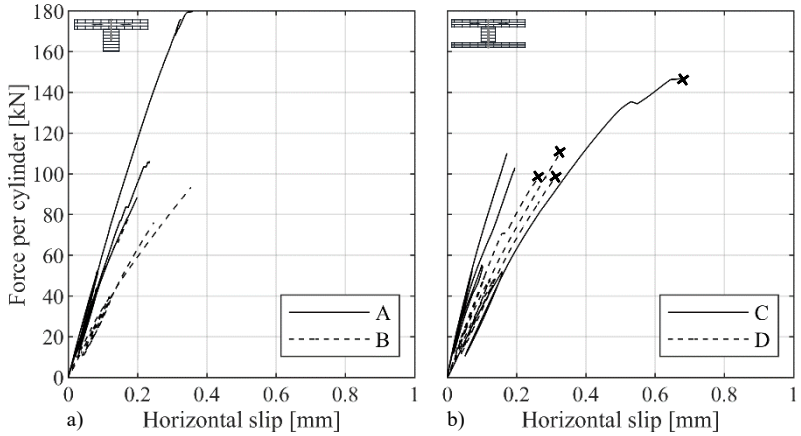

Figure 3.7. Reference tests - Horizontal slip as relative displacement between CLT plate and glulam rib of all test specimens (failed glue lines marked with x): a) T-sections; b) Box-sections.

3.3.4 Discussion

Composite action and glue line quality

The horizontal slip was measured at the location of the highest shear force, i.e. at the supports (Table 3.2). A mean value of 0.24 mm is reached for the unfailed glue line. Frangi and Fontana (2000) tested timber-concrete composite slabs. For the connection between the composite components defined as rigid, horizontal slip between timber and concrete was measured

less than 0.50 mm. Gu (2017) performed bending tests on cross-laminated timber rib panels tested as hollow-core system using mechanical connectors (i.e. inclined screws) to attach the CLT plates to the glulam ribs. Horizontal slip less than 2.00 mm was measured, defining the connection as quasi-rigid. Jacquier and Girhammar (2015) performed bending tests on cross-laminated timber rib panels using a flexible connection of double-sided punched metal plate fasteners and inclined screws. The test series were compared to a single reference test made with screw-press gluing, representing full composite action. A one-component polyurethane glue Purbond HB110 (250 g/m^2) was used in combination with vertical SFS Intec screws WFD-T-H12-8×180 with large washer heads of 28 mm diameter. Failure in the glue line was not observed (Jacquier 2015). Horizontal slip up to 15 mm was measured between the CLT plate and the glulam rib, while less than 0.10 mm was measured for the single reference test. The comparison to experimental data from the literature confirms the rigid composite action by means of screw-press gluing.
According to the experimental loadbearing capacities, tensile bending failure was expected to be decisive for all test specimens. The test specimen assembled as box-sections were expected to fail in the bottom CLT plate. The unexpected glue line failures opened the investigation on the glue line quality. During assembly of the test specimens, it was observed that the surface quality of the box-sections' ribs of smaller heights was noticeably different from that of the T-sections' ribs. Dimensional deviations of up to 10 mm / 5.20 m (3.8 mm / 2.00 m) were observed. In parallel to the experimental program, a simplified analytical approach for the SPG-design was published by Bratulic, Augustin, and Schickhofer (2019) for the same type of adhesive. Here, the necessity was explained to compensate possible dimensional deviations due to shrinkage and swelling of timber members, or varying production quality. The approach increases the minimum required pressure by an additional pressure to compensate these dimensional production inaccuracies estimated with about 2.5 mm / 2.00 m for CLT and glulam components (section 2.4.1). The large dimensional inaccuracies of the box-sections' ribs have not been compensated by the minimum required pressure representing ideal gluing conditions. As a result, smaller screw spacings would have been required, at least for the box-sections.

Comparison of experimental and estimated deflection

Figure 3.8a and b compares the estimated deflections w_{est} with the experimental deflections w of the single CLT plates and glulam ribs. The results show perfect correlation. The estimated shear deflections $w_{\mathrm{v,est}}$ account maximum 3% of the estimated deflections w_{est}. Thus, the influence of the shear flexibility was negligible; especially for the slender CLT plates.
Figure 3.8c compares the estimated deflections $w_{\mathrm{EC5:20xx}}$ according to prEN 1995-1-1 with the experimental deflections w (Table 3.2) of the specimens assembled as cross-laminated timber rib panels. The estimated shear deflections $w_{\mathrm{v,est}}$ result on average in 7.5 mm, which is below the average value of the experimental shear deflections $w_{\mathrm{v,test}}$ of 10 mm. In the case of T-sections, the results show perfect correlation. In the case of box-sections, the analytical approach overestimates the experimental deflections by 12% for the test specimens C1-C3, and by 30% for the test specimens D1-D3. The latter represent the cross-section with the smallest

Table 3.3. Reference tests - Experimental effective bending stiffness, effective width, and degrees of utilisation of the loadbearing capacities (decisive failure highlighted in bold letters).

Test specimen	Cross-section type	Effective bending stiffness		Effective width	Tensile bending	Shear in rib	Shear in glue line
		$(EI)_{\mathrm{ef,g}}$	$(EI)_{\mathrm{ef,l}}$	$b_{\mathrm{ef,test}}$	$\sigma_{\mathrm{N,test}}/f_{\mathrm{t,mean}} + \sigma_{\mathrm{M,test}}/f_{\mathrm{m,mean}}$	$\tau_{\mathrm{COG,test}}/f_{\mathrm{v,mean}}$	$\tau_{\mathrm{GL,test}}/f_{\mathrm{v,x,mean}}$
		[MNm^2]	[MNm^2]	[m]	[-]	[-]	[-]
A1	T	18.6	24.2	0.92	**1.73**	0.74	0.61
A2		14.8	20.9	0.90	**0.83**	0.37	0.31
A3		15.4	19.1	0.74	**1.04**	0.45	0.37
B1		10.6	12.8	0.73	**1.18**	0.48	0.40
B2		10.0	12.2	0.63	**1.04**	0.41	0.34
B3		10.5	12.0	0.65	**1.01**	0.40	0.33
C1	Box	16.0	20.9	0.80	0.79	**0.49**	0.39
C2	Box	15.9	20.7	0.74	1.24	0.69	**0.54**
C3		15.4	19.9	0.74	0.87	0.53	**0.41**
D1[1)]		14.0	18.7	0.71	0.89	0.87	**0.68**
D2		14.4	18.1	0.68	0.82	0.76	**0.60**
D3		14.5	18.0	0.72	0.78	0.76	**0.60**

[1)] Blocking ends at the supports were horizontally cut.

$h_{\mathrm{rib}}/t_{\mathrm{CL}}$-ratio. The results indicate that the shear correction factor κ needs to be redetermined for box-sections. The box-sections' effective bending stiffness might be underestimated, leading to too high bending deflections.

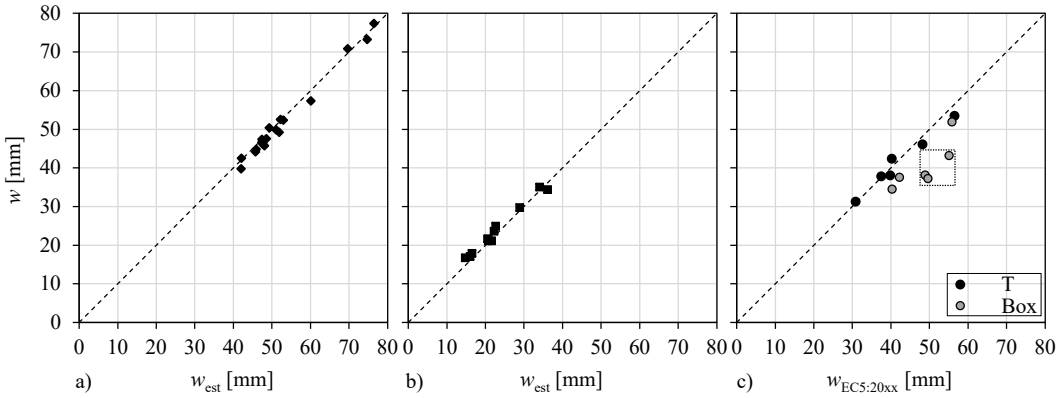

Figure 3.8. Reference tests - Experimental and estimated deflections of the components and the test specimens: a) Cross-laminated timber plates; b) Glued-laminated timber ribs; c) T- / box-sections (D1-D3 marked).

Comparison of experimental and estimated effective width

Figure 3.9a presents the experimental effective width $b_{\mathrm{ef,test}}$ of Table 3.3 in comparison to the estimated effective width b_{ef} according to prEN 1995-1-1 of each test specimen. While the

experimental effective width is on average 78% of the CLT width (SD = 0.07 m, CoV = 9%), it is estimated at 60% (SD = 0.04 m, CoV = 7%). Differences of the estimated effective widths are based on differences in dimensions and bending stiffness (Table 3.1).
Figure 3.9b presents degrees of utilisation of the experimental tensile bending capacity of Table 3.3 in comparison to the degrees of utilisation of the estimated capacity of each test specimen. For the T-sections (A2-B3), the underestimation of the composite system by the estimated effective width b_{ef} is negligible when comparing the tensile bending capacities. While an experimental degree of utilisation on average of 102% is achieved, it would be estimated to 107% according to prEN 1995-1-1. For the box-sections (C1-D3), the underestimation demonstrates a higher influence. While a degree of utilisation of the experimental tensile bending capacity on average of 90% is achieved, it would be overestimated to 122% according to prEN 1995-1-1. The reason therefor are the smaller ribs of the box-sections in combination with a higher number of longitudinal CLT layers (Figure 3.1). A decreased effective bending stiffness ratio between glulam rib and longitudinal CLT layers increases the influence of the CLT layers on the effective bending stiffness of the composite system $(EI)_{\mathrm{ef}}$ according to Formula 2.14. Thus, the influence of the effective width b_{ef} increases and the impact of the underestimation of the effective width b_{ef} is more severe.

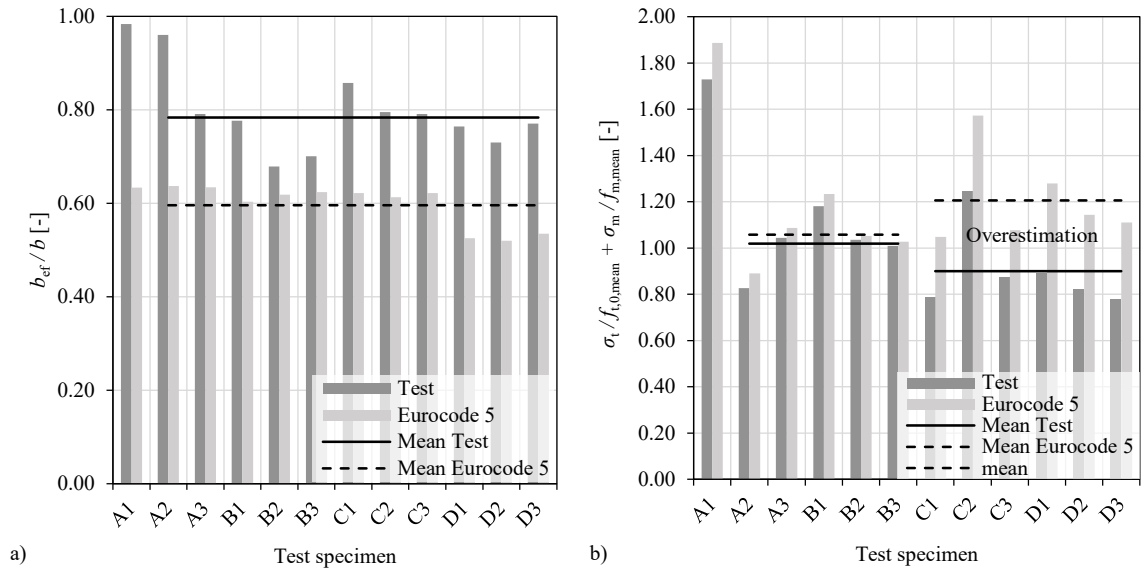

Figure 3.9. Reference tests - Experimental and estimated results of the tests specimens tested at normal temperature: a) Ratio of effective width to CLT width; b) Degrees of utilisation of the tensile bending capacity.

Influence of the effective width

Figure 3.10 presents the influence of the effective width to the CLT width ratio b_{ef}/b on the following factors per test specimen type (T-section, and box-section) and cross-section type (A, B, C, and D): the effective bending stiffness of the composite cross-section $(EI)_{\mathrm{ef}}$ according to Formula 2.14, the sum of the static moment $\sum ES_{\mathrm{y}}(z_{\mathrm{i}})$ (section 2.4.3), the bending ratio r_{m} according to Formula 3.9, and the shear ratio r_{v} according to Formula 3.10. All factors are

dependent on the effective width b_{ef}, which is varied between the rib width b_{rib} and the CLT width b. For the bending ratio, the coordinate z_{i} is taken at the top edge of the CLT plate (top), and at the bottom edge of the glulam rib or the bottom CLT plate (bot). For the shear ratio, the coordinate z_{i} is taken at the height of the glue line between CLT plate and glulam rib (GL), at the centre of gravity (COG) and at the height of the bottom glue line between bottom CLT plate and glulam rib (GL bot). Figure 3.10 shows the results calculated from the experimental effective widths $b_{\mathrm{ef,test}}$ and estimated effective widths b_{ef}, taken as mean values per cross-section type from Figure 3.9a. Dimensions and material properties are taken as mean values per cross-section type from Table 3.1.
Both the effective bending stiffness of the composite cross-section $(EI)_{\mathrm{ef}}$, and the sum of the static moment $\sum ES_{\mathrm{y}}(z_{\mathrm{i}})$ show an increase of equivalent slope with an increased effective width b_{ef}. The same applies for the bending ratio r_{m}. However, the shear ratio r_{v} remains nearly unchanged as a fraction of the effective bending stiffness and the sum of the static moment. The effective width b_{ef} has a higher influence on the bending behaviour and thus on the bending stresses than on the shear behaviour and the shear stresses.
The slopes within the figure of each stiffness factor are comparable and independent of the coordinate z_{i}, except for the bending ratio r_{m} of the T-sections. Here, a higher increase in the rate of change is achieved for coordinates z_{i} taken at the edges of the CLT plates than at the bottom edge of the glulam rib. This results from the fact that the height of the glulam rib h_{rib} has a higher influence on the bending stiffness at the bottom edge of the glulam rib than the effective width b_{ef}. In comparison, the box-sections have smaller ribs in combination with a higher number of longitudinal CLT layers and thus a higher dependency on the effective width b_{ef} (Figure 3.1). The bending ratio r_{m} and the effective bending stiffness $(EI)_{\mathrm{ef}}$ of the box-sections show a linear behaviour and a higher increase in the rate of change than the stiffness of the T-sections. As indicated by Figure 3.9, the effective width b_{ef} has a higher influence on the box-sections than on the T-sections.

3.3.5 Conclusions

In the ultimate-load tests at normal temperature, the horizontal slip and its comparison to experimental data from literature confirms the rigid composite action between CLT plate and glulam rib by means of screw-press gluing. In the case of box-sections, the glue line quality was insufficient due to not plane surface conditions during SPG-procedure. The results confirm the necessity to increase the minimum required pressure by an additional pressure in the case of dimensional inaccuracies to ensure an adequate glue line quality like proposed by Bratulic, Augustin, and Schickhofer (2019).
The comparison of experimental and estimated deflections shows perfect correlation for the single components (CLT plates and glulam ribs). The results confirm that the method of rigidly bonded components gives good results, especially in the case of the slender CLT plates ($l/t_{\mathrm{CL}} > 30$). For the fully assembled cross-laminated timber rib panels, the comparison confirms the importance to take into account the deflection caused by shear lag based on the analytical approach according to prEN 1995-1-1 (Bogensperger 2013; Thiel et al. 2014). In the case of T-sections, the results

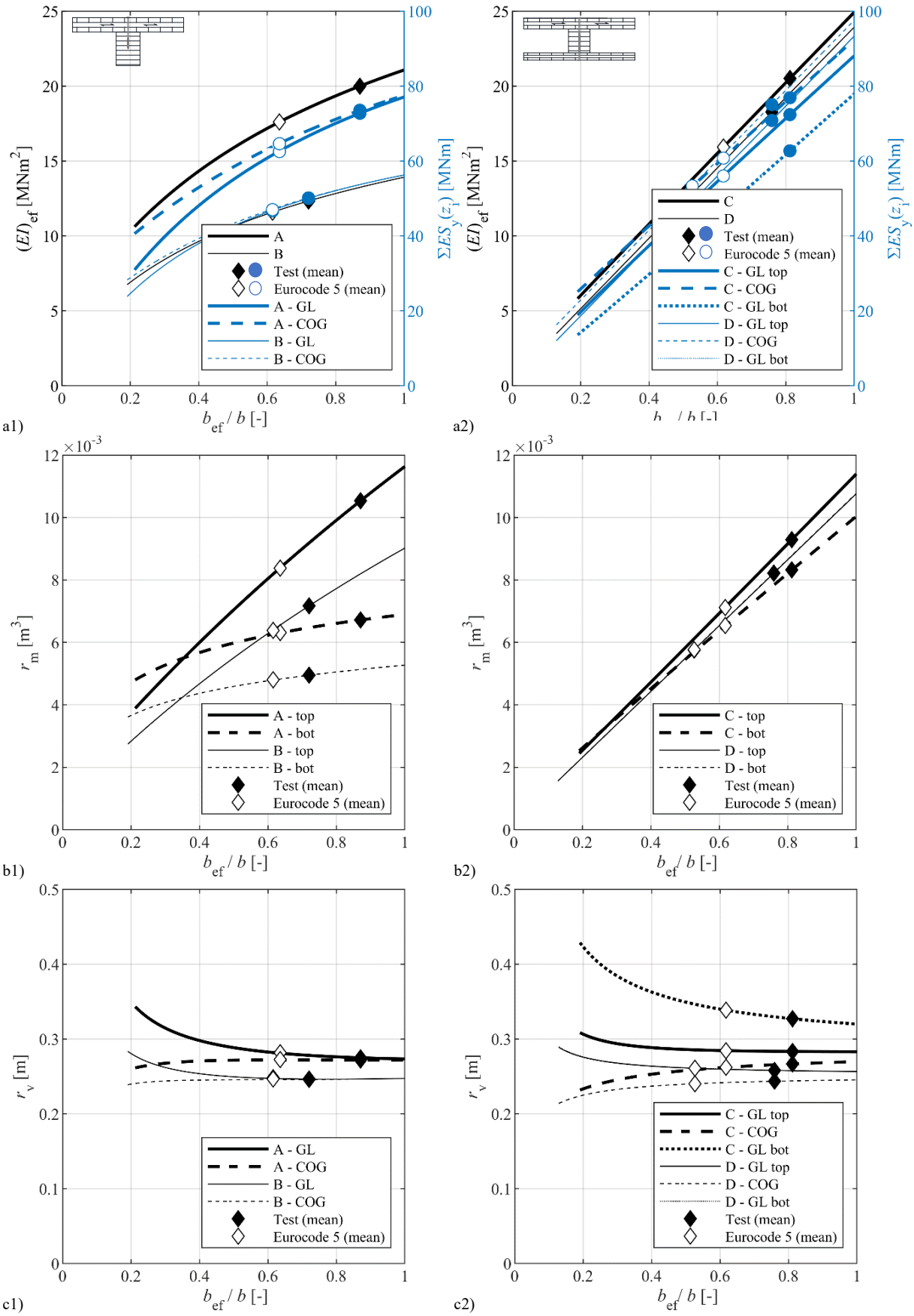

Figure 3.10. Reference tests - Influence of the effective width on 1) T-section (A,B), and 2) box-section (C,D): a) Effective bending stiffness and the sum of the static moment at the coordinate z_i of the composite cross-section; b) Bending ratio; c) Shear ratio.

show perfect correlation. In the case of box-sections, the analytical approach overestimates the experimental deflections.
The formula for the effective width at normal temperature b_{ef} according to prEN 1995-1-1 for uniformly distributed load gives results on the safe side for loading at two points. While the experimental effective width $b_{ef,test}$ is on average 78% of the CLT width, prEN 1995-1-1 estimates it to 60% of the CLT width for the given system ($b_{f,i}/l = 0.14, \sum t_x/t_{CL} = 0.67$). The experimental loadbearing capacity of test specimens tested as T-sections show very good agreement with the estimated loadbearing capacity. The experimental results correspond to the estimated mean strength values. The loadbearing capacity of test specimens tested as box-sections are substantially underestimated.
All in all, the effective width b_{ef} has a higher influence on the bending behaviour and thus on the bending stresses than on the shear behaviour and the shear stresses. Furthermore, the effective width b_{ef} has a higher influence on the box-sections than on the T-sections. Based on analyses limited to cross-sections with one CLT plate as flange on top, the determination of the effective width b_{ef} according to prEN 1995-1-1 can be evaluated as conservative approach for box-sections, underestimating the effective bending stiffness, and the loadbearing capacity. The shear correction factor κ for ribbed plates according to prEN 1995-1-1 needs to be redetermined. The box-sections' effective bending stiffness might be underestimated, leading to too high bending deflections.

3.4 Shear tests of the glue line at normal temperature

3.4.1 Test setup and procedure

From the test specimens of the reference tests including test specimen A1 (presented in section 3.3), test pieces were drilled out via tenon cutter from each glue line between CLT plate and glulam rib, as explained in Figure 3.11. CLT plates and glulam ribs had been glued together by Stora Enso by means of screw-press gluing at ETH Zurich, using the one-component polyurethane adhesive Purbond HB S709 (section 3.3.1). In total, six test pieces (three replicates per glue line) were taken from each glue line of the twelve test specimens. In the case of box-sections, the test pieces were drilled out from areas of intact glue line (from midspan until opposite support). Since box-sections have top and bottom glue lines, 18 glue lines needed to be examined. In total, 108 drill cores of 35 mm diameter were drilled out, of which one half of the replicates, i.e. 54 drill cores, were used for shear tests at normal temperature at ETH Zurich in October 2019. In addition, two test pieces of each glue line between CLT plate and glulam rib of the twelve test specimens were cut out for a further analysis of the bond line's thickness (36 test pieces in total). The bond line includes both the adhesive bulk between the wood surfaces and the penetrated wood fibres. The thickness was measured using a microscope of 100-fold magnification by Stora Enso.
In the shear tests at normal temperature, the test pieces were cut to 50 mm length and tested as core specimens of 35 mm diameter (CoV = 0.4%) following the approach of Gaspar, Cruz, and Gomes (2018). The tested glue line laid perpendicular to the axis and in the middle of the

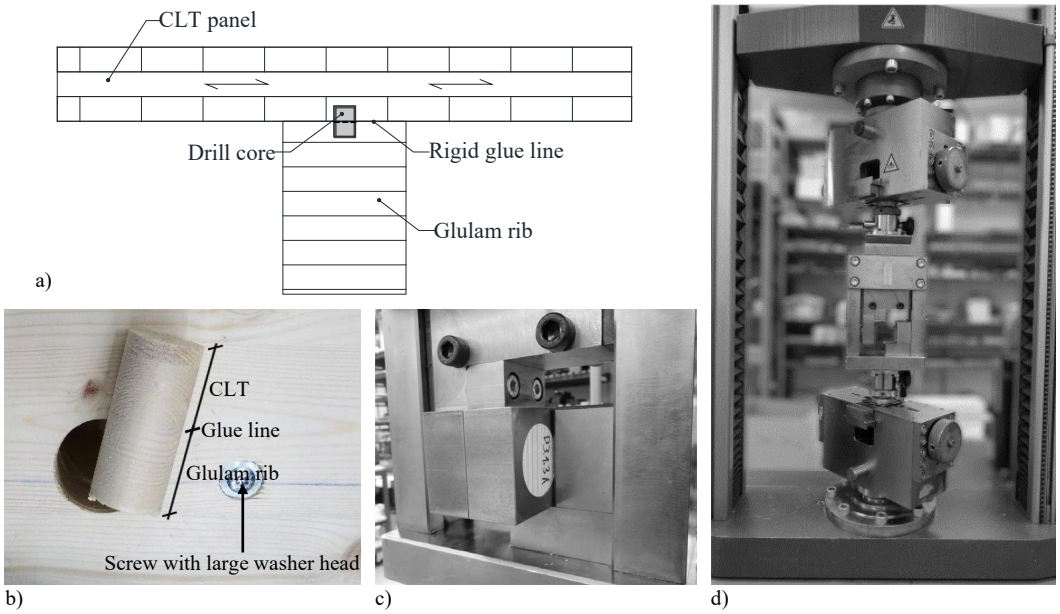

Figure 3.11. Shear tests of the glue line at normal temperature: a) Schematic of core specimen position; b) Core specimen of 35 mm diameter; c) Position of core specimen in metal cube; d) Shear testing device.

core specimens. The core specimens were conditioned to an equilibrium moisture content under standard climate 20/65 in a climate room, where the shear tests were performed later on. Before the tests, the mean density was determined as 451 kg/m^3 (CoV = 8%). After the tests, the mean moisture content of the core specimens was determined as 11.5% by kiln drying method. The shear tests until failure were performed according to EN 14080, Annex D and prEN 16351, Annex G. Figure 3.11 presents test setup and position of the core specimen during the shear test. The core specimens were loaded in the direction of the grain. The tests were performed under displacement control at a constant rate of 0.02 mm/s, reaching ultimate load within 120 s.

3.4.2 Results

A mean value of 0.07 mm results for the thickness of the bond line (CoV = 14%). Shear strengths are determined according to EN 14080 using ultimate load, sheared area, and the factor k_v modifying the shear strength for test pieces where the thickness in the grain direction of the sheared area is less than 50 mm. The relationship is given by Formula 3.17

$$k_\mathrm{v} = 0.78 + 0.0044 \cdot t \tag{3.17}$$

where t is the thickness in the grain direction of the sheared area.
The amount of wood failure percentage (WFP) of the failed sheared area per core specimen was recorded visually. It is the percentage of the area showing wood failure (= rupture in or between wood fibres) in relation to the total sheared area according to EN 14080. In advance to the shear tests, the glue line between CLT and glulam rib had been marked for differentiation with other glued joints. Figure 3.12 compares the failed sheared area of two extreme cases. The

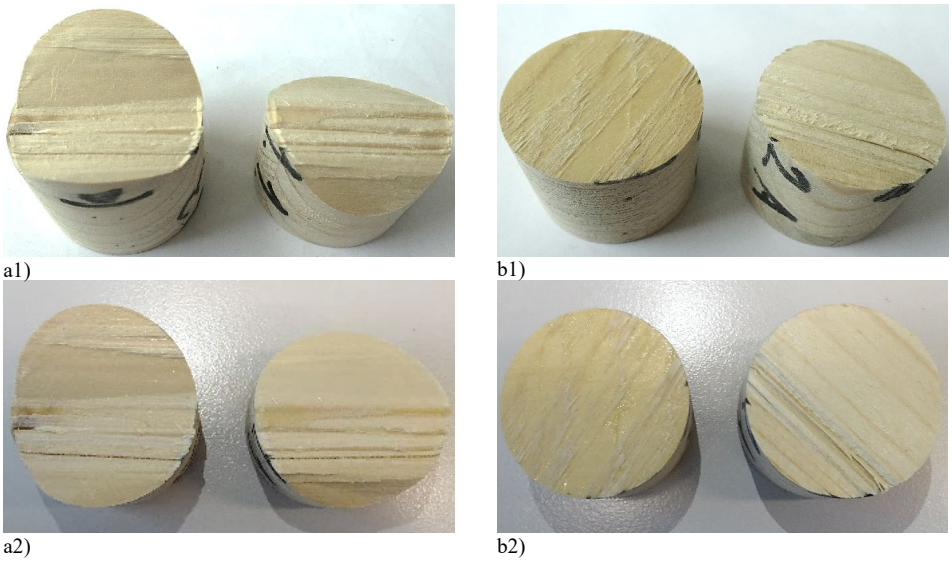

Figure 3.12. Shear tests of the glue line at normal temperature - Amount of wood failure percentage of the failed sheared area in the shear tests of the glue line: a1)+a2) A3 drill core (WFP = 95%); b1)+b2) C3 drill core (WFP = 10%).

amount of wood failure percentage was estimated for the A3 drill core at 95% (wood failure) and for the C3 drill core at 10% (glue line failure). The former shows a small amount of glue line in the centre. The latter shows regularly amount of glue line over the sheared area.
Figure 3.13 presents the shear strength f_v related to the wood failure percentage rounded off to the nearest number divisible by five. Table 3.4 presents mean value and coefficient of variation (CoV) per type of core specimen. The "T-section" core specimens exhibited shear failure in amount of wood failure percentage on average of 98%. In comparison, the "box-section" core specimens exhibited shear failure in amount of wood failure percentage on average of 71% and of almost eight time larger dispersion. In a further step, the results of box-sections are differentiated between drill cores taken from the top and the bottom glue line. The mean shear strength of "box-section - top" core specimens matches with a shear strength of 7.3 N/mm^2 and a CoV of 16% with the results of "T-section" core specimens. The absolute difference in wood failure percentage is 20%. The mean shear strength and the wood failure percentage of "box-section - bottom" core specimens result only in 5.7 N/mm^2 and 65%.

3.4.3 Discussion

The bond line thickness of 0.07 mm is in agreement with the requirement according to EN 15425 defining the maximum bond line thickness for general purpose in use as 0.3 mm. The results of "T-section" core specimens comply with the requirements of EN 14080 except in the case of one core specimen (shear strength: 3.8 N/mm^2, wood failure percentage: 100%). The experimental results are comparable to results presented by Bratulic, Augustin, and Schickhofer (2019), where the range of shear strength resulted between 2.0 and 10.0 N/mm^2 for the same type of adhesive. Of the results of "box-section" core specimens, 37% are outside the required minimum values. Furthermore, the mean shear strength of "box-section - bottom" core specimens

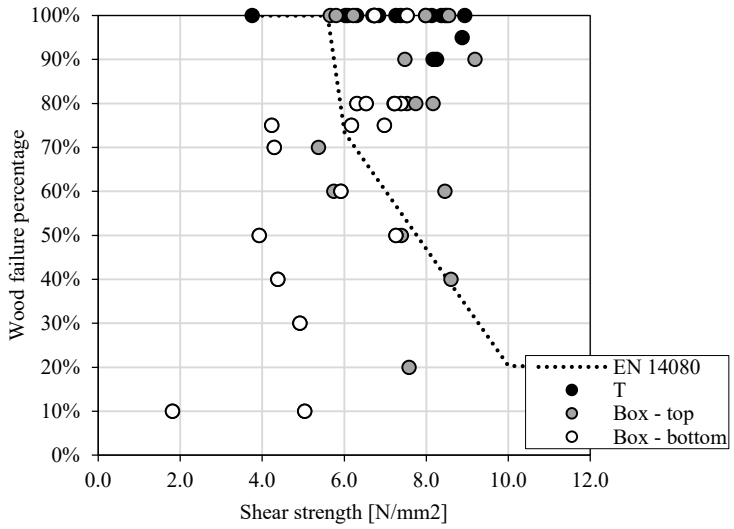

Figure 3.13. Shear tests of the glue line at normal temperature - Shear strength related to wood failure percentage (requirements according to EN 14080 included as minimum values).

Table 3.4. Shear tests of the glue line at normal temperature - Experimental results per type of specimen.

	Shear strength			Wood failure percentage		
	$f_{v,mean}$			Mean		
	[N/mm^2]			[%]		
T	7.4 (CoV = 17%)		7.4 (CoV = 16%)	98 (CoV = 5%)		88 (CoV = 22%)
Box - top	6.5 (CoV = 24%)	7.3 (CoV = 16%)		71 (CoV = 37%)	78 (CoV = 30%)	
Box - bottom	5.7 (CoV = 26%)			65 (CoV = 42%)		

results with 5.7 N/mm^2 outside the requirements. The amount of wood failure percentage results in higher adhesive failure for the bottom than the top glue lines.
In the reference tests, shear failures in the glue line were observed in both glue lines (Table 3.3). However, the results of the shear tests indicate an insufficient glue line quality especially for the bottom glue lines. This could have been caused by flipping the test specimens too early during SPG-procedure. The results indicate that the curing time of 240 min was not sufficient for the bottom glue line (section 3.1). Low air humidity of the lab may have delayed the adhesive's curing process compared to conditions in the standard climate 20/65.

3.4.4 Conclusions

The bond line thickness of 0.07 mm passes the European requirement. The results of "T-section" core specimens comply with the requirements according to EN 14080. As observed in the reference tests (section 3.3.4), the insufficient glue line quality of the box-sections is confirmed. The results of the shear tests of the glue line between CLT plate and glulam rib of

"box-section" core specimens emphasize the importance of the required quality control during the procedure of screw-press gluing as a basic requirement for sufficient glue line quality.

3.5 Shear tests of the glue line at elevated temperatures

3.5.1 Test setup and procedure

Further knowledge of the glue line's behaviour between CLT plate and glulam rib is of interest for a wider range of temperatures. Of the second half of replicates drilled out from the reference tests (section 3.4.1), 48 of 54 drill cores were sent for shear tests at elevated temperature to RISE, Stockholm. The remaining six test pieces stayed at ETH Zurich using them as dummies to define the heating period for reaching the defined target temperatures (20°C, 95°C, 140°C, and 220°C). One test piece was cut to the target dimensions and equipped with a thermocouple for measuring the temperature in the glue line area at the centre of the test piece. The thermocouple was inserted into the test piece by drilling a hole at a 90° angle. The hole was closed by an insulation tape. Afterwards, the test piece was stored in an oven at the target temperature of 220°C. Figure 3.14a presents the temperatures over time measured at the centre of the test piece in comparison to temperatures measured by another thermocouple inside the oven. Figure 3.14b presents the numerical results of thermal simulations using a 3D FE model of the test piece (see section 4.7.2) and exposing all edges to a constant temperature (95°C, 140°C, and 220°C). The experimental and numerical results are in good agreement. The heating period was defined as 45 min.

The drill cores were cut to a rectangular sheared area being directly placed into a universal testing machine. All test pieces were cut to cross-sections of 25x25 mm^2 (CoV = 9%) with 50 mm length. The tested glue line laid perpendicular to the axis and in the middle of the block specimens. The block specimens were conditioned to an equilibrium moisture content under standard climate 20/65. The shear tests until failure were performed in accordance with EN 17224, with the exception that the specimens were neither oven-dried for 48 hours nor cooled in a desiccator. As required, test setup and procedure were performed according to EN 14080, Annex D. First, the block specimens were stored in an oven for 60 min at the specific target temperature, adding a storage time to the heating period of 15 min. Then, the test pieces were taken out of the oven and tested as quickly as possible. The tests were performed under displacement control at a constant rate of 5 mm/min (= 0.08 mm/s), reaching ultimate load within 60 s. Four block specimens of each glue line type were tested per target temperature (20°C, 95°C, 140°C, and 220°C). The four temperature series represent the reference series at 20°C, the series before evaporation of water, and the series close to the ignition temperature. The target temperature of 140°C was chosen in accordance with Klippel (2014).

3.5.2 Results

Shear strengths are determined according to EN 14080 using ultimate load, sheared area, and the factor k_{v} modifying the shear strength for test pieces where the thickness in the grain direction of the sheared area is less than 50 mm, as given in Formula 3.17. For the

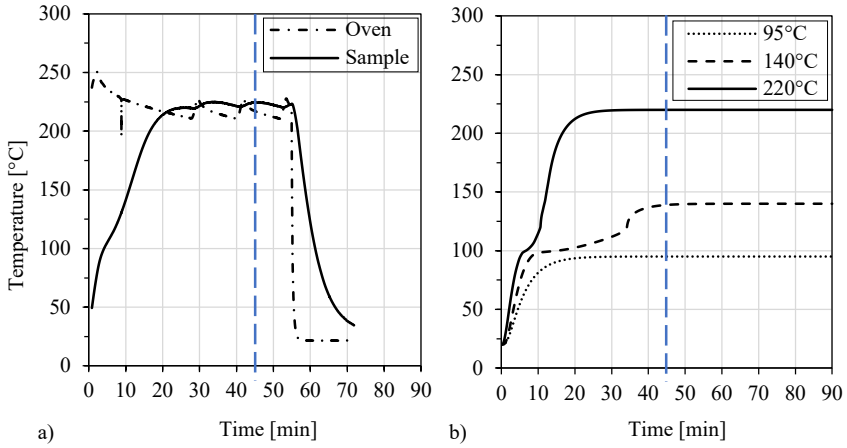

Figure 3.14. Shear test of the glue line at elevated temperatures - Heating period according to EN 17224: a) Measurements in oven; b) Numerical results of FE analysis.

determination of the sheared area, the block specimens' cross-section was measured after the test. The amount of wood failure percentage of the failed sheared area per block specimen was recorded visually according to EN 14080. No charring was observed as the temperatures stayed below the ignition temperature of wood, but the colour of wood was significantly darker at 220°C (see Figure 3.15). Figure 3.16 presents the experimental results on shear strength f_v and the wood failure percentage rounded off to the nearest number divisible by 10 in box and whisker plots. Table 3.5 presents mean value and coefficient of variation (CoV) depending on the target temperature. Due to negligible differences in wood failure percentage, the results of "T-section" and "box-section - top" block specimens are merged into one group. Until 140°C, wood failure was decisive in all tests. At 220°C, a wood failure percentage of almost 0% was observed. The mean shear strength decrease from 9.2 N/mm^2 at 20°C to 3.1 N/mm^2 at 220°C. The results of "box-section - bottom" reach lower shear strength for all tested temperatures. The wood failure percentages result in lower values with higher dispersion unless at 140°C.

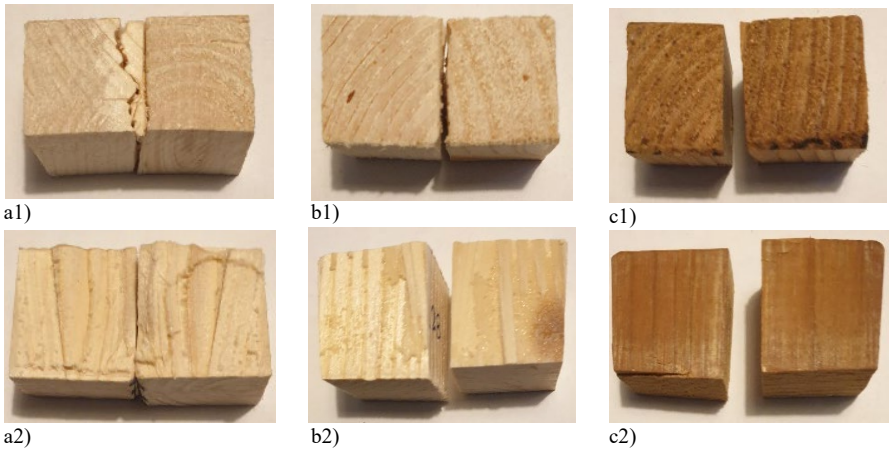

Figure 3.15. Shear test of the glue line at elevated temperatures - Wood failure percentage of the failed sheared area shown from 1) side and 2) top view: a) Block specimen tested at 20°C (WFP = 100%); b) Block specimen tested at 140°C (WFP = 40%); c) Block specimen tested at 220°C (WFP = 0%).

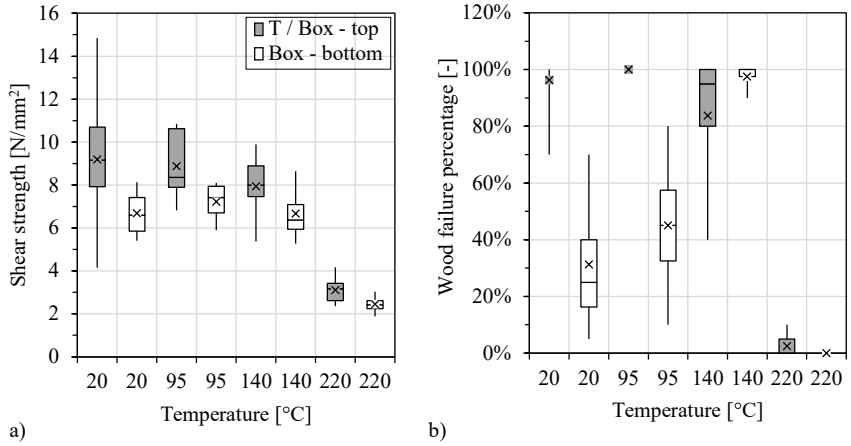

Figure 3.16. Shear test of the glue line at elevated temperatures - Results according to EN 14080 including mean, median, minimum and maximum values as well as second and third quartile: a) Shear strength; b) Wood failure percentage.

Table 3.5. Shear tests of the glue line at elevated temperatures - Experimental results per target temperature and type of specimen.

	20°C		95°C		140°C		220°C	
	Shear strength	Wood failure percentage	Shear strength	Wood failure percentage	Shear strength	Wood failure percentage	Shear strength	Wood failure percentage
	$f_{v,mean}$ [N/mm²]	Mean [%]	$f_{v,mean}$ [N/mm²]	Mean [%]	$f_{v,mean}$ [N/mm²]	Mean [%]	$f_{v,mean}$ [N/mm²]	Mean [%]
T / Box - top	9.2 (CoV = 34%)	96 (CoV = 10%)	8.9 (CoV = 17%)	100 (CoV = 0%)	7.9 (CoV = 18%)	84 (CoV = 27%)	3.1 (CoV = 18%)	3 (CoV = 0%)
Box - bottom	6.7 (CoV = 16%)	31 (CoV = 77%)	7.2 (CoV = 12%)	98 (CoV = 4%)	6.7 (CoV = 19%)	45 (CoV = 56%)	2.4 (CoV = 17%)	0 (CoV = 0%)

3.5.3 Discussion

The results indicate an insufficient quality of the glue line in the case of “box-section - bottom” block specimens. Therefore, the further discussion focuses on the results of “T- / box-section - top” block specimens. Until 95°C, failure occurred with a probability of 100% in or between wood fibres. The large dispersion might be an indication of the large scatter of wood properties. At 140°C, the amount of wood failure percentage decreases with increasing dispersion, announcing the increased thermal weakening of the glue line compared to the wood. Between 140°C and 220°C, the mode of failure changed from wood failure to adhesive failure and further from adhesion to cohesion failure, which would be difficult to separate. Figure 3.15 shows amounts of wood failure percentage and how modes of failure changed from wood to adhesive failure with increasing temperatures.

Figure 3.17a presents the results of the shear strength with increasing temperatures as single values and mean distribution including all types of wood failure percentage. In addition,

the single shear strength values of block specimens with 100% wood failure percentage are shown. Their mean values per tested temperature represent the shear strength of solid timber. Figure 3.17b presents the relative shear strength or residual shear strength ratio according to EN 17224. The non-linear reduction of the shear strength is comparable to Clauss (2011), Yeh and Brooks (2006) and Zelinka et al. (2019) (section 2.5.2) and might be explained by the interaction between shrinkage and thermal expansion. Glos and Henrici (1990) observed the effect of a temperature-related strength reduction, which is superimposed by a drying-related increase in strength properties of undried timber. Clauss (2011) observed this effect for temperatures below 110°C. Above 110°C, the test specimens reached oven-dry density. Higher relative shear strengths are obtained in comparison to Frangi, Fontana, and Mischler (2004) and Yeh and Brooks (2006). The PUR adhesive shows comparable thermal stability to the PUR adhesives presented in Clauss (2011). The relative shear strength dropped to around 30% at 220°C. A strength reduction to 0% could have been expected around 270°C extrapolating the test curve of "T- / box-section - top" block specimens in Figure 3.17.
According to ASTM D7247, it is considered acceptable if the relative shear strength does not fall below the lower 95% confidence interval on the relative shear strength for solid timber. This depends on the further development of the relative shear strength for solid timber. Based on the assumption of a strength reduction to 0% at 300°C, the relative shear strength for solid timber is extended in a simplified way in Figure 3.17b. Following this assumption, the change from wood to adhesive failure occurred around 180°C, with a relative shear strength of 60%.

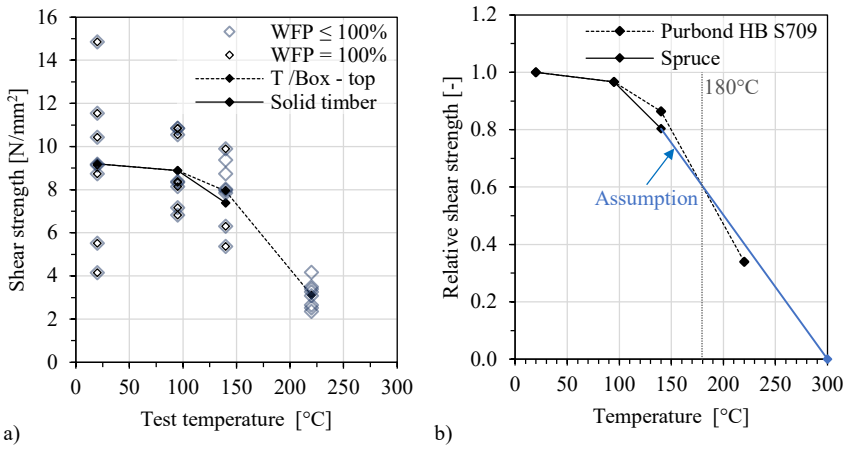

Figure 3.17. Shear test of the glue line at elevated temperatures - Results: a) Shear strength according to EN 14080; b) Relative shear strength according to EN 17224.

3.5.4 Conclusions

The glue line's behaviour between CLT plate and glulam rib is evaluated by the relative shear strength of the glue line for temperatures up to 220°C. The results of shear tests at elevated temperatures confirm the temperature-related strength reduction with increasing temperatures, for both solid timber and the glue line. The tested adhesive PUR provided thermal stability in relative shear strength above 30% for the whole tested temperature range between 20°C and

220°C. The shear strength is above the shear strength of solid timber at least up to 180°C. Until then, the relative shear strength showed a moderate reduction to a value of relative shear strength of 60%, giving information about the shear strength of timber rather than of the adhesive. Good thermal stability for temperatures up to the ignition temperature of wood is achieved through SPG-method and using the adhesive Purbond HB S709.

3.6 Fire resistance tests

3.6.1 Test setup and procedure

The full-scale fire resistance tests were performed at the laboratory of Eurofins Expert Services Oy in Helsinki, Finland, in September to October 2019 (Eurofins Expert Services Oy 2019a; Eurofins Expert Services Oy 2019b; Eurofins Expert Services Oy 2019c; Eurofins Expert Services Oy 2019d). Four tests were performed (A, B, C, and D), one test specimen per cross-section of Figure 3.1. They were performed as fire resistance tests for loadbearing floors according to EN 1363-1, prEN 1363-1, and EN 1365-2. From production day to the day of the test, the mean moisture content dropped from 12.5% to 10%. Further information on the material or its stiffness could not be obtained. The mean density of the CLT plates produced by Stora Enso was assumed as 465 kg/m^3. The mean density of the ribs certificated as quality of GL 24h were assumed as 420 kg/m^3 according to EN 14080.
The horizontal furnace had a length of 5.20 m and a width of 3.00 m (Figure 3.18). The test specimens consisted of two parts connected via lap splice in the ratio 2/3 of the width. The specimens were simply supported, had three ribs with a flange width per rib of 0.933 m and two main cavities. Two further outer ribs of 100 mm width were cut over the length every 300 mm and did not take any load. In the test setup, a constant mechanical load was uniformly applied via evenly distributed loading points (eight loading points over the length in four rows), whereby the moment at midspan corresponded to the target bending moment of the design (section 3.2), including the self-weight of the loading system and the test specimen. The self-weight of each test specimen has been weighted before being lifted on the furnace. The loading per test specimen is summarized in Table 3.6.
The measurement system included load cells for the applied cylinder forces, LVDTs at midspan above each loadbearing rib for global deflections, and LVDTs outside the furnace at both supports to measure the relative displacements between CLT plate and each rib as horizontal slip. The horizontal slip was measured at the ends of the test specimens and as close as possible to the glue line. The furnace was controlled with plate thermometers to follow the standard time-temperature curve (ISO 834-1). Thermocouples of type K-w-e-0.5/2.2/in-pa were inlaid according to recommendations by Fahrni et al. (2018). They measured temperatures parallel to the isotherms and at different levels (Figure 3.23 and Figure 3.22). They were inserted at quarter points over the length between the CLT layers during CLT plate production, on top or between gypsum plasterboards during assembling the test specimens in the fire lab, and between CLT plate and glulam rib during the SPG-procedure (Figure 3.18). Thermocouples were positioned at the test specimens' unexposed surface at five points according to EN 1363-1 in order to monitor

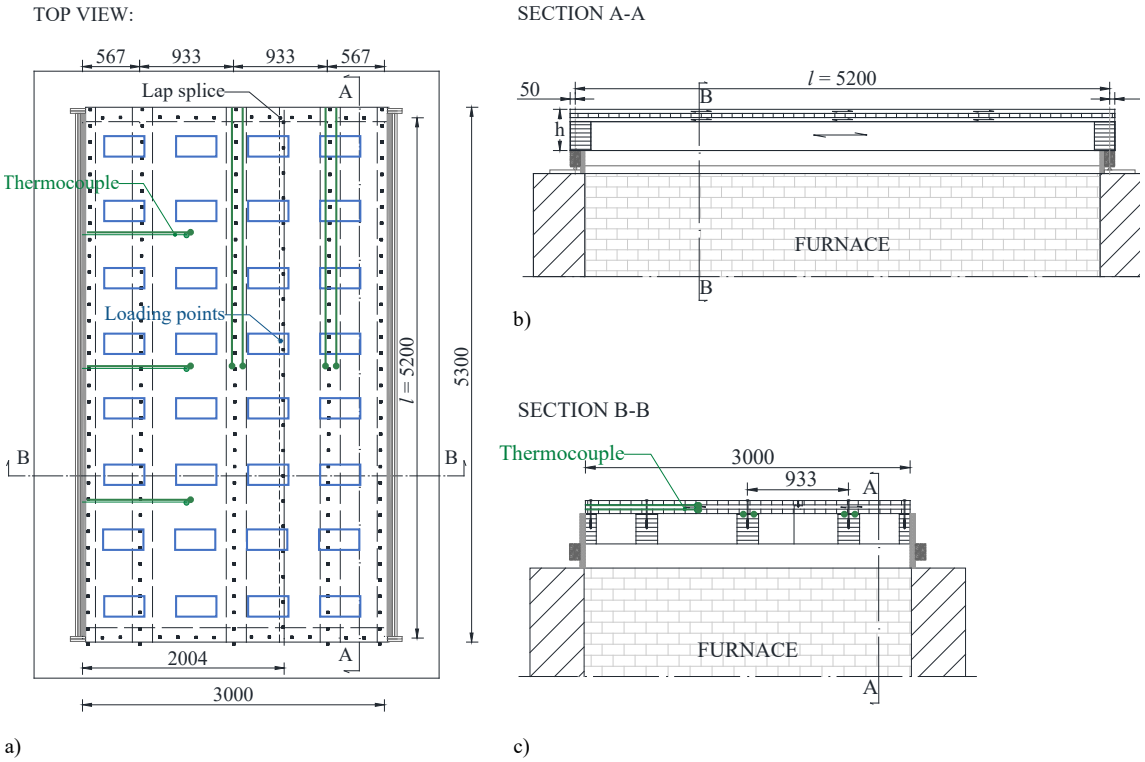

Figure 3.18. Fire resistance tests - Test setup on the horizontal furnace including loading, and thermocouple positions, in [mm]: a) Top view; b) Section A-A; c) Section B-B.

the maximum and average temperature rise and evaluate the thermal insulation of the test specimen. The integrity was evaluated throughout the cotton pad test according to EN 1363-1. The tests were performed under load control. In the first load cycle, the mechanical load was increased to reach the target bending moment and released again. In the second load cycle, the target bending moment was reached and held constant for at least 15 min before the commencement of the fire test. The fire test was continued until either structural failure, sustained flaming along the lap splice or deformations reaching linear-plastic load-deflection behaviour. The latter is defined in prEN 1363-1 as performance criteria for failure of loadbearing capacity and is determined by limitations for both the amount and the rate of deflection.

3.6.2 Results

Experimental effective bending stiffness and stresses of the initial state

The global effective bending stiffness $(EI)_{\mathrm{ef,g}}$ of the test specimens' initial state are calculated according to Formula 3.18

$$(EI)_{\mathrm{ef,g}} = \frac{5l^4}{384}\frac{\Delta F}{\Delta w_{\mathrm{mean}}} \tag{3.18}$$

where a linear regression is used to determine the slope of the load-deflection curve of the second load cycle $\Delta F/\Delta w_{\mathrm{mean}}$ before the commencement of the fire test. The mean on the deflections of the three ribs is calculated as global deflection w_{mean}. The results are presented in

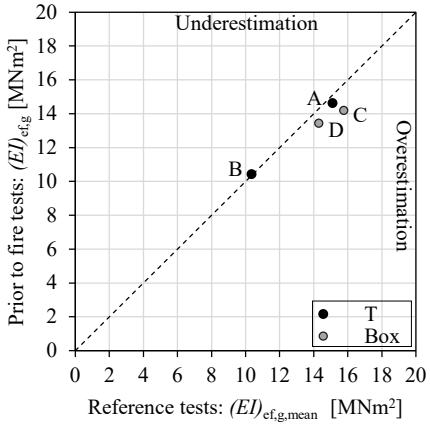

Figure 3.19. Fire resistance tests - Experimental global effective bending stiffness of the test specimens: Results of the reference tests in relation to results prior to the fire resistance tests.

Figure 3.19 in relation to the experimental results of the reference tests, taking the mean value per cross-section type from Table 3.3. The materials' stiffness are comparable. In the case of T-sections, the global effective bending stiffness fits perfectly. In the case of box-sections, the results of the reference tests overestimate the results of the fire resistance tests about 10%.

Table 3.6. Fire resistance tests - Loading, times and observations per test specimen.

	Test specimen		A	B	C	D
	Cross-section type		T	T, initially protected	Box	Box, initially protected
	$(EI)_{\mathrm{ef,g}}$	[MNm^2]	14.6	10.4	14.2	13.4
Design	Fire resistance	[min]	60	90	60	90
Design	Bending moment	[kNm/m]	47.39	48.80	47.89	48.09
Design	Self-weight	[kN/m^2]	0.84	1.07	0.98	1.00
Design	Uniformly distributed load	[kN/m^2]	13.18	13.37	13.19	13.23
Per rib	Bending moment	[kNm]	44.21	45.53	44.68	44.87
Per rib	Self-weight	[kN/m]	0.78	1.00	0.91	0.93
Per rib	Force per loading point	[kN]	7.99	8.11	8.00	8.02
Time	Failure	[min]	/	113	/	115
Time	Full mechanical load	[min]	91	119	115	120
Time	Test termination	[min]	91	120	115	120
Time	Extinguishment	[min]	116	147	142	143
	Exceeded performance criterion acc. to prEN 1363-1		Loadbearing capacity	Loadbearing capacity	Integrity	Loadbearing capacity
	Structural failure		/	Tensile bending	/	Tensile bending

Measurements and observations

The main results of the fire resistance tests are presented in Table 3.6. All test specimens exhibited fire resistance above 90 min. Test specimen D reached 120 min, and test specimen B reached 119 min. The deflections during each fire resistance test are presented in Figure 3.20. The fire resistance tests of test specimens A, B, and D were terminated as soon as the deflection rate at one rib exceeded the performance criterion according to prEN 1363-1. The fire test of test specimen C was terminated due to sustained flaming along the lap splice, which terminated the ability of the test specimen to maintain its separating function according to prEN 1363-1. After stopping the burners of the furnace (= test termination), the test specimens were lifted from the furnace as quickly as possible and extinguished (duration between 22-28 min). After extinguishment, residual cross-sections were cut out at quarter points over the length. The residual cross-sections show that test specimens B and D exhibited tensile bending cracks at midspan in two ribs (Figure 3.23). These cracks were in accordance with loud cracking sounds coming from the structures a few minutes before test termination (= time of failure). At the same time, the amount of deflection of test specimens A, B, and D showed discontinuities before test termination while the rate of deflection exceeded the limitations according to prEN 1363-1. Figure 3.21 presents the horizontal slip u for all test specimens over time including trend lines. In the case of the box-sections, the horizontal slip is shown of top and bottom glue line. The measurements show high oscillations. The high oscillations are induced by the pressure of the furnace, since pre-measurements before the fire resistance tests show no oscillations of such amplitude. The maximum horizontal slip of all top glue lines is 0.10 mm for test specimen A and of all bottom glue lines is -0.22 mm for test specimen C.

Residual cross-sections

After test termination, the thermal degradation of timber continued until extinguishment (duration between 22-28 min). Pictures through the furnace window confirmed the sustaining fire. After test termination, temperatures did not decrease until the thermocouples were cut off. Thus, the experimental residual cross-sections are compared to measurements and estimates for the time of extinguishment.

The experimental residual cross-sections at the centre rib's midspan were brushed, measured, and photographed after the tests. In relation to the original cross-section, Figure 3.23 presents on the left side the residual cross-sections of the test specimens at the centre rib's midspan after extinguishment. The screws of the bottom CLT plate were screwed out after the test. All test specimens show the residual cross-section of a T-section. No increased combustion was detected in the area of the screws. The glue line between CLT plate and glulam rib exhibited no visible damage, and shows the same quality as the glue lines within CLT and glulam. In the glue lines, no cracks or distortions are visible.

The residual cross-sections show that test specimens B and D exhibited tensile bending cracks at midspan in two ribs (Figure 3.23). Based on the design assumptions, tensile bending failure was expected to be decisive for all test specimens. The residual cross-sections were examined at the support. No evidence of shear failure was found, especially at the supports.

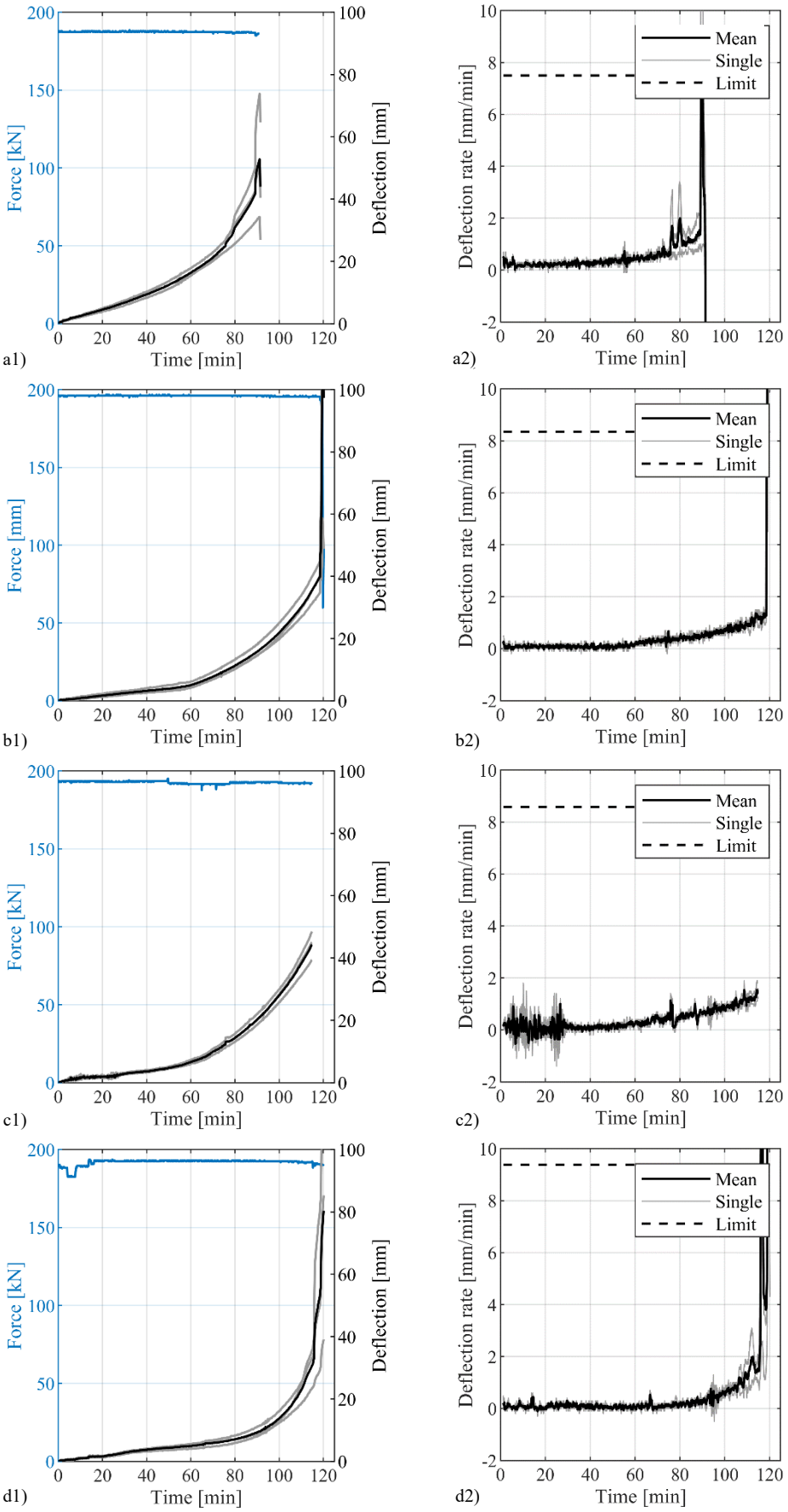

Figure 3.20. Fire resistance tests - Force and deflections during fire tests of the test specimens (until test termination): a) A; b) B; c) C; d) D.

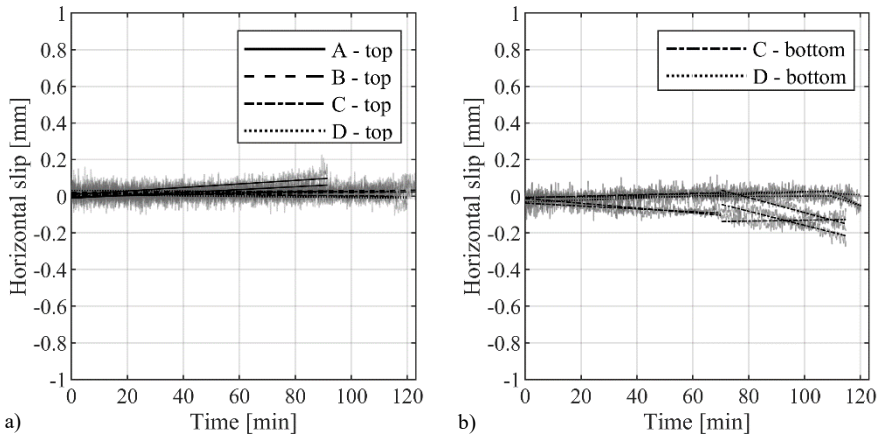

Figure 3.21. Fire resistance tests - Horizontal slip as relative displacement between CLT plate and glulam rib of the test specimens (incl. trend lines): a) T-/box-sections - top glue line; b) Box-sections - bottom glue line.

Temperatures measured in the glue line between CLT plates and glulam ribs

Thermocouples were installed in milled tracks on the rib surface in two or three depths from the outer edge of the rib to measure temperatures at midspan along the glue line between CLT plates and glulam ribs (Figure 3.18). In the top glue line, thermocouples were installed for test specimens A, B, and C. In the bottom glue line, thermocouples were installed for test specimens C, and D. In Figure 3.22, the thermocouples were facing the two main cavities. The measured temperatures are shown as single (grey colour) and mean values (black colour) of the thermocouples at 30, 60, 90 min or further time steps. The mean values are linearly linked. Further measurement points would result in a polynomial curve of higher order.

Figure 3.22 presents the temperatures in the top glue lines of test specimen A, B, and C. The temperatures at the outer rib edge are represented by the mean measurements of the plate thermometers of the furnace, neglecting the influence of convection. Test specimen A represents the initially unprotected T-section being directly exposed to fire for the longest time, i.e. 90 min. Here, the thermocouples were installed at 30 mm, 60 mm and rib centre. For longer fire exposure times, higher temperatures were measured along the glue line. The single values are in good agreement. At a distance of 30 mm, temperatures higher than 300°C were reached. At a distance of 60 mm, temperatures up to 150°C were reached. The thermocouples in the centre of the rib stayed at about 20°C. The other test specimens' results are comparable.

Figure 3.22 presents the temperatures in the bottom glue line of test specimen D. The measurements of the bottom glue line of test specimen C are excluded, as one of two thermocouples was defective. The temperatures at the outer rib edge are represented by the mean measurements of thermocouples hanging in the main cavities, neglecting the influence of convection. For test specimen D, the thermocouples were installed at 20 mm, and at rib centre. Until a fire exposure time of 90 min, the temperatures along the whole glue line stayed at 20°C. From 110 min until test termination at 120 min, the temperatures were rising evenly along the glue line up to 150°C. The temperatures in the cavities reached the furnace temperature. From 125 min, temperatures higher than 300°C were reached in the glue line at a distance of 20 mm. From

130 min, temperatures higher than 300°C were also reached at rib centre. Afterwards, the thermocouples were cut off and the recordings stopped.

Temperatures measured between and on top of different layers

The thermocouples at the test specimens' unexposed surface did not exceed 180°C or an average temperature of 140°C.

The thermocouples between the CLT layers were installed in milled tracks on the CLT layers' surface to measure temperatures within the CLT plates (Figure 3.18). The thermocouples on top or between gypsum plasterboards were stapled to the surface. Figure 3.23 presents on the right side the temperatures measured until test termination: mean value of the plate thermometers (furnace) and single and mean values of the thermocouples. Figure 3.23 presents on the left side the thicknesses of the CLT and gypsum plasterboards layers as well as the positions of the thermocouples between and on top of the different layers. Observations of fall-offs during fire exposure were limited to the point when the fire protection system failed. However, the sudden increases of the measurements to the furnace temperature indicate fall-offs of charred CLT layers and that the bond line integrity was not maintained, as explained in section 2.5.2. The temperatures between the CLT layers started to increase around 200°C.

The charred depth in the CLT plates $d_{\mathrm{char,test}}$ is tracked along the 300°C-isotherm according to EN 1995-1-2 and in accordance with the literature (König 2005). The experimental parameters are summarized in Table 3.7 per test specimen and CLT layer until extinguishment. In the case of initially protected test specimens B and D, failure times of the fire protection systems $t_{\mathrm{f,test}}$ are defined as the first local fall-offs of gypsum plasterboards parts. The start time of charring $t_{\mathrm{ch,test}}$ is defined when the average temperature on the fire-exposed side of the CLT plate reached 300°C. The fall-off times of charred CLT layers $t_{300°\mathrm{C,test}}$ is defined as the average temperature of 300°C between the CLT layers in accordance with the literature (Frangi et al. 2008; Mindeguia et al. 2020). Due to the high temperature gradient, the definition of the fall-off temperature only has minor influence on the charred depths (Frangi 2001).

In the case of test specimen A, the first CLT layer fell off at 64 min (level 2). In the residual cross-section, the charred depth reached the end of the second CLT layer. In the case of test specimen B, failures of gypsum plasterboards were observed for the first layer at 30 min and for the second layer at 55 min. At these times, the measurements indicate temperatures of 400°C (level 4') and 350°C (level 4). The measurements show that the charring started in the cavity around 55 min (level 4 / level 3) and the fall-off of the first CLT layer (level 2) occurred at 115 min. In the residual cross-section, the charred depth reached the second CLT layer. In the case of test specimen C, fall-offs of CLT layers occurred at 34 min (level 6), 38 min (level 5), 70 min (level 4 / level 3), and 107 min (level 2). In the residual cross-section, the charred depth reached the third CLT layer of the top CLT plate. In the case of test specimen D, a failure of gypsum plasterboard was observed around 30 min. During this time, the measurements indicate temperatures of 600°C (level 7). Fall-offs of CLT layers occurred at 73 min (level 6), 86 min (level 5), and 110 min (level 4 / level 3). In the residual cross-section, the charred depth reached the end of the first CLT layer of the top CLT plate.

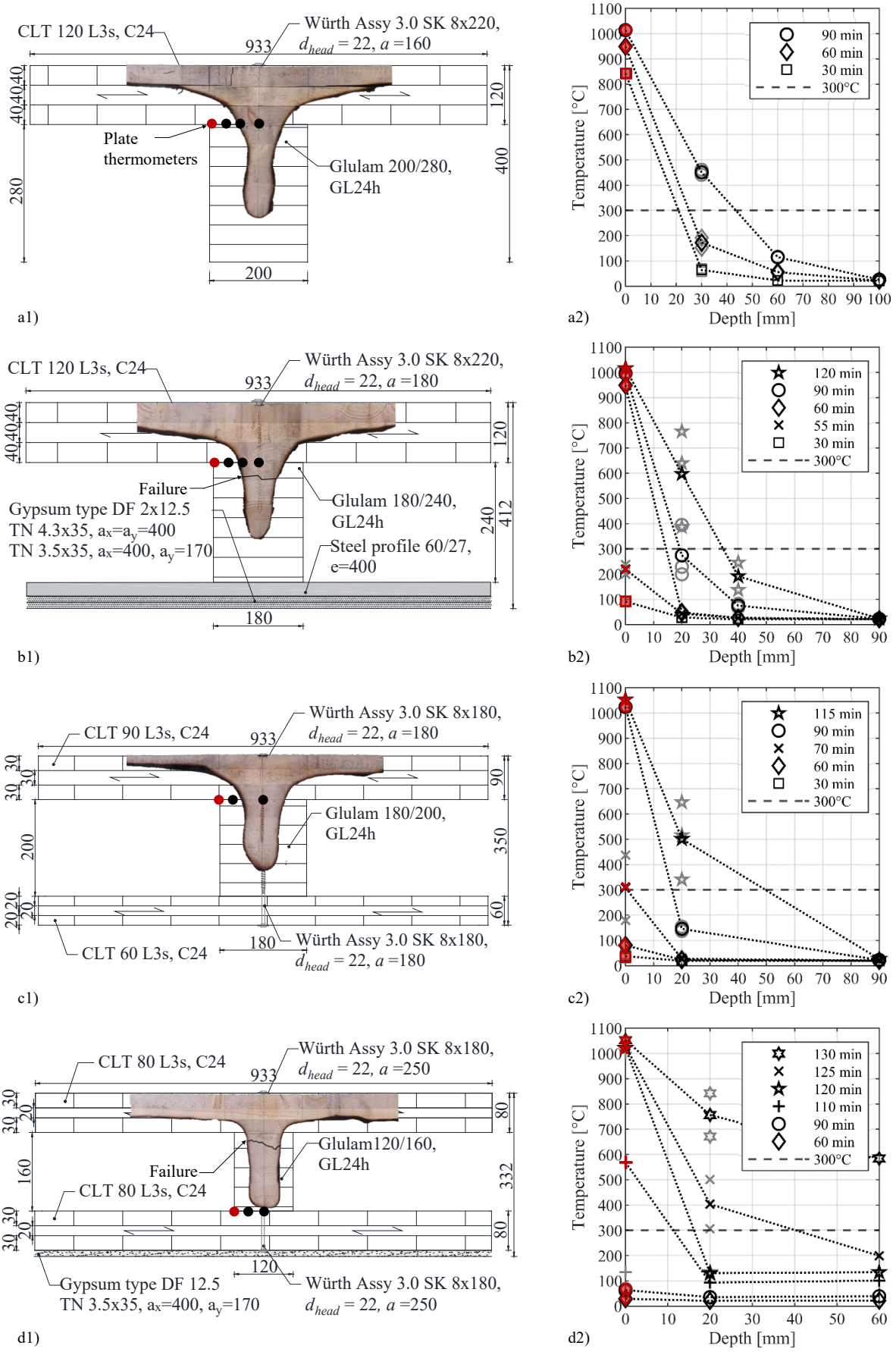

Figure 3.22. Fire resistance tests - Temperatures measured between cross-laminated timber plate and glue-laminated timber rib compared to the experimental residual cross-sections (after extinguishment, in [mm]) of the test specimens: Top glue line a) A; b) B; c) C; bottom glue line d) D.

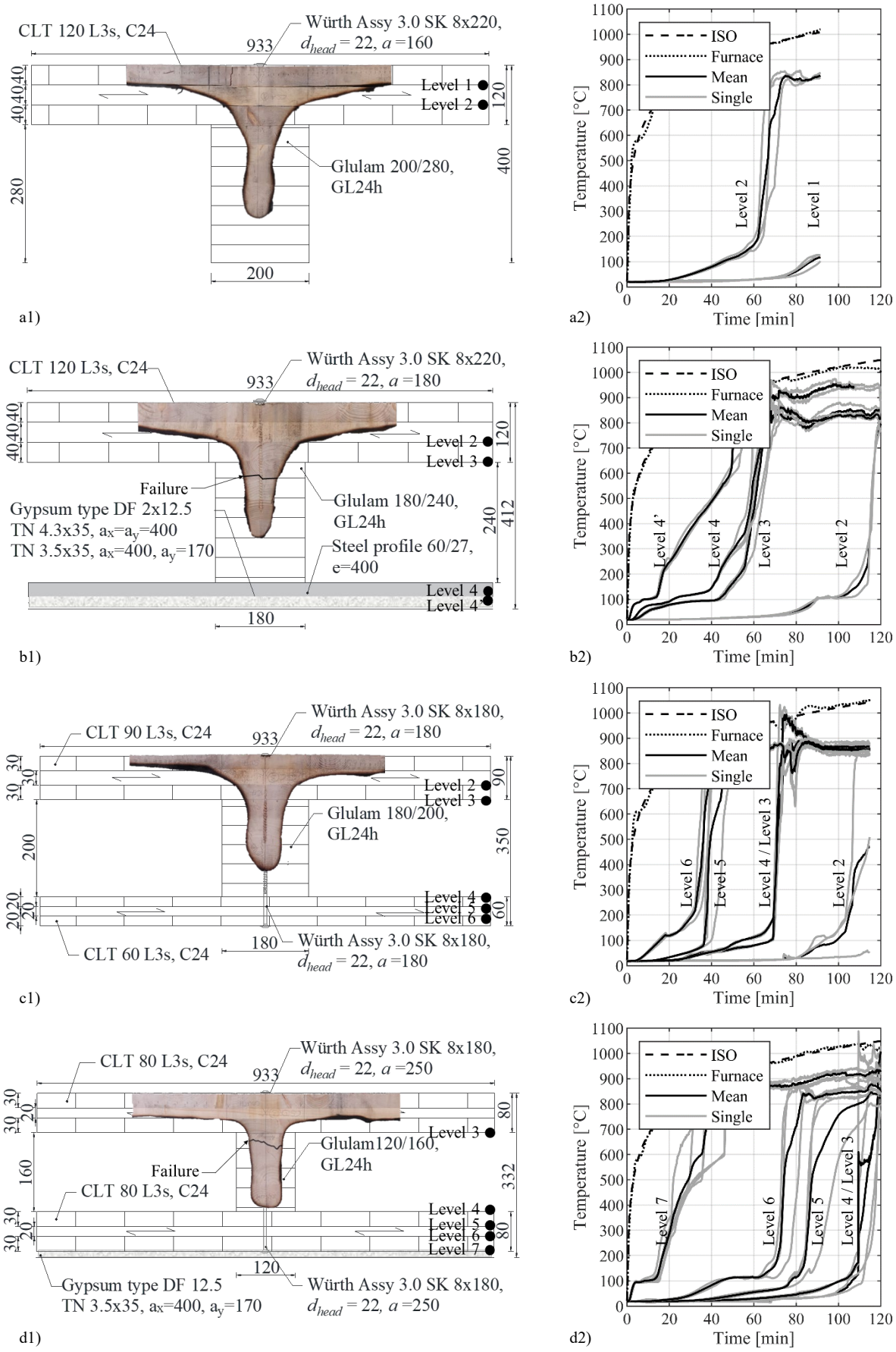

Figure 3.23. Fire resistance tests - Temperatures measured at different levels (until test termination) compared to the experimental residual cross-sections (after extinguishment, in [mm]) of the test specimens: a) A; b) B; c) C; d) D.

Table 3.7. Fire resistance tests - Experimental results per test specimen (charring rates of initially unprotected layers highlighted in bold).

Test specimen	Type of cross-section	$t_{ch,EC5}$ [min]	$t_{f,EC5}$ [min]	Fire resistance tests: $t_{ch,test}$ [min]	$t_{f,test}$ [min]	Charring progress in CLT	$d_{char,test}$ [mm]	$t_{300°C,test}$ [min]	$\beta_{CLT,test}$ [1)] [mm/min]	$\beta_{layer,test}$ [2)] [mm/min]
A	T	Initially unprotected				1st layer	40	63.5	**0.63**	**0.63**
						End	79	116	0.68	0.74
B	T	49	58	55	55	1st layer	40	114.5	0.67	0.67
						End	65	147	0.71	-
C	Box	Initially unprotected				1st layer	20	33.7	**0.59**	**0.59**
						2nd layer	40	38.3	1.04	4.35
						3rd layer	60	70	0.86	0.63
						4th layer	90	107	0.84	0.81
						End	122	142	0.86	0.91
D	Box	24	28	20	30	1st layer	30	73	0.57	0.57
						2nd layer	50	85.7	0.76	1.57
						3rd layer	80	109.5	0.89	1.26
						End	110.5	143	0.9	0.91

[1)] Charring rate of the CLT plates: $\beta_{\mathrm{CLT,test}} = d_{\mathrm{char,test}}/(t_{300°\mathrm{C,test}} - t_{\mathrm{ch,test}})$.

[2)] Charring rate of each CLT layer: $\beta_{\mathrm{layer,test}} = \Delta d_{\mathrm{char,layer,test}}/\Delta t_{300°\mathrm{C,layer,test}}$.

Comparison of experimental and estimated residual cross-sections

Figure 3.24 presents on the left side the experimental residual cross-sections' extracted coordinates per test specimen and complements these results on the right side with the analysis of the corresponding charring behaviour of the CLT plates from the start time of charring until extinguishment. The experimental charring developments of the charred depth in the CLT layers are shown as a function of the time for each test specimen. They are based on the fall-off times of charred CLT layers $t_{300°\mathrm{C,test}}$ and the mean charred depths measured at the experimental residual cross-sections $d_{\mathrm{char,test}}$ (Table 3.7). Figure 3.24 compares these experimental results with the estimated results according to EN 1995-1-2 and prEN 1995-1-2 (section 2.5.3): the estimated rectangular residual cross-sections of the glulam ribs and the estimated charred depths in the CLT plates. In the case of initially protected test specimens B and D, encapsulated phases (no charring) and protected charring phases (decreased charring rate) are defined by the estimated start times of charring $t_{\mathrm{ch,EC5}}$ and the estimated fall-off times of gypsum plasterboards $t_{\mathrm{f,EC5}}$ calculated according to prEN 1995-1-2 (Table 3.7). In the case of test specimen B, the start time of charring of the lateral side of the glulam rib corresponds with the failure time of the fire protection system. The estimated charring developments of the charred depth in the CLT plates were calculated based on the simplified model including fall-off of charred CLT layers according to prEN 1995-1-2. After the fall-off of gypsum plasterboard or of a charred CLT layer, the basic charring rate β_0 for solid wood of 0.65 mm/min is doubled to 1.30 mm/min until the charred layer reaches a thickness of 25 mm. Then the charring rate decreases again to the basic value of the charring rate β_0. For the CLT layers of test specimen C and test specimen D of 20 mm, the doubled charring rate does not decrease until the next layer, as they are thinner than 25 mm. Table 3.7 provides the experimental charring rates of the CLT plates $\beta_{\mathrm{CLT,test}}$ and of each CLT layer $\beta_{\mathrm{layer,test}}$. The experimental charring rates of the initially unprotected CLT layers

of test specimens A and C are less than or equal to the basic charring rate β_0 for solid wood of 0.65 mm/min. The experimental charring rates of the initially protected CLT layers of test specimens B and D represent decreased charring rates of protected charring phases due to the initial protection by the gypsum plasterboards. All other charring rates are higher values than the basic value of the charring rate β_0 due to increased charring after fall-off of charred CLT layers. Remarkably high are the values of the second layer of test specimen C where the charring progressed in a relatively short time. Here, the fall-off occurred at very low temperatures (<100°C), indicating delamination of the uncharred CLT layer (Zelinka et al. 2018; Zelinka et al. 2019).

3.6.3 Discussion

Composite action and glue line quality

For the analysis of the glue line's behaviour in fire, the following results are analysed: Residual cross-sections (Figure 3.23), horizontal slip measured between CLT plate and glulam ribs (Figure 3.21), and temperatures measured along the glue line (Figure 3.22).
The residual cross-sections confirm that the glue line between CLT plates and glulam ribs stayed intact. The typical effect of corner rounding in the corners of the composite section is visible. The horizontal slip was measured at the location of highest shear force, i.e. at the supports. In the case of T-sections, no increase in horizontal movements is observed indicating a failure of the glue line. Of interest are the measurements before the bottom CLT was totally charred or fallen off. Until then, the four fire resistance tests show measurements of horizontal slip smaller than 0.10 mm. The comparison to experimental data of literature outlined in section 3.3.4 confirms that the effect of the composite action was also maintained during fire exposure.
Depending on their distance to the outer edge of the rib, the thermocouples installed in the top glue line showed a slow increase of temperatures according to the increasing process of thermal degradation starting at the outer edge of the rib. In the case of test specimen B, the bigger scatter between the single measurement values demonstrates the dependence on the failure of gypsum plasterboards per cavity, which is set to 55 min in Table 3.7. The temperature slope corresponds to the steep temperature slope typically expected in glulam ribs, showing no unexpected high heat transfer (Klippel 2014). This is confirmed by the pronounced effect of corner rounding in the corners of the composite section. The glue line did not influence the fire behaviour of the slab system.
In the case of box-sections, the horizontal slip of the bottom glue line shows a sudden increase after the fall-off of the charred bottom CLT plate. The measurements of test specimen C show a sudden increase after the last charred layer of the bottom CLT plate's fell off at 70 min. The measurements of test specimen D show a sudden increase after the last charred layer of the bottom CLT plate's fell off at 110 min. Likewise, the thermocouples in the bottom glue line measured an increase of temperatures after the fall-off of the charred bottom CLT plate. However, for test specimen D, the temperatures have not risen to temperatures higher than 300°C until 5 minutes before extinguishment of the residual cross-section (130 min). It is striking that the glue line stayed at 20°C and was still protected by residual timber pieces for 15-20 min after

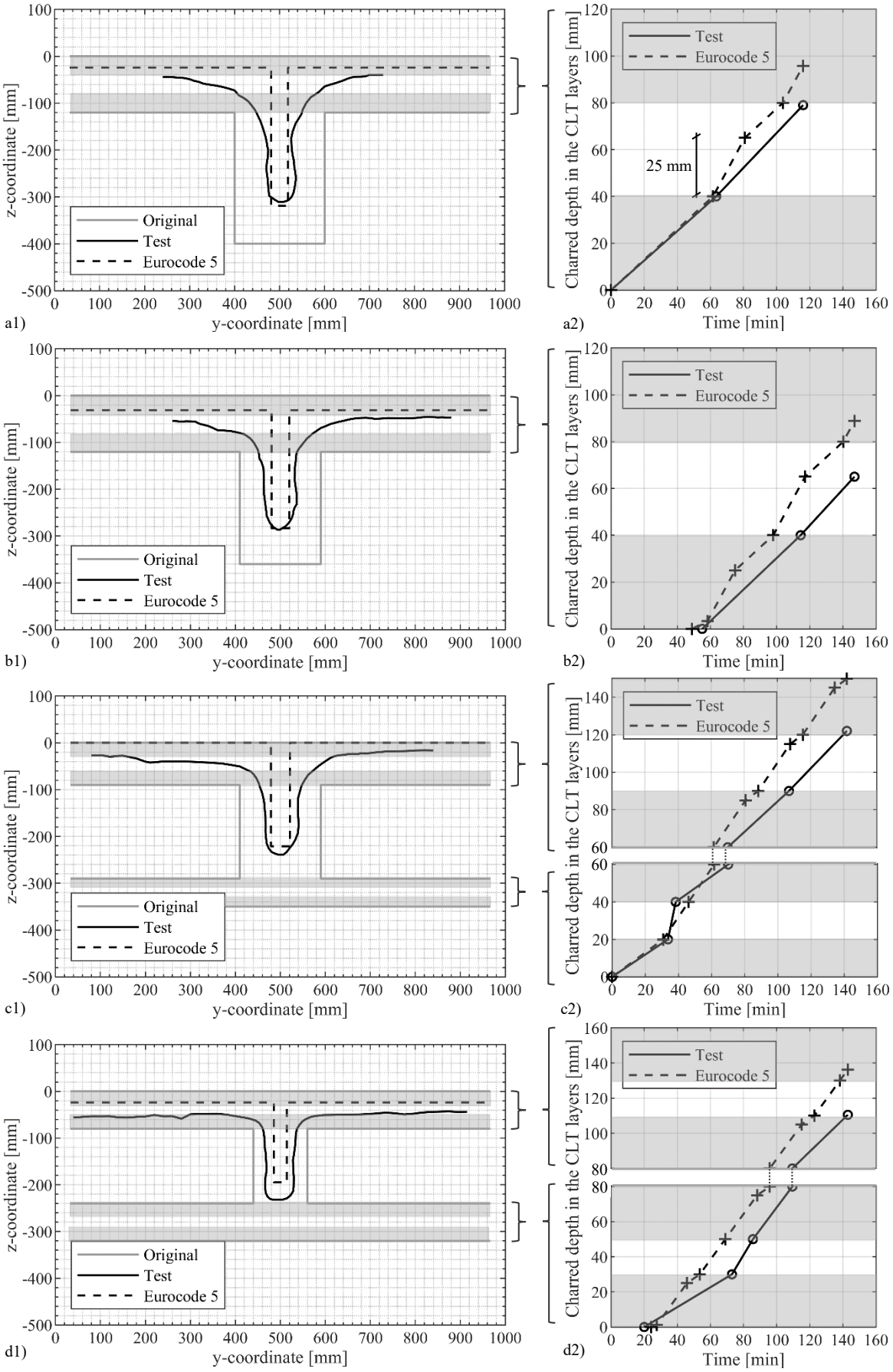

Figure 3.24. Fire resistance tests - Experimental and estimated residual cross-sections and the corresponding charred depths in the cross-laminated timber plates (after extinguishment): a) A; b) B; c) C; d) D.

the fall-off of the charred bottom CLT plate.

Influence of the screws

The experimental residual cross-sections were further examined to discuss the influence of the screws on the fire behaviour of the slab system. In the case of box-sections, the screws of the bottom CLT plate's SPG-procedure are directly exposed to fire. The screw heads ability to conduct heat into the timber and, especially to the glue line between CLT plate and glulam rib was a concern. In advance to the fire resistance tests, one model-scale fire test (approximately 1 m^2) had been performed at the former Laboratory for Fire Testing at the Swiss Federal Laboratories for Materials Science and Technology (Empa) in Dübendorf, Switzerland. Among other things, different screw distances (100 mm, 180 mm, 250 mm) of a cross-section of type C (Figure 3.1) were investigated. Kipfer (2020) documented test setup, and the results of temperature measurements in the field between the two ribs and at the screws. After the fire test, pictures were taken of the residual cross-section for a 3D photo-model analysis. The experimental results were compared to thermal simulations of 3D FE models including and excluding the screws. Higher temperatures directly at the screws were confirmed. However, the residual cross-section demonstrated that the higher heat conduction through the screw head into the cross-section remained local. Figure 3.25 shows the residual cross-section area around a screw in the bottom CLT plate of the model-scale fire test. As after the fire resistance tests, the observation was confirmed that an increased combustion was not detected in the area of the screws (section 3.6.2). The residual cross-sections of both the model-scale fire test and the fire resistance tests were cut at the position of a screw. Figure 3.25 shows pictures of both cuts. They confirm that the higher heat conduction through the screw head did not extend to the screw tip. The slab system's fire behaviour remained unaffected.

The results are in alignment with results by Palma (2016), discussing the influence of the spacing on the average charred depth between dowels based on a simplified FE model. The screws of the SPG-procedure with a diameter d of 8 mm, a minimum length of 180 mm ($= 22.5 \cdot d$), and a minimum screw spacing a of 160 mm ($= 20 \cdot d$) can be related to the case of infinite fastener spacing. There, dowels with a diameter d of 6-24 mm, a length of 120 mm or up to $50 \cdot d$, and a spacing a_1 larger than $7 \cdot d$ showed a charring behaviour between the dowels close to the basic charring rate for solid wood.

Residual cross-sections

For all test specimens, observations and measurements show good agreement. The sudden increase of the measurements to the furnace temperature confirmed the fall-off of charred CLT layers and the assumption that the bond line integrity was not maintained during fire exposure. The results are comparable with experimental results of small-scale fire tests of single CLT plates presented in Frangi et al. (2009) and Fahrni, Klippel, and Frangi (2021).

Figure 3.26 compares the ratio between the estimated and the experimental residual cross-sections. For the comparison, the cross-sectional areas were calculated between equal boundaries. The boundaries of the cross sections were defined by the width of the smallest experimental

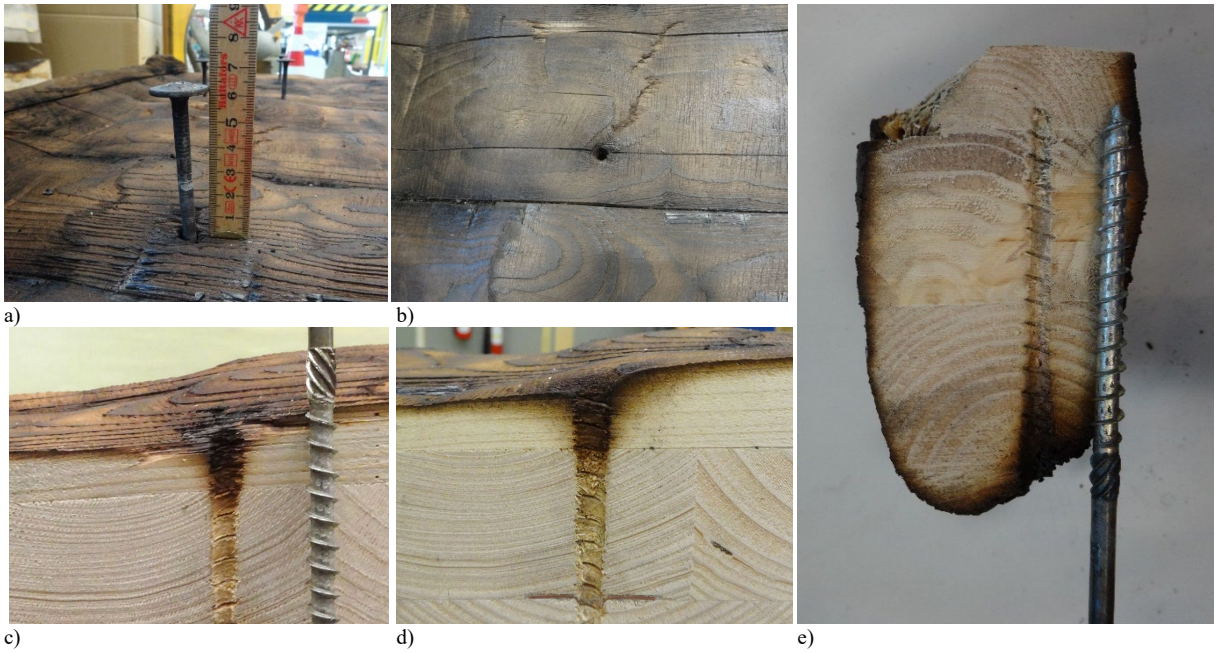

Figure 3.25. Fire tests - Experimental residual cross-sections of the bottom CLT plate (after extinguishment): Model-scale fire test documented in Kipfer (2020) a)+b) Area around a screw; c)+d) Cut at the position of the screw; Fire resistance tests e) Cut at the position of the screw (test specimen D).

cross section in Figure 3.24. Overall, the estimated, rectangular residual cross-sections agree on average to 40% with the experimental residual cross-sections. The estimation of the residual cross-section of test specimen C is with 28% of the experimental residual cross-section below the average. Here, the highest difference can be noted between experimental and estimated charred depths, namely 30 mm.

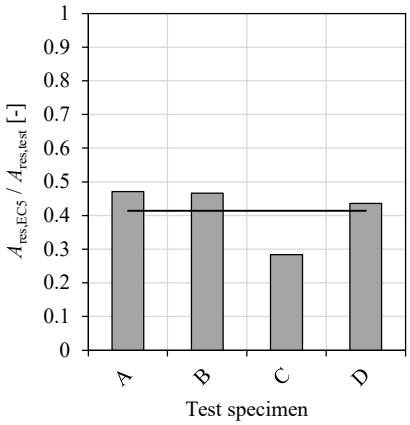

Figure 3.26. Fire resistance tests - Ratio between estimated and experimental residual cross-sections of the test specimens (after extinguishment).

The comparison of experimental and estimated results show that the simplified approach according to EN 1995-1-2 gives a good approximation of the residual cross-section of the glulam

rib and confirms that fall-off of charred glulam layers did not occur. The simplified bi-linear model including fall-off of charred CLT layers according to prEN 1995-1-2 leads to safe results for the charred depth in the CLT plates. Thus, the fall-off of charred CLT layers was less pronounced as expected in comparison to the assumption of the simplified bi-linear model. A reason for this could be a less severe fall-off of charred CLT layers but a dropping of charred CLT layer parts. The simplified approach assumes a sudden fall-off of the entire charred CLT layer. Furthermore, the experimental residual cross-sections show the high effect of corner rounding in the corners of the composite section. The total areas of the composite sections' residual cross-sections are underestimated by the estimated residual cross-sections according to EN 1995-1-2 and prEN 1995-1-2 due to the large positive effect of corner rounding between glulam rib and CLT plate. Finally, it is relevant to mention that in the fire resistance tests the temperatures no longer followed the standard fire exposure between test termination and extinguishment.

3.6.4 Conclusions

The global effective bending stiffness show a very good correlation between the test specimens of the reference tests and the initial state of the test specimens of the fire resistance tests. For the fire resistance tests, the materials' properties and stiffness can be linked to the ones of the reference tests. The results of the fire resistance tests show that the test specimens tested as T- and box-section, without and with a fire protection system, reached more than 90 min and even 120 min of fire resistance. The tests achieved or were close to structural failure. Afterwards, the residual cross-sections were analysed, which corresponded well with the measured temperatures and confirm that the screws of the SPG-procedure do not affect the global fire behaviour.
The fire resistance and, therefore, the rigid composite action in fire depend on the behaviour of the glue lines between the composite components in fire. According to the former European technical approval for cross-laminated timber rib panels of Stora Enso ETA-17/0911, the rigid composite action of the cross-section would not have been allowed to be taken into account in the fire situation. The residual cross-sections, horizontal slip and temperatures measured along the glue line confirm that the glue line between CLT plate and glulam rib stayed intact and that the effect of the composite action was maintained under standard fire exposure. The glue line did not influence the fire behaviour of the slab system. Based on the experimental results, the European technical approval was updated without restrictions for the rigid composite action of the cross-section in the fire situation ETA-20/0893.
The fall-off of charred CLT layers confirm that the bond line integrity was not maintained, even if this effect was less pronounced than expected. The fall-offs of gypsum plasterboards are well predicted based on the failure times according to prEN 1995-1-2. The simplified bi-linear model including fall-off of charred CLT layers according to prEN 1995-1-2 gives conservative estimates of the charred depths of the CLT plates. The simplified approach according to EN 1995-1-2 gives good estimates of the charred depths of the glulam ribs confirming that the bond line integrity was maintained. However, the total area of the residual cross-section of the composite cross-section is underestimated since the effect of corner rounding in the corners of the composite

section has a positive influence on the charring behaviour. Furthermore, the structural behaviour in fire of the test specimens designed for fire resistance times of 60 min (A, C) and 90 min (B, D) was underestimated due to the conservative assumption that the effective width is limited to the rib width of the effective cross-section in fire $b_{\mathrm{ef,fi}} = b_{\mathrm{rib,ef}}$.

3.7 Comparison of the shear tests of the glue line at normal and at elevated temperatures

The experimental results of the shear tests at normal temperature performed at ETH Zurich are compared to the experimental results of the shear tests at 20°C performed at RISE. Core specimens were tested at ETH Zurich, while block specimens were tested at RISE. A smaller number of specimens were tested at RISE. The shear strengths of both Table 3.4 and Table 3.5 covered the factor k_{v} taking into account the size effect of the specimens on the shear strength. Both test series confirm the outcome of an insufficient glue line quality for the box-sections' bottom glue line. The amount of wood failure percentage of "T- / box-section - top" is in a similar range for core and block specimens. For "box-section - bottom", the amount of wood failure percentage of the block specimens is half the size with a two times larger dispersion. The mean shear strength of "T- / box-section - top" block specimens of 9.2 N/mm^2 exceed the core specimens' results by 25%. The mean shear strength of "box-section - bottom" block specimens of 6.7 N/mm^2 exceed the core specimens' results by 18%.
Similar tendencies are recognisable between the results of the core specimens and block specimens. The results confirm the results given by Gaspar, Cruz, and Gomes (2018), which showed a good correlation between core and block specimens and confirmed that core specimens were suitable to measure the shear strength of glue lines. The higher mean shear strength values of the block specimens might result from the higher loading rate, namely four times higher.

3.8 Comparison of the shear tests at elevated temperatures and the fire resistance tests

The experimental results of the shear tests at elevated temperatures, and the fire resistance tests are related to each other. The relative shear strength at elevated temperatures is used to draw conclusions for the glue line's performance, and therefore thermal stability under standard fire exposure. Although, no cracks or distortions are visible in the glue line after the fire resistance tests, it needs to be considered that the shear strength decreases with increasing temperatures and that not the full uncharred width of the glue line contributes to the composite action in fire. It is difficult to predict how the results from steady-state heating condition are correlated with the results of the fire resistance tests under standard fire exposure. In accordance with EN 17224, the approach is followed to ensure that the performance of the glue line meets or even exceeds the performance of solid timber at elevated temperatures. Even if, as stated by Frangi (2001) and Wiesner (2019), the temperature-dependent reduction of the strength of timber decreases under transient compared to steady-state heating condition due

to loading method and moisture movement, the approach would be on the safe side focusing on the adhesive. The tested adhesive provided relative shear strength above 30% for the whole tested temperature range between 20°C and 220°C (Figure 3.17). The question remains at which temperature the relative shear strength of the glue line fell below the relative shear strength of solid timber. The extreme scenarios would be the following:

- The relative shear strength of solid timber stays below the relative shear strength of the glue line for the whole temperature range. Wood failure is decisive for all temperatures along the glue line. The full uncharred width of the glue line contributes to the composite action in fire.
- The relative shear strength of solid timber continues according to the assumption in Figure 3.17. Even though a relative shear strength of the glue line is obtained for high temperatures, it falls below the relative shear strength of solid timber for temperatures higher than 180°C. In the fire resistance tests, a certain amount of the uncharred glue line's width had the risk of adhesive failure instead of wood failure.

The charring process of timber can be tracked along the 300°C-isotherm (EN 1995-1-1). Thus, temperatures below 300°C can be linked to the residual cross-section of the loadbearing system. For this residual cross-section, a glue line's tributary width can be defined depending on the strength reduction of the glue line in comparison to solid timber with increasing temperatures. Figure 3.27 focuses on the temperatures in the top glue line of test specimen A at 90 min, representing the initially unprotected T-section being directly exposed to fire for the longest time. Temperatures above 300°C are reached at a depth of 43 mm. The uncharred glue line's width can be set to 114 mm ($= 2 \cdot 57$ mm). Following the first extreme scenario, the glue line's tributary width agrees with the uncharred glue line's width. Following the second extreme scenario, approximately 10 mm on each side of the glue line exhibiting temperatures between 180°C and 300°C do not contribute to the composite action in fire. In that case, the glue line's tributary width decreases to 82% of the uncharred glue line's width. However, the relative reduction is very small and confirms that most of the glue line stays intact in fire.

3.9 Conclusions

The results of an **experimental program** on the structural behaviour, fire behaviour, and fire resistance of cross-laminated timber rib panels are presented. The rigid composite action is achieved through screw-press gluing (SPG) using the one-component polyurethane adhesive Purbond HB S709. Different cross-sections types (T-sections, box-sections) have been designed for fire resistance times of 60 min (A, C) and 90 min (B, D) for a system length of 9 m. Based on the size of the furnace, the cross-sections were tested at a span of 5.2 m.
In the **ultimate-load tests at normal temperature**, the experimental results confirm the rigid composite action between CLT plate and glulam rib and the importance to consider the shear flexibility out of shear lag for the design of the composite cross-section. While the experimental effective width $b_{\mathrm{ef,test}}$ is on average 78% of the CLT width, it would be estimated

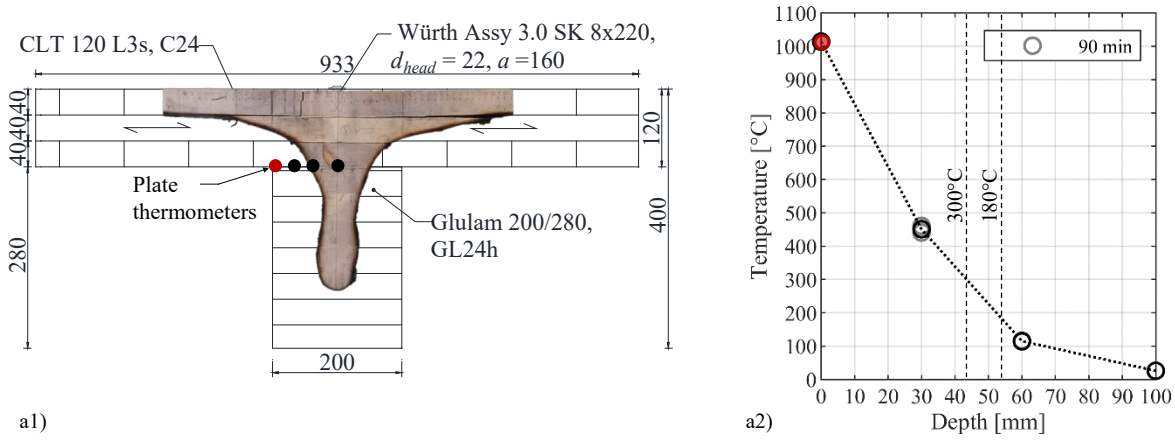

Figure 3.27. Fire resistance tests - Experimental residual cross-section of test specimen A (after extinguishment, in [mm]) compared to measured temperatures in the top glue line at 90 min.

at 60% for the given system based on the effective width b_{ef} according to prEN 1995-1-1. For test specimens tested as T-sections, the experimental loadbearing capacity shows very good agreement with the estimated loadbearing capacity. The experimental and estimated deflections show perfect correlation. For test specimens tested as box-section, the design rules according to prEN 1995-1-1 are conservative. The effective bending stiffness is substantially underestimated. The **shear test at normal temperature** of the glue line between CLT plate and glulam rib confirm the outcome of an insufficient glue line quality for the box-sections' bottom glue line. The results outline the importance of quality control during the SPG-procedure as a basic requirement for sufficient glue line quality.

The results of **shear tests at elevated temperatures** confirm the temperature-related strength reduction with increasing temperatures, for both solid timber and the glue line. For the glue line, good thermal stability for temperatures up to the ignition temperature of wood is determined. The shear strength of the glue line is above the shear strength of solid timber at least up to 180°C.

The **fire resistance tests** confirm that the effect of the composite action is maintained under standard fire exposure. The residual cross-sections confirm that the higher heat conduction through the screw head remained local and did not extend to the screw tip. The fire behaviour of the floor system remains unaffected by both the screws of the SPG-procedure and the glue line. Maximum 10 mm on each side of the glue line exhibit temperatures between 180°C and 300°C and do not contribute to the composite action in fire. The reduction of the glue line's tributary width to maximum 82% of the uncharred glue line's width confirms that most of the glue line stays intact in fire. The results show that the test specimens tested as T- and box-section, without and with a fire protection system, reached more than 90 min and even 120 min of fire resistance. The fall-offs of gypsum plasterboards are well predicted based on the failure times according to prEN 1995-1-2. The fall-off of charred CLT layers confirms that the bond line integrity was not maintained between the face-bonded CLT layers. The simplified bi-linear model including fall-off of single or multiple charred CLT layers according to prEN 1995-1-2

gives conservative estimates of the charred depths of the CLT plates. The simplified approach according to EN 1995-1-2 gives good estimates of the charred depths of the glulam ribs. The structural behaviour in fire was underestimated due to the effect of corner rounding in the corners of the composite section as well as due to the conservative assumption that the effective width is limited to the rib width of the effective cross-section in fire $b_{\mathrm{ef,fi}} = b_{\mathrm{rib,ef}}$.

4. Numerical investigations

4.1 Overview

In this chapter, the developed framework of the advanced design methods for modelling cross-laminated timber rib panels in fire is presented. First, the modelling assumptions, and the basic input parameters of the models are presented. The numerical investigations of the advanced design methods cover thermal, mechanical and, uncoupled thermo-mechanical simulations using finite-element (FE) models. The complexity of the FE models and thus the computation time of the FE calculations are increased step by step. The investigations start with 2D thermal simulations as heat transfer models of the four tested cross-section types (Figure 3.1) and end with 3D thermo-mechanical simulations as flexible-in-shear multi-layered models. All FE models are validated against the experimental results. Finally, a parametric study analyzes the structural behaviour of the floor system in fire and thus the effective width in fire $b_{\mathrm{ef,fi}}$ for a parameter range expected in practice.

4.2 Finite element models

4.2.1 Modelling assumptions

The following assumptions were derived from the experimental investigations (section 3.9):

- The composite action is maintained under standard fire exposure.
- The reduction of the glue line's tributary width in fire is negligible. It is assumed that the entire uncharred width of the glue line stays intact in fire.
- The influence of the screws and thus the screws themselves are neglected in the thermal simulation, since the screw distances are not less than the minimum tested spacing of 100 mm. Their loadbearing behaviour is not activated in the mechanical and thermo-mechanical simulations.
- The thermal simulation takes into account the fall-off of charred CLT layers but not the fall-off of charred glulam layers.
- For comparison with the experimental results, the charred depth is tracked along the 300°C-isotherm according to EN 1995-1-2.

- The shear lag effect of the ribbed cross-section is taken into account. An effective width is considered in the mechanical and thermo-mechanical simulations.
- The effective width at normal temperature b_{ef} according to prEN 1995-1-1 (Formulae 2.9-2.10) leads to results on the safe side.

4.2.2 Heat transfer

Heat is transferred by conduction, convection, and radiation. Conduction determines the heat transfer in and through solids. Convection describes the heat exchange between a moving gas or liquid and a solid. Radiation does not require an intervening medium. It is the heat transfer or rather energy transfer by electromagnetic waves. (Drysdale 2011)

Conduction

Transient temperature field calculations are based on non-steady, time-dependent heat transfer considering the transfer of heat in a solid material; i.e. the cross-section. The conductive heat flux can be described with the Fourier law of heat conduction according to Formula 4.1

$$\frac{d}{dx}(\lambda_{\mathrm{x}} \cdot \frac{d\theta}{dx}) + \frac{d}{dy}(\lambda_{\mathrm{y}} \cdot \frac{d\theta}{dy}) + \frac{d}{dz}(\lambda_{\mathrm{z}} \cdot \frac{d\theta}{dz}) = \rho \cdot c \cdot \frac{d\theta}{dt} - \dot{Q}''' \tag{4.1}$$

where λ_{x}, λ_{y}, and λ_{z} are the values of the thermal conductivity of the solid material in x-, y-, and z-direction, ρ is the density, and c is the specific heat capacity. $d\theta/dx$, $d\theta/dy$, and $d\theta/dz$ are the temperature-gradients in x-, y-, and z-direction. $d\theta/dt$ is the rate of change of thermal energy, and $\dot{Q}'''$ is the heat release rate per unit volume. If equal thermal conditions can be assumed along the longitudinal axis ($d\theta/dx = 0$) and no differentiation is made between heat transfer in y-, and z-direction ($\lambda_{\mathrm{y}} = \lambda_{\mathrm{z}}$), the formula can be simplified to Formula 4.2

$$\frac{d^2\theta}{dy^2} + \frac{d^2\theta}{dz^2} = \frac{\rho \cdot c}{\lambda} \cdot \frac{d\theta}{dt} - \frac{\dot{Q}'''}{\lambda} \tag{4.2}$$

where the right side of the formula represents the term of heat storage and of heat generation.

Convection and Radiation

The boundary conditions at the surface of the member are determined by the gas temperature in the furnace. The gas temperature follows the standard time-temperature curve (ISO 834-1) according to Formula 4.3

$$\theta_{\mathrm{g}} = 20 + 345 \cdot \log_{10}(8 \cdot t + 1) \tag{4.3}$$

where θ_{g} is the gas temperature in °C, and t is the time in minutes.
The thermal interactions are determined as the net heat flux $\dot{h}_{\mathrm{net}}$ to the surface of the member according to Formula 4.4

$$\dot{h}_{\mathrm{net}} = \dot{h}_{\mathrm{net,c}} + \dot{h}_{\mathrm{net,r}} \tag{4.4}$$

where $\dot{h}_{\mathrm{net,c}}$ and $\dot{h}_{\mathrm{net,r}}$ are the net convective and radiative heat flux components in $\mathrm{W/m^2}$ according to EN 1991-1-2.
The net convective heat flux component is determined according to Formula 4.5

$$\dot{h}_{\mathrm{net,c}} = \alpha_{\mathrm{c}} \cdot (\theta_{\mathrm{g}} - \theta_{\mathrm{m}}) \tag{4.5}$$

where α_{c} is the coefficient of heat transfer by convection ($c = 25\mathrm{W/(m^2K)}$ on exposed surfaces, $c = 4\mathrm{W/(m^2K)}$ on unexposed surfaces), θ_{g} is the gas temperature in the vicinity of the fire exposed surface, and θ_{m} is the surface temperature.
The net radiative heat flux component is determined according to Formula 4.6

$$\dot{h}_{\mathrm{net,r}} = \Phi \cdot \epsilon_{\mathrm{m}} \cdot \epsilon_{\mathrm{f}} \cdot \sigma_{\mathrm{SB}} \cdot [(\theta_{\mathrm{r}} + 273)^4 - (\theta_{\mathrm{m}} + 273)^4] \tag{4.6}$$

where Φ is the configuration factor of the exposed surface, ϵ_{m} is the surface emissivity of the member ($\epsilon_{\mathrm{m}} = 0.8$ for timber, timber products, and gypsum in accordance with EN 1995-1-2), ϵ_{f} is the emissivity of the fire taken as 1.0, σ_{SB} is the Stephan Boltzmann constant taken as $5,67 \cdot 10^{-8}\mathrm{W/(m^2K^4)}$, θ_{r} is the effective radiation temperature of the fire environment in °C ($\theta_{\mathrm{r}} = \theta_{\mathrm{g}}$ for fully engulfed members), and θ_{m} is the surface temperature in °C.

4.2.3 Thermal properties

The thermal simulations depend on temperature-dependent thermal properties of the solid materials defining the heat transfer by conduction. Heat transfer in longitudinal direction was not considered. Therefore, no distinction between longitudinal and transversal direction was necessary for the thermal conductivity.
For wood, thermal properties were used according to EN 1995-1-2 (Eurocode 5). König and Walleij (1999; 2000) proposed thermal properties for initially unprotected and protected timber members exposed to the standard time-temperature curve. In combination with ENV 1995-1-2, they formed the basis for the thermal properties of EN 1995-1-2 (2004). These calibrated thermal properties are not physically correct, but effective and take into account complex physical processes such as water evaporation, moisture transport, pyrolysis, cracks in charcoal, and combustion of char layer (König and Walleij 1999). Figure 4.1 presents the temperature dependence of the thermal properties listed in Table 4.1: the thermal conductivity in the direction perpendicular to the grain λ_θ, the specific heat capacity c_θ, and the ratio of the density to the dry density $\rho_\theta/\rho_{\mathrm{dry}}$ of wood. The density was set to 465 $\mathrm{kg/m^3}$ for the CLT plates (Table 2.2) and as 420 $\mathrm{kg/m^3}$ for the glulam ribs (Table 2.4). The initial moisture content is taken as 10% as measured in the fire resistance tests (section 3.6.1).
For gypsum plasterboard, thermal properties were used according to prEN 1995-1-2, based on *FSITB* 2010 and Schleifer (2009). Figure 4.2 presents the temperature dependence of the thermal properties listed in Table 4.2: the thermal conductivity λ_θ, the specific heat capacity c_θ, and the ratio of the density to the density at normal temperature $\rho_\theta/\rho_{20°\mathrm{C}}$ of gypsum plasterboard. The density was set to 800 $\mathrm{kg/m^3}$ according to EN 520.

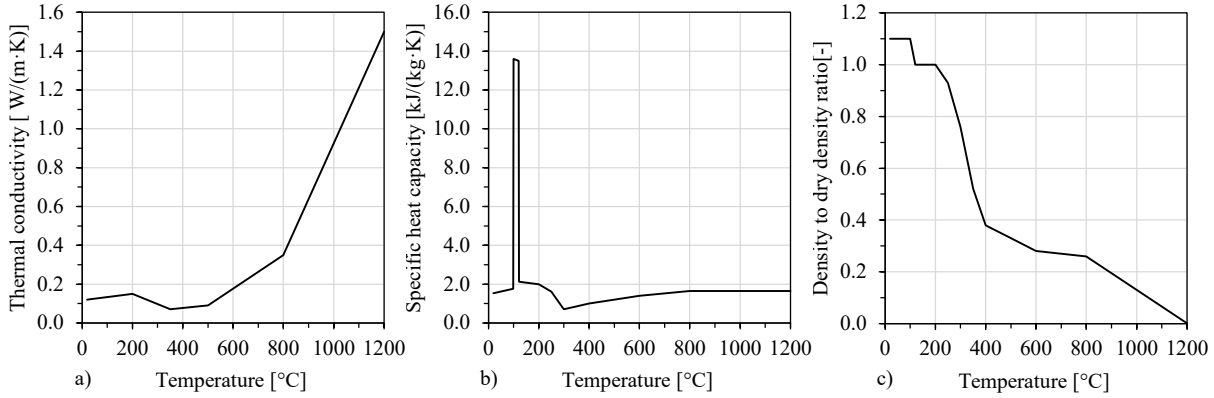

Figure 4.1. Temperature-dependent thermal properties for wood according to EN 1995-1-2: a) Thermal conductivity; b) Specific heat capacity; c) Density to dry density ratio.

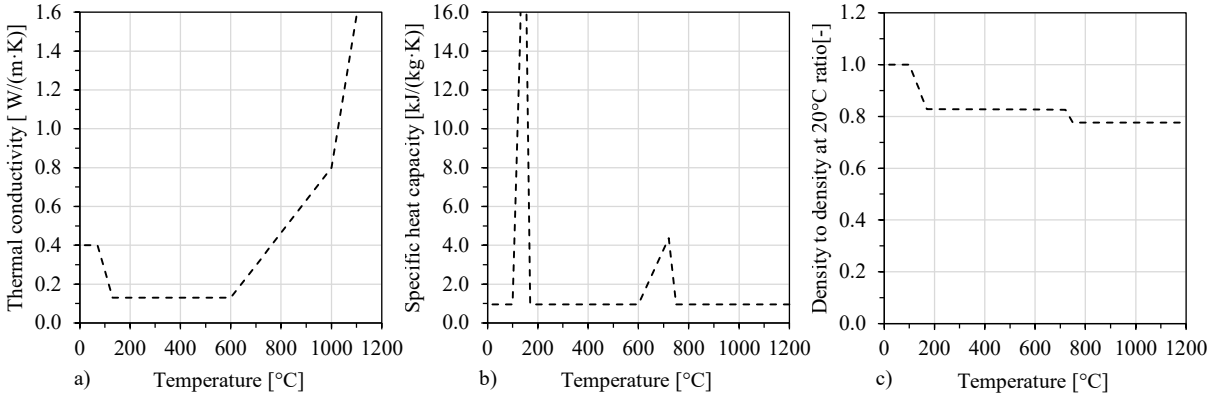

Figure 4.2. Temperature-dependent thermal properties for gypsum plasterboard according to prEN 1995-1-2: a) Thermal conductivity; b) Specific heat capacity; c) Density to density at normal temperature ratio.

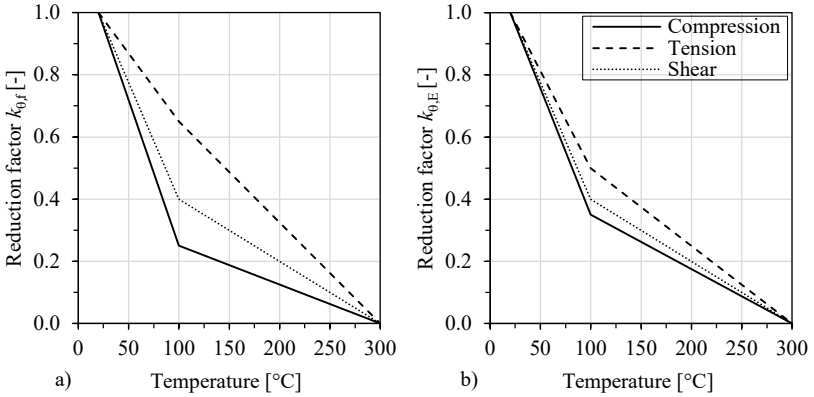

Figure 4.3. Temperature-dependent reduction factors for strength and stiffness parallel to the grain for wood according to EN 1995-1-2: a) Strength; b) Stiffness.

Table 4.1. Temperature-dependent thermal properties for wood according to EN 1995-1-2.

Temperature θ	Thermal conductivity λ_θ	Specific heat capacity c_θ	Density to dry density ratio ρ_θ/ρ_{dry}
[°C]	[W/(mK)]	[kJ/(kgK)]	[-]
20	0.120	1.53	1.10
99	0.133	1.77	1.10
100	0.133	13.60	1.10
120	0.137	13.50	1.00
121	0.137	2.12	1.00
200	0.150	2.00	1.00
250	0.123	1.62	0.93
300	0.097	0.71	0.76
350	0.070	0.85	0.52
400	0.077	1.00	0.38
500	0.090	1.20	0.33
600	0.177	1.40	0.28
800	0.350	1.65	0.26
1200	1.500	1.65	0.01

Table 4.2. Temperature-dependent thermal properties for gypsum plasterboard according to prEN 1995-1-2.

Temperature θ	Thermal conductivity λ_θ	Specific heat capacity c_θ	Density to 20°C density ratio $\rho_\theta/\rho_{20°C}$
[°C]	[W/(mK)]	[kJ/(kgK)]	[-]
20	0.400	0.96	1.00
70	0.400	0.96	1.00
100	0.270	0.96	1.00
130	0.130	0.96	1.00
140	0.130	14.90	0.93
150	0.130	25.20	0.90
170	0.130	21.70	0.88
600	0.130	0.96	0.83
720	0.330	0.96	0.83
750	0.380	4.36	0.83
1000	0.800	0.96	0.78
1200	2.370	0.96	0.78

4.2.4 Mechanical properties

The material behaviour is modelled as linear-elastic orthotropic. The material strength behaviour is modelled simplified as brittle in tension and in compression. The material properties and material strength values at normal temperature (20°C) are taken from Tables 2.1 and 2.2 for cross-laminated timber, and from Table 2.3 and 2.4 for glued-laminated timber. The stiffness and strength values for gypsum plasterboards are set close to zero as non-loadbearing material. The thermo-mechanical simulations have to take into account the effect of elevated temperatures on the mechanical properties of the loadbearing materials. EN 1995-1-2 (2004) considers a bi-linear

behaviour of the temperature dependence of the strength values and the modulus of elasticity, as proposed for timber members exposed to the standard time-temperature curve by König and Walleij (2000). The relationships include the effects of transient creep of timber. Figure 4.3 presents the temperature-related reduction by temperature-dependent reduction factors, which are multiplied by the corresponding mechanical property: the temperature-dependent reduction factor for local compression $k_{\theta,\mathrm{f,c}}$, for local tension $k_{\theta,\mathrm{f,t}}$, for local shear $k_{\theta,\mathrm{f,v}}$, and the temperature-dependent reduction factor for the modulus of elasticity parallel to the grain in compression $k_{\theta,\mathrm{E,c}}$ and in tension $k_{\theta,\mathrm{E,t}}$. The bi-linear relationships are valid between normal temperature and charring temperatures. At 20°C, the mechanical property is fully applied ($k_{20°\mathrm{C}} = 1.0$). At 100°C, the residual mechanical property is defined by the reduction factor ($k_{100°\mathrm{C}} < 1.0$). For temperatures above 300°C, the mechanical property is taken close to zero ($k_{300°\mathrm{C}} = 0$).

4.2.5 Effective width

The effective width defines an equivalent cross-section that provides the same maximum bending stress and effective bending stiffness as the actual cross-section, as explained in section 2.4.2. The bending stresses of the transversal CLT layers were neglected, thus only the bending stresses within the longitudinal CLT layers were considered. Formula 4.7 shall apply for the determination of the numerical effective width $b_{\mathrm{ef,sim}}$

$$b_{\mathrm{ef,sim}} = \frac{\int \sigma_{\mathrm{x,sim}}(y,z)\,dy\,dz}{\sigma_{\mathrm{x,max,sim}}(z)} = \frac{F_{\mathrm{x,tot}}}{F_{\mathrm{x,max}}} \tag{4.7}$$

where $\int \sigma_{\mathrm{x,sim}}(y,z)\,dy\,dz$ is the integral of all longitudinal bending stresses along the height and along the width of the CLT plate, defined as total force $F_{\mathrm{x,tot}}$, and $\sigma_{\mathrm{x,max,sim}}(z)$ is the maximum longitudinal bending stress distribution along the height of the CLT plate at rib centre of the FE model, defined as trapezoidal force at rib centre $F_{\mathrm{x,max}}$.
Under standard fire exposure, Formula 4.8 shall apply for the determination of the numerical effective width in fire $b_{\mathrm{ef,fi,sim}}$

$$b_{\mathrm{ef,fi,sim}} = \frac{\int \sigma_{\mathrm{x,fi,sim}}(y,z)\,dy\,dz}{\sigma_{\mathrm{x,max,fi,sim}}(z)} = \frac{F_{\mathrm{x,tot,fi}}}{F_{\mathrm{x,max,fi}}} \tag{4.8}$$

where $\int \sigma_{\mathrm{x,fi,sim}}(y,z)\,dy\,dz$ is the integral of all temperature-dependent longitudinal bending stresses along the height and along the width of the CLT plate, defined as total force in fire $F_{\mathrm{x,tot,fi}}$, and $\sigma_{\mathrm{x,max,fi,sim}}(z)$ is the maximum temperature-dependent longitudinal bending stress distribution along the height of the CLT plate at rib centre of the FE model, defined as trapezoidal force at rib centre in fire $F_{\mathrm{x,max,fi}}$.

4.3 Thermal simulations (2D)

4.3.1 Objectives

Heat transfer analyses using 2D FE models were performed modelling the distribution of the temperatures within the cross-section of a T-section or box-section. The numerical results of the four tested cross-section types (Figure 3.1) are presented and compared with the experimental results of the fire resistance tests. First, the focus is made on the temperatures obtained from the thermal simulations within the CLT plates. The numerical results were calibrated with the experimental results. A new set of thermal properties after the fall-off of gypsum plasterboards or charred CLT layers is presented and validated against further experimental results taken from literature. Based on the new set of thermal properties, the numerical simulations were re-calculated and the results of the entire cross-sections are compared to both the experimental results of the fire resistance tests and the analytical results based on prEN 1995-1-2.
Some results presented in this section have been published in Kleinhenz, Just, and Frangi (2021).

4.3.2 Model

Modelling framework

The Python programming language (Python Software Foundation 2015) was used to generate the input file of the heat transfer model, based on the geometry, CLT layup, material properties, thermal interactions, and thickness of gypsum plasterboards. The thermal simulation was conducted using SAFIR® version 2019.a.6, a nonlinear FE software for modelling structures in fire (Franssen and Gernay 2017). An output file and a TEM-file was created by SAFIR® after the thermal simulation. The simulation stopped when a maximum defined time was reached. The post-processor DIAMOND (University of Liège 2016) was installed to view the model, and to view and extract the results of the output file.

Finite element models

2D FE models were created as cross-section of a T-section (Figure 4.4) or box-section with a cross-laminated timber width b of 0.933 m. The vertical symmetry in the middle of the cross section was exploited by modelling it as an adiabatic surface. Convective and radiative thermal interactions were defined for the outer timber surfaces. The standard fire exposure was applied at the bottom edges. The top edge was exposed to a constant temperature of 20°C. The heat transfer is influenced by the void cavities. For radiation inside the void cavity, the emissivity of the materials enclosing the void was considered. For convection inside the void cavity, the coefficient of convection on unexposed surfaces was used, regardless of the temperature of the air in the void. Air movement within the cavity was not considered (Franssen and Gernay 2017). The materials were user defined as CLT, glulam, and gypsum plasterboards, based on their density and temperature-dependent thermal properties. The simulated sections were discretised into rectangular elements. The sizes of the elements varied between 4x4 mm^2 and 5x5 mm^2. The element size was halved at the exposed edges of the cross-section. Element size and refinement

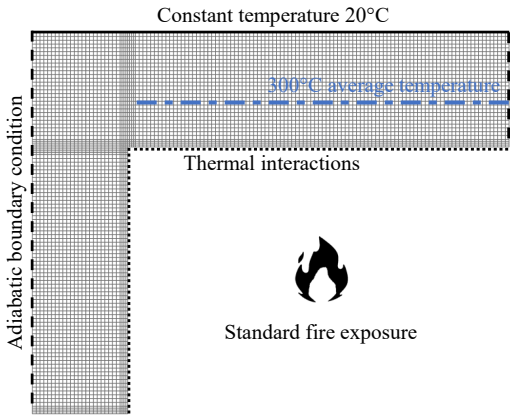

Figure 4.4. Thermal simulations (2D) - 2D FE model of a T-section (scale 1:80).

had been optimized in a sensitivity analysis. The intervals between the time steps were kept at maximum 5 seconds. SAFIR® uses an iterative procedure to converge on the correct solution for each increment. The thermal simulations were calculated with a precision of 1.0E-2 to reach convergence to a state of equilibrium.

Procedure

As criterion for the fall-off time of gypsum plasterboards $t_{\mathrm{f,sim}}$, the failure times of the fire resistance tests $t_{\mathrm{f,test}}$ were used to remove the elements defined as gypsum plasterboards in the FE model. The fall-offs of charred CLT layers $t_{300°\mathrm{C,sim}}$ were defined as time steps of the thermal simulations when the average temperature between the CLT layers exceeded 300°C. In a further simulation step, the FE model without the fallen-off layer was re-created in a new input file and the calculation was continued from the fall-off time as restart time until the next charred CLT layer fell off (Fischer 2019). For each input file, the corresponding output and TEM-files were created by SAFIR®. At the end, the numerical results were sequenced together.

4.3.3 Results based on Eurocode 5

Figure 4.5 presents the numerical temperatures per cross-section type as mean value over the length of the CLT layer and gypsum plasterboards until test termination. Furthermore, the experimental temperatures are shown as single (grey colours) and mean values (black colour), measured by the thermocouples installed on top or between the CLT layers and gypsum plasterboards. The results are taken from section 3.6.2 (Figure 3.23). The thermal simulations predict a significantly earlier fall-off of the charred CLT layers compared to the experimental results. The error increases with the number of fall-offs of both gypsum plasterboard and charred CLT layers. The number of fall-offs would have been overestimated by up to three CLT layers. Table 4.3 provides the experimental, analytical, and numerical charring rates of the CLT plates until the last experimental fall-off of charred CLT layers before test termination. The experimental results are taken from Table 3.7. The analytical results were calculated according to prEN 1995-1-2. The analytical charred depths of the CLT plates were estimated according to the

Table 4.3. Thermal simulations - Experimental, analytical, and numerical results per cross-section type (until test termination).

Test specimen	Type of cross-section	$t_{ch,test}$	$t_{f,test} = t_{f,sim}$	$t_{ch,EC5}$	$t_{f,EC5}$	Charring progress	$\beta_{CLT,test}$[1)]	$\beta_{CLT,EC5}$[1)]	$\beta_{CLT,sim,EC5}$[1)]
		[min]	[min]	[min]	[min]	until fall-off of	[mm/min]	[mm/min]	[mm/min]
A	T	Initially unprotected				1st layer	0.63	0.65	0.64
B	T	55	55	49	58	1st layer	0.67	0.82	1.16
C	box	Initially unprotected				4th layer	0.84	1.02	1.23
D	box	20	30	24	28	3rd layer	0.89	1.07	1.42

[1)] Charring rate of the CLT plates: $\beta_{\mathrm{CLT,test}} = d_{\mathrm{char,test}}/(t_{300°\mathrm{C,test}} - t_{\mathrm{ch,test}})$.

simplified design method including fall-off of charred CLT layers (section 2.5.3). The simplified design method including fall-off of charred CLT layers leads to safe results for the charring rate in the CLT plates, as discussed in section 3.6.3. However, the numerical charring rates are higher than both the experimental and the analytical charring rates, giving an incorrect prediction of the fire behaviour of the CLT plates. As an advanced design method, the thermal simulations should lead to less conservative predictions than the simplified design method and should be able to predict the actual behaviour. The exception is the initially unprotected cross-section A with only one fall-off of a charred CLT layer, showing a charring rate close to the basic charring rate β_0 for solid wood of 0.65 mm/min.

4.3.4 Calibration of temperature-dependent thermal properties for wood after fall-off

The objective was to achieve a better prediction of the fire behaviour of the CLT plates including multiple fall-offs of both gypsum plasterboards and charred CLT layers. The fall-off temperature of the charred CLT layers was kept as 300°C in order to follow the charred depth along the 300°C isotherm. Due to the high temperature gradient, adjusting the definition of the fall-off temperature only leads to minor differences in the fall-off times (Frangi 2001; Schleifer 2009). The temperatures obtained through the heat transfer models are mainly influenced by the choice of temperature-dependent thermal properties. The thermal properties for wood according to EN 1995-1-2 2004 were re-calibrated to the experimental results.

The thermal properties for wood according to EN 1995-1-2 2004 had been proposed for initially unprotected and protected timber members exposed to the standard time-temperature curve (König and Walleij 1999; König and Walleij 2000). The thermal properties were derived by calibration to test results of initially unprotected linear timber members. To fit the test results of initially protected members, the thermal simulations were adjusted in the following way (König and Walleij 1999): The thermal simulation was run without modelling the fire protection system, however following the standard time-temperature curve with a 10-fold time scale. When the surface temperature of the member exceeded 300°C, the gas temperature was increased to the value of the standard time-temperature curve corresponding to the start time of charring in the fire tests, following the standard time-temperature curve with normal scale.

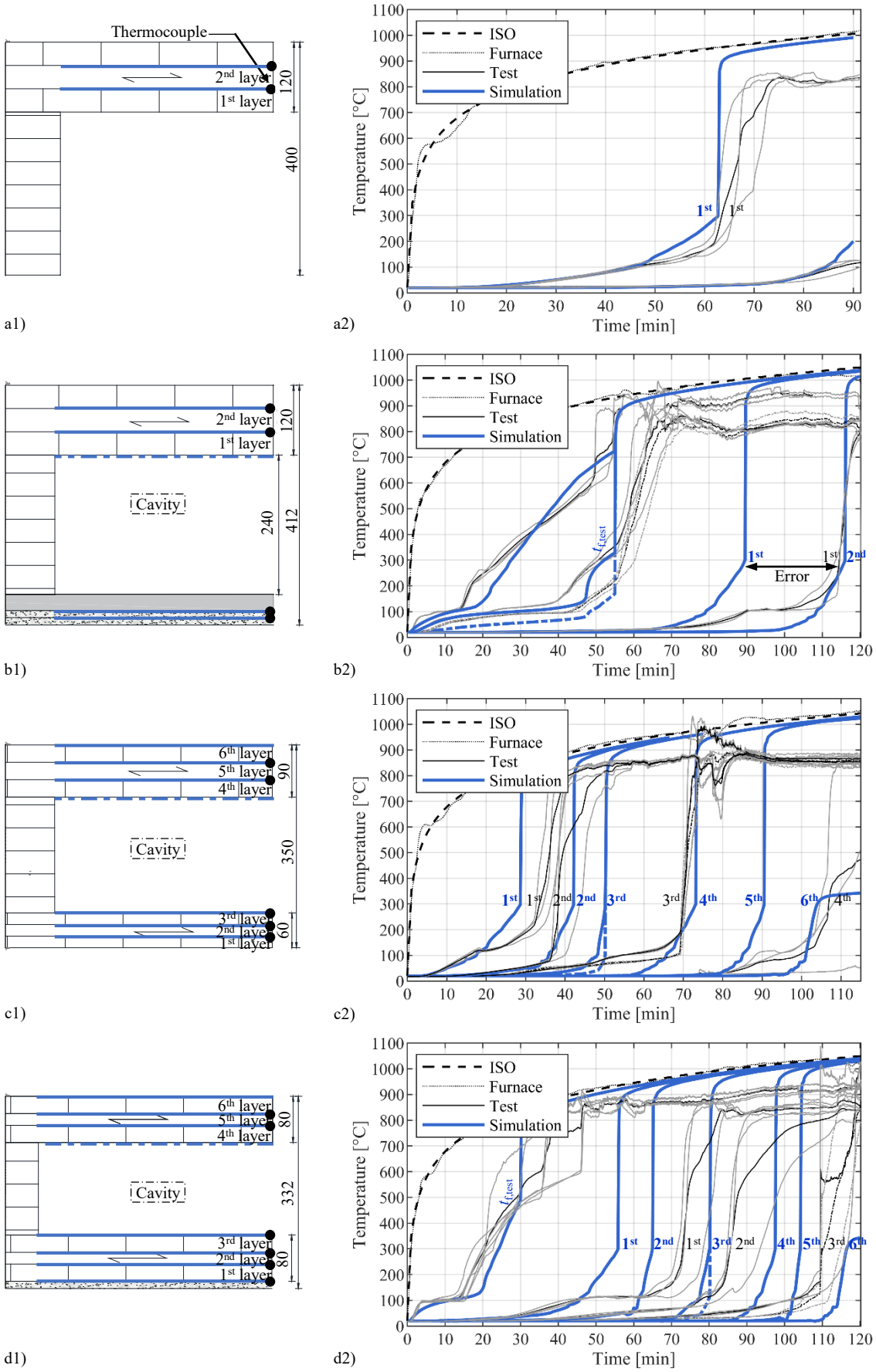

Figure 4.5. Thermal simulations (2D) - Numerical temperatures at different levels based on EN 1995-1-2 in comparison to the experimental results of the cross-sections (until test termination): a) A; b) B; c) C; d) D.

In this thesis, it was aimed to run the thermal simulation, following the standard time-temperature curve with normal scale from the beginning of the simulation. After removing multiple fallen-off layers in the FE model, the time-temperature dependence of the thermal properties must be different, since the relationship between time and temperature differs compared to the standard time-temperature curve. It was aimed to reduce the conductive heat transfer after the fall-off of both - the fire protection system or a charred CLT layer - by revising the thermal properties according to EN 1995-1-2 2004. This should be achieved by an evolution of the given Eurocode 5 values rather than a revolution. A conventional calibration was conducted minimizing the error of the fall-off time of the first charred CLT layer in the case of cross-section B between experimental result $t_{300°C,\text{test}}$ and numerical result $t_{300°C,\text{sim}}$ (Figure 4.5).
The best fit is presented in Figure 4.6 and Table 4.4: the revised thermal conductivity in the direction perpendicular to the grain $\lambda_{\theta,rev}$, the revised specific heat capacity $c_{\theta,rev}$, and the not revised density to dry density ratio $\rho_\theta/\rho_{\text{dry}}$. Revisions in the given Eurocode 5 values were based on literature and physical knowledge. The new set of thermal properties is based on two changes:

- An endothermic reaction heat was included during pyrolysis.
- The effect of thermal insulation by the char layer was increased.

In the literature, a controversial discussion was found whether the pyrolysis can be considered as endothermic or exothermic (Fredlund 1988; Roberts 1971; Mehaffey, Cuerrier, and Carisse 1994). König and Walleij (1999) concluded that the reaction heat during pyrolysis could be neglected in their calibration, since the pyrolysis process in wood was expressed by the effective values of thermal conductivity. Hofmann (2022) took into account an endothermic reaction heat during pyrolysis between 150°C and 500°C for the calibration of thermal properties for bio-based insulation material (cellulose and wood fibres). In this thesis, an endothermic reaction heat was included between 200°C and 350°C as triangular distribution for the specific heat capacity following the approach in Frangi (2001) and Schleifer (2009). For the activation of the pyrolysis, an endothermic reaction heat $q_{\text{pyr}} = 370kJ/kg$ was considered according to Roberts (1971). This reaction heat corresponds to the triangular area under the curve of the specific heat capacity between 200°C and 350°C (Figure 4.6b).
As second step, the thermal insulation of the char layer was increased. The literature was searched for lower values of thermal conductivity for temperatures above 350°C. After comparison of Janssens (1994), Mehaffey, Cuerrier, and Carisse (1994), and Thomas (1997), the distribution of the thermal conductivity was adapted between 350°C and 1200°C based on the value of 0.18 W/(mK) at 800°C according to Janssens (1994) (Figure 4.6a).

The thermal simulations of all cross-sections were conducted using the new set of thermal properties after either the fall-off of the gypsum plasterboards (cross-sections B and D) or the fall-off of the first charred CLT layer (cross-sections A and C). In this thesis, the combination of thermal properties of the current Eurocode 5 and the new set after fall-off is called the revision. Figure 4.7 presents the numerical temperatures per cross-section type based on the revision in comparison to the experimental temperatures measured on top or between the CLT layers

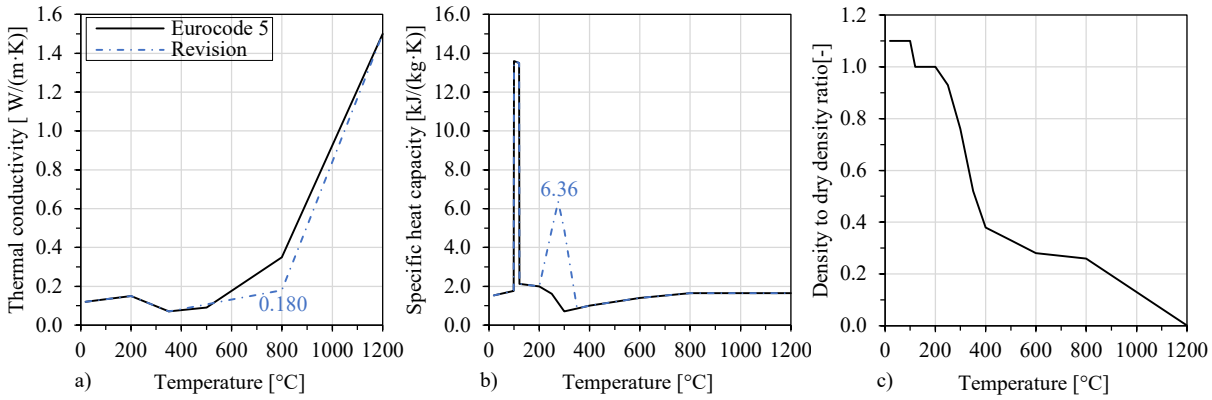

Figure 4.6. Revised set of temperature-dependent thermal properties for wood after fall-off in comparison to the set according to EN 1995-1-2 (Eurocode 5): a) Thermal conductivity; b) Specific heat capacity; c) Density to dry density ratio.

Table 4.4. New set of temperature-dependent thermal properties for wood after fall-off (revised values are highlighted in bold)

Temperature θ	Thermal conductivity $\lambda_{\theta,rev}$	Specific heat capacity $c_{\theta,rev}$	Density to dry density ratio $\rho_{\theta,rev}/\rho_{dry}$
[°C]	[W/(mK)]	[kJ/(kgK)]	[-]
20	0.120	1.53	1.10
99	0.133	1.77	1.10
100	0.133	13.60	1.10
120	0.137	13.50	1.00
121	0.137	2.12	1.00
200	0.150	2.00	1.00
250	0.123	**4.91**	0.93
275	0.110	**6.36**	0.85
300	0.097	**4.91**	0.76
350	0.070	0.85	0.52
400	**0.082**	1.00	0.38
500	**0.107**	1.20	0.33
600	**0.131**	1.40	0.28
800	**0.180**	1.65	0.26
1200	1.500	1.65	0.01

Table 4.5. Thermal simulations - Experimental, analytical, and numerical results per cross-section type (until test termination) (values based on the revision are highlighted in bold).

Test specimen	Type of cross-section	$t_{ch,test}$	$t_{f,test} = t_{f,sim}$	$t_{ch,EC5}$	$t_{f,EC5}$	Charring progress	$\beta_{CLT,test}$[1)]	$\beta_{CLT,EC5}$[1)]	$\beta_{CLT,sim,rev}$[1)]
		[min]	[min]	[min]	[min]	until fall-off of	[mm/min]	[mm/min]	[mm/min]
A	T	Initially unprotected				1st layer	0.63	0.65	**0.64**
B	T	55	55	49	58	1st layer	0.67	0.82	**0.69**
C	box	Initially unprotected				4th layer	0.84	1.02	**0.90**
D	box	20	30	24	28	3rd layer	0.89	1.07	**0.93**

[1)] Charring rate of the CLT plates: $\beta_{\mathrm{CLT,test}} = d_{\mathrm{char,test}}/(t_{300°\mathrm{C,test}} - t_{\mathrm{ch,test}})$.

and gypsum plasterboards. It shows graphically the reduced or even eliminated error between experimental and numerical results. The number of fall-offs would not have been overestimated. Table 4.5 provides the experimental, analytical, and numerical charring rates of the CLT plates until last experimental fall-off of charred CLT layers. The experimental and analytical results remain unchanged compared to Table 4.3. The numerical charring rates are now in a reasonable range, giving a safe prediction of the charring behaviour of the CLT plates without being overly conservative.

Figure 4.8 presents the errors per CLT layer of each cross-section. The error between experimental and numerical results of cross-section B could thus be corrected from 25 to 3 min. The error of cross-section A remained unchanged, as there was no further fall-off of charred CLT layers. Likewise, the error of the first layer of cross-section C remained unchanged, since the revised properties apply only after the first fall-off. However, the errors of the following layers of cross-sections C and D were reduced significantly or could even be eliminated. The error of the second layer of cross-section C is still comparatively high. Here, fall-offs occurred in the test at very low temperatures ($< 100°$C) and the charring progressed in a relatively short time (section 3.6.3).

4.3.5 Model validation

The revision was validated against further experimental results of initially unprotected CLT plates, taken from literature and collected into a database. The CLT plates were exposed to standard fire and showed more than one fall-off. Table 4.6 summarizes the 29 fire tests of the database. Thermal simulations were conducted using the thermal properties based on Eurocode 5 as well as the revision. The sizes of the elements were 1x1 mm^2 of a CLT slice of 5 mm width. The interval between the time steps was kept at 1 second.

Figure 4.9 compares the charring rates obtained from the numerical results of the single CLT plates with the experimental charring rates. The difference between numerical and experimental charring rates is expressed by the root mean square error (RMSE). The revision fits 3-times better the experimental data (RMSE = 0.09 mm/min) than the current Eurocode 5 (RMSE = 0.28 mm/min). The comparison based on the revision shows a relationship between experimental and numerical charring rates on the safe side or within an error corridor of 10%. Figure 4.9

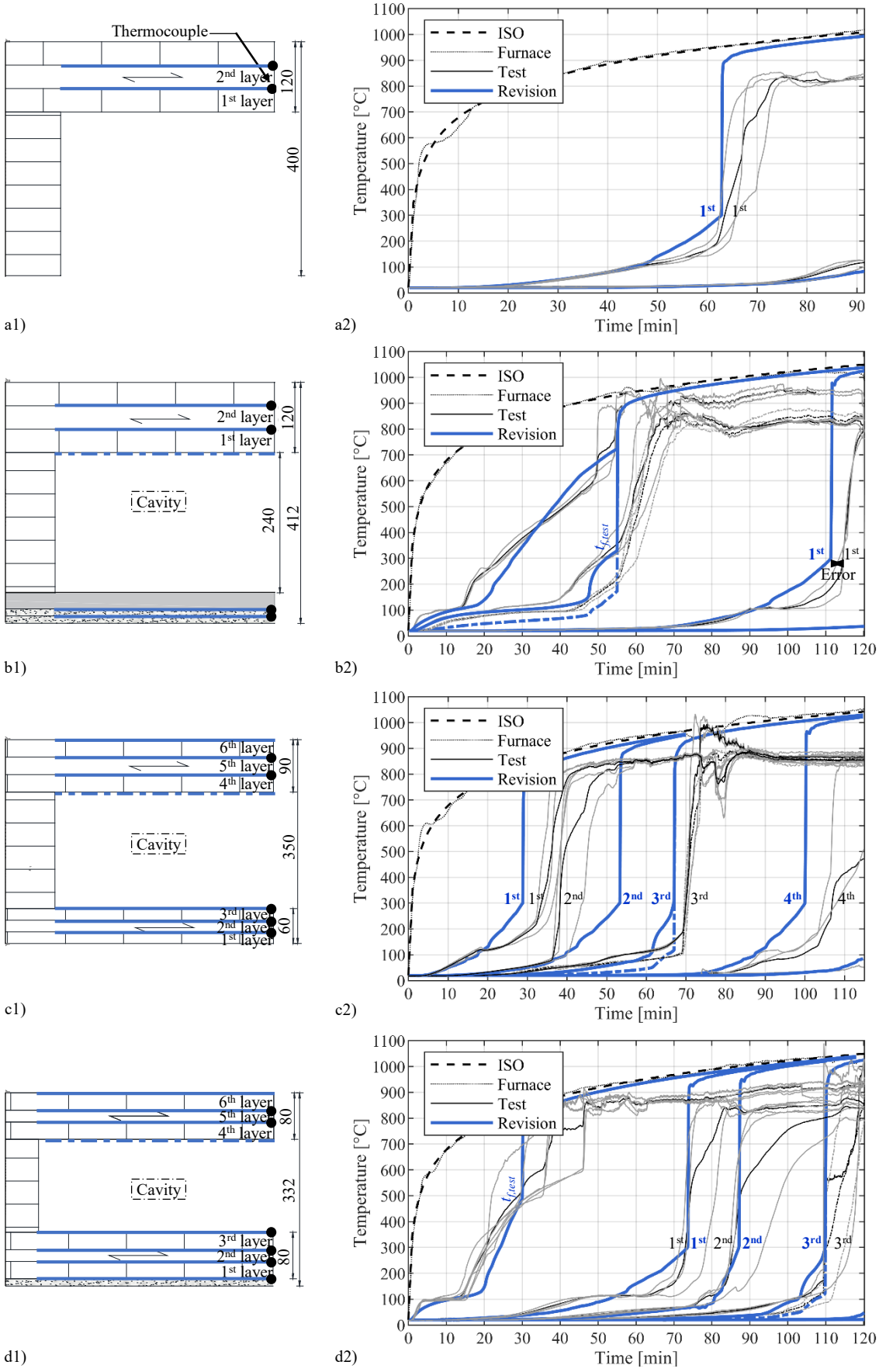

Figure 4.7. Thermal simulations (2D) - Numerical temperatures at different levels of the cross-sections based on the revision in comparison to the experimental results (until test termination): a) A; b) B; c) C; d) D.

distinguishes between different layer thicknesses (10 – 40 mm) and number of fall-offs of charred CLT layers (2 – 5 fall-offs). The latter can also be associated with longer fire exposure times. Thicker layer thicknesses and fewer fall-offs lead to results close to the basic charring rate β_0 for solid wood of 0.65 mm/min. Thinner layer thicknesses and multiple fall-offs result in higher charring rates up to 1.1 mm/min.

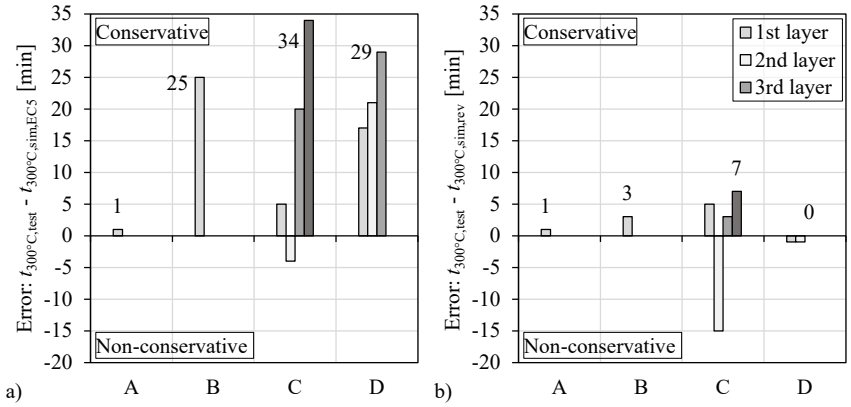

Figure 4.8. Thermal simulations (2D) - Error between experimental and numerical fall-off times of charred CLT layers per cross-section type (until test termination) comparing: a) Based on Eurocode 5; b) Based on the revision.

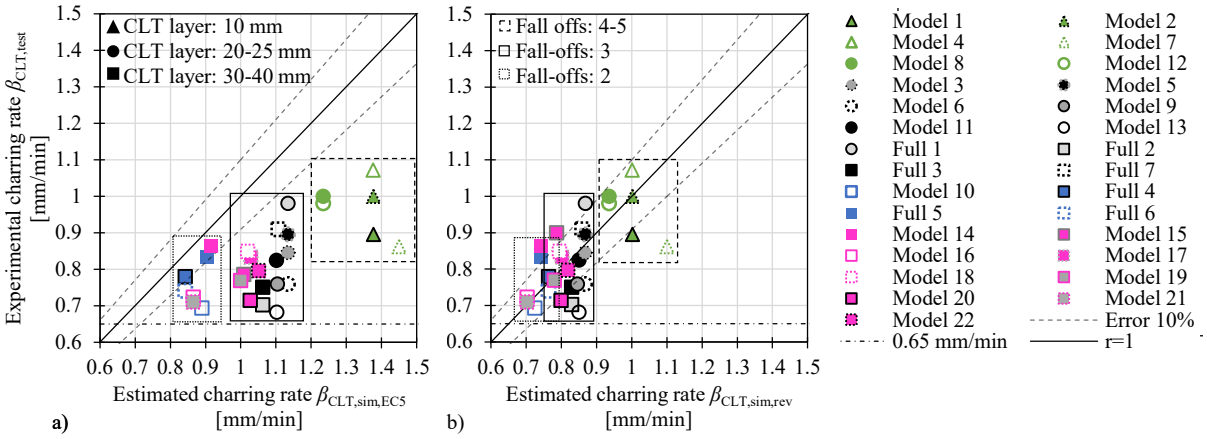

Figure 4.9. Thermal simulations (2D) - Comparison of experimental and numerical charring rates of the database: a) Based on Eurocode 5; b) Based on the revision.

4.3.6 Results based on the revision

Residual cross-sections

Figure 4.11 presents on the left side the experimental and numerical residual cross-sections after extinguishment. The results are compared to the estimated results according to EN 1995-1-2 and prEN 1995-1-2: the estimated rectangular residual cross-sections of the glulam ribs and the estimated charred depths in the CLT plates. The experimental and estimated results are taken

Table 4.6. Thermal simulations - Experimental, analytical, and numerical results per cross-section type (until test termination) (values based on the revision are highlighted in bold).

Reference	Specimen	Adhesive	Layup	Total thickness	Layer thickness	Specimen size	Density	Moisture content	Fire exposure time	Type of fire test	Number of fall-offs
			[mm]	[mm]	[mm]	[mm2]	[kg/m3]	[%]	[min]		[-]
Frangi et al. (2009)	Model-scale 1	PUR	10/10/10/10/20	60	10	800x1000	445.0	10.0	67	unloaded	5
	Model-scale 2	PUR	10/10/10/10/20	60	10	800x1000	445.0	10.0	60	unloaded	5
	Model-scale 3	PUR	3x20	60	20	800x1000	445.0	10.0	71	unloaded	3
	Model-scale 4	PUR	10/10/10/10/20	60	10	800x1000	445.0	10.0	56	unloaded	5
	Model-scale 5	PUR	3x20	60	20	800x1000	445.0	10.0	67	unloaded	3
	Model-scale 6	PUR	3x20	60	20	800x1000	445.0	10.0	79	unloaded	3
Fahrni, Klippel, and Frangi (2021)	Model-scale 7	PUR	5x10	80	10	800x1000	463.5	12.0	60	unloaded	5
	Model-scale 8	PUR	7x25	175	25	800x1000	447.5	12.0	120	unloaded	4
	Model-scale 9	PUR	7x20	140	20	800x1000	471.0	12.0	90	unloaded	3
	Model-scale 10	PUR	5x35	175	35	800x1000	456.8	12.0	120	unloaded	2
	Model-scale 11	PUR	7x25	175	25	800x1000	433.0	12.0	120	unloaded	3
	Model-scale 12	PUR	7x25	175	25	800x1000	431.7	12.0	120	unloaded	4
	Model-scale 13	PUR	7x25	175	25	800x1000	454.6	12.0	120	unloaded	3
RISE Fire Research (2022)	Model-scale 14	Unknown	7x30	210	30	600x1900	445.3	11.0	120	unloaded	2
	Model-scale 15	Unknown	7x30	210	30	600x1900	487.1	9.0	130	unloaded	3
	Model-scale 16	PRF	7x30	210	30	600x1900	483.3	9.8	130	unloaded	2
	Model-scale 17	MUF	7x30	210	30	600x1900	473.3	9.9	120	unloaded	3
	Model-scale 18	PUR	7x30	210	30	600x1900	477.0	8.8	120	unloaded	3
	Model-scale 19	EPI	7x30	210	30	600x1900	488.7	7.6	130	unloaded	3
	Model-scale 20	Unknown	7x30	210	30	600x1900	469.5	7.8	130	unloaded	3
	Model-scale 21	PUR	7x30	210	30	600x1900	478.7	8.0	130	unloaded	2
	Model-scale 22	Unknown	7x30	210	30	600x1900	454.1	8.9	130	unloaded	3
Bühlmann (2014)	Full-scale 1	PUR	10x20	200	20	2850x5210	450.0*	12.0*	84	loaded	3
Mindeguia et al. (2020)	Full-scale 2	PUR	5x33	165	33	3900x5600	450.0	12.6	203	loaded	3
	Full-scale 3	PUR	5x33	165	33	3900x5600	450.0	11.6	179	loaded	3
Stora Enso (2021)	Full-scale 4	PUR	40/20/20/20/40	140	40/20	2250x4500	480.0	12.0*	86	loaded	2
	Full-scale 5	PUR	5x40	200	40	2340x4500	430.0	12.0*	126	loaded	2
	Full-scale 6	PUR	40/20/40/20/40/20/40	220	40/20	2250x4500	480.0	12.0*	145	loaded	2
	Full-scale 7	PUR	2x30/30/40/30/2x30	220	30	2340x4500	430.0	12.0*	143	loaded	3

*Assumption

from section 3.6.2 (Figure 3.24). The numerical residual cross-section was created by extracting the 300°C iso-surface at a specified time step, which agrees with the time duration in the fire resistance tests until extinguishment (Table 3.6). The thermal simulations of all cross-sections were repeated using the new set of thermal properties also for the glulam ribs after either the fall-off of the gypsum plasterboards (cross-sections B) or the fall-off of the bottom CLT plates (cross-sections C and D). Thus, the numerical results were calculated applying the revision on the entire composite cross-section and not only on the CLT plates. The 300°C iso-surfaces in the glulam ribs fit perfectly the experimental shapes, except for cross-section D.
Figure 4.11 complements these results on the right side with the analysis of the corresponding charring behaviour of the CLT plates from the start time of charring until extinguishment. The numerical charring developments are based on the fall-off times of charred CLT layers of the thermal simulations. Until test termination, the numerical charred depths fit well with the experimental charred depths. After test termination, they show a faster progression of the charred depths. The charred depths in the CLT layers propagate less severe for the numerical calculation than the estimated calculation.

Temperatures in the glue line between CLT plates and glulam ribs

Figure 4.12 presents the temperatures obtained by the thermal simulations in the glue line between CLT plates and glulam ribs at specific time steps. The experimental temperatures of the fire resistance tests are included as mean values, taken from section 3.6.2 (Figure 3.22).
Figure 3.22 presents the temperatures in the top glue lines of cross-sections A, B, and C. At the rib centre and depths close to the rib centre (60 mm or 40 mm), the numerical temperatures agree well with the measured temperatures. At depths close to the outer rib edge (30 mm or 20 mm), the thermal simulations overestimate the temperatures with later time steps. At the outer rib edge, the thermal simulations underestimate the temperatures at later time steps.
Figure 4.12 presents the temperatures in the bottom glue line of cross-section D. Until a fire exposure time of 90 min, the temperatures along the whole glue line stayed at 20°C. From 110 min, the experimental temperatures were rising slowly along the glue line, while the numerical temperatures show a sudden increase to 900°C along the entire glue line.

4.3.7 Discussion

Residual cross-sections

Figure 4.10 compares the ratios between the numerical and the experimental residual cross-sections. Here, the numerical results are based on both approaches: applying the revision only for the CLT plates, and for all timber materials (CLT plates and glulam ribs). The cross-sectional areas were calculated between equal boundaries. The boundaries of the cross sections were defined by the width of the smallest experimental cross section in Figure 4.11. Overall, the numerical residual cross sections agree on average to 59% with the experimental residual cross sections in the first case and to 73% in the second case. The results show a significant improvement when applying the new set of thermal properties after fall-off for

all timber materials. The thermal simulations lead to less conservative predictions than the simplified design method. The estimated, rectangular residual cross-section areas fit on average only to 40% with the experimental residual cross-section areas (Figure 3.26).
Figure 4.11 shows that the advanced design method gives a good approximation of the residual cross-sections. However, the numerical residual cross-sections show lower degrees of corner rounding in the corners of the composite section than the experimental residual cross-sections. A reason for this could be a less severe fall-off of charred CLT layers but a dropping of charred CLT layer parts. The advanced design method assumes a sudden fall-off of the entire charred CLT layer, resulting in less visible corner rounding, as in the case of the simplified design method (section 3.6.3).
After test termination, the numerical results show a faster progression of the charred depths in the CLT layers. In the fire resistance tests, the fire exposure cannot be defined as standard fire exposure in the period between test termination and extinguishment (up to 25 minutes). The furnace was turned off and the gas temperature did not follow the standard time-temperature curve, anymore. Thermocouples showed an almost constant temperature of 1000°C before they were cut off before extinguishment. A corresponding adjustment of the thermal simulations improved the agreement between numerical and experimental residual cross sections. The numerical residual cross sections agreed on average to 82% with the experimental residual cross sections, especially due to the better fit of the final charred depths in the top CLT plates.

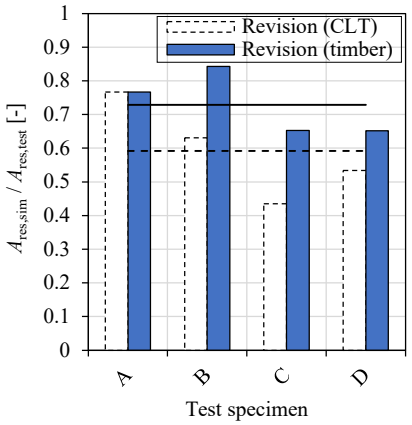

Figure 4.10. Thermal simulations (2D) - Ratio between numerical and experimental residual cross-sections of the test specimens (after extinguishment).

Temperatures in the glue line between CLT plates and glulam ribs

At later time steps, the temperatures along the glue line are overestimated by the thermal simulations in comparison to the experimental results. This confirms the discussion that the numerical residual cross-sections show lower degrees of corner rounding in the corners of the composite section. At later time steps, the temperatures at the outer rib edge are underestimated by the thermal simulations. Here, the experimental temperatures were measured by the plate thermometers of the furnace, and by the thermocouples hanging in the cavities. In both cases, the influence of convection were neglected.

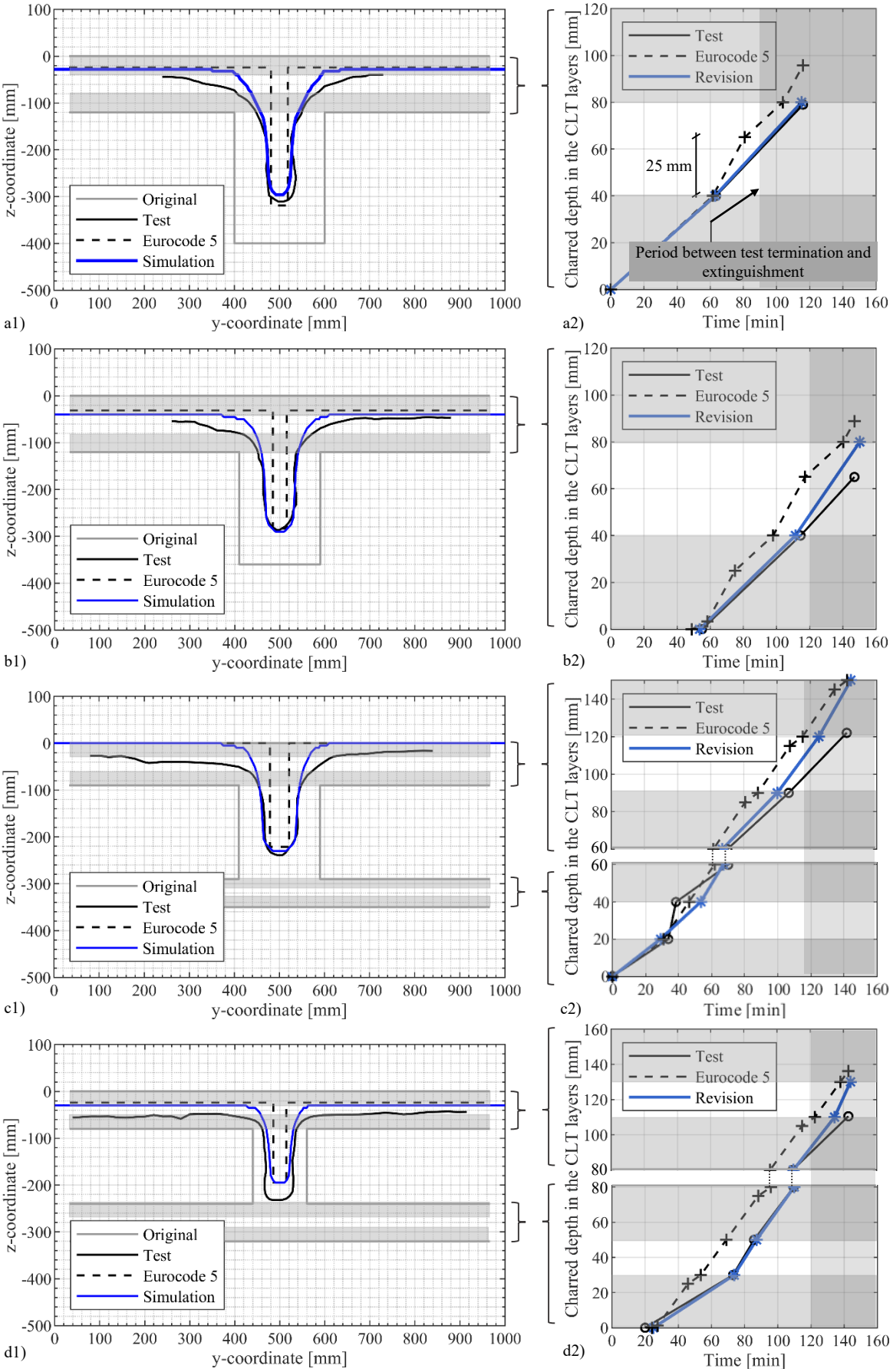

Figure 4.11. Experimental, estimated, and numerical residual cross-sections (after extinguishment) and the corresponding charred depths in the cross-laminated timber plates based on the revision: a) A; b) B; c) C; d) D.

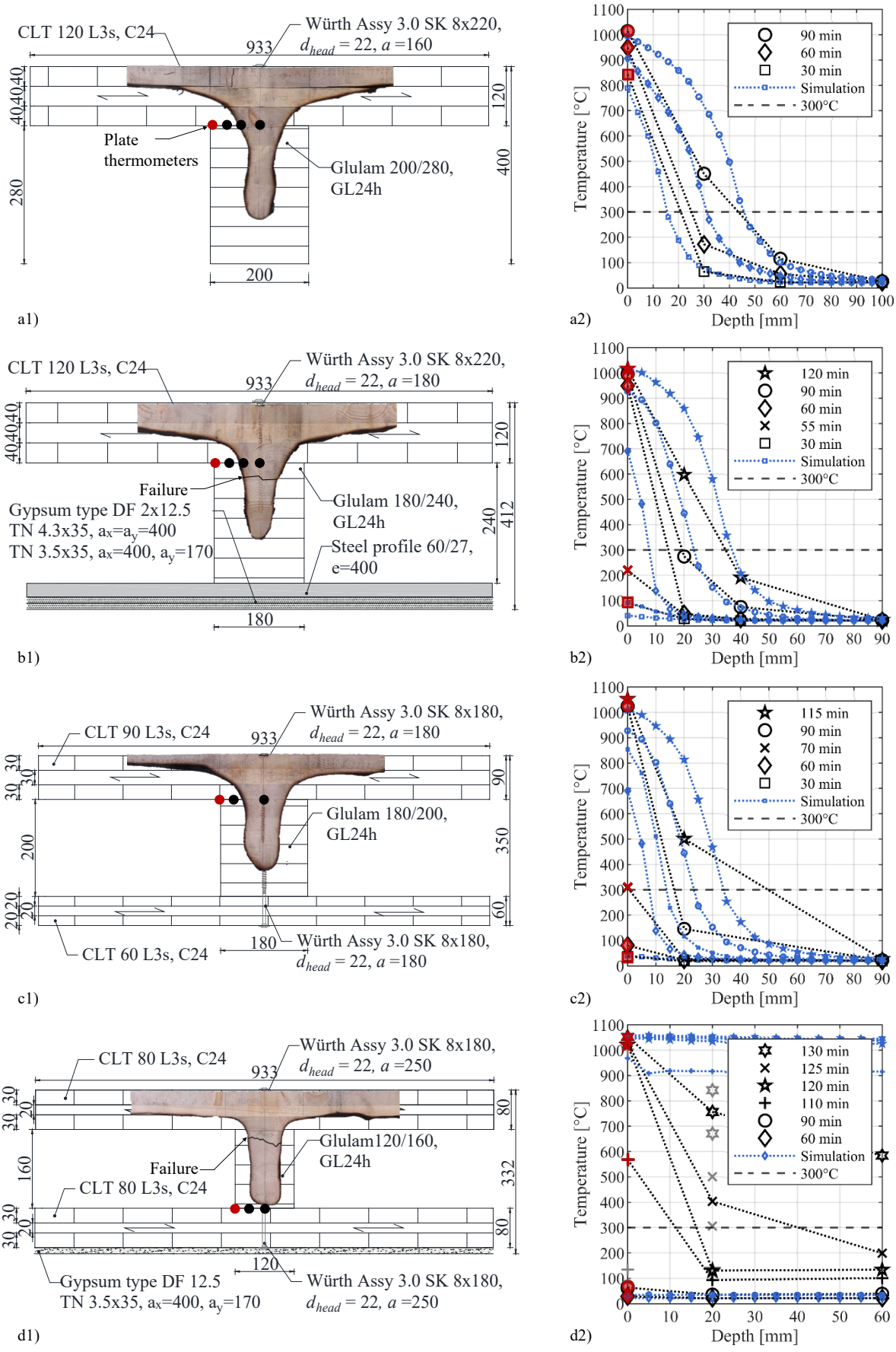

Figure 4.12. Numerical temperatures between cross-laminated timber plate and glue-laminated timber rib based on the revision in comparison to the experimental results (after extinguishment, in [mm]): Top glue line a) A; b) B; c) C; bottom glue line d) D.

4.3.8 Conclusions

Heat transfer analyses using 2D FE models were performed modelling the cross-section of a T-section or box-section. The temperature-dependent thermal properties according to Eurocode 5 (EN 1995-1-2) were not calibrated to model the post-fall-off behaviour of wood. A new set of thermal properties is proposed for wood after the fall-off of both a fire protection system or a charred CLT layer. The combination of Eurocode 5 and the new set is called the revision. The validation was made by a database of CLT plates exposed to standard fire from one side with layer thicknesses of 10 – 40 mm.
The comparison with experimental results shows that the FE heat transfer models provide good estimates of the experimental temperatures. The experimental residual cross-sections show good agreement with the numerical residual cross-sections (= 300°C iso-surface) when the new set of thermal properties is applied after fall-off to all timber materials; i.e. also for the glulam ribs. The degrees of corner rounding are more pronounced in the corners of the composite section of the experimental cross-sections and lead to overestimated temperatures along the glue line between CLT plates and glulam ribs by the thermal simulations.

4.4 Thermo-mechanical simulations (beam)

4.4.1 Objectives

Uncoupled thermo-mechanical simulations were performed using a 2D FE model of a linear beam system for discussion of the structural behaviour under fire exposure. The numerical results of the four tested cross-section types (Figure 3.1) are presented and compared with the experimental results of the fire resistance tests. Depending on the modelled cross-section, the influence of the effective width on the numerical results is investigated.

4.4.2 Model

Modelling framework

The uncoupled thermo-mechanical simulation was conducted using SAFIR® version 2019.b.0, a nonlinear FE software for modelling structures in fire (Franssen and Gernay 2017). The simulation depended on the pre-defined cross-section and the temperature history of a 2D FE cross-section from the thermal simulations (section 4.3). An output file was created by SAFIR® after the thermo-mechanical simulation. The simulation stopped because either a maximum defined deflection was reached or convergence to a state of equilibrium was not obtained. The post-processor DIAMOND (University of Liège 2016) was used to view the structure, and to view and extract the results of the output file.

Finite element models

The input file of a linear FE model was generated for submission to SAFIR®, modelling the system of the fire resistance tests as a simply supported 2D beam system with a length of 5.20 m

in accordance with the length of the furnace (Figure 3.18) and as one-rib system. The supports were defined as fixed (or pinned) and roller support. The structure was discretized by 16 beam elements of 0.352 m length, thus smaller than the height of the cross-sections (Figure 4.13). As in the test setup, the uniformly distributed load was represented by eight loading points over the length. The point loads and the self-weight were taken from Table 3.6 as force per loading point per rib and self-weight per rib. The self-weight was taken as constant value. Mass-loss of the cross-section due to pyrolysis was neglected. Materials were modelled as linear-elastic and temperature-dependent orthotropic, brittle in tension and in compression. The mechanical properties of the materials were user defined by the modulus of elasticity in x-direction, one value for the Poisson's ratio (taken as 0.4), and the compressive and tensile mean strength values taken from section 4.2.4. The cross-section and its temperature history was read from a specific TEM-file of the thermal simulations, which needed to be in the same folder as the input file of the thermo-mechanical simulation. The temperature field was non-uniform perpendicular to the axis of the beam system, but no heat transfer was taken into account along the axis of the beam system.
SAFIR® uses Bernoulli-type beam finite elements. Thus, the influence of shear deformations is neglected and the stress distribution along the CLT width is uniform. The shear lag effect of the ribbed cross-sections needed to be taken into account by applying an effective width to the cross-section. Following section 3.3.5, cross-sections were considered based on the following cases of the effective width:

- Case 1: 60% of the cross-laminated timber width, representing the average result for the effective width at normal temperature according to prEN 1995-1-1
- Case 2: 80% of the cross-laminated timber width, representing the average result for the effective width of the ultimate-load tests at normal temperature (reference tests)
- Case 3: 100% of the cross-laminated timber width, representing the extreme case

Depending on the element size, cross-sections were generated with the CLT width corresponding to the respective effective width, rounded down to the nearest full element. The fall-off times of the CLT layers are affected by the ratio between clear CLT width between the glulam ribs and width of the glulam rib. The differences of the fall-off times were within 30 s. The fall-off times of the original systems (cross-laminated timber width b of 0.933 m) were used as fall-off times for all cases.
When requesting the creation of a TEM-file from SAFIR®, the nodeline needed to be included in the input file of the thermal simulation. It was defined as the position of the neutral axis of the original composite cross-section based on the method of rigidly bonded components (Formula 2.13). A sensitivity study demonstrated that the exact position of the nodeline did not affect the results of the thermo-mechanical simulation, since no extension or contraction of the beam system was investigated (Ehrenberg 2020). Furthermore, the thermal simulations needed to be extended by the definition of the vertical symmetry axis in the middle of the cross section. The transversal CLT layers were defined as new material, which still had the same temperature-dependent thermal properties as the longitudinal CLT layers but no loadbearing

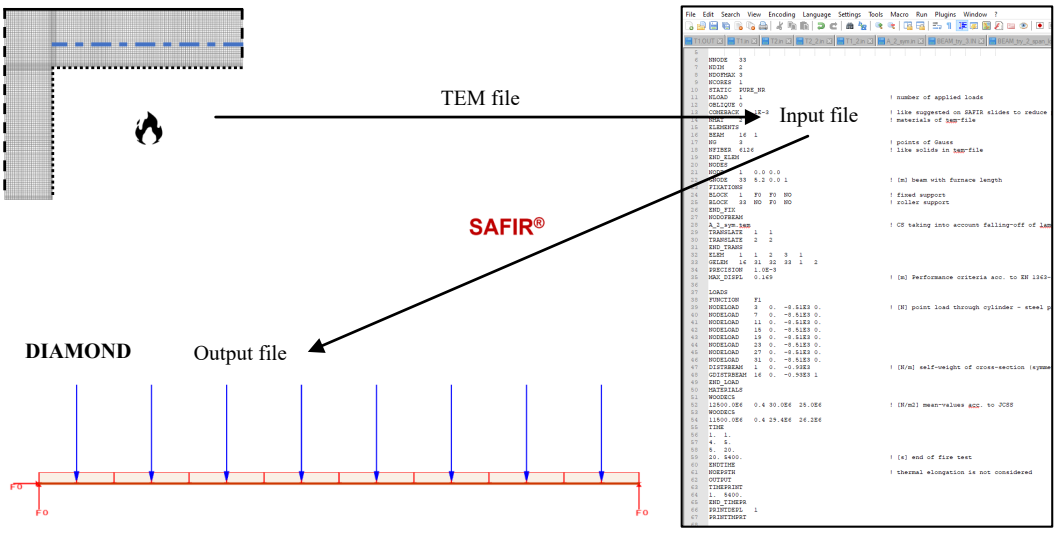

Figure 4.13. Thermo-mechanical simulations (beam) - Linear FE beam model.

mechanical properties.

The intervals between the time steps were kept at maximum 20 seconds. Calculations with smaller intervals did not result in higher accuracy. SAFIR® uses an iterative procedure to converge on the correct solution for each increment. The simulation stop occurred, when SAFIR® has not obtained convergence at a specific increment. The convergence aims an equilibrium of stresses over the height of the cross-section based on the defined restrictions for the mechanical properties. The distribution of stresses depend on the reduced stiffness per fibre (= element of the thermal simulation) based on temperature-dependent reduction factors for stiffness. The maximum stress per fibre depends on the reduced strength value based on temperature-dependent reduction factors for strength. SAFIR® runs the calculations by default based on the temperature-dependent reduction factors for compression and tension according to EN 1995-1-2. The definition of user defined reduction factors was possible. Since a redistribution of the stresses is not considered by SAFIR®, the simulation stopped as soon as convergence was not obtained with the defined comeback time of the iterative procedure of 0.0001 seconds.

Procedure

The thermal simulations of section 4.3.6 were repeated for the three cases of the effective width, including the requested nodeline. For each cross-section type and effective width, the thermo-mechanical simulations were conducted based on the TEM-files of the thermal simulations. The content of the input file of the thermo-mechanical simulations was changed to adapt the point loads and the self-weight based on the cross-section type. The filename of the TEM-file was exchanged to import the temperature history of a specific thermal simulation. For each TEM-file, an output file was created by SAFIR® after the thermo-mechanical simulation. At the end, the numerical results were sequenced together.

4.4.3 Results

Temperature-dependent deflections

Figure 4.14 presents per cross-section type the numerical deflections for the three cases of the effective width (60%, 80%, and 100% of the CLT width) until simulation stop. Furthermore, the experimental deflections are shown as single (grey colour) and mean values (black colour), taken from section 3.6.2 (Figure 3.20). The instantaneous deflections due to self-weight were removed. The numerical deflections show higher values for a cross-section with a smaller effective width. Figure 4.14a and b present the results of the T-sections (A, B). The original numerical results (light blue colour) show a clear underestimation of the experimental measurements. The linear FE beam model does not account for deflections caused by shear deformations. To compensate for the neglected shear deflections, a certain proportion is added to the numerical bending deflections (blue colour). From the reference tests (Table 3.2), the proportion due to shear deflections w_v/w was determined on average as 28% of the deflections for cross-section A, and as 18% of the deflections for cross-section B. Multiplying the original numerical results by the ratio $100/(100 - w_\mathrm{v}/w)$, the revised numerical results show very good agreement with the experimental measurements. The difference between the results based on the cross-sections with 60% and 100% CLT widths is up to 7 mm. For cross-section B, the influence of the initial fire protection becomes visible through the comparison with the equivalent initially unprotected cross-section. The temperature increase in the initially protected cross-section is delayed by the failure time $t_{\mathrm{f,test}}$ of the fire protection system. Figure 4.14c and d present the results of the box-sections (C, D). Again, a certain proportion is added to the numerical bending deflections (light blue colour) to account for the neglected shear deflections (blue colour). From the reference tests (Table 3.2), the proportion due to shear deflections w_v/w was determined on average as 26% of the deflections. The numerical results disagree with the experimental measurements, especially after the fall-off of the second charred CLT layer.
In the fire resistance tests, the test specimens were screwed on top of a wood frame for lifting on the furnace. In the case of T-sections (A, B), the wood frame was attached to non-loadbearing elements of the test specimens. In the case of box-sections (C, D), the wood frame was attached to the bottom CLT plates. The support situations on both ends of the system might have been capable to resist forces acting in any direction of the plane. In a further step, both supports of the FE beam model were defined as fixed supports for cross-sections C and D and the thermo-mechanical simulations were repeated. Figure 4.15 presents the numerical deflections per cross-section type, including the revised results of cross-section types C and D. The revised numerical results show good agreement with the experimental measurements. The numerical results show a higher increase in the rate of change after the fall-off of the second charred CLT layer than the experimental measurements. The difference between the results based on the cross-sections with 60% and 100% CLT widths is up to 18 mm.

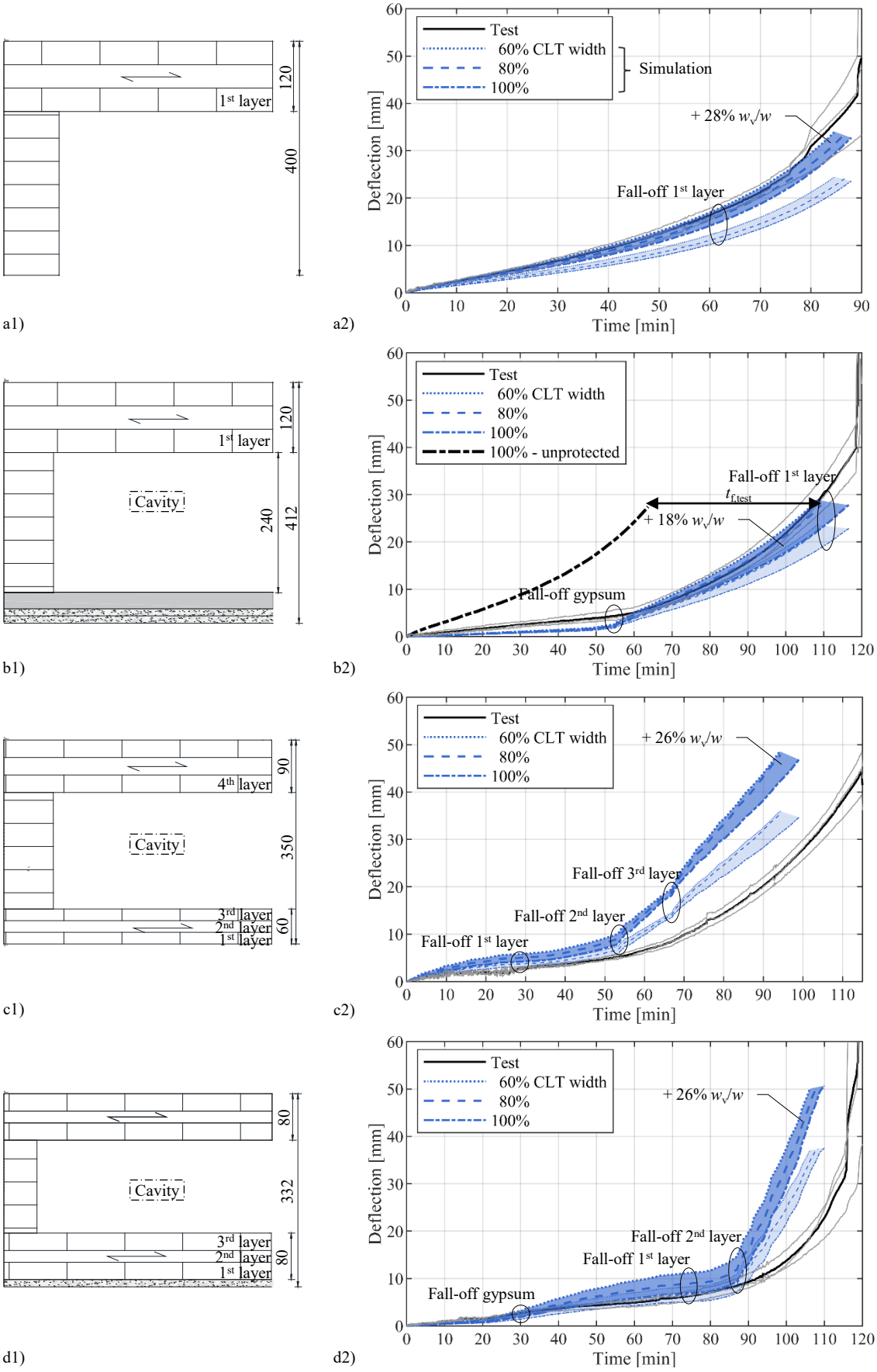

Figure 4.14. Thermo-mechanical simulations (beam) - Numerical deflections per cross-section type for the three cases of the effective width excl. / incl. proportion due to shear deflections (until simulation stop) in comparison to the experimental results (until test termination): a) A; b) B; c) C; d) D.

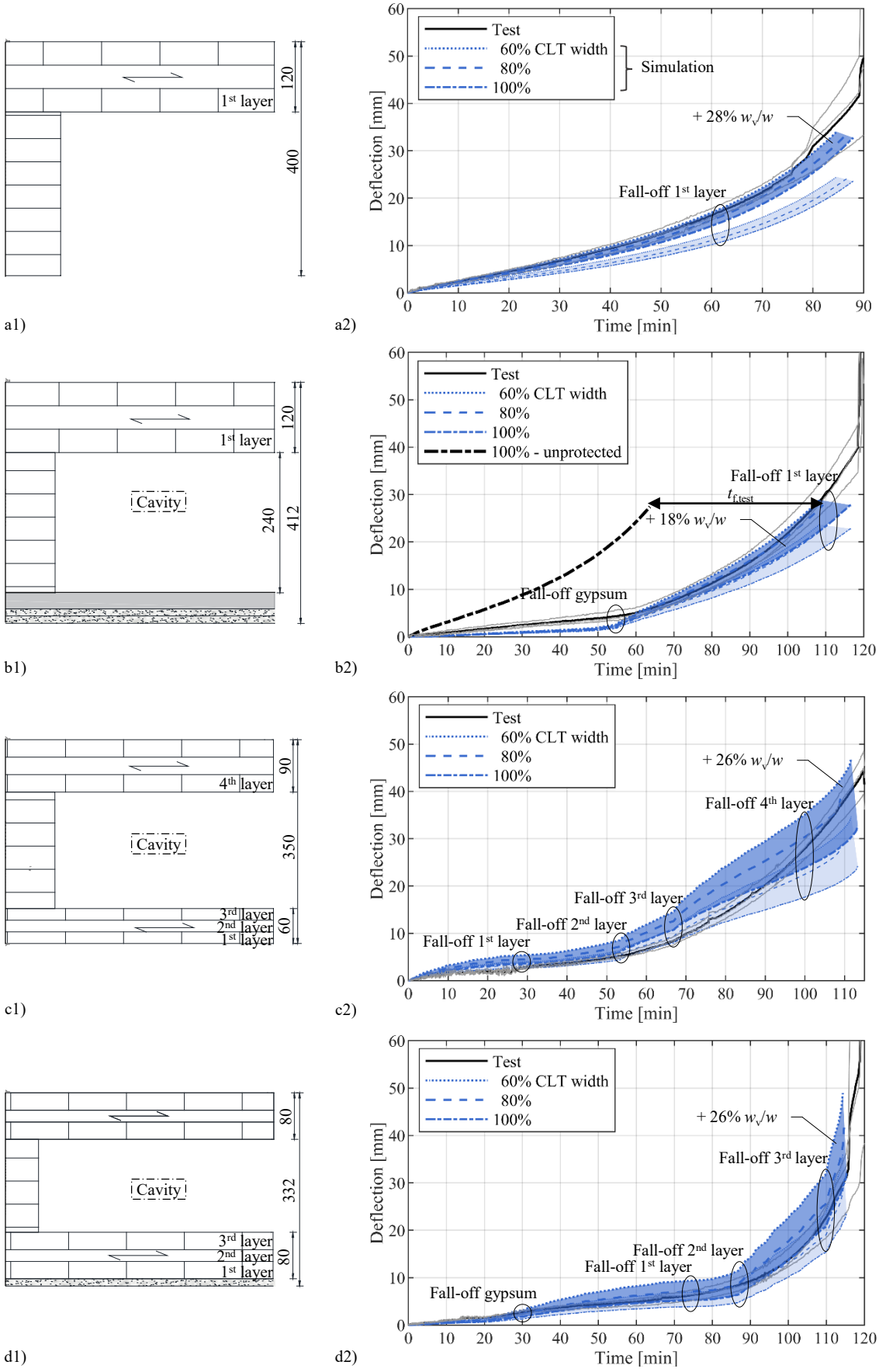

Figure 4.15. Thermo-mechanical simulations (beam) - Numerical deflections of the cross-sections for the three cases of the effective width (until simulation stop) excl./incl. the proportion due to shear deflections in comparison to the experimental results (until test termination): a) A; b) B; c) C (fixed supports); d) D (fixed supports).

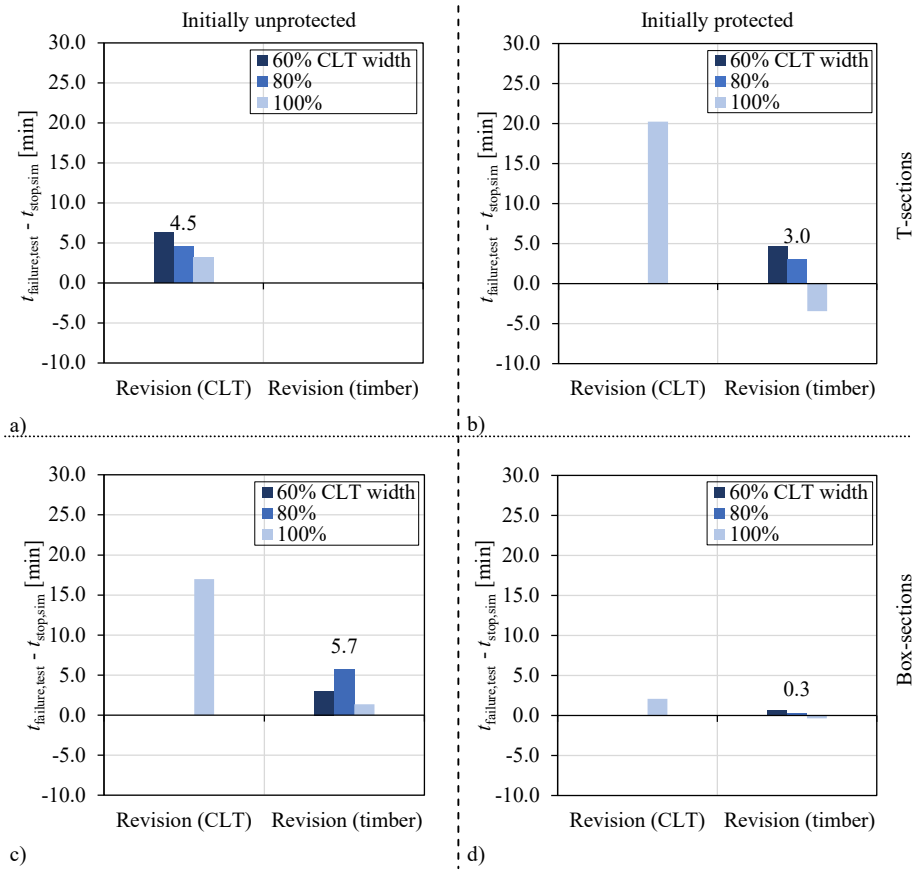

Figure 4.16. Thermo-mechanical simulations (beam) - Error between experimental time of failure and simulation stop per cross-section type for the three cases of the effective width: a) A; b) B; c) C; d) D.

Simulation stop

Figure 4.16 presents the error between experimental time of failure and time of simulation stop per cross-section type for the three cases of the effective width (60%, 80%, and 100% of the CLT width). The revised support situation of cross-section types C and D is taken into account. The experimental failure times were taken from Table 3.6 either as time of failure (B, D) or as time of test termination (A, C). In addition, the comparison for cross-sections B, C, and D is made if the revision was applied in the thermal simulations only for the CLT plates (CLT) or for all timber materials (timber). A positive error means that the time step, where convergence could not be obtained in the simulation, is smaller than the failure time of the fire resistance test. A negative error means that the time step is larger than the failure time of the fire resistance test. All results led to a positive error, except for the system of cross-section B with 100% of the CLT width. The calculation gave up to 8-times higher error values when using the revision only for CLT and not for timber. The error of the systems with 80% of the CLT width was maximum 5.7 min and on average 3.4 min. The difference between the systems with 60% and 80% of the CLT width or 80% and 100% of the CLT width was maximum 6.4 min.

Temperature-dependent stresses

Figure 4.17 presents the numerical stress distributions per cross-section type at simulation stop. The revised support situation of cross-section types C and D is taken into account. The numerical results were taken from the systems with 80% of the CLT width (case 2) at midspan (= beam 8). In the figure, the positions of the neutral axis are added per cross-section type. The increase of outer fibre bending stresses due to shear deformations caused by the shear-soft transversal layers of the CLT plates was not taken into account given the high slenderness of the CLT plates.
All test specimens show the residual cross-section of a T-section. In the case of cross-section A, the simulation stopped after the fall-off of the first CLT layer. In the case of cross-section B, the simulation stopped right before the fall-off of the first CLT layer. In the case of cross-section C, the simulation stopped after the fall-off of the fourth CLT layer. In the case of cross-section D, the simulation stopped after the fall-off of the bottom CLT plate (third CLT layer). The results confirm that the transversal CLT layers were defined as non-loadbearing material. Due to the temperature-dependent reduction factors, fibres exhibiting temperatures above 300°C do not take any strains (see 300°C iso-surfaces as residual cross-sections in Figure 4.11). Based on the Bernoulli-theory, the strains and stress distributions along the CLT width are uniform. The cross-sections exhibit tensile stresses above 20 N/mm^2 at the exposed bottom edge, and compressive stresses between 6 N/mm^2 and 12 N/mm^2 at the unexposed top edge.

4.4.4 Discussion

Temperature-dependent deflections

In the case of cross-sections C and D, changing the roller support of the simply supported beam system to another fixed support (no resistance to rotation) improved the compatibility with the experimental measurements. The numerical results of cross-section C show the greatest discrepancy with the experimental measurements as in the thermal simulations. The numerical deflections outline the importance to take into account the shear deflections. The shear flexibility is increased by the effect of shear lag of the composite cross-section, and to a certain extent by the shear-soft transversal layers of the CLT plates. Especially in the case of box-sections, the proportion due to shear deflections w_v/w cannot be considered as constant value over time. Furthermore, the effective width in fire $b_{\mathrm{ef,fi}}$ cannot be considered as a constant value over time or equal to the initial value at normal temperature. The results based on the cross-sections with 60% and 100% CLT widths show a larger difference for the box-sections than for the T-sections, which outlines that the effective width b_ef has a higher influence on the box-sections than on the T-sections.
The numerical deflections depend on the temperature-dependent reduction factors for stiffness. Since the tensile zone lays at the exposed edge, the reduction factor for stiffness in tension $k_{\theta,\mathrm{E,t}}$ governs the structural behaviour of the floor system. Adjustments of the reduction factor at 100°C for stiffness in compression $k_{100°\mathrm{C,E,c}}$ left the results unchanged. Figure 4.18 presents the numerical deflections of the initially unprotected T-section (A) and box-section

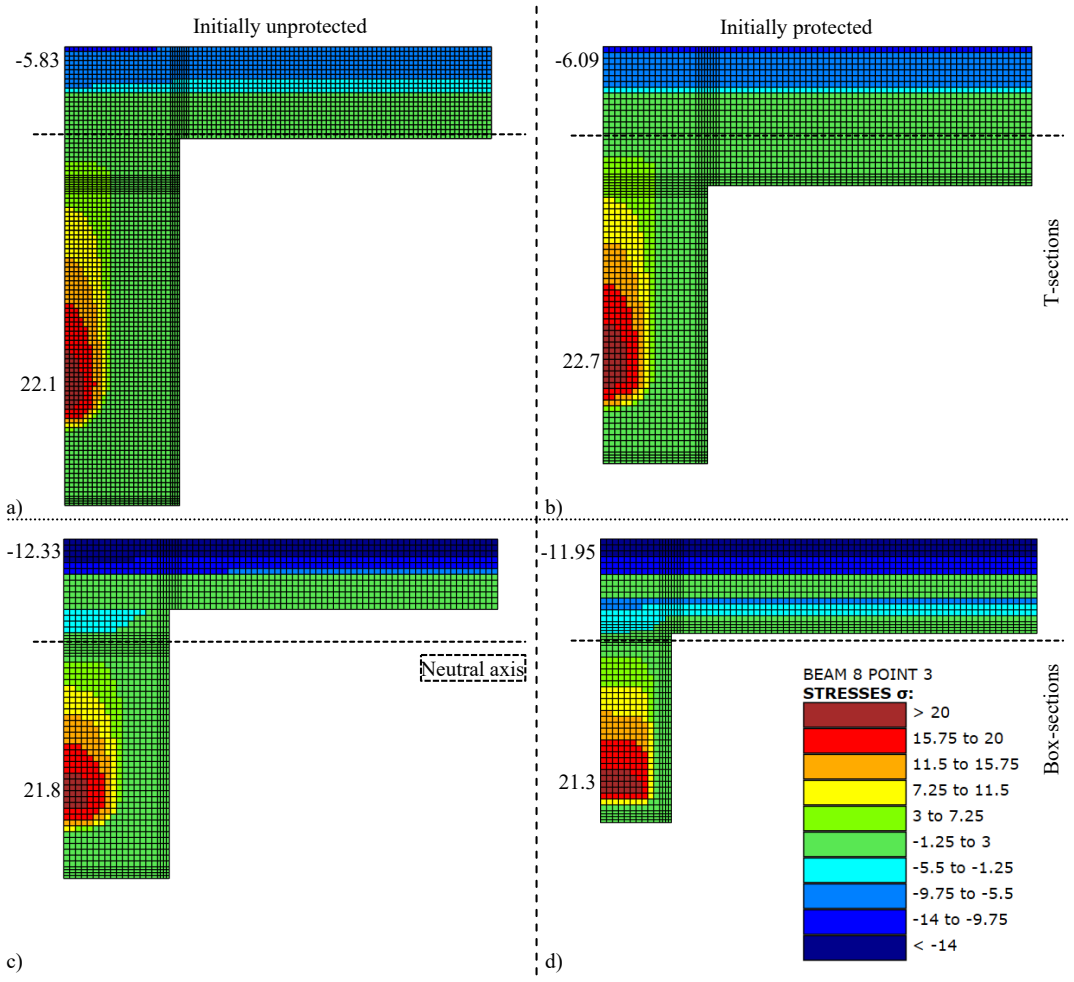

Figure 4.17. Thermo-mechanical simulations (beam) - Numerical stresses per cross-section type at simulation stop in N/mm^2 for case 2 (80% of the CLT width): a) A; b) B; c) C; d) D.

(C) until simulation stop, including the proportion due to shear deflections w_v/w of 28%. The experimental deflections are added as single values (grey colour) and mean value (black colour). The comparison is made between the former results based on the temperature-dependent reduction factors according to EN 1995-1-2 (blue colour), and numerical results based on a reduction factor at 100°C for stiffness in tension $k_{100°C,E,t} = 0.35$ (dark blue colour). This leads to a higher reduction of the modulus of elasticity parallel to the grain in tension. Figure 4.18 shows an increase of the temperature-dependent deflections by 8% for cross-section A and 4% for cross-section C, followed by an earlier simulation stop by maximum 2 min.

Time of failure

In comparison to the fire resistance tests, the thermo-mechanical simulations lead to an estimated failure time (= simulation stop) on the safe side. The results show a significant improvement when applying the revision in the thermal simulations for all timber materials; i.e. also for the glulam ribs. Then, the error was maximum 6 min. The CLT width of the cross-section has a minor influence on the simulation stop. If further improvement is required,

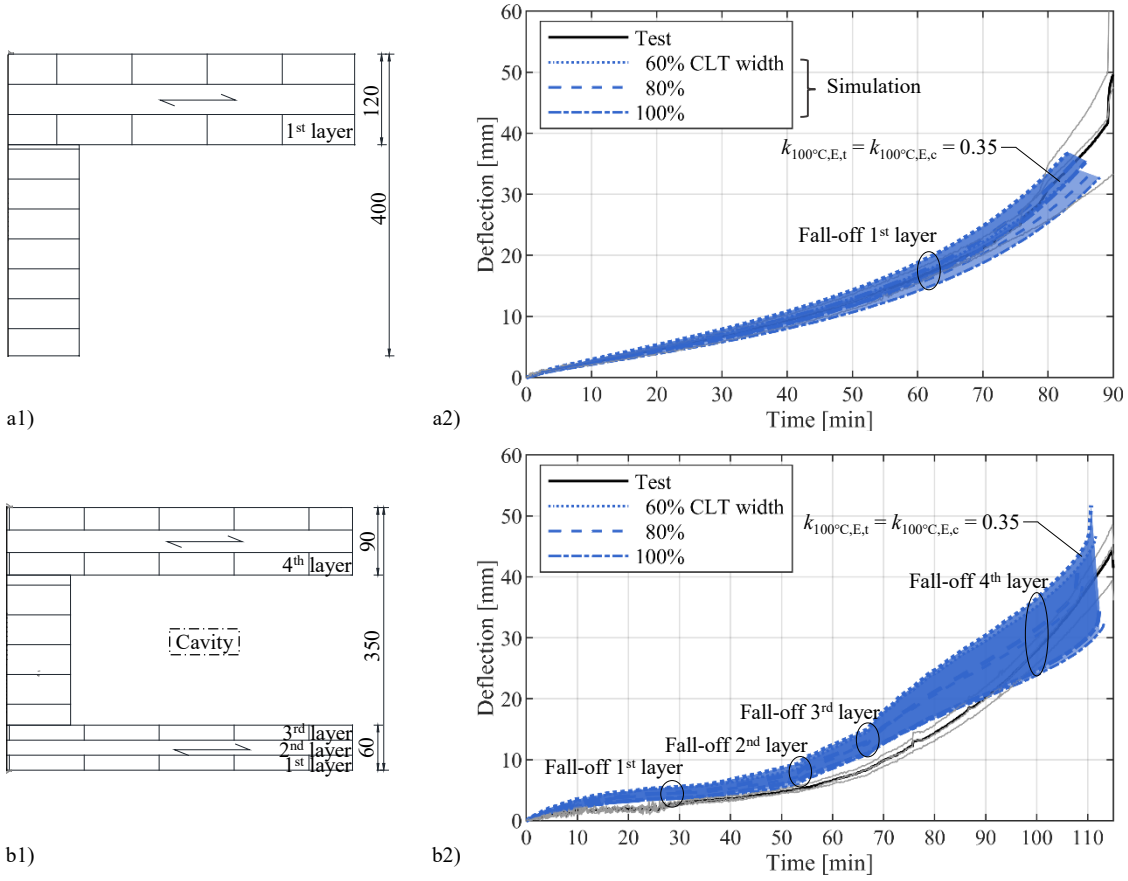

Figure 4.18. Thermo-mechanical simulations (beam) - Numerical deflections of the cross-sections for the three cases of the effective width (until simulation stop) incl. the proportion due to shear deflections in comparison to the experimental results (until test termination): a) A; b) C.

increased local compressive and tensile strength values could be implemented in the model (Källsner and König 2000; Schmid et al. 2018). Nevertheless, the results already give very good estimates of the fire resistance times.

Temperature-dependent stresses

The stress distribution obtained from the numerical results are verified based on the simplified assumptions of the model. The loadbearing residual cross-section is represented by the fibres above the 300°C iso-surface at simulation stop. Maximum tensile stresses exhibited by the glulam rib are of comparable magnitude; i.e. 21-22 N/mm^2. The tensile mean strength value for glulam at normal temperature of 26.2 N/mm^2 was reduced, depending on the temperature exhibited by the corresponding fibre. The smaller residual cross-sections of the box-sections exhibit higher maximum compressive stresses at the unexposed edge of the top CLT plate than the T-sections. The compressive mean strength value for CLT at normal temperature of 33.9 N/mm^2 was minorly reduced. The tensile strength at elevated temperatures was decisive. The numerical stresses depend on the temperature-dependent reduction factors for strength. Since the tensile zone lays at the exposed edge, the temperature-dependent reduction factor for local tension $k_{\theta,\mathrm{f,t}}$ governs the structural behaviour of the floor system. In a sensitivity

analysis, the temperature-dependent reduction factors at 100°C were adjusted for both local tension $k_{100°C,f,t}$ and local compression $k_{100°C,f,c}$. The latter resulted in minor changes. The first delayed the simulation stop by up to 8 min, when the reduction factor was set to an extreme value of 0.95 based on Gerhards (1982).

4.4.5 Conclusions

Uncoupled thermo-mechanical simulations were performed using a linear 2D FE beam model. The thermo-mechanical model is validated against the experimental results of the fire resistance tests. The mechanical simulations depend on the cross-section and its temperature history of the thermal simulations. Materials were modelled as linear-elastic and temperature-dependent orthotropic, brittle in tension and in compression.

In the case of cross-sections C and D, changing the roller support of the simply supported beam system to another fixed support (no resistance to rotation) improved the compatibility with the experimental measurements. Adjustments of the reduction factor at 100°C for stiffness in compression $k_{100°C,E,c}$ left the results unchanged. Adjustments of the reduction factor for stiffness at 100°C in tension $k_{100°C,E,t}$ gave minor changes. The numerical deflections outline the importance to take into account the shear deflections. Based on the results of the reference tests, the shear deflections account for up to 28% of the deflections. Still, the proportion due to shear deflections w_v/w cannot be considered as constant value over time. Furthermore, the effective width in fire $b_{ef,fi}$ cannot be considered as constant value over time or equal to the initial value at normal temperature.

The simulation stop occurred, when SAFIR® has not obtained convergence at a specific increment. The results give very good estimates of the fire resistance times (maximum error: 6 min). The stress distribution obtained from the numerical results are verified based on the simplified assumptions of the model. The loadbearing residual cross-section is represented by the fibres above the 300°C iso-surface at simulation stop. The tensile strength at elevated temperatures was decisive. Adjustments of the reduction factor at 100°C for strength in local compression $k_{100°C,f,c}$ left the results unchanged. Adjustments of the reduction factor at 100°C for strength in local tension $k_{100°C,f,t}$ gave minor changes.

To study the influence of the chosen effective width on the resulting deflection, three different approaches were compared for the tested cross-section types: representing the average result for the effective width b_{ef} according to prEN 1995-1-1 (60% of the CLT width), the average result for the effective width of the reference tests $b_{ef,test}$ (80% of the CLT width), and the extreme case (100% of the CLT width). The differences in the resulting deflections using these three approaches for the effective widths are larger for the box-sections than for the T-sections, as concluded from the reference tests (section 3.3.5). Higher deflections are obtained for a cross-section with a smaller effective width. However, the differences are small in all cases and therefore it can be concluded that an underestimation of the effective width in fire $b_{ef,fi}$ still results in good approximations.

Overall, the numerical results confirm that the FE model gives very good approximations of the structural behaviour in fire. A good fit is obtained based on the material properties and

strength values, the temperature-dependent reduction factors according to EN 1995-1-2, and using linear-elastic brittle material behaviour.

4.5 Thermo-mechanical model for the determination of the resistance moment in fire

4.5.1 Objectives

A thermo-mechanical model determined the resistance moment in fire at specific time steps based on the thermo-mechanical simulations of the linear 2D FE beam model. The objective is the investigation of the loadbearing capacity as a bending resistance in fire. The numerical results of the four tested cross-section types (Figure 3.1) are presented and compared with the experimental bending resistance at failure time of the fire resistance tests. Depending on the modelled cross-section, the influence of the effective width on the numerical results is investigated.

4.5.2 Model

Modelling framework

The Python programming language (Python Software Foundation 2015) was used to implement a thermo-mechanical model and to estimate the resistance moment at a specific time step. The calculation depended on the pre-defined cross-section and the temperature history of a 2D FE cross-section from the thermal simulations (section 4.3) as well as on the stress distributions of the 2D FE beam system from the thermo-mechanical simulations (section 4.4).

Thermo-mechanical model

Basics

The calculation method of rigidly bonded components (Bernoulli-beam) is applied. Based on a linear elastic material behaviour, the strain distribution over the total height of the cross-section is continuous. $\epsilon_{\mathrm{x,i}}$ is the strain in longitudinal direction of fibre i, determined by Formula 4.9

$$\epsilon_{\mathrm{x,i}} = -\kappa_{\mathrm{m}} \cdot z_{\mathrm{i}} \tag{4.9}$$

where κ_{m} is the bending curvature, and z_{i} is the distance of the centroid of fibre i to the centre of gravity.

The stress exhibited by the fibre depends on its stiffness. $\sigma_{\mathrm{x,i}}$ is the stress in longitudinal or x-direction of fibre i, determined by Formula 4.10

$$\sigma_{\mathrm{x,i}} = E_{\mathrm{x,i}} \cdot \epsilon_{\mathrm{x,i}} \tag{4.10}$$

where $E_{\mathrm{x,i}}$ is the modulus of elasticity in x-direction of fibre i. Under fire exposure, the stiffness of the fibre i is reduced by a temperature-dependent reduction factor for stiffness $k_{\theta,\mathrm{E}}(\theta_{\mathrm{i}})$

depending on the temperature exhibited by fibre i. $\sigma_{\mathrm{x,fi,i}}$ is the stress in longitudinal or x-direction of fibre i in fire, determined by Formula 4.11

$$\sigma_{\mathrm{x,fi,i}} = k_{\theta,\mathrm{E}}(\theta_{\mathrm{i}}) \cdot E_{\mathrm{x,i}} \cdot \epsilon_{\mathrm{x,i}} \tag{4.11}$$

The continuous strain distribution results in one global neutral axis for the composite cross-section. The neutral axis is located in the centre of gravity of the composite cross-section z_{s} according to Formula 2.13. The position of the neutral axis is independent of the loading condition. Under fire exposure, the position changes depending on the temperature dependence of the stiffness of the fibres. The neutral axis in fire is located in the centre of gravity of the cross-section in fire $z_{\mathrm{s,fi}}$, determined by Formula 4.12

$$z_{\mathrm{s,fi}} = \frac{\sum(k_{\theta,\mathrm{E}}(\theta_{\mathrm{i}}) \cdot E_{\mathrm{x,i}} \cdot A_{\mathrm{i}} \cdot a_{\mathrm{i}})}{\sum(k_{\theta,\mathrm{E}}(\theta_{\mathrm{i}}) \cdot E_{\mathrm{x,i}} \cdot A_{\mathrm{i}})} \tag{4.12}$$

where $E_{\mathrm{x,i}}$ is the modulus of elasticity in x-direction of fibre i, A_{i} is the area of fibre i, and a_{i} is the distance to the centroid of fibre i from a selected origin. The temperature-dependent reduction factor for stiffness $k_{\theta,\mathrm{E}}(\theta_{\mathrm{i}})$ is defined according to Figure 4.3 depending on whether fibre i is in the tension or compression zone.

Step 1: Search of the neutral axis in fire at a specific time step

In the thermo-mechanical model, the stress distribution from the thermo-mechanical simulation was used to determine the neutral axis in fire at a specific time step. Starting at the top edge of the cross-section, the row of fibres was searched in which the switch from compressive to tensile forces occurred and thus the neutral axis in fire was contained (rough determination). Then, the position of the neutral axis in fire was defined based on the slope of the stress distribution between the previous row and the current row (fine determination).

Step 2: Determination of the maximum bending curvature at a specific time step

Only strains in x-direction were considered (Figure 4.19). The assumption was made, that the fibre exhibiting the highest tensile strain under loading would also exhibit the highest tensile strain for the maximum strain distribution of the bending resistance. For the specified fibre, the highest tensile strain of the bending resistance $\epsilon_{\mathrm{t,max}}$ was determined by Formula 4.13

$$\epsilon_{\mathrm{t,max}} = \frac{k_{\theta,\mathrm{f,t}}(\theta) \cdot f_{\mathrm{t,mean}}}{k_{\theta,\mathrm{E,t}}(\theta) \cdot E_{\mathrm{x}}} \tag{4.13}$$

where $k_{\theta,\mathrm{f,t}}(\theta)$ and $k_{\theta,\mathrm{E,t}}(\theta)$ are the temperature-dependent reduction factors for strength and stiffness in tension depending on the temperature of the fibre. $f_{\mathrm{t,mean}}$, and E_{x} are the mean tensile strength at normal temperature and the modulus of elasticity in x-direction of the material assigned to the fibre.

The bending curvature of the bending resistance $\kappa_{\mathrm{m,max}}$ was determined by Formula 4.14

$$\kappa_{\mathrm{m,max}} = \frac{\epsilon_{\mathrm{t,max}}}{z_{\mathrm{t,max}}} \tag{4.14}$$

where $z_{\mathrm{t,max}}$ is the distance of the centroid of the fibre exhibiting the highest tensile strain to the centre of gravity in fire.

Step 3: Calculation of the strains per fibre at a specified time step
The strain of each fibre ϵ_{i} was determined by Formula 4.15

$$\epsilon_{\mathrm{i}} = -\kappa_{\mathrm{m,max}} \cdot z_{\mathrm{i}} \tag{4.15}$$

where $\kappa_{\mathrm{m,max}}$ is the bending curvature of the bending resistance, and z_{i} is the distance of the centroid of fibre i to the centre of gravity in fire.

Step 4: Calculation of the resistance moment at a specified time step
The resistance moment in fire $M_{\mathrm{R,fi}}$ was calculated according to Formula 4.16

$$M_{\mathrm{R,fi}} = F_{\mathrm{c}} \cdot e_{\mathrm{c}} + F_{\mathrm{t}} \cdot e_{\mathrm{t}} = \sum_{i=1}^{n} (F_{\mathrm{i}} \cdot z_{\mathrm{i}}) \tag{4.16}$$

with

$$F_{\mathrm{c}} = F_{\mathrm{t}} \tag{4.17}$$

$$F_{\mathrm{i}} = \sigma_{\mathrm{fi,i}} \cdot A_{\mathrm{i}} \tag{4.18}$$

where F_{c} and F_{t} are the inner forces in compression and tension, e_{c} and e_{t} are the distances of the inner forces to the neutral axis in fire, and F_{i}, z_{i}, and A_{i} are the force, the distance to the centre of gravity in fire, and the area of fibre i. $\sigma_{\mathrm{fi,i}}$ is the stress of fibre i in fire according to Formula 4.11. The modulus of elasticity of the transversal CLT layers is taken as zero. The temperature-dependent reduction factor for stiffness $k_{\theta,\mathrm{E}}(\theta_{\mathrm{i}})$ is defined according to Figure 4.3 depending on whether fibre i is in the tension or compression zone.

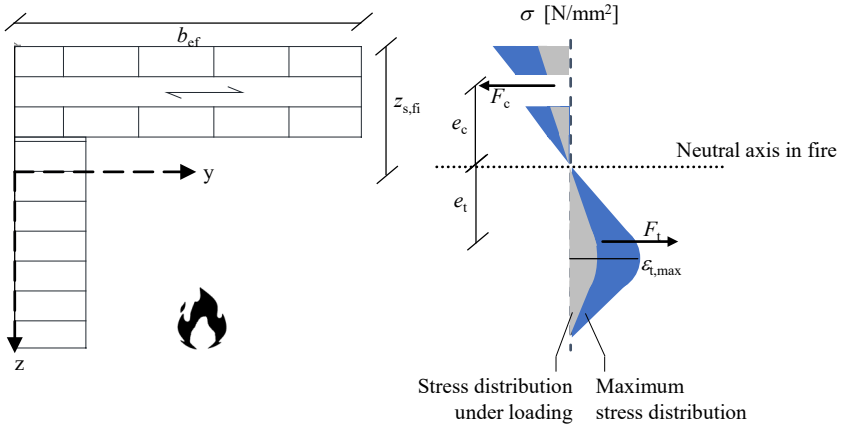

Figure 4.19. Thermo-mechanical model - Equilibrium of forces of the bending resistance in fire at a specified time step.

Procedure

The output files of the thermo-mechanical simulations (section 4.4) contained the required input data per fibre (ID, coordinates of the centroid, area, material, mean temperature, strain, and stress of loading). Based on the output-files, the calculation was performed by a Python script for specific time steps until simulation stop of the thermo-mechanical simulations. For each cross-section type and each case of the effective width, the thermo-mechanical model was used to define the position of the neutral axis in fire and to calculate the resistance moment. A text-file was created after the calculation for further post-processing. At the end, the numerical results were sequenced together.

4.5.3 Results

Temperature-dependent resistance stresses

Figure 4.20 presents the resistance stress distributions obtained from the thermo-mechanical model for case 2 (80% of the CLT width). The results at specific time steps are shown as stress distributions over the height per cross-section type. The transversal CLT layers do not contribute to the bending resistance in fire. The initial state at time step $t = 0$ represents the stress distribution of the bending resistance at normal temperature. The results are presented in 2D plots, in which the stress distribution along the width is plotted on top of each other. At the beginning, the stress distribution along the width is uniform. Once the rib is exposed to fire from three sides, fibres of the same row experience different elevated temperatures and the stresses within the row are no longer uniform. In the case of cross-section A, the rib is exposed to fire from three sides from the beginning. In the case of cross-section B, this occurs after the fall-off of the gypsum plasterboards at 55 min. In the case of cross-sections C and D, this occurs after fall-offs of the bottom CLT plates at 67 min and 110 min (Figure 4.7). The stress distributions per cross-section type show how the neutral axis in fire moves upwards until simulation stop.

Bending resistance in fire

Figure 4.21 presents on the right side the bending resistance in fire per cross-section type for the three cases of the effective width (60%, 80%, and 100% of the CLT width) until simulation stop. The bending resistance in fire is defined as a fraction of the resistance moment in fire at a specific time step and the initial resistance moment at time step $t = 0$ of the cross-section with 100% CLT width, or in short $M_{\mathrm{R,fi}}(t)/M_{\mathrm{R,fi,100}}(t = 0)$. The results show a temperature-dependent reduction of the bending resistance in fire with an increased exposure time. The bending resistance is higher for a cross-section with a larger effective width. Figure 4.21 presents on the left side the position of the neutral axis in fire for the three cases of the effective width until simulation stop. The position of the neutral axis in fire moves upwards with an increased exposure time.

Cross-section A represents the initially unprotected T-section, showing a reduction of the bending resistance in fire in the form of a concave upward movement. The bending resistance in

Table 4.7. Thermo-mechanical model - Resistance moment in fire of the cross-sections for the three cases of the effective width ($t = 0$) in comparison to the experimental loading and the estimated resistance moment at normal temperature.

		Test specimen	A	B	C	D
		Cross-section type	T	T, initially protected	Box	Box, initially protected
M_{test}	[kNm]		44.2	45.5	44.7	44.9
$t_{failure,test}$	[min]		91	113	115	115
$M_{R,100,est}$	[kNm]	100% CLT width	185.8	139.0	277.7	292.7
$M_{R,EC5,est}$	[kNm]	prEN 1995-1-1	170.1	126.6	185.6	163.8
$M_{R,fi,100}(t = 0)$	[kNm]	100% CLT width	189.1	141.5	288.8	305.3
$M_{R,fi,80}(t = 0)$	[kNm]	80% CLT width	178.7	133.5	220.5	227.2
$M_{R,fi,60}(t = 0)$	[kNm]	60% CLT width	168.0	126.2	173.0	172.8

fire of cross-section B remains unchanged or rather increases until the two layers of gypsum plasterboards fall off and the T-section is exposed to fire as in the case of cross-section A. Each T-section shows curves of equal shape for the different cases of the effective width. The differences between the curves are maximum 6% in absolute terms. Cross-section C represents the initially unprotected box-section, showing a reduction of the bending resistance in fire in the form of a concave downward movement. Again, the bending resistance in fire of cross-section D remains nearly unchanged until the layer of gypsum plasterboard falls off. Each box-section shows curves of similar shape for the different cases of the effective width. The differences between the curves are up to 26% in absolute terms and decrease until fall-off of the bottom CLT plates. Both cross-sections C and D show a change to the form of a concave upward movement when the cross-sections change to a T-section after fall-off of the bottom CLT plates. For all cross-sections, the results of the different effective widths lead to final bending resistance in fire of equal magnitude at simulation stop.

The experimental results are defined as resistance moments at failure time of the fire resistance tests, which are equated with the moments caused by loading: $M_{\mathrm{R,fi,test}}(t_{\mathrm{failure,test}}) = M_{\mathrm{test}}$. Table 4.7 lists the moment caused by loading and the failure time per cross-section type. The experimental bending resistance at failure time are included as dots in Figure 4.21, taken as $M_{\mathrm{R,fi,test}}(t_{\mathrm{failure,test}})\ / M_{\mathrm{R,fi,100}}(t = 0)$.

4.5.4 Discussion

Temperature-dependent resistance stresses

The resistance stress distributions obtained from the thermo-mechanical model illustrate the implemented temperature-dependent reduction for stiffness and strength. The capacity of the fibres exhibiting elevated temperatures decrease while fibres exhibiting temperatures above 300°C do not contribute to the bending resistance in fire. Thus, the neutral axis in fire moves upwards (see Figure 4.21) and the bending curvature is increased per time step. The compressive stress values at the top edge of the top CLT plate increase with an increased exposure time.

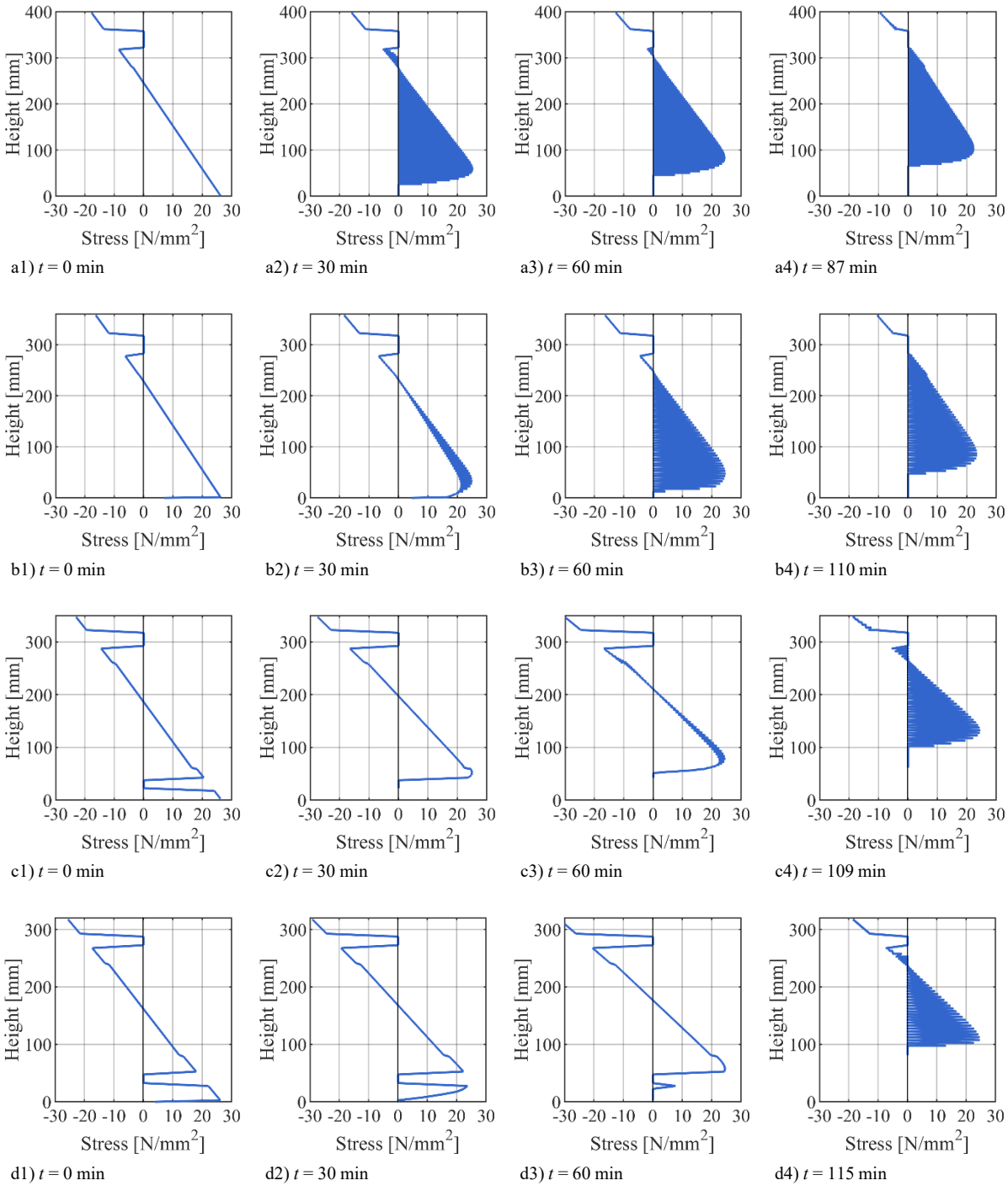

Figure 4.20. Thermo-mechanical model - Numerical resistance stress distributions in fire over the height per cross-section type at specific time steps for case 2 (80% of the CLT width) (until simulation stop): a) A; b) B; c) C; d) D.

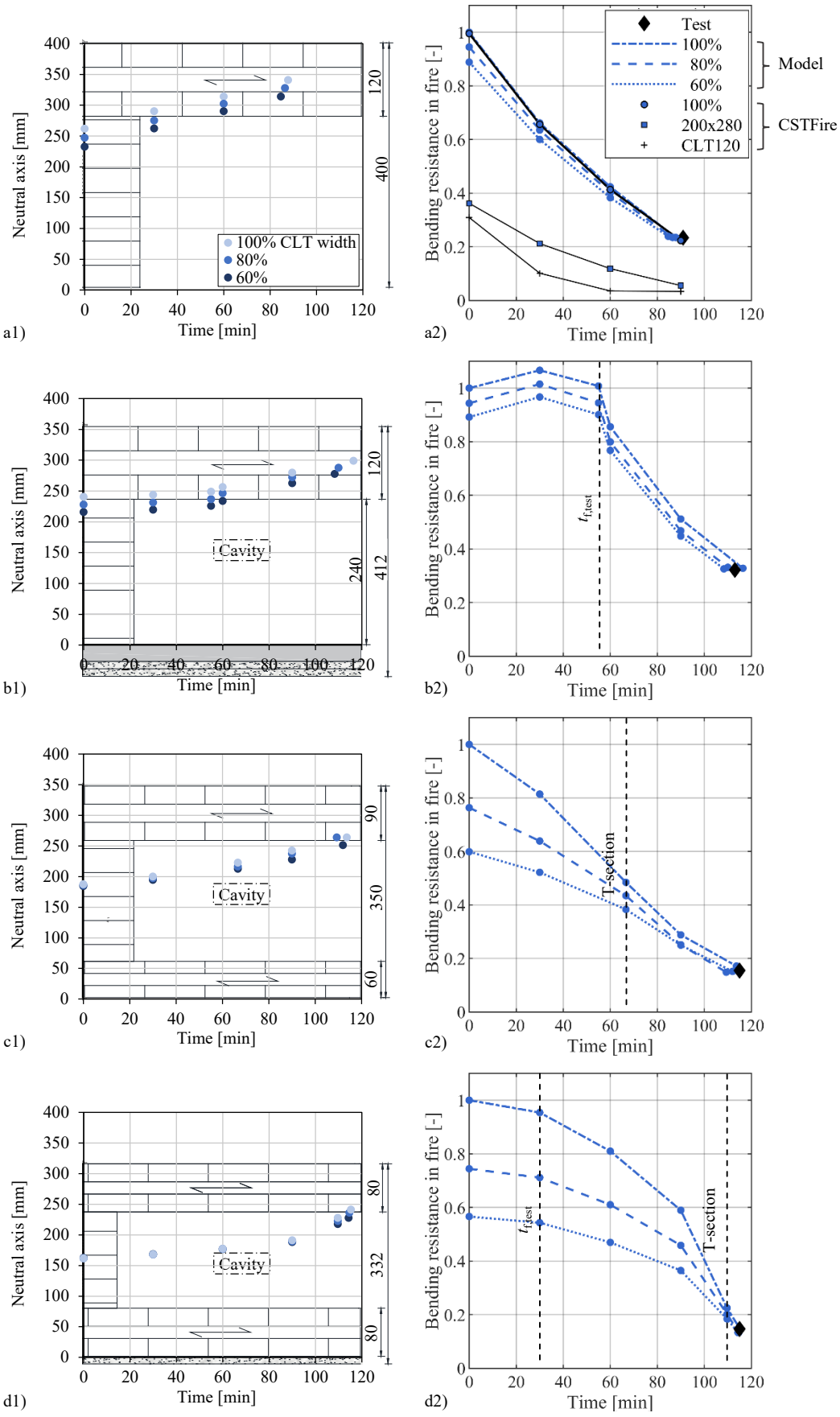

Figure 4.21. Thermo-mechanical model - Neutral axis and bending resistance in fire per cross-section type for the three cases of the effective width (until simulation stop) in comparison to the experimental results (at failure time): a) A; b) B; c) C; d) D.

Bending resistance in fire

The numerical results show a temperature-dependent reduction with an increased exposure time. For cross-section B, the bending resistance in fire shows even an increase until the two layers of gypsum plasterboards fall off. This is explained by the bi-linear definition of the temperature dependence for stiffness and strength in tension (Figure 4.3). The fibres close to the gypsum plasterboards exhibiting elevated temperatures up to 100°C undergo a slower reduction in strength than in stiffness, which means the maximum strain increases with increasing temperature (Frangi 2001). The curves for the different effective widths are of similar shape for the T-sections and box-sections. The differences in bending resistance between the different effective widths are larger for the box-sections than for the T-sections. For all cross-sections, the numerical results of the different effective widths lead to final bending resistance in fire of equal magnitude at simulation stop. This final bending resistance in fire corresponds with the experimental bending resistance at failure time. The results give very good estimates of the fire resistance times (maximum error: 6 min), as discussed in section 4.4.4.

Verification of the model

The initial resistance moments obtained from the thermo-mechanical model ($t = 0$) can be compared to estimations for the resistance moments at normal temperature $M_{\mathrm{R,est}}$ based on the calculation method of rigidly bonded components according to Formula 4.19

$$M_{\mathrm{R,est}} = \frac{f_{\mathrm{t,mean}} \cdot (EI)_{\mathrm{ef}}}{E_{\mathrm{x}} \cdot z_{\mathrm{bot}}} \tag{4.19}$$

where $f_{\mathrm{t,mean}}$ is the mean tensile strength of the glulam rib (parallel to the grain) or the bottom CLT plate (in-plane), $(EI)_{\mathrm{ef}}$ is the effective bending stiffness of the composite cross-section about the y-axis according to Formula 2.14, E_{x} is the modulus of elasticity in x-direction of the glulam rib or the bottom CLT plate, and z_{bot} is the z-coordinate at the bottom edge of the glulam rib or at the bottom edge of the bottom CLT plate.
For verification of the model, the initial resistance moments at time step $t = 0$ of the cross-sections with 100% CLT width $M_{\mathrm{R,fi,100}}(t = 0)$ were compared to the estimates of the resistance moments at normal temperature for cross-sections with 100% CLT width $M_{\mathrm{R,100,est}}$. Table 4.7 lists the reference moments per cross-section type, which are in good agreement. The initial resistance moments at time step $t = 0$ of the cross-sections with 80% and 60% CLT width are also listed, showing a reduction with a decreased CLT width. The latter are in good agreement with the estimates of the resistance moments at normal temperature for cross-sections with effective widths according to prEN 1995-1-1 ($M_{\mathrm{R,EC5,est}}$).
The thermo-mechanical model was verified by comparison with another thermo-mechanical model. CSTFire is a Visual Basic Macro embedded in Excel and had been developed to perform structural analysis of fire-exposed cross-laminated timber (Schmid, König, and Köhler 2010; Schmid et al. 2018). Contrary to the thermo-mechanical model of this thesis, CSTFire considers bi-linear, linear-elastic perfectly plastic material behaviour in compression. It is inconvenient to use for the definition of a non-rectangular cross-section and for the import of the temperature

field. The macro-based calculation runs in the background as a black box. As a comparative calculation, CSTFire was used to calculate the resistance moment of cross-section A with an effective width of 100% CLT width. Figure 4.21a2 shows the bending resistance in fire obtained by CSTFire in relation to the initial resistance moment at time step $t = 0$ min of the cross-section with 100% CLT width obtained by the thermo-mechanical model. The results between the model and CSTFire show very good agreement. In the case of CSTFire, the final bending resistance is reached 6 min later, which could be explained by the bi-linear, linear-elastic perfectly plastic material behaviour in compression. Further, the bending resistance were calculated for a rectangular cross-section representing the glulam rib of cross-section A (200x280 m^2), and a rectangular cross-section representing the CLT plate of cross-section A (CLT 120). The results show a reduction of the initial resistance moment to less than 40% in absolute terms, and a temperature-dependent reduction with an increased exposure time to values below 5%.

4.5.5 Conclusions

A thermo-mechanical model determined the neutral axis, and the resistance moment in fire at specific time steps. The calculations are based on the thermo-mechanical simulations of the linear 2D FE beam model and were performed for the three cases of the effective width (60%, 80%, and 100% of the CLT width). The resistance stress distribution obtained from the thermo-mechanical model are verified based on the simplified assumptions of the model. The neutral axis in fire moves upwards. The numerical results show a temperature-dependent reduction of the resistance moment with an increased exposure time. The resistance moment is higher for a cross-section with a larger effective width. The differences in resistance moment between the different effective widths are larger for the box-sections than for the T-sections, which outlines that the effective width has a higher influence on the box-sections than on the T-sections, as concluded from the reference tests (section 3.3.5).
The initial resistance moments at time step $t = 0$ of cross-sections with 100% CLT width were verified by estimations for the resistance moments based on the calculation method of rigidly bonded components. As a comparative calculation, CSTFire was used to calculate the resistance moment of cross-section A with an effective width of 100% CLT width. The results between the model and CSTFire show very good agreement. The resistance moments of the single glulam rib and CLT plate of cross-sections A outline the improvement in bending resistance of the composite cross-section. The thermo-mechanical model gives a very good approximation of the resistance moment in fire. The final resistance moments show good agreement with the experimental resistance moments at failure time. This confirms that the test specimens of the fire resistance tests were close to structural failure.

4.6 Mechanical simulations (3D)

4.6.1 Objectives

Mechanical simulations were performed using 3D FE models for validation of the mechanical properties of the FE model. The FE models were created as a flexible-in-shear multi-layered

model resulting in a non-uniform strain distribution along the CLT width. The numerical results of the four tested cross-section types (Figure 3.1) are presented and compared with the experimental results of the ultimate-load tests under normal temperature, the reference tests. Finally, the effective width $b_{\mathrm{ef,sim}}$ is obtained from the simulation.
Further validation of the FE model was conducted by Brogli (2019) against experimental results of cross-laminated timber rib panels reported by VTT Expert Services LTD (2017).

4.6.2 Model

Modelling framework

The Python programming language (Python Software Foundation 2015) was used to generate the Python script of the mechanical model based on geometry, CLT layup, material properties, and mechanical load. Abaqus Unified FEA software suite for finite element analysis (Dassault Systemes 2013) generated the FE model (*.cae* file) using the Abaqus' Python scripting interface and conducted the simulation. After the analysis was completed, the created output database containing the results (*.odb* file) was analysed using the Abaqus' Python scripting interface. A text file was created containing the relevant model information and the requested results.

Finite element models

The cross-section of a T-section or box-section was sketched and extruded to one deformable part. As in the reference tests, the model represented a one-rib system of 0.933 m width and 5.20 m length (Figure 3.2). A geometric symmetry simplification was considered in the form of a vertical symmetry plane in the middle of the cross-section in longitudinal direction and a vertical symmetry plane at midspan (Figure 4.22a). The support was defined as roller support with a distance from the end of 0.1 m. The generated part was partitioned into flange and rib. The flange was partitioned into three layers, the material orientations of which were defined by local coordinate systems. Materials were modelled as linear-elastic orthotropic using the material properties of section 4.2.4 for the nine engineering constants. The materials were assigned to the layers of the flange as cross-laminated timber and the rib as glued-laminated timber. The contact interactions between flange and rib, and the three layers were considered as rigid. A gravity load could be included depending on the gravitational acceleration taken as 9806.65 mm/s^2. As in the reference tests, the mechanical load was applied uniformly at the position of the cylinder along the flange width over a depths of 200 mm. The meshing size was set as 20 mm. In the generated mesh, the stress/displacement element type C3D8I was used, an 8-node linear brick element for incompatible modes, which showed a comparably stable behaviour but a lower computation time compared to the 20-node quadratic brick element with reduced integration C3D20R. Element size and element type had been optimized in a sensitivity analysis (Hodel 2021).
The blocking ends at the supports (see Figure 3.5) were neglected in the FE model. A comparison between the model with and without blocking ends at the supports was performed and concluded that the influence of the blockings on the deflection, thus the stiffness of the system, and

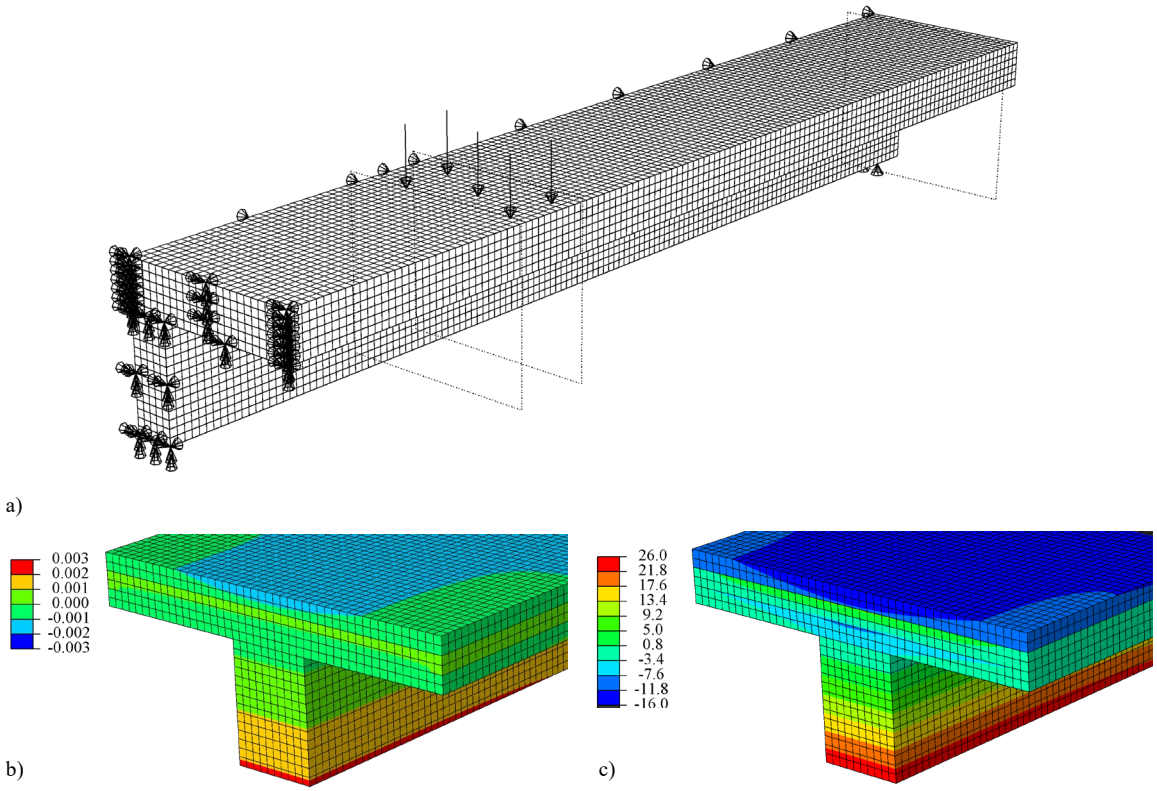

Figure 4.22. Mechanical simulations (3D) - Numerical results mirrored by the vertical symmetry plane (b) and c)): a) 3D FE model; b) Longitudinal strains at midspan, in [-]; c) Longitudinal stresses at midspan, in [N/mm^2].

the maximum stress value was negligible (Brogli 2019; Lamberti 2019). The influence of the blockings was limited to local effects at the support.

Procedure

The FE model was generated for each test specimen of the reference tests (A1-A3, B1-B3, C1-C3, and D1-D3) based on the specified dimensions, density, and the determined local modulus of elasticity as modulus of elasticity in x-direction of the single components (CLT plates and glulam ribs) taken from Table 3.1. The maximum load per cylinder of the reference tests was applied as listed in Table 3.2. First, the gravity load was activated in the FE model and stresses in longitudinal direction of the FE model were requested from the created output database. Secondly, the gravity load was deactivated and deflections of the FE model were requested in the post-processing.

4.6.3 Results

Deflection

The deflection at midspan was located at the bottom edge in the middle of the cross-section of the FE model. Figure 4.23a presents per test specimen the numerical deflection in comparison to the experimental deflection taken from section 3.3.3 (Table 3.2). The results show perfect correlation.

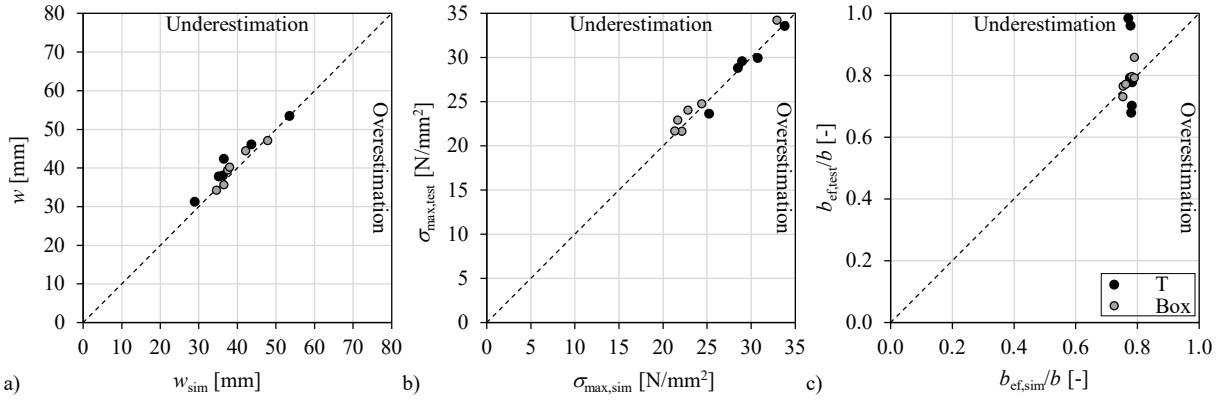

Figure 4.23. Mechanical simulations (3D) - Experimental results in relation to the numerical results of the test specimens: a) Deflections at midspan; b) Maximum stresses at the bottom edge; c) Ratio of effective width to CLT width.

Maximum bending stresses

The maximum stress at midspan was located at the bottom edge in the middle of the cross-section of the FE model (Figure 4.22c). Figure 4.23b presents per test specimen the numerical maximum stress in comparison to the experimental maximum stress taken from section 3.3.3. The results show perfect correlation.

Effective width

The flexible-in-shear multi-layered model led to non-uniform strain distributions along the CLT width (Figure 4.22b). The numerical effective width $b_{\mathrm{ef,sim}}$ was determined according to Formula 4.7. The longitudinal bending stresses of the longitudinal CLT layers of the FE model were summed up as total force of the CLT plate $F_{\mathrm{x,tot}}$; i.e. the sum of half of the CLT plate was doubled (Figure 4.22c). The longitudinal bending stresses were taken along the CLT width, and along the thickness of the longitudinal CLT layers at 5 mm intervals. Furthermore, the trapezoidal force at rib centre $F_{\mathrm{x,max}}$ was calculated from the maximum longitudinal bending distribution of the longitudinal CLT layers at the rib centre. The numerical effective width $b_{\mathrm{ef,sim}}$ was determined as a fraction of the total force of the CLT plate $F_{\mathrm{x,tot}}$ and the trapezoidal force $F_{\mathrm{x,max}}$. Figure 4.23c presents per test specimen the numerical effective width $b_{\mathrm{ef,sim}}$ in comparison to the experimental effective width $b_{\mathrm{ef,test}}$ taken from section 3.3.3 (Table 3.2). Both the numerical and experimental effective width result in a mean value of 78% of the CLT width. While the numerical results give a constant value (SD = 0.01 m, CoV = 2%), the experimental results show larger deviation (SD = 0.07 m, CoV = 9%).

4.6.4 Discussion

Nine engineering constants are necessary for the definition of the orthotropic material model: three moduli of elasticity E, three shear moduli G, and three Poisson's ratios v. The material properties were implemented for CLT plates in accordance with the consolidated draft of Euro-

code 5 for the informal enquiry (prEN 1995-1-1) and for glulam ribs according to EN 14080. Replacing the modulus of elasticity in x-direction by the determined local modulus of elasticity of the single components (CLT plates and glulam ribs), deflections and maximum stresses show perfect correlation. The agreement between the mean values of the numerical and experimental effective widths confirms the approach for determining the numerical effective width $b_{\mathrm{ef,sim}}$. The constant numerical effective width illustrates that the effective width depends mainly on geometric parameters as the ratio of clear rib distance to span $b_{\mathrm{f,i}}/l$, here $b_{\mathrm{f,i}}/l = 0.14$. The larger deviation of the experimental effective widths $b_{\mathrm{ef,test}}$ shows the higher probability of inaccuracy of the experimental investigation.

4.6.5 Conclusions

Mechanical simulations were performed using 3D FE models as a flexible-in-shear multi-layered model. The nine engineering constants of the orthotropic material model were implemented for CLT plates in accordance with the consolidated draft of Eurocode 5 for the informal enquiry (prEN 1995-1-1) and for glulam ribs according to EN 14080, as defined in section 4.2.4. The FE model was validated against the experimental results of the reference tests. The numerical effective widths $b_{\mathrm{ef,sim}}$ were determined from the non-uniform strain distribution within the CLT width, as defined in section 4.2.5. In agreement with the experimental results, the determination of the numerical effective width $b_{\mathrm{ef,sim}}$ results in 78% of the CLT width for the given system.

4.7 Thermal simulations (3D)

4.7.1 Objectives

Heat transfer analyses using 3D FE models were performed as a basis for the uncoupled thermo-mechanical simulations (3D) of section 4.8 and the parametric study of section 4.9. This chapter presents and verifies the model. First, a 2D heat transfer model in Abaqus is compared with the 2D heat transfer model in SAFIR® (section 4.3). Then, the comparison between the 2D and 3D heat transfer models in Abaqus is made. The comparisons are based on the numerical results of cross-section A, the initially unprotected T-section (Figure 3.1).

4.7.2 Model

Modelling framework

The Python programming language (Python Software Foundation 2015) was used to generate the Python script of the heat transfer model based on geometry, CLT layup, thermal properties, and thermal interactions. Abaqus Unified FEA software suite for finite element analysis (Dassault Systemes 2013) generated the FE model (*.cae* file) using the Abaqus' Python scripting interface and conducted the simulation. The simulation stopped when a maximum defined time was reached. After the analysis was completed, the created output database containing the results (*.odb* file) was analysed using the Abaqus' Python scripting interface. A text file was created

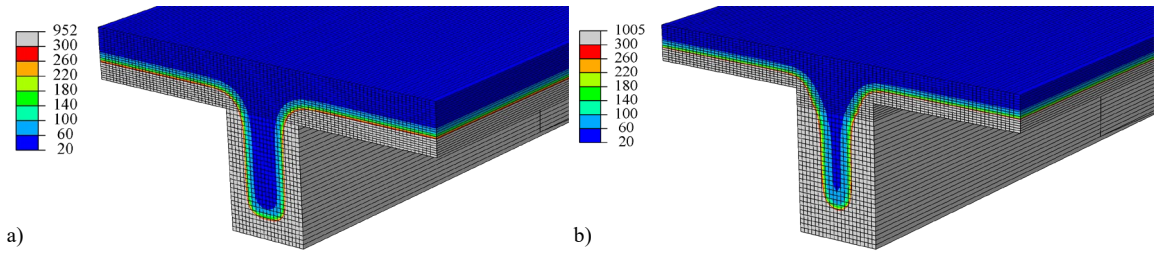

Figure 4.24. Thermal simulations (3D) - Numerical temperatures of cross-section A at midspan mirrored by the vertical symmetry plane, in [°C]: a) Fall-off time of first layer; b) Simulation time of 90 min (test termination).

containing the relevant model information and the requested temperatures at specified locations and time steps.

Finite element models

The FE model was created following the FE model presented in the mechanical simulations (Figure 4.22a). The cross-section of a T-section was sketched and extruded to one deformable part, modelling a one-rib system. A geometric symmetry simplification was considered in the form of a vertical symmetry plane in the middle of the cross-section in longitudinal direction and a vertical symmetry plane at midspan. The support was defined as roller support with a distance from the end of 0.05 m. The generated part was partitioned into flange and rib. The flange was partitioned into three layers, the material orientations of which were defined by local coordinate systems. Materials were modelled based on their temperature-dependent thermal properties. The materials were assigned to the layers of the flange as cross-laminated timber and the rib as glued-laminated timber. Since no heat transfer in longitudinal direction was considered, the end surfaces at the support were defined as adiabatic. The symmetry planes and the vertical end of the CLT plate at field centre were also defined as adiabatic surfaces. Convective and radiative thermal interactions were defined for the rest of the outer timber surfaces. The top edge was exposed to a constant temperature of 20°C. The thermal interactions of the surfaces at the bottom edges followed a previously defined amplitude of the standard time-temperature curve starting from a predefined temperature field of 20°C. An element size of 10x10 mm^2 was chosen for the cross-section. The element size was halved in height in the layers of the flange; i.e. 10x5 mm^2. The element size in longitudinal direction corresponded to the length of the FE model based on the omitted heat transfer in longitudinal direction. The heat transfer element type DC3D8 was used, an 8-node linear brick element, which showed a comparably stable behaviour but a lower computation time compared to the 20-node quadratic brick element DC3D20. Element size and element type had been optimized in a sensitivity analysis as a result of the thermal analyses of this section and of the thermo-mechanical analyses of section 4.8 (Hodel 2021). The interval between the time steps was kept at 5 seconds.

Procedure

During post-processing, fall-offs of charred CLT layers $t_{300°C,sim}$ were defined as time steps of the thermal simulations when the average temperature between the CLT layers along a path

at midspan exceeded 300°C. The number of the path intervals discretised the path into 5-25 mm long sections depending on the ratio between CLT width to rib width. In a further simulation step, the FE model without the fallen-off layer was generated by Abaqus (*.cae* file) based on the new set of temperature-dependent thermal properties after fall-off for wood according to Table 4.4. The simulation was continued from the fall-off time by re-defining the amplitude and starting from a predefined temperature field imported from the *.odb* file of the previous simulation (tolerance of the interpolation: 10 mm). For each new FE model and its simulation, *.odb* files were created by Abaqus. At the end, the numerical results were sequenced together (Figure 4.24).

4.7.3 Results

In a first step, a 2D heat transfer model was generated in Abaqus, by not extruding the part in length and defining the thermal boundary conditions as interactions at the outer timber borders. An element size of 4x4 mm^2 was chosen for the cross-section for comparison with SAFIR®. Figure 4.25 compares numerical temperatures of cross-section A obtained from SAFIR® with the ones obtained from Abaqus. Figure 4.25a presents the temperatures over time between the first and the second CLT layers. Figure 4.25b presents the temperatures along the rib width at half height of the rib at 90 min, which represents the time of test termination of the fire resistance test (see Table 3.6). The results were taken from the first thermal models, thus were not sequenced together with the results of the second thermal models after the fall-off of the first CLT layer. The thermal simulations of SAFIR® were conducted based on a user defined wood material (User) and on the predefined material by SAFIR® (WoodEC5). The differences between User and WoodEC5 are negligible. The average temperature of 300°C is reached between the CLT layers at 60.5 min in Abaqus und at 62.0 min in SAFIR®. Temperatures along the rib width show at 90 min a discrepancy in average of 6°C. The highest discrepancy is shown at a depth of 60 mm of 30°C.
In a next step, the 3D heat transfer model of cross-section A was generated in Abaqus. Figure 4.26 compares the temperatures over time between the first and the second CLT layers between the 2D and the 3D FE model in Abaqus. The results from the first thermal models were sequenced together with the results of the second thermal models after the fall-off of the first CLT layer. The fall-off of the charred CLT layer $t_{300°C,sim}$ was defined as time step when the average temperature between the CLT layers exceeded 300°C. The fall-off occurred at 62.4 min in the 2D FE model and at 63 min in the 3D FE model.

4.7.4 Discussion

The verification was performed for the 2D model in Abaqus by comparing it to the 2D model in SAFIR®. The error for the average temperature of 300°C between the CLT layers is 1.5 min. The highest discrepancy of temperatures along the rib width is 30°C. The error for the fall-off time and the discrepancy along the rib width are within a reasonable range. The 3D heat transfer model in Abaqus provided results of very good agreement with the results obtained from the 2D model in Abaqus. The error for the fall-off time of the first CLT layer is 0.6 min.

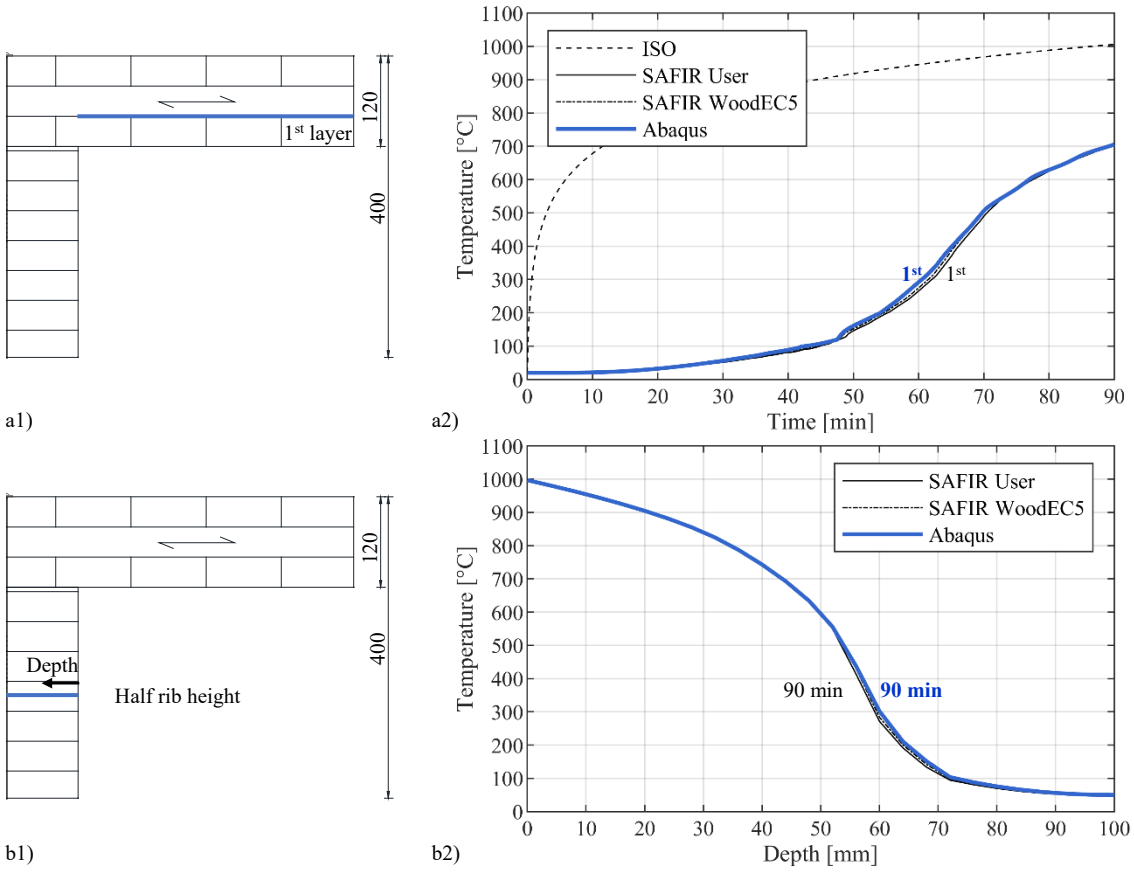

Figure 4.25. Numerical temperatures of cross-section A obtained from SAFIR® and from Abaqus (until test termination): a) Temperatures over time between first and second cross-laminated timber layers; b) Temperatures at 90 min along the rib width at half rib height.

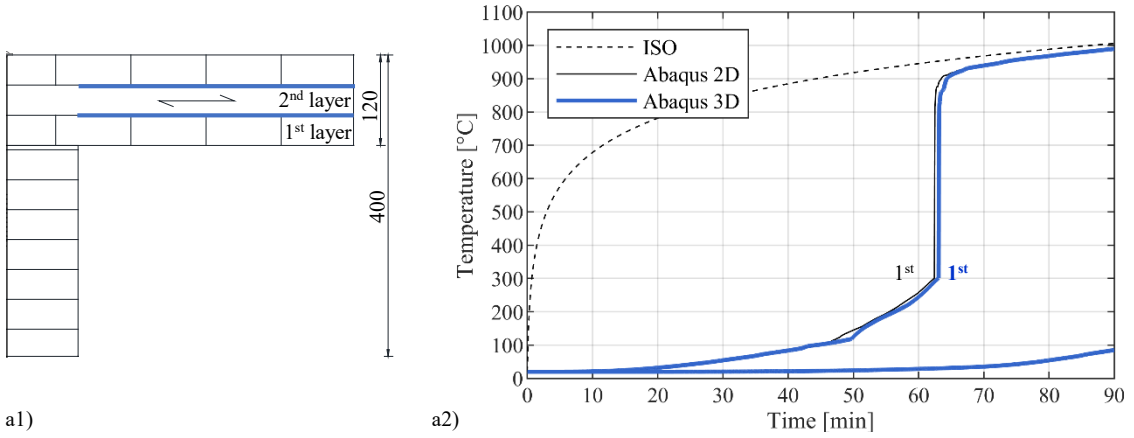

Figure 4.26. Numerical temperatures of cross-section A obtained from Abaqus 2D and 3D FE model (until test termination)

4.7.5 Conclusions

The 3D heat transfer FE models were the basis for the uncoupled thermo-mechanical simulations (3D) of section 4.8 and the parametric study of section 4.9. The verification was achieved by comparing a 2D version of the FE model in Abaqus with the 2D model in SAFIR® and then comparing the 2D version in Abaqus with the 3D FE model in Abaqus. The results are in good agreement and confirm the reliability of the model.

4.8 Thermo-mechanical simulations (3D)

4.8.1 Objectives

Uncoupled thermo-mechanical simulations using a 3D FE model were performed as a basis for the parametric study of section 4.9. The FE model was created as a flexible-in-shear multi-layered model resulting in a non-uniform, temperature-dependent strain distribution along the CLT width. In this section, the numerical results of the initially unprotected T-section (cross-section A in Figure 3.1), are presented and compared with the experimental results of the fire resistance test, and the numerical results of the 2D FE beam model presented in section 4.4. The influence of the temperature-dependent reduction factors for the nine engineering constants of the orthotropic material model is investigated. Finally, the effective width in fire $b_{\mathrm{ef,fi,sim}}$ is obtained from the simulation.

4.8.2 Model

Modelling framework

The Python programming language (Python Software Foundation 2015) was used to generate the Python script of the thermo-mechanical model based on geometry, CLT layup, material properties, and mechanical load. Abaqus Unified FEA software suite for finite element analysis (Dassault Systemes 2013) generated the FE model (*.cae* file) using the Abaqus' Python scripting interface and conducted the simulation. The simulation depended on the temperature history from the thermal simulations of section 4.7. After the analysis was completed, the created output database containing the results (*.odb* file) was analysed using the Abaqus' Python scripting interface. A text file was created containing the relevant model information and the requested results.

Finite element models

The FE model was created based on the 3D FE model of the mechanical simulation following the geometry of the 3D FE heat transfer model (section 4.7). In comparison, the mechanical load was applied uniformly over the surface. For cross-section A, the uniformly distributed load was taken from the fire resistance test (Table 3.6). The gravity load was activated depending on the gravitational acceleration taken as 9806.65 mm/s^2. Mass-loss of the cross-section due to pyrolysis was taken into account by defining the density of the materials as temperature-dependent.

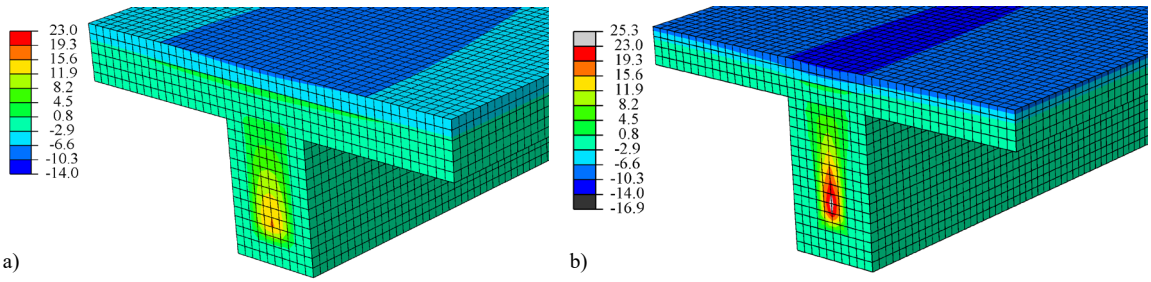

Figure 4.27. Thermo-mechanical simulations (3D) - Numerical stresses of cross-section A at midspan mirrored by the vertical symmetry plane, in [N/mm^2]: a) Before the fall-off at 63 min; b) Simulation time of 90 min (test termination).

The predefined temperature field of a specified time step was imported from the *.odb* file of the corresponding thermal simulation (tolerance of the interpolation: 10 mm). The materials were modelled as linear-elastic orthotropic and as temperature-dependent through temperature-dependent reduced mechanical properties, as defined in section 4.2.4. Temperature-independent materials were assigned to a partitioned part of the model between the end and the support. The 20-node quadratic brick element with reduced integration C3D20R was used for the layers of the flange defined as longitudinal CLT layers.

Procedure

The uncoupled thermo-mechanical analysis was chosen. The thermal simulation was performed with a specific interval between the time steps until a maximum defined time was reached, as described in section 4.7. The thermo-mechanical simulation was performed as a temperature-dependent function by importing predefined temperature fields of the corresponding thermal simulation for certain increments of specified time steps. Sensitivity analyses for the discussion of the mesh, element type or the temperature-dependent reduction factors were carried out with an acceptable computing time, since the thermal simulation had only to be calculated once (Hodel 2021). Furthermore, different element sizes could be used for the thermal and the thermo-mechanical simulations. In a coupled analysis, a fixed mesh must be selected, since only one model is used for the coupled calculation over a defined simulation time (Shi et al. 2022). In a uncoupled analysis, however, the calculations of individual time steps needed to be compiled. Geometry and CLT layup needed to be identical of the 3D FE models for thermal and thermo-mechanical simulation. Therefore, a corresponding thermo-mechanical FE model was generated for each new FE heat transfer model after fall-off of charred CLT layers. For each new FE model and its simulation, *.odb* files were created by Abaqus. At the end, the numerical results were sequenced together (Figure 4.27).

4.8.3 Results

Temperature-dependent residual stiffness

The temperature dependence of the materials was modelled based on the bi-linear behaviour according to EN 1995-1-2 (section 4.3). There, temperature-dependent reduction factors at

Table 4.8. Thermo-mechanical simulations (3D) - Temperature-dependent reduction factors for the engineering constants according to Chen et al. (2020) based on EN 1995-1-2.

Temperature	$k_{\theta,\mathrm{E,i}}$, $k_{\theta,\mathrm{G,ij}}$	$k_{\theta,\mathrm{v,ij}}$
[°C]	[-]	[-]
20	1.00	1.00
100	0.425	1.00
300	0.01	1.00

100°C for stiffness are defined only for the modulus of elasticity parallel to the grain (in x-direction), but the distinction is made between compression ($k_{100°\mathrm{C,E,c}} = 0.35$) and tension ($k_{100°\mathrm{C,E,t}} = 0.50$). By default, Abaqus does not reduce the mechanical property of an element based on the tensile or compressive stress of the element. The reduction is defined regardless of the type of load. Nine engineering constants are necessary for the definition of the orthotropic material model: modulus of elasticity in x-direction E_x, in y-direction E_y, and in z-direction E_z, shear modulus loaded in-plane in y-direction G_xy, out-of-plane in z-direction G_xz, and out-of-plane in z-direction G_yz (= rolling shear modulus of cross-laminated timber G_r), and the three Poisson's ratios v_ij between passive deformation ϵ_j and active deformation ϵ_i. In this thesis, the temperature-dependent reduction factors at 100°C for the engineering constants $k_{100°\mathrm{C,E,i}}$, $k_{100°\mathrm{C,G,ij}}$, and $k_{100°\mathrm{C,v,ij}}$ were defined according to Formulae 4.20-4.22

$$k_{100°\mathrm{C,E,i}} = \frac{E_{\mathrm{i},100°\mathrm{C}}}{E_\mathrm{i}} \tag{4.20}$$

$$k_{100°\mathrm{C,G,ij}} = \frac{G_{\mathrm{ij},100°\mathrm{C}}}{G_\mathrm{ij}} \tag{4.21}$$

$$k_{100°\mathrm{C,v,ij}} = \frac{v_{\mathrm{ij},100°\mathrm{C}}}{v_\mathrm{ij}} \tag{4.22}$$

where $E_{\mathrm{i},100°\mathrm{C}}$, $G_{\mathrm{ij},100°\mathrm{C}}$, and $v_{\mathrm{ij},100°\mathrm{C}}$ are the temperature-related reduced engineering constants at 100°C, and E_i, G_ij, and v_ij are the engineering constants at normal temperature. Following the approach by Chen et al. (2020), the temperature-dependent reduction factors for the engineering constants were implemented as summarized in Table 4.8. At 100°C, the moduli of elasticity and the shear moduli were multiplied by the mean value of the reduction factors for the modulus of elasticity parallel to the grain in compression and in tension ($k_{100°\mathrm{C,E,x}} = 0.425$) according to EN 1995-1-2. The Poisson's ratios were kept unchanged.

In literature, different reduction factor were found for the modulus of elasticity parallel to the grain (in x-direction) (Gerhards 1982; Glos and Henrici 1990; Thomas 1997; Young and Clancy 2001). A sensitivity analysis of the temperature-dependent reduction factors at 100°C for the engineering constants was performed based on Table 4.8 (Hodel 2021). No distinction was made between reduction factors for the engineering constants of cross-laminated timber or glulam. Figure 4.28 presents the temperature-related reduction of the deflection at midspan after standard fire of 60 min depending on the variation of the temperature-dependent reduction factor at 100°C for an engineering constant. The reduction is related to the maximum deflection

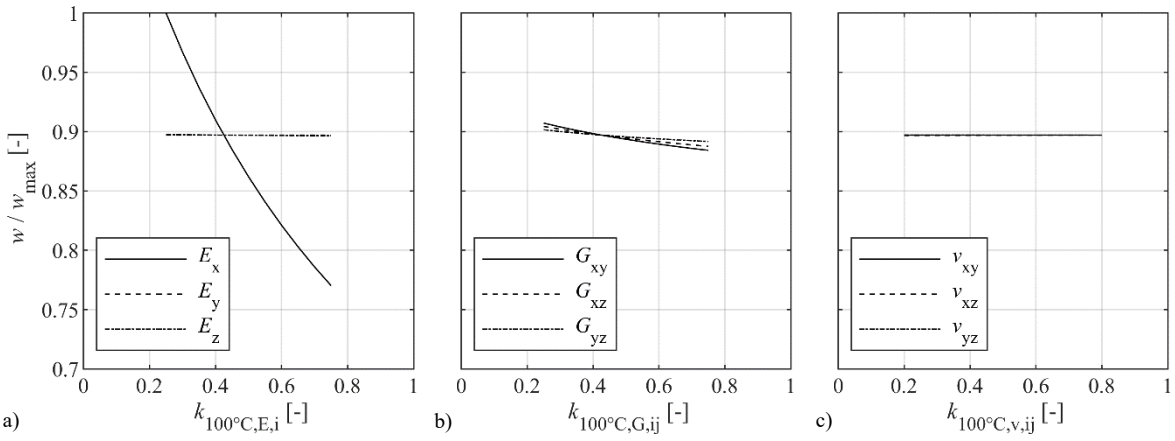

Figure 4.28. Thermo-mechanical simulations (3D) - Relative deflection at midspan after standard fire of 60 min depending on the temperature-dependent reduction factor at 100°C for each engineering constant (Hodel 2021): a) Modulus of elasticity E_{i}; b) Shear modulus G_{ij}; c) Poisson ratio v_{ij}

that occurs for a temperature-dependent reduction factor at 100°C for the modulus of elasticity in x-direction, $k_{100°\mathrm{C,E,x}} = 0.25$. A variation of the reduction factors at 100°C for the moduli of elasticity in y-direction $k_{100°\mathrm{C,E,y}}$ and z-direction $k_{100°\mathrm{C,E,z}}$, and for the Poisson's ratios $k_{100°\mathrm{C,v,ij}}$ results in no change (CoV = 0%). A variation of the reduction factors at 100°C for the shear moduli $k_{100°\mathrm{C,G,ij}}$ results in a minor deviation (CoV = 0.3-0.8%). A variation of the reduction factor at 100°C for the modulus of elasticity in x-direction $k_{100°\mathrm{C,E,x}}$ results in the highest deviation (CoV = 8%).

Temperature-dependent deflections

The deflection at midspan was taken at the bottom edge in the middle of the cross-section of the FE model. Figure 4.29 presents for cross-section A the numerical deflections obtained from the 3D FE model in Abaqus. The experimental deflections are shown as single values (grey colour) and mean value (black colour), taken from section 3.6.2 (Figure 3.20). Numerical and experimental deflections are shown until test termination. The instantaneous deflections due to self-weight were removed. Figure 4.29a shows the numerical results based on different temperature-dependent reduction factors at 100°C for the modulus of elasticity in x-direction:

1. As mean value of the reduction factors at 100°C for the modulus of elasticity in compression and in tension according to EN 1995-1-2: $k_{100°\mathrm{C,E,x}} = 0.425$

2. As reduction factor at 100°C for the modulus of elasticity in tension according to EN 1995-1-2: $k_{100°\mathrm{C,E,x}} = 0.50$.

3. As reduction factor at 100°C for the modulus of elasticity in tension according to EN 1995-1-2 for glued-laminated timber ($k_{100°\mathrm{C,E,x}} = 0.50$), and the reduction factor at 100°C for the modulus of elasticity in compression according to EN 1995-1-2 for cross-laminated timber ($k_{100°\mathrm{C,E,x}} = 0.35$).

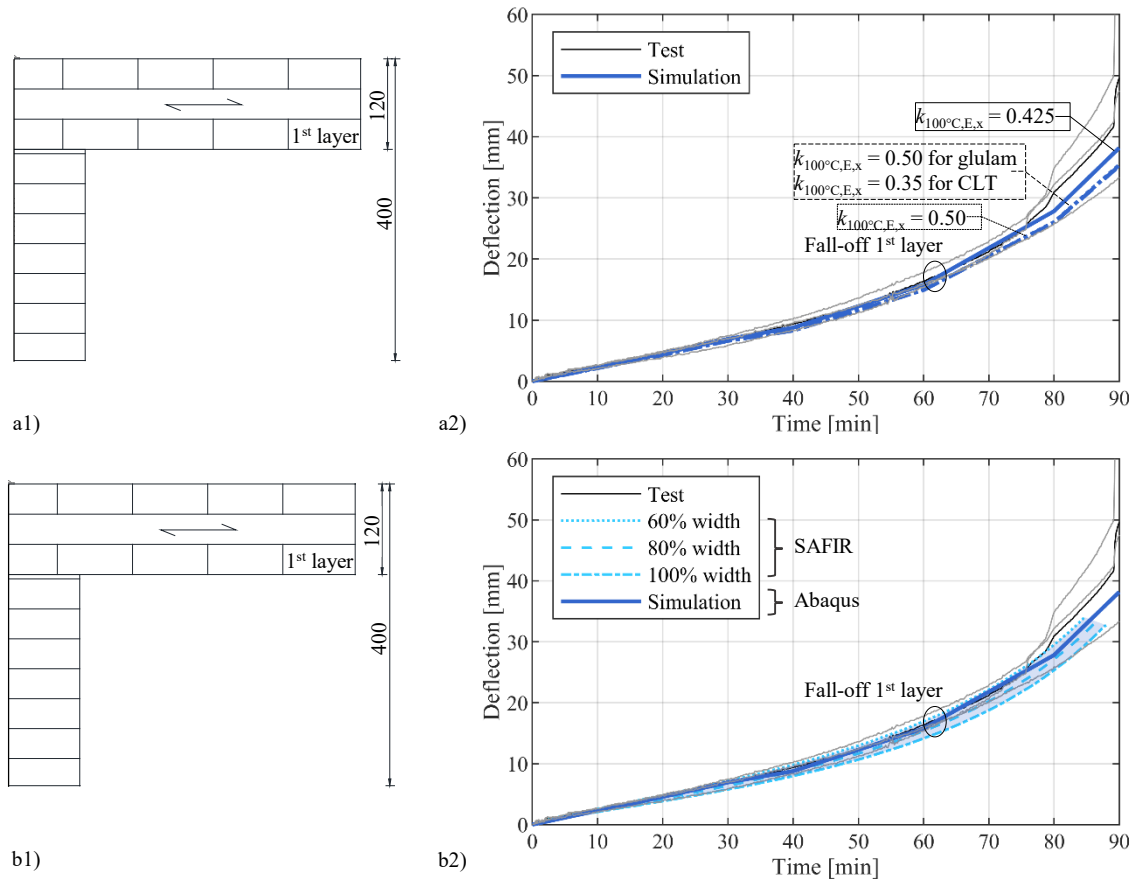

Figure 4.29. Thermo-mechanical simulations (3D) - Numerical deflections of cross-section A in comparison to the experimental results (until test termination): a) Comparison of reduction factors at 100°C for the modulus of elasticity in x-direction; b) Inclusion of the results obtained by SAFIR for the three cases of the effective width (until simulation stop).

The results are identical for the approaches 2) and 3). Increasing the reduction factor leads to a smaller reduction of the modulus of elasticity in x-direction. Thus, the numerical deflections decrease for the approaches 2) and 3) by 8% in comparison to approach 1).
Figure 4.29b presents the numerical deflections obtained from the 3D FE model in Abaqus based on $k_{100°C,E,x} = 0.425$. Furthermore, the numerical deflections obtained from the 2D FE beam model in SAFIR® are shown for the three cases of the effective width (60%, 80%, and 100% of the CLT width), taken from Figure 4.15. The numerical deflections obtained from Abaqus lay in between the extreme cases of 60% and 100% obtained from SAFIR®. The numerical deflections obtained from Abaqus show good agreement with the mean value of the experimental deflections until an exposure time of 76 min. Then, the experimental deflections show a higher increase in the rate of change.

Temperature-dependent stresses

Figure 4.30 presents the numerical stress distributions over the height at the rib centre of cross-section A. The results are shown at specific time steps. The transversal CLT layers do not contribute to the determination of the effective width. The initial state at time step $t = 0$

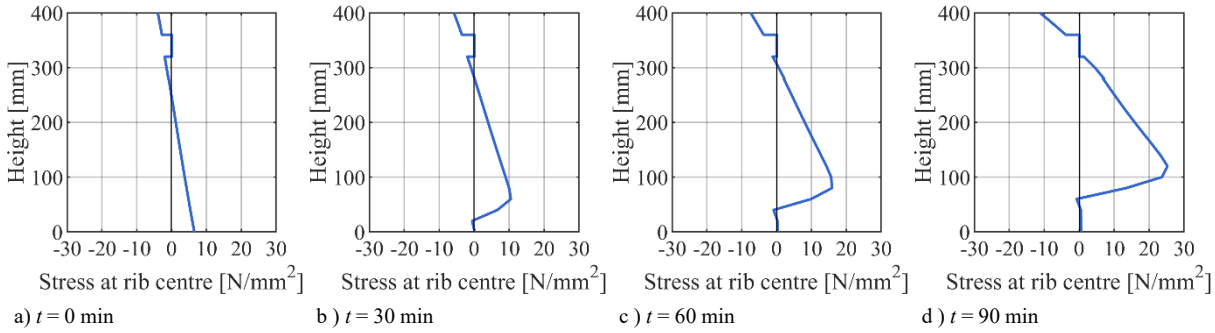

Figure 4.30. Numerical stress distributions at the rib centre over the height of cross-section A at specific time steps.

represents the stress distribution at normal temperature. The stress distribution is uniform over the height. Once the rib is exposed to fire, elements exhibit elevated temperatures and the strains and thus stresses are reduced. Elements exhibiting temperatures above 300°C do not take any strains. The stress distributions show how the neutral axis in fire moves upwards with an increased exposure time. The maximum tensile stress in the rib increases from 6.5 N/mm^2 up to 25.3 N/mm^2. The maximum compressive stress at the top edge of the CLT plate increases from 4.0 N/mm^2 up to 11.2 N/mm^2.

Effective width in fire

The flexible-in-shear multi-layered model led to non-uniform, temperature-dependent strain and stress distributions along the CLT width (Figure 4.27). The numerical effective width in fire $b_{\mathrm{ef,fi,sim}}$ was determined according to Formula 4.8 and following the approach at normal temperature in section 4.6.3. The temperature-dependent longitudinal bending stresses of the longitudinal CLT layers of the FE model were summed up as total force of the CLT plate in fire $F_{\mathrm{x,tot,fi}}$; i.e. the sum of half of the CLT plate was doubled. The temperature-dependent longitudinal bending stresses were taken along the CLT width at 5-20 mm intervals depending on the CLT width, and along the thickness of the longitudinal CLT layers at 5 mm intervals. Furthermore, the trapezoidal force at rib centre in fire $F_{\mathrm{x,max,fi}}$ was calculated from the maximum temperature-dependent longitudinal bending distribution of the longitudinal CLT layers at the rib centre. Since the neutral axis in fire is moving upwards, stresses in the flange could change from compressive to tensile stresses (see Figure 4.30). The total force of the CLT plate in fire $F_{\mathrm{x,tot,fi}}$ was taken as sum of compressive and tensile stresses. The distribution of stresses of the trapezoidal force at rib centre in fire $F_{\mathrm{x,max,fi}}$ took the possibility of tensile stresses into account. The temperature-related reduction of the stiffness of the elements based on Table 4.8 led to a reduction close to zero for temperatures above 300°C. Elements in the layers of the flange did not contribute to the longitudinal bending stresses as soon as their mean temperature reached 300°C. As outlined in the state of the art section (Figure 2.7), elements in the transition zone above the rib would still contribute to the longitudinal bending stresses in the flange, even though elements next to them in the CLT plate exhibited stresses close to zero or were even deleted after the fall-off of a CLT layer. Longitudinal bending stresses in the transition zone

distorted especially the trapezoidal force at rib centre in fire $F_{\mathrm{x,max,fi}}$. The approach was taken to consider only elements above the CLT plate's 300°C isotherm. As a simplified approach, the position of the 300°C isotherm in the CLT plate, thus the charred depth in CLT layer i on the fire-exposed side $d_{\mathrm{char,layer,i,sim}}$ was estimated according to Formula 4.23

$$d_{\mathrm{char,layer,i,sim}} = \beta_{\mathrm{layer,i,sim}} \cdot (t - t_{300°\mathrm{C,layer,i\text{-}1,sim}}) \tag{4.23}$$

with

$$\beta_{\mathrm{layer,i,sim}} = \frac{d_{\mathrm{layer,i,sim}}}{(t_{300°\mathrm{C,layer,i,sim}} - t_{300°\mathrm{C,layer,i\text{-}1,sim}})} \tag{4.24}$$

where $\beta_{\mathrm{layer,i,sim}}$ is the charring rate of CLT layer i in mm/min, t is the specified time step for the import of the temperature field from the thermal simulation, $d_{\mathrm{layer,i,sim}}$ is the thickness of CLT layer i of the FE model, $t_{300°\mathrm{C,layer,i,sim}}$ is the fall-off time of CLT layer i, and $t_{300°\mathrm{C,layer,i\text{-}1,sim}}$ is the fall-off time of the previous CLT layer.
Figure 4.31 presents the numerical results of the thermo-mechanical simulation of cross-section A. The experimental results are included for the charred depth in the CLT layers, the deflection taken from Figure 4.29b, and the deflection rate. The performance criteria for failure of the loadbearing capacity as limit values for the amount of the deflection and the deflection rate according to prEN 1363-1 were not reached. Figure 4.31c1 presents the total force of the CLT plate in fire $F_{\mathrm{x,tot,fi}}$ and the trapezoidal force at rib centre in fire $F_{\mathrm{x,max,fi}}$, based on the simplified approach and based on a precise approach (determination of the 300°C isotherm obtained from the thermal simulations). For the simplified approach, the specific times steps were defined as 0 min, 30 min, $t_{300°\mathrm{C,layer,i,sim}}$, and 90 min. For the precise approach, an interval of 15 min was chosen. The two approaches differ only marginally. The curves show a temperature-dependent increase with an increased exposure time. After the fall-off of the charred CLT layer, the trapezoidal force in fire $F_{\mathrm{x,max,fi}}$ shows a 4-fold higher increase in the rate of change than the total force of the CLT plate in fire $F_{\mathrm{x,tot,fi}}$. The numerical effective width in fire $b_{\mathrm{ef,fi,sim}}$ was determined as a fraction of the total force of the CLT plate in fire $F_{\mathrm{x,tot,fi}}$ and the trapezoidal force in fire $F_{\mathrm{x,max,fi}}$. Figure 4.31c2 shows the ratios of effective width in fire to CLT width $b_{\mathrm{ef,fi,sim}}/b$. Differences between simplified and precise approach are maximum 4% in absolute terms. The ratio of effective width in fire to CLT width $b_{\mathrm{ef,fi,sim}}/b$ at time step $t = 0$ min is 84%. First, the effective width in fire $b_{\mathrm{ef,fi,sim}}$ remains unchanged. After the fall-off of the charred CLT layer, the ratio of effective width in fire to CLT width $b_{\mathrm{ef,fi,sim}}/b$ decreases to 69%.

4.8.4 Discussion

Temperature-dependent residual stiffness

The deflection is independent of the temperature-dependent reduction factors at 100°C for the Poisson's ratios $k_{100°\mathrm{C,v,ij}}$ and the moduli of elasticity in y-direction $k_{100°\mathrm{C,E,y}}$ and z-direction $k_{100°\mathrm{C,E,z}}$. The deflection changes minorly depending on the reduction factors at 100°C for the shear moduli $k_{100°\mathrm{C,G,ij}}$. The reduction factor at 100°C for the modulus of elasticity in x-direction $k_{100°\mathrm{C,E,x}}$ has the highest impact on the deflection. The sensitivity analysis confirms the approach

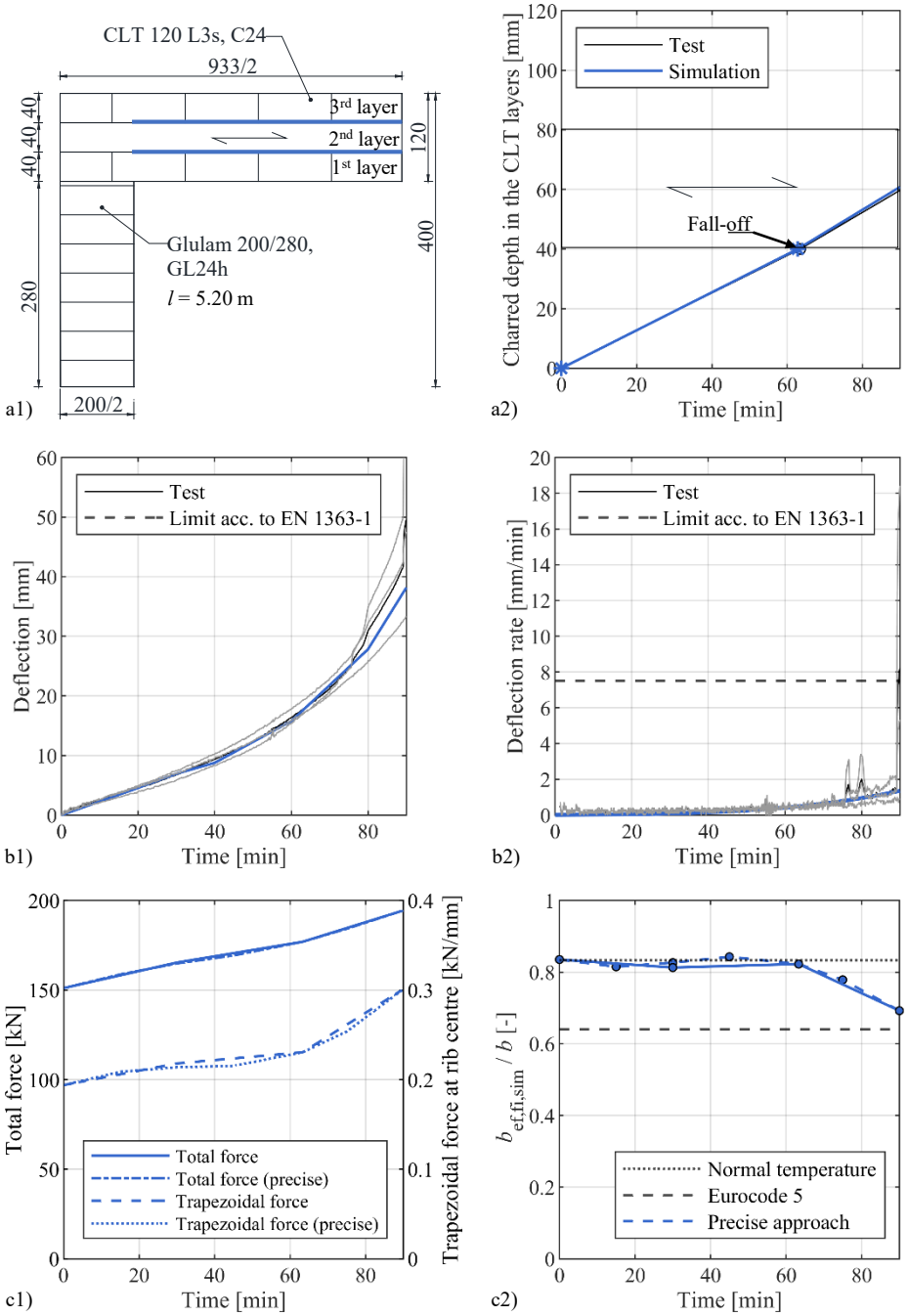

Figure 4.31. Thermo-mechanical simulations (3D) - Numerical results of cross-section A including the experimental results (until test termination): a1) Cross-section; a2) Charred depth in CLT layers; b1)+b2) Deflection and deflection rate compared to the performance criteria according to prEN 1363-1; c1) Total force and trapezoidal force at rib centre in fire; c2) Effective width in fire compared to the effective width at normal temperature according to prEN 1995-1-1 (Eurocode 5).

by Chen et al. (2020) in Table 4.8.

Temperature-dependent deflections

Since the glulam rib lays in the tensile zone and is exposed to fire from three sides, the reduction factor at 100°C for the modulus of elasticity in x-direction $k_{100°C,E,x}$ of the glulam rib governs the structural behaviour of the floor system. The numerical deflections show very good agreement with the mean value of the experimental deflections based on the mean value of the reduction factors at 100°C for the modulus of elasticity in compression and in tension $k_{100°C,E,x} = 0.425$ according to EN 1995-1-2. The results confirm the choice for the reduction factor at 100°C for the modulus of elasticity in x-direction $k_{100°C,E,x}$ of Chen et al. (2020). The deflections lay between the extreme cases of cross-sections with 60%, and 100% CLT widths of the numerical deflections obtained from the 2D FE beam model in SAFIR®. This confirms the approach for the 2D FE beam model and the inclusion of the proportion due to shear deflections based on the reference tests of section 4.4.

Temperature-dependent stresses

The stress distributions at the rib centre illustrate the implemented temperature-dependent reduction for stiffness. The capacity of the elements exhibiting elevated temperatures decrease while fibres exhibiting temperatures above 300°C do not contribute to the stress distribution. Thus, the neutral axis in fire moves upwards as observed in section 4.5.4 and the bending curvature is increased per time step. At $t = 90$ min, the maximum tensile stress in the rib confirms the maximum tensile stress obtained from the linear 2D FE beam model in section 4.4.3 (Figure 4.17a). However, the maximum compressive stress at the top edge of the CLT plate is double the size of the maximum compressive stress obtained from the linear 2D FE beam model. The latter is modelled as Bernoulli-type beam elements resulting in uniform stress distributions along the CLT width. In comparison, the flexible-in-shear multi-layered model results in a non-uniform strain distribution along the CLT width with a maximum stress value at the rib centre. Furthermore, the increase of outer fibre bending stresses due to shear deformations was not taken into account in the linear 2D FE beam model.

Effective width in fire

For the determination of the numerical effective width in fire $b_{ef,fi,sim}$, only elements were considered above the 300°C isotherm of the CLT plate. As a simplified approach, the charred depth in the CLT layer on the fire-exposed side $d_{char,layer,i,sim}$ was estimated based on the charring rate of each CLT layer $\beta_{layer,sim}$. This simplification led to minor errors for the determination of the total force of the CLT plate in fire $F_{x,tot,fi}$ and the trapezoidal force in fire $F_{x,max,fi}$. The effective width in fire $b_{ef,fi,sim}$ shows good estimates based on the simplified approach.
The ratio of effective width in fire to CLT width $b_{ef,fi,sim}/b$ at time step $t = 0$ min is 84%, which represents the ratio of effective width at normal temperature to CLT width $b_{ef,sim/b}$. The value is higher than the experimental result in section 4.6.3. The ratio of experimental effective width

to CLT width $b_{ef,test}/b$ results in 78%. The comparison shows the influence of the type of loading on the effective width and the small increase of the effective width with a uniformly distributed load instead of loading at two points.
The results show a temperature-dependent reduction of the numerical effective width in fire $b_{ef,fi,sim}$ after the fall-off of the charred CLT layer at 63 min. First, the effective width in fire $b_{ef,fi,sim}$ remains unchanged, since the total force of the CLT plate in fire $F_{x,tot,fi}$ and the trapezoidal force in fire $F_{x,max,fi}$ show comparable increase in the rate of change. After the fall-off, the trapezoidal force in fire $F_{x,max,fi}$ shows a 4-fold higher increase in the rate of change, which leads to a reduction of the effective width in fire $b_{ef,fi,sim}$. The stresses are accumulated in the part of the remaining CLT plate at the rib centre. Figure 4.27 shows the local increase of bending stresses at rib centre between the two time steps of 63 min (before the fall-off) and 90 min. The ratio of effective width at normal temperature to CLT width b_{ef}/b according to prEN 1995-1-1 results in 64%. The value is included in Figure 4.31c2 (Eurocode 5). The ratio of effective width in fire to CLT width $b_{ef,fi,sim}/b$ remains above this value. Until test termination, thus a fire resistance of 90 min, the effective width at normal temperature b_{ef} according to prEN 1995-1-1 gives an approximation of the effective width in fire $b_{ef,fi,sim}$ on the safe side.

4.8.5 Conclusions

Uncoupled thermo-mechanical simulations using a 3D FE model were performed as a basis for the parametric study of section 4.9. The FE model was created as a flexible-in-shear multi-layered model resulting in a non-uniform, temperature-dependent strain distribution along the CLT width. The sensitivity analysis for the discussion of the temperature-dependent reduction factors at 100°C for the engineering constants confirms the approach by Chen et al. (2020) (Table 4.8). The reduction factor at 100°C for the modulus of elasticity in x-direction $k_{100°C,E,x}$ has the highest impact on the deflection. The numerical deflections of cross-section A show very good agreement with the experimental deflections based on the mean value of the reduction factors at 100°C for the modulus of elasticity in compression and in tension $k_{100°C,E,x} = 0.425$ according to EN 1995-1-2. The deflections lay between the extreme cases of the numerical deflections obtained from the 2D FE beam model in SAFIR® (effective width as 60%, and 100% of the CLT width).
The maximum tensile stress in the rib at $t = 90$ min confirms the maximum tensile stress obtained from the linear 2D FE beam model in section 4.4.3 (Figure 4.17a). The maximum compressive stress at the top edge of the CLT plate is double the size of the maximum compressive stress obtained from the linear 2D FE beam model, where beam elements are modelled as Bernoulli-type beams.
The results show a temperature-dependent reduction of the numerical effective width in fire $b_{ef,fi,sim}$. The numerical effective width in fire $b_{ef,fi,sim}$ remains between the values of 84% for the numerical effective width at normal temperature $b_{ef,sim}$ and 64% for the estimated effective width at normal temperature b_{ef} according to prEN 1995-1-1. Until test termination, thus a fire resistance of 90 min, the effective width at normal temperature b_{ef} according to prEN 1995-1-1 gives an approximation of the effective width in fire $b_{ef,fi,sim}$ on the safe side.

4.9 Parametric study on the effective width in fire

4.9.1 Objectives

A parametric study was performed based on uncoupled thermo-mechanical simulations using the 3D FE models presented in sections 4.7 and 4.8. Materials were modelled as linear-elastic and temperature-dependent orthotropic. In a sensitivity analysis, extreme cases were defined based on a parameter range expected in practice. The investigation was limited to cross-sections of a T-section (Figure 2.1), since the experimental and numerical investigations conclude that an underestimation of the effective width leads to a severe underestimation of the structural behaviour for the box-section. It is assumed that the limits of the effective width in fire $b_{\mathrm{ef,fi}}$ for T-sections should also apply to box-sections. The objective was the investigation of the effective width in fire obtained from the simulation $b_{\mathrm{ef,fi,sim}}$. The findings presented and discussed in section 4.8 were taken into account. Under certain conditions, the effective width at normal temperature b_{ef} according to prEN 1995-1-1 gives an approximation on the safe side of the effective width in fire $b_{\mathrm{ef,fi,sim}}$.

4.9.2 Model

Finite element models

The FE model with a cross-section of a T-section was created based on the 3D FE models presented in sections 4.7 and 4.8. In comparison, the mechanical load was applied as uniformly distributed load based on the design approach of the experimental investigations in section 3.2. According to the combination of actions for accidental design situations according to EN 1990, the uniformly distributed load $p_{\mathrm{k,fi}}$ was calculated according to Formula 4.25

$$p_{\mathrm{k,fi}} = g_{\mathrm{k,S}} + \psi_1 \cdot q_{\mathrm{k}} = 1.50 + 0.5 \cdot 4.50 = 3.75 \text{ kN/m}^2 \tag{4.25}$$

where $g_{\mathrm{k,S}}$ is the characteristic value of the superimposed action on the floor system, ψ_1 is the factor for frequent value of a variable action, and q_{k} is the characteristic value of the variable action of the floor system. Here, ψ_1 is 0.5 according to EN 1990 for Category B: office areas. Depending on the size of the model, the meshing size for the thermo-mechanical model was set as 10-20 mm.

Parameter range

The following parameter range of the parametric study was chosen in accordance with the parameter range expected in practice from section 2.4.3:

- $0.02 \leq b_{\mathrm{f,i}}/l \leq 0.25$, for the ratio of clear rib distance to span
- $0.18 \leq \Sigma t_{\mathrm{x}}/t_{\mathrm{CL}} \leq 0.80$, for the ratio of total thickness of the longitudinal CLT layers to height of the CLT plate
- $14 \leq l/h \leq 22$, for the ratio of span to overall height.

Figure 4.32 presents the influence of the different parameters on the ratio of the effective width to CLT width b_{ef}/b. The interesting areas of the parametric study are marked in blue. The effective width is determined as effective width at normal temperature b_{ef} according to prEN 1995-1-1, based on Formulae 2.9-2.10. The basic model of the sensitivity analysis is defined by the system of cross-section A of the experimental investigations presented in Figure 3.1 ($b_{f,i} = 0.733$ m, $l = 5.2$ m, $\sum t_x = 80$ mm, $t_{CL} = 120$ mm). The modulus of elasticity in x-direction of the CLT plate $E_{x,CLT}$ is 12500 N/mm^2, and the shear modulus loaded in-plane in y-direction of the CLT plate $G_{xy,CLT}$ is 450 N/mm^2. The ratio of the effective width to CLT width b_{ef}/b results for cross-section A in 64%.

Figure 4.32a1 shows that a change of the modulus of elasticity in x-direction of the CLT plate $E_{x,CLT}$ leads to minor changes. The same applies in Figure 4.32a2 for the shear modulus loaded in-plane in y-direction of the CLT plate $G_{xy,CLT}$. Figure 4.32b1 shows a linear reduction with an increased ratio of clear rib distance to span $b_{f,i}/l$, which means a reduction of the floor stiffness. This results in a ratio of effective width to CLT width b_{ef}/b between 97% and 25% for span lengths between 5 m and 20 m. Figure 4.32b2 shows the influence of the ratio of total thickness of the longitudinal CLT layers to height of the CLT plate $\Sigma t_x/t_{CL}$. The ratio of effective width to CLT width b_{ef}/b results between 80% and 56% for thicknesses of the CLT plates between 60 mm (5-layered) and 200 mm (3-layered). The results show a reduction with an increased $\Sigma t_x/t_{CL}$-ratio, which means a reduction of the shear stiffness in-plane. The reduction is 3-times lower than for the ratio of clear rib distance to span $b_{f,i}/l$. Typical CLT layups are ratios of total thickness of the longitudinal CLT layers to height of the CLT plate $\Sigma t_x/t_{CL}$ between 0.43 and 0.80 according to prEN 1995-1-2 (Eurocode 5 layups). Here, the ratios of effective width to CLT width b_{ef}/b result only between 65% and 56%. The sensitivity analysis emphasizes that the material properties have a negligible influence on the effective width b_{ef}, in comparison to the geometry of the floor system. As outlined in the discussion of the mechanical model in section 4.6.4, the effective width b_{ef} mainly depends on the stiffness of the floor system. The influence of CLT layups is generally small and even negligible for CLT layups of prEN 1995-1-2 (Eurocode 5 layups).

Extreme cases

Table 4.9 gives an overview of the defined extreme cases: the geometry in accordance with Figure 2.3, the resulting ratios, the effective widths at normal temperature b_{ef} according to prEN 1995-1-1, and the fall-off times of the CLT layers. The extreme cases are included in Figure 4.32c and divided into three groups:

- Group 1: thin layers of 20 mm, 3-layered CLT plate
- Group 2: thin layers of 20 mm, 5-layered CLT plate
- Group 3: thick layers of 40 mm, 3-layered CLT plate

The thickness of the CLT layers and the number of n layers have an influence on the fire behaviour of the CLT plate and the fall-off times of the charred CLT layers. Thin layers will

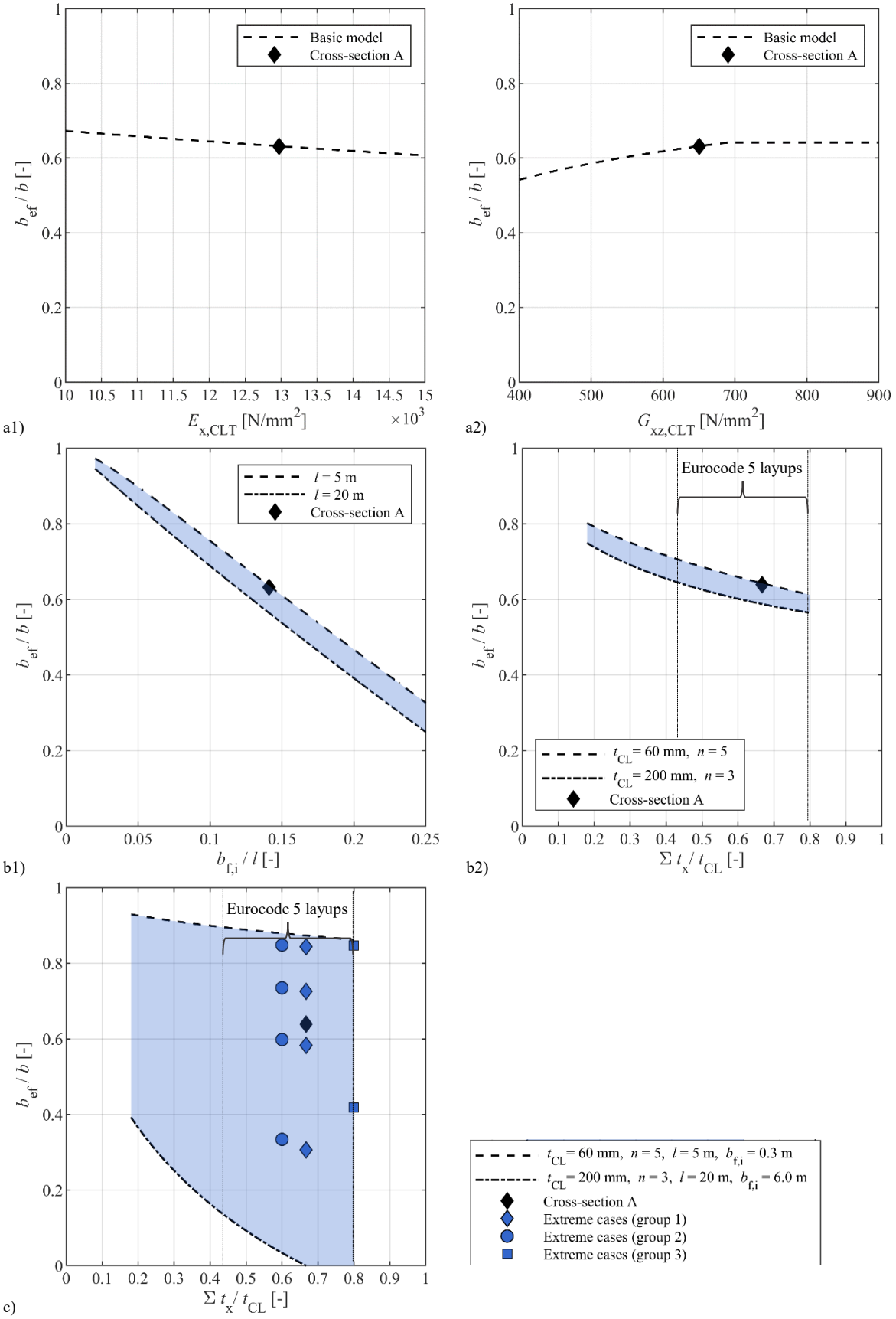

Figure 4.32. Parametric study - Influence on the effective width according to prEN 1995-1-1: a1) Modulus of elasticity in x-direction of the CLT plate; a2) Shear modulus loaded in-plane in y-direction of the CLT plate; b1) The ratio of clear rib distance to span; b2) The ratio of the total thickness of the longitudinal CLT layers to the height of the CLT plate; c) Combination of b1) and b2) including the extreme cases.

Table 4.9. Parametric study - Extreme cases defined by the ratio of clear rib distance to span $b_{f,i}/l$, and layer thickness (highlighted in bold).

	Extreme cases	l	$b_{f,i}$	$b_{f,i}/l$	h_{rib}	b_{rib}	b	h	l/h	t_{CL}	n	Layup	$\Sigma t_x/t_{CL}$	b_{ef}	b_{ef}/b	Fire exposure time	Fall-off 1	Fall-off 2	Fall-off 3	Fall-off 4
		[m]	[m]	[-]	[m]	[m]	[m]	[m]	[-]	[mm]	[-]	[mm]	[-]	[mm]	[-]	[min]	**[min]**	**[min]**	**[min]**	**[min]**
Group 1 (thin layers, 3-layered)	1b	5	0.30	**0.06**	0.18	0.10	0.40	0.24	21	60	3	**3x20**	0.67	338	0.85	30	29	54	71	
	2b	5	0.50	**0.10**	0.18	0.10	0.60	0.24	21	60	3	**3x20**	0.67	436	0.73	30	29	54	71	
	5b	5	0.75	**0.15**	0.18	0.10	0.85	0.24	21	60	3	**3x20**	0.67	496	0.58	30	29	54	71	
	3b	5	1.25	**0.25**	0.18	0.10	1.35	0.24	21	60	3	**3x20**	0.67	413	0.31	30	29	54	70	
+ no fall-off	7	5	0.30	**0.06**	0.18	0.10	0.40	0.24	21	60	3	**3x20**	0.67	338	0.85	30				
Group 2 (thin layers, 5-layered)	1	10	0.50	**0.05**	0.36	0.18	0.68	0.46	22	100	5	**5x20**	0.60	577	0.85	60	29	54	72	86
	2	10	1.00	**0.10**	0.36	0.18	1.18	0.46	22	100	5	**5x20**	0.60	867	0.73	60	29	54	72	86
	5	10	1.50	**0.15**	0.36	0.18	1.68	0.46	22	100	5	**5x20**	0.60	1005	0.60	60	29	54	71	86
	3	10	2.50	**0.25**	0.36	0.18	2.68	0.46	22	100	5	**5x20**	0.60	895	0.33	60	29	54	71	86
Group 3 (thick layers)	6	5	0.30	**0.06**	0.18	0.14	0.44	0.28	18	100	3	**40/20/40**	0.80	373	0.85	60	64	80	118	
	A	5.2	0.733	**0.14**	0.28	0.20	0.933	0.40	13	120	3	**3x40**	0.67	597	0.64	90	63	115		
	4	5	1.00	**0.20**	0.18	0.14	1.14	0.28	18	100	3	**40/20/40**	0.80	477	0.42	60	63	79	118	

lead to an increased charring behaviour and a faster reduction of the effective width in fire $b_{\mathrm{ef,fi}}$. Based on the sensitivity analysis, each group covers different ratios of clear rib distance to span $b_{\mathrm{f,i}}/l$ to account for different floor stiffness values. To reduce the computation time, the system lengths were kept small depending on the size of the cross-section. The geometries were chosen based on the typical dimensions for cross-laminated timber rib panels (see section 2.4.1), the typical CLT layups according to prEN 1995-1-2, and a homogeneous ratio between CLT plate and glulam rib:

- Span length: 5 m $\leq l \leq$ 16.50 m
- Total height: $h \geq$ 160 mm
- CLT width: $b \leq$ 3.50 m
- Thickness of the CLT plate: 60 mm $\leq h_{\mathrm{CL}} \leq$ 200 mm
- Rib width: $b_{\mathrm{rib}} \geq$ 60 mm
- Rib height: $h_{\mathrm{rib}} \geq$ 100 mm
- Thickness of CLT layer: $t_{\mathrm{x}} = t_{\mathrm{y}} = \{20; 30; 40\}$
- CLT layup: 3-/5-layered
- Clear rib distance: $b_{\mathrm{f,i}} \geq 2 \cdot b_{\mathrm{rib}}$
- Ratio between thickness of the rib width and the CLT plate: $b_{\mathrm{rib}}/h_{\mathrm{CL}} \approx 2$

4.9.3 Results

General

Figures 4.33-4.35 present the results of the thermo-mechanical simulations of the extreme cases per group of Table 4.9. The results are shown at the initial time step $t = 0$ min, at each fall-off time $t_{300°\mathrm{C,layer,i,sim}}$ of layer i, and up to the time step at which the penultimate CLT layer fell off. The effective width in fire $b_{\mathrm{ef,fi,sim}}$ was determined as a fraction of the total force in fire $F_{\mathrm{x,tot,fi}}$ and the trapezoidal force in fire $F_{\mathrm{x,max,fi}}$ according to Formula 4.8, based on the simplified approach discussed in section 4.8. Figures 4.33-4.35a1 show the minimum cross-sections with the highest floor stiffness. Figures 4.33-4.35a2 show the maximum cross-sections with the lowest floor stiffness. Figures 4.33-4.35b1 show the charred depths in the CLT layers based on the fall-off times of Table 4.9. The charred depths in the CLT layers are consistent in each group. In Figures 4.33-4.35b2, the deflections over time are presented per extreme case. The deflections are higher for extreme cases of lower floor stiffness. In Figures 4.33-4.35c1, the total forces of the CLT plate in fire $F_{\mathrm{x,tot,fi}}$ and the trapezoidal forces at rib centre in fire $F_{\mathrm{x,max,fi}}$ are presented per extreme case. Figures 4.33-4.35c2 show the ratios of effective width in fire to CLT width $b_{\mathrm{ef,fi,sim}}/b$ per extreme case. The results are presented separately for each extreme case in Annexes A to C.

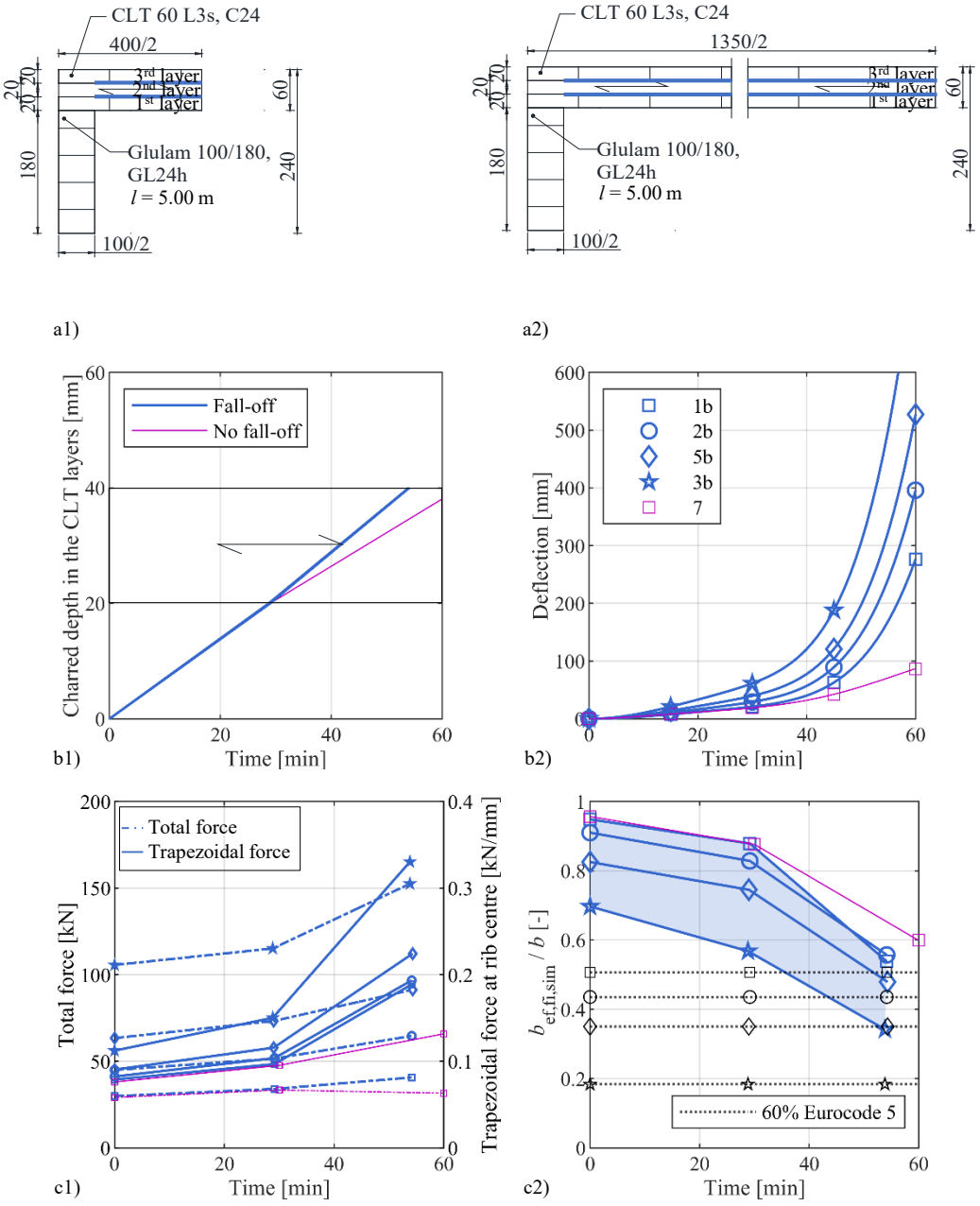

Figure 4.33. Parametric study - Numerical results over time of the extreme cases of group 1 'thin layers, 3-layered': a1) Extreme case 1b (highest floor stiffness); a2) Extreme case 3b (lowest floor stiffness); b1) Charred depth in CLT layers; b2) Deflection; c1) Total force and trapezoidal force at rib centre in fire; c2) Ratio of effective width in fire to CLT width $b_{\mathrm{ef,fi,sim}}/b$ related to a limit value based on prEN 1995-1-1 (Eurocode 5).

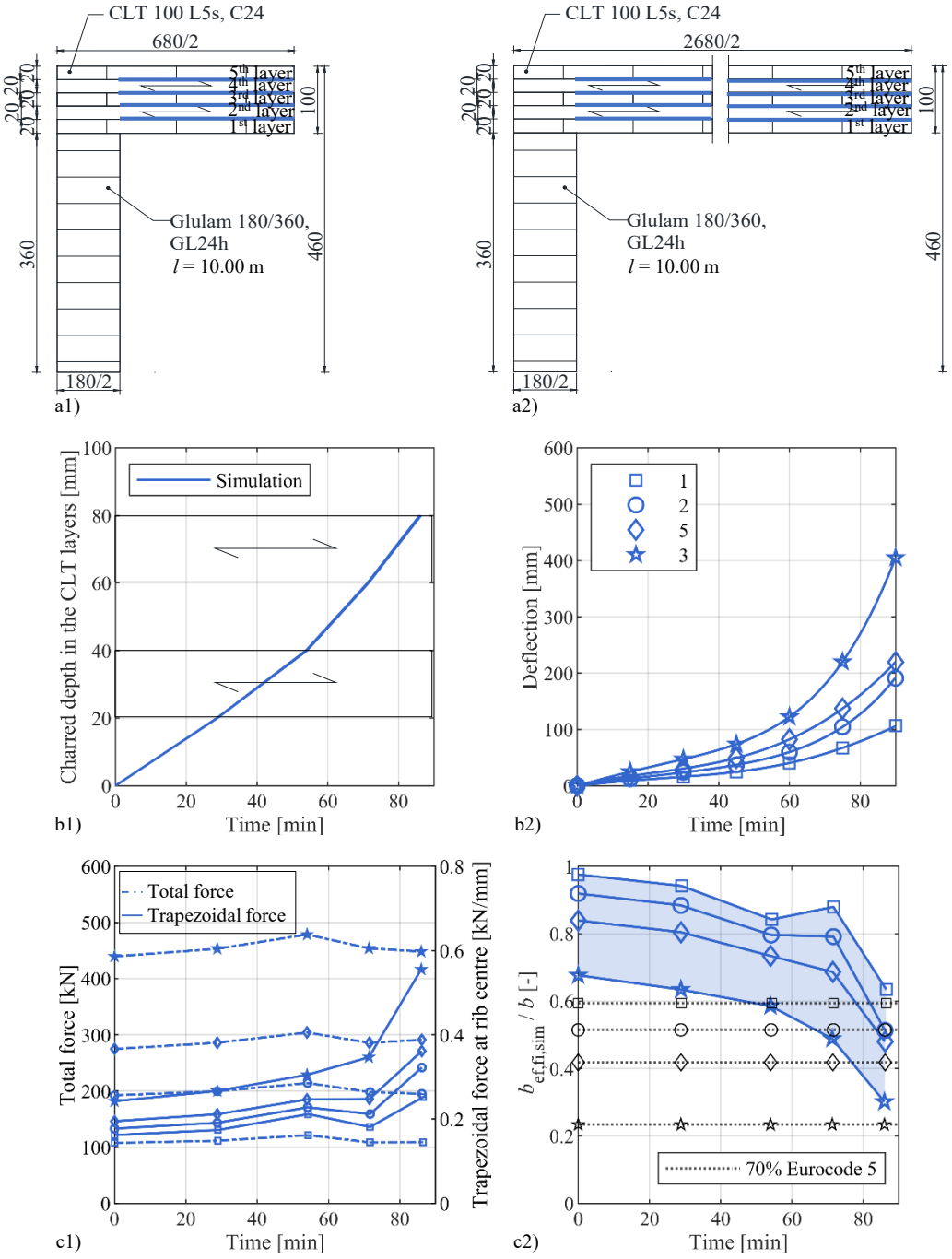

Figure 4.34. Parametric study - Numerical results over time of the extreme cases of group 2 'thin layers, 5-layered': a1) Extreme case 1 (highest floor stiffness); a2) Extreme case 3 (lowest floor stiffness); b1) Charred depth in CLT layers; b2) Deflection; c1) Total force and trapezoidal force at rib centre in fire; c2) Ratio of effective width in fire to CLT width $b_{\mathrm{ef,fi,sim}}/b$ related to a limit value based on prEN 1995-1-1 (Eurocode 5).

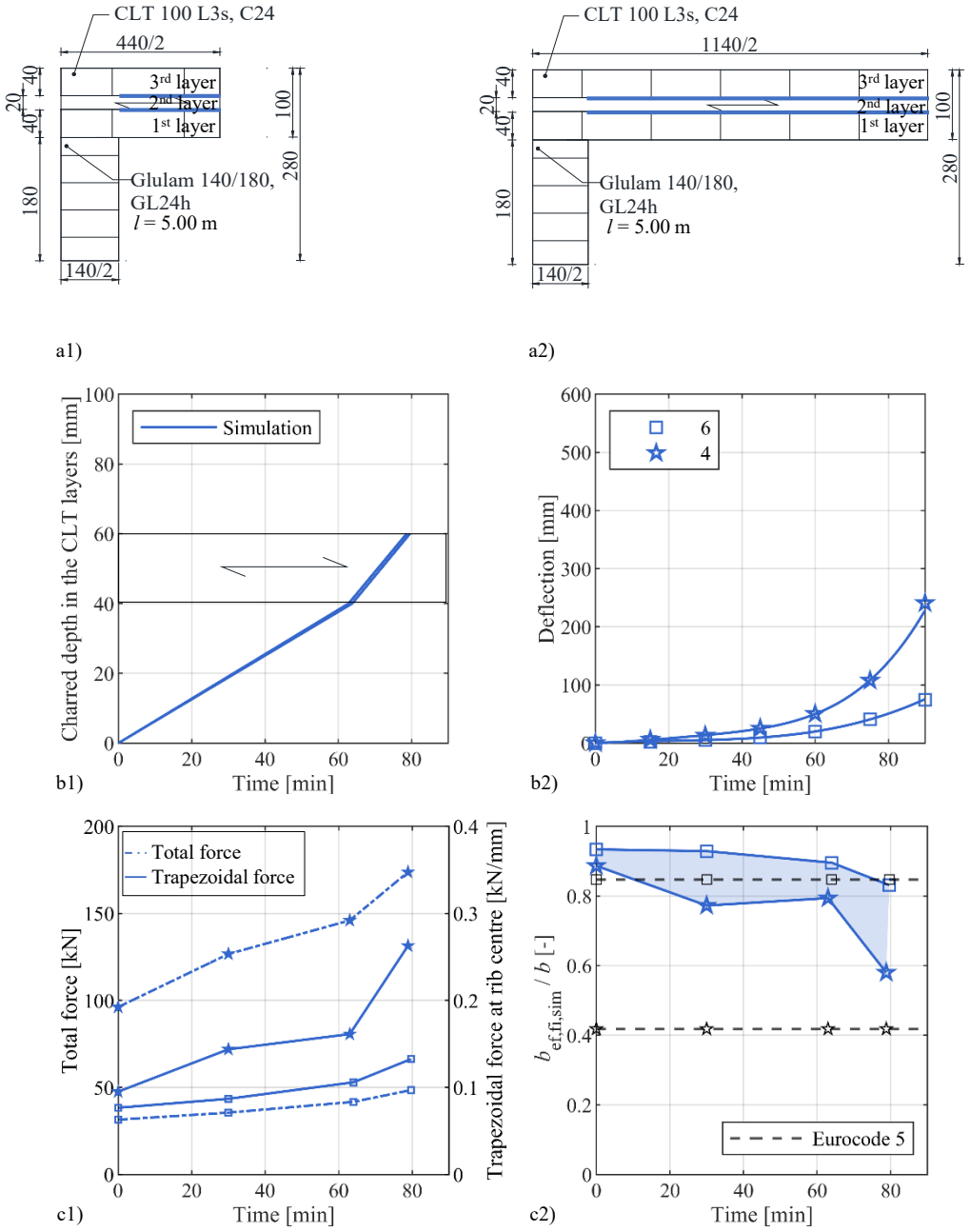

Figure 4.35. Parametric study - Numerical results over time of the extreme cases of group 3 'thick layers, 3-layered': a1) Extreme case 6 (highest floor stiffness); a2) Extreme case 4 (lowest floor stiffness); b1) Charred depth in CLT layers; b2) Deflection; c1) Total force and trapezoidal force at rib centre in fire; c2) Ratio of effective width in fire to CLT width $b_{\mathrm{ef,fi,sim}}/b$ related to a limit value based on prEN 1995-1-1 (Eurocode 5).

Group 1 'thin layers, 3-layered'

Figure 4.33 presents the results of group 1 covering the ratios of clear rib distance to span $b_{\mathrm{f,i}}/l$ between 0.06 and 0.25. The minimum cross-section with the highest floor stiffness is represented by extreme case 1b. The maximum cross-section with the lowest floor stiffness is represented by extreme case 3b. The duration of the simulations was less than 60 min. The total force in fire $F_{\mathrm{x,tot,fi}}$ and the trapezoidal force in fire $F_{\mathrm{x,max,fi}}$ show a temperature-dependent increase with an increased exposure time. The values are higher for extreme cases of decreased stiffness. After the fall-off of the first charred CLT layer, the total force in fire $F_{\mathrm{x,tot,fi}}$ shows a 2- to 5-fold increase in the rate of change. The trapezoidal force in fire $F_{\mathrm{x,max,fi}}$ shows an up to 6-fold increase in the rate of change, up to 3-times higher than the total force in fire $F_{\mathrm{x,tot,fi}}$.
The effective widths in fire $b_{\mathrm{ef,fi,sim}}$ show a temperature-dependent reduction with an increased exposure time. The reduction increases after the fall-off of the first charred CLT layer. The ratios of effective width in fire to CLT width $b_{\mathrm{ef,fi,sim}}/b$ at time step $t = 0$ min result between 96% and 70%. Until the fall-off of the second charred CLT layer, the ratios of effective width in fire to CLT width $b_{\mathrm{ef,fi,sim}}/b$ decrease to values between 56% and 34%.
The results of extreme case 7 are presented for comparison with extreme case 1b. The extreme case 7 is identical to extreme case 1b with the exception that fall-off of charred CLT layers was not taken into account. The final deflection are 87 mm for extreme case 7 and 276 mm for extreme case 1b. Until the fall-off of the second charred CLT layer, the ratios of effective width in fire to CLT width $b_{\mathrm{ef,fi,sim}}/b$ decrease to 60% for extreme case 7 and 54% for extreme case 1b.

Group 2 'thin layers, 5-layered'

Figure 4.34 presents the results of group 2 covering the ratios of clear rib distance to span $b_{\mathrm{f,i}}/l$ between 0.05 and 0.25. The minimum cross-section with the highest floor stiffness is represented by extreme case 1. The maximum cross-section with the lowest floor stiffness is represented by extreme case 3. The duration of the simulations was less than 90 min. The total force in fire $F_{\mathrm{x,tot,fi}}$ and the trapezoidal force in fire $F_{\mathrm{x,max,fi}}$ show a slow temperature-dependent increase with an increased exposure time. The values are higher for extreme cases of decreased stiffness. After the fall-off of the third charred CLT layer, the total force in fire $F_{\mathrm{x,tot,fi}}$ remains unchanged, while the trapezoidal force in fire $F_{\mathrm{x,max,fi}}$ shows an up to 6-fold increase in the rate of change.
The effective widths in fire $b_{\mathrm{ef,fi,sim}}$ show a temperature-dependent reduction with an increased exposure time. The reduction increases after the fall-off of the third charred CLT layer. The ratios of effective width in fire to CLT width $b_{\mathrm{ef,fi,sim}}/b$ at time step $t = 0$ min result between 98% and 68%. Until the fall-off of the fourth charred CLT layer, the ratios of effective width in fire to CLT width $b_{\mathrm{ef,fi,sim}}/b$ decrease to values between 63% and 30%.

Group 3 'thick layers, 3-layered'

Figure 4.34 presents the results of group 3 covering the two extreme $b_{\mathrm{f,i}}/l$-ratios of 0.06 and 0.20. The duration of the simulations was less than 90 min. The total force in fire $F_{\mathrm{x,tot,fi}}$ and

the trapezoidal force in fire $F_{x,max,fi}$ show a temperature-dependent increase with an increased exposure time. The values are higher for extreme case 4. After the fall-off of the first charred CLT layer, the total force in fire $F_{x,tot,fi}$ shows a 2-fold increase in the rate of change. The trapezoidal force in fire $F_{x,max,fi}$ shows an up to 4-fold increase in the rate of change, 2-times higher than the total force in fire $F_{x,tot,fi}$.
The effective width was additionally determined at $t = 30$ min. The effective widths in fire $b_{ef,fi,sim}$ show a temperature-dependent reduction with an increased exposure time. The reduction increases after the fall-off of the first charred CLT layer. The ratios of effective width in fire to CLT width $b_{ef,fi,sim}/b$ result between 93% and 89% at time step $t = 0$ min, and decrease to values between 93% and 77% at time step $t = 30$ min. Until the fall-off of the first charred CLT layer, the ratios of effective width in fire to CLT width $b_{ef,fi,sim}/b$ remain unchanged. Until the fall-off of the second charred CLT layer, the ratios of effective width in fire to CLT width $b_{ef,fi,sim}/b$ decrease to values between 83% and 58%.

4.9.4 Discussion

General

The charred depths in the CLT layers are consistent in each group, except when fall-off was not taken into account. The total force in fire $F_{x,tot,fi}$ and the trapezoidal force in fire $F_{x,max,fi}$ show a temperature-dependent increase with an increased exposure time. The stresses are accumulated in the part of the remaining CLT plate. The values are higher for extreme cases of decreased stiffness, since the CLT width of the system and thus the applied load per rib are higher.
The effective width in fire $b_{ef,fi,sim}$ was determined up to the time step at which the penultimate CLT layer fell off, which means that one CLT layer was still in place. The total force of the CLT plate in fire $F_{x,tot,fi}$ shows a smaller increase in the rate of change than the trapezoidal force in fire $F_{x,max,fi}$. As a fraction of the total force of the CLT plate in fire $F_{x,tot,fi}$ and the trapezoidal force in fire $F_{x,max,fi}$, the effective widths in fire $b_{ef,fi,sim}$ decreases with an increased exposure time. The influence of the shear lag effect of the ribbed floor system increases. The stresses are accumulated in the part of the remaining CLT plate at the rib centre, while parts far from the rib experience higher shear deformations. A sharp increase of the effective width's reduction is observed when effectively only one longitudinal CLT layer remains.
The ratios of effective width in fire to CLT width $b_{ef,fi,sim}/b$ at time step $t = 0$ min represent the ratios of effective width at normal temperature to CLT width $b_{ef,sim}/b$. Annexes A to C confirm that these initial values are above the values of the effective widths at normal temperature b_{ef} according to prEN 1995-1-1 (Eurocode 5). Extreme cases with lower stiffness values have a higher possibility to be underestimated by the effective widths at normal temperature b_{ef}.

Comparison between the groups

The results for group 1 and group 2 ('thin layers') are in a comparable range. The initial ratios of effective width at normal temperature to CLT width $b_{ef,sim}/b$ result in average between

95% and 69%. Until the fall-off of the penultimate charred CLT layer, the ratios of effective width in fire to CLT width $b_{\mathrm{ef,fi,sim}}/b$ decrease in average by 35% in absolute terms. The charring behaviour is comparable since the thicknesses of the CLT layers are the same. The results of the two groups differ with regard to the duration of fire exposure. The results of group 2 ('thin layers, 5-layered') show comparable results over a longer fire exposure time. The higher number of CLT layers delays the charring progress and thus the increasing influence of the shear lag effect. The same applies when fall-off of charred CLT layers is not taken into account.
The results of group 3 ('thick layers') show throughout a less pronounced temperature-dependent reduction. Until the fall-off of the penultimate charred CLT layer, the ratios of effective width in fire to CLT width $b_{\mathrm{ef,fi,sim}}/b$ decrease by 20% in absolute terms. The thicker CLT layers delay the charring progress and stabilise the effective width in fire $b_{\mathrm{ef,fi,sim}}$.

Group 1 'thin layers, 3-layered'

The ratios of effective widths at normal temperature to CLT width b_{ef}/b according to prEN 1995-1-1 are presented per extreme case in Annex A. Except for extreme case 3b, all values are undercut by the effective widths in fire $b_{\mathrm{ef,fi,sim}}$. The effective widths in fire stay above a limit value determined as 60% of the effective widths at normal temperature according to prEN 1995-1-1: $b_{\mathrm{ef,fi,sim}} \geq 0.60 \cdot b_{\mathrm{ef}}$. The values are included per extreme case in Figure 4.33c2.
The extreme case 7 (no fall-off) is identical to extreme case 1b until the first CLT layer is charred. While the elements of the first CLT layer were removed for extreme case 1b, they protected the elements of the second CLT layer in the case of extreme case 7. Extreme case 7 exhibits 3-times lower final deflection. Until the fall-off of the penultimate charred CLT layer, the effective width in fire $b_{\mathrm{ef,fi,sim}}$ is up to 10% higher in absolute terms. Extreme case 7 still undercuts the value of the estimated effective width at normal temperature b_{ef} according to prEN 1995-1-1, shown in Annex A.

Group 2 'thin layers, 5-layered'

The ratios of effective widths at normal temperature to CLT width b_{ef}/b according to prEN 1995-1-1 are presented per extreme case in Annex B. All values are undercut by the effective widths in fire $b_{\mathrm{ef,fi,sim}}$. The effective widths in fire stay above a limit value determined as 70% of the effective widths at normal temperature according to prEN 1995-1-1: $b_{\mathrm{ef,fi,sim}} \geq 0.70 \cdot b_{\mathrm{ef}}$. The values are included per extreme case in Figure 4.34c2.

Group 3 'thick layers, 3-layered'

Until the fall-off of the first charred CLT layer, the effective widths in fire $b_{\mathrm{ef,fi,sim}}$ show a stabilisation comparable to the results of cross-section A in section 4.8.3. After the fall-off, the trapezoidal force in fire $F_{\mathrm{x,max,fi}}$ shows an up to 2-times higher increase than the total force in fire $F_{\mathrm{x,tot,fi}}$, which leads to an increased reduction of the effective width in fire $b_{\mathrm{ef,fi,sim}}$.
The ratios of effective widths at normal temperature to CLT width b_{ef}/b according to prEN 1995-1-1 are included per extreme case in Figure 4.35c2. The effective widths in fire $b_{\mathrm{ef,fi,sim}}$ stay above the values.

4.9.5 Conclusions

A parametric study was performed based on uncoupled thermo-mechanical simulations using the 3D FE models presented in sections 4.7 and 4.8. The objective was the investigation of the effective width in fire obtained from the simulation $b_{\mathrm{ef,fi,sim}}$ for a parameter range expected in practice. The investigation was limited to cross-sections of a T-section, assuming that the limits of the effective width in case of fire for T-sections should also apply to box-sections. Based on a sensitivity analysis, extreme cases were defined focusing on different thicknesses of the CLT layers, and different ratios of clear rib distance to span $b_{\mathrm{f,i}}/l$ to cover a range of floor stiffness values.

The effective widths in fire $b_{\mathrm{ef,fi,sim}}$ were determined up to the time step at which the penultimate CLT layer fell off, which means that one CLT layer was still in place. The ratios of effective width in fire to CLT width $b_{\mathrm{ef,fi,sim}}/b$ at time step $t = 0$ min represent the initial ratios of effective width at normal temperature to CLT width $b_{\mathrm{ef,sim}}/b$. The values are above values of the effective widths at normal temperature b_{ef} according to prEN 1995-1-1 (Eurocode 5). The effective widths in fire $b_{\mathrm{ef,fi,sim}}$ show a temperature-dependent reduction with an increased exposure time. The influence of the shear lag effect of the ribbed floor system increases. The stresses are accumulated in the part of the remaining CLT plate at the rib centre, while parts far from the rib experience higher shear deformations.

The results for group 1 and group 2 ('thin layers') are in a comparable range. The charring behaviour is the same based on the same layer thickness. The difference is the duration of fire exposure. A higher number of CLT layers, a thicker CLT plate, and no fall-off of charred CLT layers delay the charring progress and the influence of the shear lag effect. The results of group 3 ('thick layers') show throughout a less pronounced temperature-dependent reduction. The thicker CLT layers and thus the thicker CLT plates delay the charring progress and stabilise the effective width in fire $b_{\mathrm{ef,fi,sim}}$.

Under certain conditions, the effective width at normal temperature b_{ef} according to prEN 1995-1-1 might give an approximation on the safe side of the effective width in fire $b_{\mathrm{ef,fi,sim}}$. The results of group 3 ('thick layers of 40 mm') stay above the values of the effective widths at normal temperature b_{ef} (Eurocode 5). The results of group 1 and group 2 ('thin layers of 20 mm') undercut the values of the effective widths at normal temperature (Eurocode 5) and require a limit value of 60% of the effective widths at normal temperature: $b_{\mathrm{ef,fi,sim}} \geq 0.60 \cdot b_{\mathrm{ef}}$.

4.10 Conclusions

The **numerical investigations** cover thermal, mechanical, and thermo-mechanical simulations using FE models. The modelling assumptions derived from the experimental investigations, and the basic input parameters of the FE models are presented. Temperature-dependent thermal and mechanical properties were implemented according to Eurocode 5 (EN 1995-1-2). The material behaviour was modelled as linear-elastic.

Heat transfer analyses using 2D FE models were performed in SAFIR® modelling the four tested cross-section types. The fall-off behaviour of charred layers was taken into account for the CLT plates but not for the glulam ribs. A new set of thermal properties is proposed for wood after the fall-off of the fire protection system or a charred CLT layer. The combination of Eurocode 5 and the new set is called the revision. Comparison with experimental results of a database shows that the FE heat transfer models provide good estimations for the experimental temperatures.

Uncoupled thermo-mechanical simulations using a linear 2D FE beam model were performed in SAFIR®. Material strength behaviour was modelled simplified as brittle in tension and in compression. The deflections obtained from the model outline the importance to take into account the shear deflections in fire. To study the influence of the chosen effective width on the resulting deflection, three different approaches were compared for the tested cross-section types: representing the average result for the effective width b_{ef} according to prEN 1995-1-1 (60% of the CLT width), the average result for the effective width of the reference tests $b_{\text{ef,test}}$ (80% of the CLT width), and the extreme case (100% of the CLT width). The differences in the resulting deflections using these three approaches for the effective widths are larger for the box-sections than for the T-sections. However, the differences are small in all cases and it can be concluded that an underestimation of the effective width in fire $b_{\text{ef,fi}}$ still results in good approximations.

A **thermo-mechanical model** determined the neutral axis, and the resistance moment in fire at specific time steps based on the thermo-mechanical simulations of the linear 2D FE beam model. The numerical results show a temperature-dependent reduction of the resistance moment with an increased exposure time. The resistance moment is higher for a cross-section with a larger effective width. The differences in resistance moment between different effective widths are larger for the box-sections than for the T-sections. The final resistance moments show good agreement with the experimental resistance moments at failure time. This confirms that the test specimens of the fire resistance tests were close to structural failure.

Mechanical simulations using 3D FE models were performed in Abaqus. The FE models were created as a flexible-in-shear multi-layered model resulting in a non-uniform strain distribution along the CLT width. The validation of the mechanical 3D model was made against the experimental results of the ultimate-load tests at normal temperature. The results confirm the implementation of the nine engineering constants of the orthotropic material model in accordance with the consolidated draft of Eurocode 5 for the informal enquiry (prEN 1995-1-1) for CLT plates, and according to EN 14080 for glulam ribs.

Heat transfer analyses using 3D FE models were performed in Abaqus as a basis for the uncoupled thermo-mechanical simulations (3D) and the parametric study. The reliability of the

model was confirmed through comparison with the 2D FE model in SAFIR®.

Uncoupled thermo-mechanical simulations using a 3D FE model were performed in Abaqus based on the FE model of the mechanical simulations and as a basis for the parametric study. The reduction factor at 100°C for the modulus of elasticity in x-direction $k_{100°C,E,x}$ has the highest impact on the deflection. The validation was made against the experimental results of one fire resistance test. The numerical deflections show very good agreement with the experimental deflections based on the mean value of the reduction factors at 100°C for the modulus of elasticity in compression and in tension $k_{100°C,E,x} = 0.425$ according to EN 1995-1-2. The results show a temperature-dependent reduction of the effective width in fire obtained from the simulation $b_{ef,fi,sim}$ after the fall-off of the first charred CLT layer. Until test termination, thus a fire resistance of 90 min, the effective width at normal temperature b_{ef} according to prEN 1995-1-1 gives an approximation of the effective width in fire $b_{ef,fi}$ on the safe side.

The **parametric study** was performed based on the uncoupled thermo-mechanical simulations. The objective was the investigation of the numerical effective width in fire $b_{ef,fi,sim}$ for a parameter range expected in practice. The investigation was limited to cross-sections of a T-section, based on the assumption that the limits of the effective width in case of fire valid for T-sections should also apply to box-sections. Based on a sensitivity analysis, extreme cases were defined focusing on different thicknesses of the CLT layers and covering a range of floor stiffness values. The effective widths in fire $b_{ef,fi,sim}$ were determined up to the time step at which the penultimate CLT layer fell off, which means that one CLT layer was still in place. The initial ratios of effective width to CLT width $b_{ef,sim}/b$ are above the values of the effective widths at normal temperature b_{ef} according to prEN 1995-1-1 (Eurocode 5). The effective widths in fire $b_{ef,fi,sim}$ show a temperature-dependent reduction with an increased exposure time. A higher number of CLT layers, thicker CLT layers, and no fall-off of charred CLT layers delay the charring progress and the influence of the shear lag effect. The results of the extreme cases 'thick layers of 40 mm' stay above the values of the effective widths at normal temperature b_{ef} (Eurocode 5). The results of the extreme cases 'thin layers of 20 mm' undercut the values of the effective widths at normal temperature (Eurocode 5) and require a limit value of 60% of the effective widths at normal temperature: $b_{ef,fi,sim} \geq 0.60 \cdot b_{ef}$.

5. Design of cross-laminated timber rib panels in fire

5.1 Overview

In this chapter, the developed framework of the simplified design method for modelling cross-laminated timber rib panels in fire is presented, following the principles of section 2.5.3. The framework is improved based on the assumptions derived from the experimental investigations and used for the numerical investigations, presented in section 4.2.1. Shortcomings of the current design rule for the effective width in fire $b_{\mathrm{ef,fi}}$ are discussed and improvements are proposed, taking into account the findings presented and discussed in the parametric study (section 4.9). First, the bending resistance in fire based on the simplified design method is compared with the bending resistance in fire based on the advanced design method, presented and discussed in the section 4.5. The comparison is made for the four tested cross-section types (Figure 3.1). Then, the bending resistance in fire is calculated on the basis of the design strength values in fire and compared with the experimental bending resistance at failure time of the fire resistance tests. Degrees of utilisation of the loadbearing capacities in fire are set in relation to each other, based on the failure times of the fire resistance tests. The influence of the effective width in fire $b_{\mathrm{ef,fi}}$ is investigated.

5.2 Simplified design method

Effective cross-section

The framework of the simplified design method uses the terminology of Eurocode 5 (EN 1995-1-2) and the final draft of the Eurocode 5 part 1-2 revision (prEN 1995-1-2). The start time of charring of initially protected cross-sections (with or without insulation material) and the failure time of the fire protection systems should be calculated in accordance with the separating function method. The effective cross-section method is applied as explained in section 2.5.3 to determine the part of the cross-section which strength and stiffness properties are assumed to be unaffected for a certain fire resistance time (effective cross-section). Figure 2.7 illustrates how the effective cross-section is calculated adding the zero-strength layer d_0 to the charred depth d_{char} to reduce the initial cross-section from each fire exposed side by the effective charred depth d_{ef}. Despite the charring process, the rib gains height in the area of transition to the CLT plate, defined as transition zone.

Method of rigidly bonded components

The composite action is maintained under standard fire exposure. The method of flexibly connected bending beams can be omitted, with regard to section 2.5.3. For the effective cross-section, the calculation method of rigidly bonded components (Bernoulli-beam) is applied as in the case under normal temperature (section 2.4.3). The neutral axis in fire is located in the centre of gravity in fire of the effective cross-section $z_{\mathrm{s,fi}}$, determined by Formula 5.1

$$z_{\mathrm{s,fi}} = \frac{\sum(E_{\mathrm{i}} \cdot A_{\mathrm{i,ef}} \cdot a_{\mathrm{i,fi}})}{\sum(E_{\mathrm{i}} \cdot A_{\mathrm{i,ef}})} \tag{5.1}$$

where E_{i} is the mean value of the individual component's modulus of elasticity, $A_{\mathrm{i,ef}}$ is its cross-section area of the effective cross-section in fire, and $a_{\mathrm{i,fi}}$ is the distance to its centroid from a selected origin in fire.
The effective bending stiffness of the composite cross-section about the y-axis in fire $(EI)_{\mathrm{ef,fi}}$ is defined by Formula 5.2

$$(EI)_{\mathrm{ef,fi}} = \sum_{i=1}^{n+1}(EI)_{\mathrm{i,fi}} = \sum_{i=1}^{n+1}(\frac{E_{\mathrm{i}} \cdot b_{\mathrm{i,ef}} \cdot h_{\mathrm{i,ef}}^3}{12} + E_{\mathrm{i}} \cdot b_{\mathrm{i,ef}} \cdot h_{\mathrm{i,ef}} \cdot z_{\mathrm{i,fi}}^2) \tag{5.2}$$

where $(EI)_{\mathrm{i,fi}}$ is the individual component's bending stiffness in fire, E_{i} is the mean value of its modulus of elasticity, $b_{\mathrm{i,ef}}$ is its width of the effective cross-section in fire, $h_{\mathrm{i,ef}}$ is its height of the effective cross-section in fire, and $z_{\mathrm{i,fi}}$ is the distance of its centroid to the global centre of gravity in fire $z_{\mathrm{s,fi}}$. The effective width in fire $b_{\mathrm{ef,fi}}$ defines the width of the effective cross-section in fire $b_{\mathrm{i,ef}}$ of n-longitudinal CLT layers ($n = 1$ for top CLT layer, $n = 2$ for second CLT layer etc.). Therefore, it is involved in both the determination of the global centre of gravity in fire $z_{\mathrm{s,fi}}$, and the effective bending stiffness of the composite cross-section in fire $(EI)_{\mathrm{ef,fi}}$. The rib is considered as (n+1)-component.

Effective width in fire

A determination method of an effective width in fire is not included in Eurocode 5 (EN 1995-1-2; prEN 1995-1-2). The effective width in fire $b_{\mathrm{ef,fi}}$ was limited to the rib width of the effective cross-section in fire $b_{\mathrm{rib,ef}}$. Based on the conclusions of the parametric study, simplified design rules are proposed for the effective width in fire $b_{\mathrm{ef,fi}}$. The following approaches for the determination of the effective with in fire $b_{\mathrm{ef,fi}}$ are discussed in this chapter:

- Eurocode 5: $b_{\mathrm{ef,fi}} = b_{\mathrm{rib,ef}}$
- Proposal 1: $b_{\mathrm{ef,fi}} = \begin{cases} b_{\mathrm{ef}}, & \text{for } t_{\mathrm{x}} \geq 40 \text{ mm} \\ b_{\mathrm{ef,fi}} = 0.60 \cdot b_{\mathrm{ef}}, & \text{for } t_{\mathrm{x}} < 40 \text{ mm} \end{cases}$
- Proposal 2: $b_{\mathrm{ef,fi}} = 0.60 \cdot b_{\mathrm{ef}}$

where $b_{\mathrm{rib,ef}}$ is the rib width of the effective cross-section in fire, b_{ef} is the effective width at normal temperature according to prEN 1995-1-1 (section 2.4.2), and t_{x} is the thickness of the

longitudinal CLT layer. The design rules apply for both the effective width in fire at midspan and the effective width in fire at the support.

Resistance moment in fire

The resistance moment in fire $M_{\mathrm{R,fi}}$ is determined according to Formula 5.3

$$M_{\mathrm{R,fi}} = \frac{f_{\mathrm{t,mean}} \cdot (EI)_{\mathrm{ef,fi}}}{E_{\mathrm{i}} \cdot z_{\mathrm{bot,fi}}} \tag{5.3}$$

where $f_{\mathrm{t,mean}}$ is the mean tensile strength of the glulam rib (parallel to the grain) or the bottom CLT plate (in-plane), $(EI)_{\mathrm{ef,fi}}$ is the effective bending stiffness of the composite cross-section about the y-axis in fire, E_{i} is the mean value of the modulus of elasticity of the glulam rib or the bottom CLT plate, and $z_{\mathrm{bot,fi}}$ is the z-coordinate at the bottom edge of the glulam rib or at the bottom edge of the bottom CLT plate of the effective cross-section in fire.

Design resistance moment in fire

The design resistance moment in fire $M_{\mathrm{R,d,fi}}$ is determined according to Formula 5.4

$$M_{\mathrm{R,d,fi}} = \frac{f_{\mathrm{t,d,fi}} \cdot (EI)_{\mathrm{ef,fi}}}{E_{\mathrm{i}} \cdot z_{\mathrm{bot,fi}}} \tag{5.4}$$

where $f_{\mathrm{t,d,fi}}$ is the design tensile strength in fire of the glulam rib (parallel to the grain) or the bottom CLT plate (in-plane) according to Formula 2.63.

Verification of stresses in fire

Based on the loading situation of the fire resistance tests, the design value of the sum of actions in fire $p_{\mathrm{d,fi}}$ confirms with the uniformly distributed load of the fire resistance tests according to Formula 5.5

$$p_{\mathrm{d,fi}} = g_{\mathrm{d,SW}} + \cdot q_{\mathrm{d}} \tag{5.5}$$

where $g_{\mathrm{d,SW}}$ is the design value of the self-weight taken from Table 3.6, and q_{d} is the design value of the uniformly distributed load taken from Table 3.6.

The verification of normal and shear stresses in fire is carried out in accordance with the verification of stresses under normal temperature (section 2.4.3). The calculations are made for an effective cross-section in fire of a T-section. The maximum normal stress at the bottom edge of the glulam rib in fire $\sigma_{\mathrm{rib,d,fi}}(z_{\mathrm{bot,fi}})$ is calculated according to Formula 5.6

$$\sigma_{\mathrm{rib,d,fi}}(z_{\mathrm{bot,fi}}) = \sigma_{\mathrm{N,rib,d,fi}} + \sigma_{\mathrm{M,rib,d,fi}} = \frac{M_{\mathrm{y,d,fi}} \cdot E_{\mathrm{rib}}}{(EI)_{\mathrm{ef,fi}}} \cdot z_{\mathrm{bot,fi}} \tag{5.6}$$

with

$$\sigma_{\mathrm{N,rib,d,fi}} = \frac{M_{\mathrm{y,d,fi}} \cdot E_{\mathrm{rib}}}{(EI)_{\mathrm{ef,fi}}} \cdot z_{\mathrm{rib,fi}} \tag{5.7}$$

$$\sigma_{\mathrm{M,rib,d,fi}} = \frac{M_{\mathrm{y,d,fi}} \cdot E_{\mathrm{rib}}}{(EI)_{\mathrm{ef,fi}}} \cdot \frac{h_{\mathrm{rib,ef}}}{2} \tag{5.8}$$

where $M_{\mathrm{y,d,fi}}$ is the design bending moment about y-direction in fire, $(EI)_{\mathrm{ef,fi}}$ is the effective bending stiffness of the composite cross-section in fire, E_{rib} is the mean value of the rib's modulus of elasticity, $z_{\mathrm{rib,fi}}$ is the distance of its centroid to the global centre of gravity in fire, and $h_{\mathrm{rib,ef}}$ is its height of the effective cross-section in fire.
The expression according to Formula 5.9 shall be satisfied

$$\frac{\sigma_{\mathrm{N,rib,d,fi}}}{f_{\mathrm{t,0,d,fi}}} + \frac{\sigma_{\mathrm{M,rib,d,fi}}}{f_{\mathrm{m,d,fi}}} \leq 1 \tag{5.9}$$

where $f_{\mathrm{t,0,d,fi}}$ is the design tensile strength parallel to the grain of glued-laminated timber in fire according to Formula 2.63, and $f_{\mathrm{m,d,fi}}$ is the design bending strength of glued-laminated timber in fire according to Formula 2.63.

The verification of rolling shear $\tau_{\mathrm{r,d}}(z_{\mathrm{r}})$ should be considered for CLT plates without edge-bonded laminations. The verification of shear in the glue line in fire $\tau_{\mathrm{GL,d,fi}}(z_{\mathrm{GL,fi}})$ is calculated according to Formula 5.10

$$\tau_{\mathrm{GL,d,fi}}(z_{\mathrm{GL,fi}}) = \frac{V_{\mathrm{z,d,fi}} \cdot E_{\mathrm{rib}} \cdot S_{\mathrm{y,fi}}(z_{\mathrm{GL,fi}})}{(EI)_{\mathrm{ef,fi}} \cdot b(z_{\mathrm{GL,fi}})} \tag{5.10}$$

with

$$S_{\mathrm{y,fi}}(z_{\mathrm{GL,fi}}) = b_{\mathrm{rib,ef}} \cdot h_{\mathrm{rib,ef}} \cdot (z_{\mathrm{s,fi}} - h_{\mathrm{rib,ef}}/2) \tag{5.11}$$

$$b(z_{\mathrm{GL,fi}}) = b_{\mathrm{rib,ef}} \tag{5.12}$$

where $V_{\mathrm{z,d,fi}}$ is the design shear force in z-direction in fire, E_{rib} is the rib's modulus of elasticity, $S_{\mathrm{y,fi}}(z_{\mathrm{GL,fi}})$ and $b(z_{\mathrm{GL,fi}})$ are the static moment in fire and the tributary width at the height of the glue line in fire, $(EI)_{\mathrm{ef,fi}}$ is the effective bending stiffness of the composite cross-section at the support in fire, $b_{\mathrm{rib,ef}}$ and $h_{\mathrm{rib,ef}}$ are the rib's width and height of the effective cross-section in fire, and $z_{\mathrm{s,fi}}$ is the centre of gravity of the composite cross-section in fire.
The expression according to Formula 5.13 shall be satisfied

$$\tau_{\mathrm{GL,d,fi}}(z_{\mathrm{GL,fi}}) \leq f_{\mathrm{v,x,d,fi}} \tag{5.13}$$

where $f_{\mathrm{v,x,d,fi}}$ is the design strength for longitudinal shear out-of-plane of cross-laminated timber in fire according to Formula 5.10.
The verification of the maximum shear parallel to the grain in fire $\tau_{\mathrm{COG,d,fi}}(z_{\mathrm{s,fi}})$ can be decisive at the centre of gravity in fire (probably in the glulam rib), calculated according to Formula 5.14

$$\tau_{\mathrm{COG,d,fi}}(z_{\mathrm{s,fi}}) = \frac{V_{\mathrm{z,d,fi}} \cdot E_{\mathrm{rib}} \cdot S_{\mathrm{y,fi}}(z_{\mathrm{s,fi}})}{(EI)_{\mathrm{ef,fi}} \cdot b(z_{\mathrm{s,fi}})} \tag{5.14}$$

with

$$S_{\mathrm{y,fi}}(z_{\mathrm{s,fi}}) = b_{\mathrm{rib,ef}} \cdot z_{\mathrm{s,fi}} \cdot z_{\mathrm{s,fi}}/2 \tag{5.15}$$

$$b(z_{\mathrm{s,fi}}) = b_{\mathrm{rib,ef}} \tag{5.16}$$

where $V_{z,d,fi}$ is the design shear force in z-direction in fire, E_{rib} is the rib's modulus of elasticity, $S_{y,fi}(z_{s,fi})$ and $b(z_{s,fi})$ are the static moment in fire and the tributary width at the centre of gravity in fire, $(EI)_{ef,fi}$ is the effective bending stiffness of the composite cross-section at the support in fire, $b_{rib,ef}$ is the rib's width of the effective cross-section in fire, and $z_{s,fi}$ is the centre of gravity of the composite cross-section in fire.
The expression according to Formula 5.17 shall be satisfied

$$\tau_{COG,d,fi}(z_{s,fi}) \leq f_{v,d,fi} \tag{5.17}$$

where $f_{v,d,fi}$ is the design shear strength of glued-laminated timber in fire according to Formula 5.10.

5.3 Bending resistance in fire

Figure 5.1 presents on the left side the positions of the neutral axis in fire and on the right side the bending resistance in fire per cross-section type. The numerical and experimental results are taken from Figure 4.21. The numerical results for the three cases of the effective width (60%, 80%, and 100% of the CLT width) represent the results of the advanced design method. Furthermore, Figure 5.1 presents the analytical results of the simplified design method, which are calculated based on Formula 5.3. The analytical results depend on the approach for the determination of the effective width in fire $b_{ef,fi}$ (Eurocode 5, proposal 1, and proposal 2). The bending resistance in fire is defined as a fraction of the resistance moment in fire of a specific exposure time and the initial resistance moment at time step $t = 0$ min of the cross-section with 100% CLT width of the advanced design method, or in short $M_{R,fi}(t)/M_{R,fi,100}(t = 0)$. The results are shown until simulation stop and failure time.
The position of the neutral axis moves upwards with an increased exposure time. The results of the simplified design method show a temperature-dependent reduction of the bending resistance in fire with an increased exposure time. The reduction and shape of the curves comply well with the results of the advanced design method. The bending resistance is higher for a cross-section with a larger effective width in fire $b_{ef,fi}$. Cross-sections A and B with a thickness of the CLT layers of 40 mm show different analytical results for proposal 1 or proposal 2. Proposal 1 takes the effective width at normal temperature as effective width in fire $b_{ef,fi} = b_{ef}$. The results agree well with the numerical results using 60% of the CLT width as effective width in fire $b_{ef,fi} = 0.60 \cdot b$, representing the average result for the effective width at normal temperature b_{ef} of the four tested cross-section types. Proposal 2 takes only 60% of the effective width at normal temperature as effective width in fire $b_{ef,fi} = 0.60 \cdot b_{ef}$ and leads to values that are on average 10% lower than for proposal 1. Eurocode 5 limits the effective width in fire to the rib width of the effective cross-section in fire $b_{ef,fi} = b_{rib,ef}$ and leads to values that are on average 30% lower than for proposal 1. The thicknesses of the CLT layers of cross-sections C and D are thinner than 40 mm. Thus, the analytical results for proposal 1 and proposal 2 are identical. Proposal 2 leads to values that are on average 50% lower than for the numerical results using 60% of the CLT width as effective width in fire $b_{ef,fi} = 0.60 \cdot b$. Eurocode 5 leads to values that

Table 5.1. Analytical results of the simplified design method according to prEN 1995-1-2 in comparison to numerical results of the advanced design method based on the revision (until test termination).

Test specimen	Type of cross-section	Simplified design method				Advanced design method			
		$t_{ch,EC5}$	$t_{f,EC5}$	Charring progress	$t_{300°C,est}$	$t_{ch,sim}$	$t_{f,sim} = t_{f,test}$	Charring progress	$t_{300°C,sim}$
		[min]	[min]	in CLT	[min]	[min]	[min]	in CLT	[min]
A	T	Initially unprotected		1st layer	61.5	Initially unprotected		1st layer	62.8
B	T	49	58	1st layer	97.9	53	55	1st layer	111.4
C	Box	Initially unprotected		1st layer	30.8	Initially unprotected		1st layer	28.8
				2nd layer	46.2			2nd layer	53.3
				3rd layer	61.5			3rd layer	66.9
				4th layer	88.5			4th layer	100.1
D	Box-section	24	28	1st layer	53.4	24	30	1st layer	73.7
				2nd layer	68.8			2nd layer	87.2
				3rd layer	95.7			3rd layer	109.8

are on average 70% lower. Again, the differences in bending resistance between the different effective widths are larger for the box-sections than for the T-sections.
Differences between the results of the simplified design method and the advanced design method are influenced by the fall-off times of charred CLT layers $t_{300°C}$, presented in Table 5.1. The results of the simplified design method according to EN 1995-1-2 and prEN 1995-1-2, as explained in section 2.5.3, give estimates on the safe side, showing earlier fall-off times than for the advanced design method. For the initially unprotected cross-sections A and C, the differences are maximum 12 min. Higher discrepancies are shown for the initially protected cross-sections B and D, influenced by the start times of charring t_{ch} and the fall-off times of gypsum plasterboards t_f. Encapsulated phases (no charring) and protected charring phases (decreased charring rate) are defined by the estimated start times of charring $t_{ch,EC5}$ and the estimated fall-off times of gypsum plasterboards $t_{f,EC5}$. The failure times of the fire resistance tests were used as criterion for the fall-off time of gypsum plasterboards in the advanced design method, $t_{f,sim} = t_{f,test}$. As start times of charring $t_{ch,sim}$, the time steps of the numerical models are listed, when the temperatures at the bottom side of the glulam rib or of the bottom CLT plate exceed 300°C. The start times of charring t_{ch} and the fall-off times of gypsum plasterboards t_f are in good agreement. Still, the fall-off times of charred CLT layers show differences of up to 20 min.

5.4 Design bending resistance in fire

Figure 5.2 presents the design values of the bending resistance in fire per cross-section type, which are calculated based on Formula 5.4. The bending resistance in fire is again related to the initial resistance moment at time step $t = 0$ min of the advanced design method based on the cross-section with 100% CLT width $M_{R,d,fi}(t)/M_{R,fi,100}(t = 0)$. The results of the simplified design method are compared with the experimental bending resistance at failure time of the fire resistance tests, taken from Figure 4.21.
For cross-sections A and B, the results are reduced by 16% consistently, using the design tensile strength parallel to the grain $f_{t,0,d,fi}$ instead of the mean tensile strength parallel to the grain

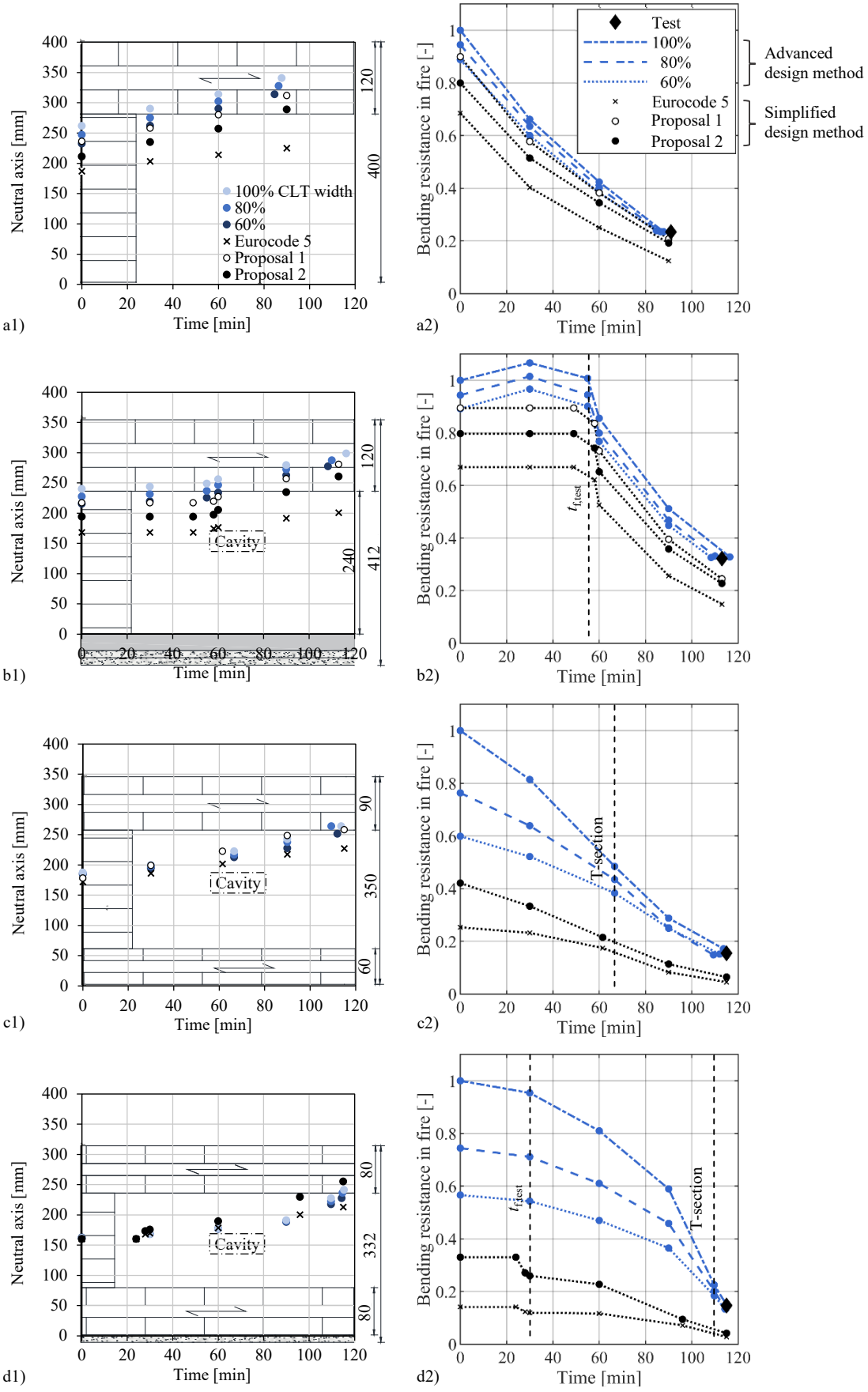

Figure 5.1. Neutral axis and bending resistance in fire per cross-section type for the three cases of the effective width (until simulation stop) in comparison to the experimental and the analytical results (at/until failure time): a) A; b) B; c) C; d) D.

$f_{t,0,mean}$ of the glued-laminated timber. After fall-off of the bottom CLT plate, the same applies for cross-sections C and D. Then, the cross-sections change to a T-section. Up to then, the results are reduced by 32% consistently, using the design tensile strength in-plane $f_{t,x,d,fi}$ instead of the mean tensile strength in-plane $f_{t,x,mean}$ of cross-laminated timber for the bottom CLT plate. When the cross-section is a box-section, the reduction from mean value to design value is twice as high. The determination of the mean strength values was based on the probabilistic models according to the JCSS guidelines (JCSS 2006). For cross-laminated timber, the probabilistic models of structural timber are used to determine the mean strength values, listed in Table 2.2. For glued-laminated timber, the probabilistic models of glued-laminated timber are used to determine the mean strength values listed in Table 2.4. In both cases, the coefficient of variation (CoV) of the tensile strength is 1.2 times the CoV of the bending strength. However, the CoV of the bending strength for structural timber is 0.25, while for glued-laminated timber only 0.15. The larger deviation leads to a smaller characteristic, and thus smaller design value of the tensile strength.
The design values of the bending resistance in fire provide information on when the bending capacity of the cross-section is exceeded for the design in fire according to EN 1995-1-2. In Figure 5.2, the fire exposure times are marked when the design bending resistance in fire coincides with the experimental bending resistance at failure time. For cross-sections A and B, proposal 1 gives good estimates: 78 min and 92 min as estimates for failure times of 91 min and 113 min. The difference to proposal 2 is minor. The results show an improvement compared to Eurocode 5 of up to 20 min. For cross-sections C and D, the underestimation is higher. The estimates are almost half of the failure times: 70 min and 65 min as estimates for failure times of 115 min. Still, the results show an improvement compared to Eurocode 5 of 22 min for cross-section C. For cross-section D, the initial resistance moment at time step $t = 0$ min based on the Eurocode 5 approach is already smaller than the experimental bending resistance at failure time.

5.5 Loadbearing capacity in fire

Table 5.2 compares the degrees of utilisation of the loadbearing capacities in fire between the different approaches for the determination of the effective width in fire $b_{ef,fi}$ (Eurocode 5, proposal 1, and proposal 2). Stresses in fire are compared to mean strength values determined according to JCSS and to design strength values in fire determined according to EN 1995-1-2. Therefore, the loadbearing capacities are calculated for tensile bending at the bottom edge of the glulam rib in fire (Formulae 5.6), for the maximum shear parallel to the grain at the centre of gravity in fire (Formulae 5.17), and shear in the glue line in fire (Formulae 5.13). Design bending moments in fire $M_{d,fi}$ and fire resistance times were taken as the moment out of loading M_{load} and the failure times of the fire resistance tests in Table 3.6. The effective bending stiffness of the composite cross-section $(EI)_{ef}$ are shown for the initial cross-sections according to Formula 2.14.
The tensile bending capacity is decisive for all cross-sections. The degrees of utilisation are greater than 1.0 and show a clear increase using design strength values instead of mean strength values. The results show a decrease in the degree of utilisation when increasing the effective

width in fire $b_{\text{ef,fi}}$. For cross-sections A and B, proposal 1 and proposal 2 lead to improvements by 36% and 32% in comparison to the Eurocode 5 approach. The differences between proposal 1 and proposal 2 are minor. For cross-sections C and D, the improvement is 29%. The degrees of utilisation for the verification of shear stresses in fire are comparable for all approaches and smaller than 1.0 except for cross-section D. The results outline that the effective width in fire $b_{\text{ef,fi}}$ has a low influence on the shear stresses in fire, as discussed for shear stresses at normal temperature in section 3.3.4.

Table 5.2. Degrees of utilisation of the loadbearing capacities in fire of the simplified design method depending on the design approach for the determination of the effective width in fire (decisive failure highlighted in bold letters).

					Eurocode 5			
					Tensile bending (mean)	Tensile bending (design)	Shear in COG (design)	Shear in glue line (design)
Test specimen	Cross-section type	$(EI)_{ef}$	$M_{d,fi} = M_{load}$	Fire resistance time	$\sigma_{N,fi}/f_{t,0,mean} + \sigma_{M,fi}/f_{m,mean}$	$\sigma_{N,d,fi}/f_{t,0,d,fi} + \sigma_{M,d,fi}/f_{m,d,fi}$	$\tau_{COG,d,fi}/f_{v,d,fi}$	$\tau_{GL,d,fi}/f_{v,x,d,fi}$
		[MNm^2]	[kNm]	[min]	[-]	[-]	[-]	[-]
A	T	17.6	44.2	91	1.68	**1.92**	0.71	0.62
B	T	12.1	45.5	113	1.95	**2.24**	0.75	0.68
C	Box	15.6	44.7	115	3.08	**3.53**	0.91	0.82
D	Box	12.1	44.9	115	4.82	**5.53**	1.30	1.20
					Proposal 1			
					1.05	**1.22**	0.66*	0.66
					1.23	**1.44**	0.71*	0.69
					2.21	**2.56**	0.84	0.83
					3.30	**3.83**	1.22*	1.22
					Proposal 2			
					1.13	**1.31**	0.65	0.65
					1.32	**1.53**	0.70*	0.69
					2.21	**2.56**	0.84	0.83
					3.30	**3.83**	1.22*	1.22

* Centre of gravity in the longitudinal CLT layer of the transition zone.

5.6 Conclusions

The developed framework of the simplified design method for modelling cross-laminated timber rib panels in fire is presented, following the principles of Eurocode 5 (EN 1995-1-2; prEN 1995-1-2). The effective cross-section method is applied. Since the composite action is maintained under standard fire exposure, the calculation method of rigidly bonded components (Bernoulli-beam) is applied as in the case under normal temperature. Eurocode 5 limits the effective width in fire to the rib width of the effective cross-section in fire $b_{\text{ef,fi}} = b_{\text{rib,ef}}$. Simplified

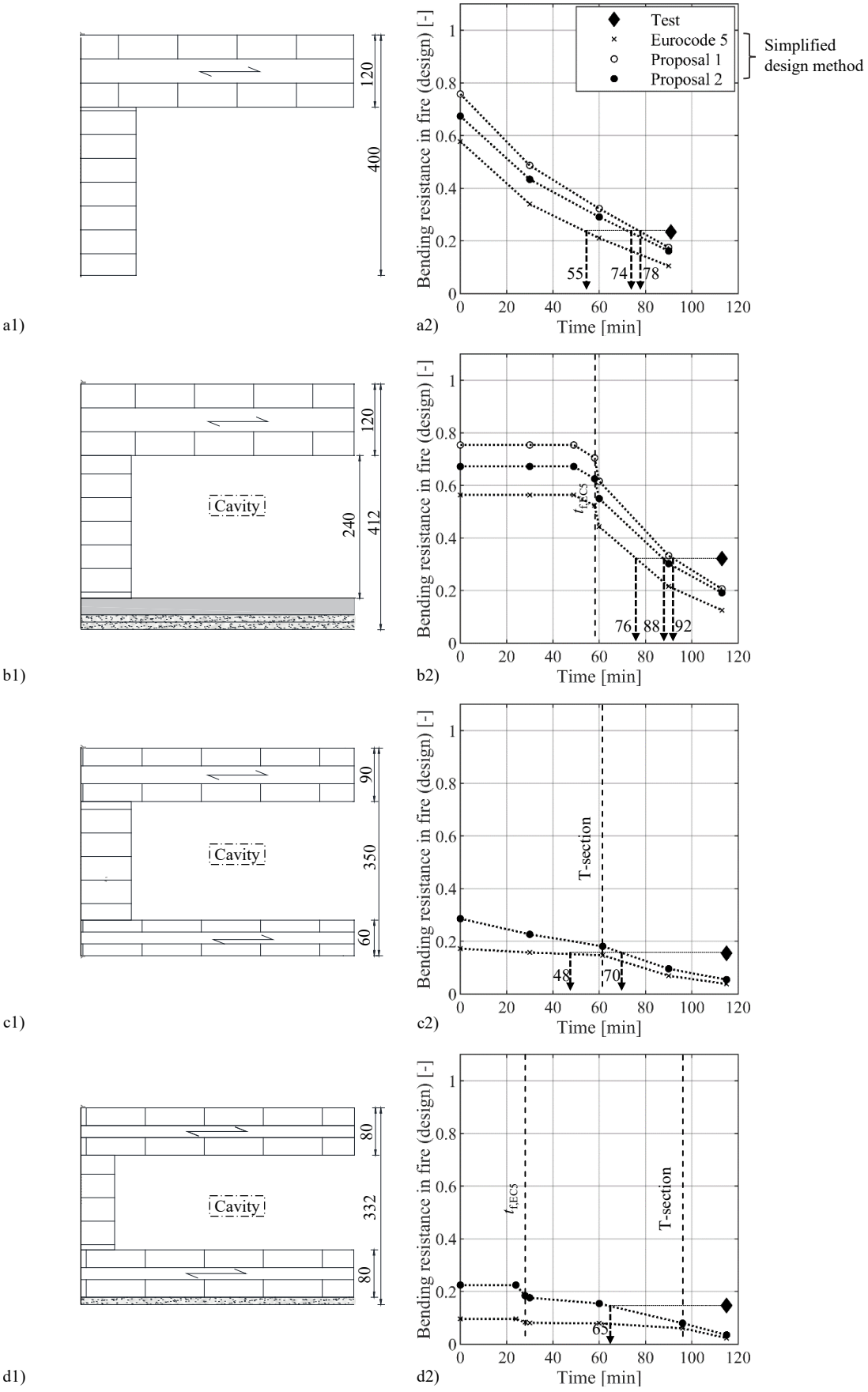

Figure 5.2. Bending resistance in fire based on the design tensile strength per cross-section type of the analytical results in comparison to the experimental results (at/until failure time): a) A; b) B; c) C; d) D.

design rules are proposed as improvements for the determination of the effective width in fire $b_{ef,fi}$ (proposal 1, and proposal 2) based on the effective width at normal temperature b_{ef} according to prEN 1995-1-1. The design rules are applied for both the effective width in fire at midspan and the effective width in fire at the support.

The bending resistance in fire of the four tested cross-sections are calculated based on the current Eurocode 5 approach and the proposed improvements. The shape of the curves and the temperature-dependent reduction with an increased exposure time comply well with the results of the advanced design method. The bending resistance is higher for a cross-section with a larger effective width in fire $b_{ef,fi}$. Fire exposure times are determined when the design bending resistance in fire coincides with the experimental bending resistance at failure time of the fire resistance tests. For T-sections, proposal 2 leads to no or small differences compared to proposal 1. Compared to the Eurocode 5 approach, a clear improvement is noted. For box-sections, the high influence of the effective width in fire $b_{ef,fi}$ leads to higher differences and an underestimation of the fire resistance.

Based on the failure times, the degrees of utilisation of the tensile bending capacity in fire are greater than 1.0. The results show a decrease in the degree of utilisation when increasing the effective width in fire $b_{ef,fi}$. Proposal 1 and proposal 2 lead to clear improvements compared to the Eurocode 5 approach. The differences between proposal 1 and proposal 2 are minor. The degrees of utilisation for the verification of shear stresses in fire emphasize the low influence of the effective width in fire $b_{ef,fi}$ on the shear stresses in fire.

6. Conclusions and outlook

6.1 Conclusions

6.1.1 Experimental investigations

Cross-laminated timber rib panels are floor systems consisting of cross-laminated timber plates rigidly bonded to glued-laminated timber ribs. The composite action is achieved by screw-press gluing using a one-component polyurethane adhesive Purbond HB S709. The structural behaviour, fire behaviour, and fire resistance of cross-laminated timber rib panels were studied. The experimental program considered four cross-section types (2xT-sections, 2xbox-sections) designed for fire resistance times of 60 min and 90 min for a system length of 9 m. Based on the size of the furnace, the cross-sections were tested at a span of 5.2 m.

In the **ultimate-load tests at normal temperature**, the experimental results confirm the rigid composite action between CLT plate and glulam rib and the importance to consider the shear flexibility of the floor system for the design of the composite cross-section. While the experimental effective width $b_{\mathrm{ef,test}}$ is on average 78% of the CLT width, it would be estimated at 60% for the given system based on the effective width b_{ef} according to prEN 1995-1-1. For test specimens tested as T-sections, the experimental loadbearing capacity shows very good agreement with the estimated loadbearing capacity. The experimental and estimated deflections show perfect correlation. For test specimens tested as box-section, the experimental loadbearing capacity is underestimated comparing it to the estimated loadbearing capacity based on prEN 1995-1-1.

The **shear test at normal temperature** of the glue line between CLT plate and glulam rib outline the importance of quality control during the SPG-procedure as a basic requirement for sufficient glue line quality.

The results of **shear tests at elevated temperatures** confirm the temperature-related strength reduction with increasing temperatures. For the glue line, good thermal stability for temperatures up to the ignition temperature of wood is determined. The shear strength of the glue line is above the shear strength of solid timber at least up to 180°C.

The **fire resistance tests** confirm that the effect of the composite action is maintained under standard fire exposure. The fire behaviour of the floor system remained unaffected by both the screws of the SPG-procedure and the glue line. The results show that the test specimens tested as T- and box-section, without and with a fire protection system, reached more than 90 min and even 120 min of fire resistance. The fall-offs of gypsum plasterboards are well predicted based

on the failure times according to prEN 1995-1-2. The fall-off of charred CLT layers confirms that the bond line integrity was not maintained between the face-bonded CLT layers. The simplified bi-linear model including fall-off of single or multiple charred CLT layers according to prEN 1995-1-2 gives conservative estimates of the charred depths of the CLT plates. The simplified approach according to EN 1995-1-2 gives good estimates of the charred depths of the glulam ribs. The structural behaviour was underestimated due to the effect of corner rounding in the corners of the composite section as well as due to the conservative assumption that the effective width is limited to the rib width of the effective cross-section in fire $b_{\mathrm{ef,fi}} = b_{\mathrm{rib,ef}}$.

6.1.2 Numerical investigations

The **modelling assumptions** of the Finite Element (FE) models were derived from the experimental investigations. Temperature-dependent thermal and mechanical properties were implemented according to Eurocode 5 (EN 1995-1-2). The material behaivour was modelled as linear-elastic orthotropic.

Heat transfer analyses were performed modelling the four tested cross-section types. The fall-off behaviour of charred layers was taken into account for the CLT plates but not for the glulam ribs. A new set of thermal properties is implemented for wood after the fall-off of the fire protection system or a charred CLT layer. The validation of the heat transfer models was made against the experimental results of the fire resistance tests, and the experimental results of fire tests collected into a database.

Uncoupled thermo-mechanical simulations were performed using a linear 2D FE beam model. Material strength behaviour was modelled simplified as brittle in tension and in compression. The deflections obtained from the model outline the importance to take into account the shear deflections. To study the influence of the chosen effective width on the resulting deflection, three different approaches were compared for the tested cross-section types: representing the average result for the effective width b_{ef} according to prEN 1995-1-1 (60% of the CLT width), the average result for the effective width of the reference tests $b_{\mathrm{ef,test}}$ (80% of the CLT width), and the extreme case (100% of the CLT width). The differences in the resulting deflections using these three approaches for the effective widths are larger for the box-sections than for the T-sections. However, the differences are small in all cases and therefore it can be concluded that an underestimation of the effective width in fire $b_{\mathrm{ef,fi}}$ still results in good approximations.

A **thermo-mechanical model** determined the neutral axis, and the resistance moment in fire at specific time steps. The numerical results show a temperature-dependent reduction of the resistance moment with an increased exposure time. The resistance moment is higher for a cross-section with a larger effective width. The differences in resistance moment between different effective widths are larger for the box-sections than for the T-sections. The final resistance moments show good agreement with the experimental resistance moments at failure time. This confirms that the test specimens of the fire resistance tests were close to structural failure.

Mechanical simulations were performed using 3D FE models. The FE models were created as a flexible-in-shear multi-layered model resulting in a non-uniform strain distribution along

the CLT width. The validation of the mechanical 3D model was made against the experimental results of the ultimate-load tests at normal temperature.

Uncoupled thermo-mechanical simulations were performed as a basis for the parametric study. The validation was made against the experimental results of one fire resistance test. The results show a temperature-dependent reduction of the numerical effective width in fire $b_{\mathrm{ef,fi,sim}}$ after fall-off of the first charred CLT layer. Until test termination of the fire resistance test, the effective width at normal temperature b_{ef} according to prEN 1995-1-1 gives an approximation of the effective width in fire $b_{\mathrm{ef,fi}}$ on the safe side.

In the **parametric study**, the numerical effective width in fire $b_{\mathrm{ef,fi,sim}}$ was investigated for a parameter range expected in practice. The investigation was limited to cross-sections of a T-section. The effective widths in fire $b_{\mathrm{ef,fi,sim}}$ were determined up to the time step at which the penultimate CLT layer fell off, i.e. one CLT layer was still in place. The values at $t = 0$ min are above the values of the effective widths at normal temperature b_{ef} according to prEN 1995-1-1. The effective widths in fire $b_{\mathrm{ef,fi,sim}}$ show a temperature-dependent reduction with an increased exposure time. A higher number of CLT layers, thicker CLT layers, a thicker CLT plate, and no fall-off of charred CLT layers delay the charring progress and the increasing influence of the shear lag effect. The extreme cases 'thick layers' stay above the values of the effective widths at normal temperature b_{ef}. The extreme cases 'thin layers' undercut the values of the effective widths at normal temperature and require a limit value of 60% of the effective widths at normal temperature: $b_{\mathrm{ef,fi,sim}} \geq 0.60 \cdot b_{\mathrm{ef}}$.

6.1.3 Design of cross-laminated timber rib panels in fire

The developed framework of the simplified design method for modelling cross-laminated timber rib panels in fire uses the terminology of Eurocode 5 (EN 1995-1-2) and the final draft of the Eurocode 5 part 1-2 revision (prEN 1995-1-2). The start time of charring of initially protected cross-sections (with or without insulation material) and the failure time of the fire protection systems should be calculated in accordance with the separating function method. The effective cross-section method is applied. The calculation method of rigidly bonded components (Bernoulli-beam) is applied as in the case under normal temperature.

The Eurocode 5 approach defines the limitation of the effective width in fire to the rib width of the effective cross-section in fire $b_{\mathrm{ef,fi}} = b_{\mathrm{rib,ef}}$. Simplified design rules are proposed as improvements for the determination of the effective width in fire $b_{\mathrm{ef,fi}}$ based on the effective width at normal temperature b_{ef} according to prEN 1995-1-1. Due to the low influence of the effective width in fire $b_{\mathrm{ef,fi}}$ on the shear stresses in fire, the design rules are applied for both the effective width in fire at midspan and the effective width in fire at the support. For thicknesses of CLT layers of 40 mm, proposal 1 takes the effective width at normal temperature as effective width in fire $b_{\mathrm{ef,fi}} = b_{\mathrm{ef}}$. For thicknesses of CLT layers smaller than 40 mm, proposal 1 takes only 60% of the effective width at normal temperature as effective width in fire $b_{\mathrm{ef,fi}} = 0.60 \cdot b_{\mathrm{ef}}$. Proposal 2 does not distinguish between thick and thin layer thicknesses and always takes 60% of the effective width at normal temperature as effective width in fire $b_{\mathrm{ef,fi}} = 0.60 \cdot b_{\mathrm{ef}}$.

The bending resistance in fire of the four tested cross-sections is calculated based on the current

Eurocode 5 approach and the proposed improvements. The results show higher values for a cross-section with a larger effective width in fire $b_{\mathrm{ef,fi}}$. Fire exposure times are determined when the design bending resistance in fire coincides with the experimental bending resistance at failure time of the fire resistance tests. Based on the failure times, the degrees of utilisation of the tensile bending capacity in fire are determined. The results show a decrease in the degree of utilisation when increasing the effective width in fire $b_{\mathrm{ef,fi}}$. For T-sections, differences between proposal 1 and proposal 2 are minor. A clear improvement is noted compared to the Eurocode 5 approach. For box-sections, the high influence of the effective width in fire $b_{\mathrm{ef,fi}}$ leads to a higher underestimation of the fire resistance. In summary, a limit value of 60% of the effective width at normal temperature provides a safe estimate of the effective width in fire: $b_{\mathrm{ef,fi}} \geq 0.60 \cdot b_{\mathrm{ef}}$.

6.2 Outlook

6.2.1 Experimental investigations

The fire behaviour of cross-laminated timber rib panels was investigated without insulation material in the cavities. For the simplified design method, the separating function method is used for the calculation of the start time of charring of initially protected cross-sections and the failure time of the fire protection system. The influence of insulation materials and the size of the cavity on the fire behaviour should be further studied to confidently provide design guidance. In particular, box-sections filled with insulation material in the cavities should be investigated. There, the bottom CLT plate contributes as a solid wood panel.

The fall-off of charred CLT layers might not only depend on the thermal stability of the adhesive (bond line integrity) but also on the clear distance between the ribs. A retention effect is to be expected for small distances, which is of particular interest when multiple fall-offs have to be considered.

The strength properties of the glue line were investigated by small-scale tests at constant elevated temperatures, as being a simple test method for the evaluation of the thermal stability of the adhesive. The difficulty was addressed in how to implement the results from steady-state heating condition to fire tests under fire exposure. Further research is needed to draw conclusions on the correlation of test methods at elevated temperatures to full-scale fire tests.

The fire resistance tests were based on the standard time-temperature curve (ISO 834-1). The standard time-temperature curve represents a normative testing curve used as an international reference system, rather than a real fire. Performance-based design includes the verification of burnout. Further research is needed to investigate the influence of exposed surfaces of ribbed floor systems on the fire dynamics in compartments.

6.2.2 Numerical investigations

The consolidated draft of Eurocode 5 for the informal enquiry (prEN 1995-1-1) contains simplified formulae for the determination of the effective width at normal temperature b_{ef}. The formulae were derived based on FE analyses restricted to a simply supported system under a positive moment and to cross-sections with one CLT plate as top flange. In this thesis,

improvements are proposed for the determination of the effective width in fire $b_{\mathrm{ef,fi}}$ based on a parametric study also restricted to T-sections. The experimental, numerical and analytical investigations conclude that an underestimation of the effective width leads to a more severe underestimation of the structural behaviour for box-sections than for T-sections. For box-sections, the design rules according to prEN 1995-1-1 as well as the proposed design rules in fire are conservative. Further research is needed to optimize the determination of the effective width for box-sections at normal temperature and in fire.
If required in practice, a more pronounced differentiation in fire could be achieved with regard to the thickness of the CLT layers and the thermal stability of the adhesive (bond line integrity). However, the investigations conclude that different effective widths lead to small differences in the results, especially for T-sections.
The effect of elevated temperatures on the mechanical properties of the cross-section's components was taken into account based on the bi-linear temperature dependence of the strength values and the modulus of elasticity according to EN 1995-1-2. The temperature dependence had been proposed for linear timber members exposed to the standard time-temperature curve (König and Walleij 1999; König and Walleij 2000). Further research is needed to confirm the applicability of the model for cross-laminated timber.
The development of thermal and thermo-mechanical models, in which the thermal and mechanical properties are automatically modified based on the average temperature between the CLT layers, would be a significant step forward in the capability to simulate cross-laminated timber rib panels in fire including fall-off of charred CLT layers. The modified thermal and mechanical properties could be implemented by defining field variables, e.g. based on a subroutine in ABAQUS (Jans 2013).

6.2.3 Design of cross-laminated timber rib panels in fire

According to prEN 1995-1-2, the stepwise bi-linear model was used to determine the charred depth d_{char} of a CLT plate, when the glue line integrity was not maintained in fire. The model showed to be a time-consuming design method, when the charred depths d_{char} of a CLT plate are required for different fire exposure times. The implementation of the model in a computer program is highly prone to mistakes, if different CLT layups and thickness of CLT layers need to be taken into account. In practice, a simplified model would make the calculation process more flexible. After the fall-off of the first charred CLT layer, the solution could be to consider one single modified charring rate covering both post-protected charring and consolidated charring, as presented in CEN/TC 250/SC 5/WG4 N197.
The structural behaviour in fire was underestimated due to the effect of corner rounding in the corners of the composite section. An optimization of the residual cross-section could be investigated, e.g by adding a certain proportion of area to the residual cross-section to account for the effect of corner rounding. One way to do that would be to implement the corner rounding model introduced by Fahrni (2021), which considers the corner rounding depending on the effective charred depth d_{ef}.

Nomenclature

Abbreviations

CLT	Cross-laminated timber
CoV	Coefficient of Variation
EPI	Emulsion polymer isocyanate adhesive
FE	Finite Element
GLT	Glued-laminated timber
LVDT	Linear variable differential transformer
max	Maximum value
mc	Moisture content
min	Minimum value
MOE	Modulus of elasticity
MUF	Melamine urea-formaldehyde adhesive
PRF	Phenol-resorcinol-formaldehyde adhesive
PUR	Polyurethane adhesive
RMSE	Root mean square error
SD	Standard deviation
SLS	Serviceability limit state
SPG	Screw-press gluing
TC	Thermocouple
ULS	Ultimate limit state
WFP	Wood failure percentage

Latin upper-case letters

$(EA)_{\mathrm{x}}$	In-plane stiffness of the longitudinal CLT layers per meter width
$(EI)_{\mathrm{ef,fi}}$	Effective bending stiffness of the composite cross-section in fire
$(EI)_{\mathrm{ef,m,g}}$	Global effective bending stiffness according to EN 408

$(EI)_{\mathrm{ef,m,l}}$	Local effective bending stiffness according to EN 408
$(EI)_{\mathrm{ef}}$	Effective bending stiffness
$(EI)_{\mathrm{i,fi}}$	Bending stiffness of component i in fire
$(EI)_{\mathrm{i}}$	Bending stiffness of component i
$(GA)_{\mathrm{ef}}$	Effective shear stiffness out-of-plane of the composite cross-section
$(GA)_{\mathrm{i}}$	Shear stiffness out-of-plane of component i
$(GA)_{\mathrm{xy}}$	Shear stiffness in-plane of the gross cross-section of the CLT plate per meter width
$\sum ES_{\mathrm{y}}(z)$	Sum of the static moment at the coordinate z of the composite cross-section
A	Cross-section area
$A_{\mathrm{i,ef}}$	Cross-section area of component i of the effective cross-section in fire
A_{i}	Cross-section area of component i or area of fibre i
$E_{\mathrm{i},100°\mathrm{C}}$	Temperature-related reduced modulus of elasticity i-direction at 100°C
E_{i}	Modulus of elasticity of component i or in i-direction
$E_{\mathrm{x,i}}$	Modulus of elasticity in x-direction of fibre i
E_{x}	Modulus of elasticity in x-direction
E_{y}	Modulus of elasticity in y-direction
E_{z}	Modulus of elasticity in z-direction
F	Force or load
F_1	10% of estimated maximum load
F_2	40% of estimated maximum load
F_{cyl}	Experimental load of one cylinder
F_{c}	Inner force in compression
F_{i}	Force in fibre i
$F_{\mathrm{max,est}}$	Estimated maximum load
F_{max}	Experimental maximum load (= ultimate load)
F_{t}	Inner force in tension
$F_{\mathrm{x,max,fi}}$	Trapezoidal force at rib centre in fire
$F_{\mathrm{x,max}}$	Trapezoidal force at rib centre
$F_{\mathrm{x,tot,fi}}$	Total force of the CLT plate in fire
$F_{\mathrm{x,tot}}$	Total force of the CLT plate

$G_{\mathrm{ij,100°C}}$	Temperature-related reduced shear modulus in ij-direction at 100°C
G_{ij}	Shear modulus in ij-direction
G_{i}	Shear modulus out-of-plane of component i
G_{r}	Rolling shear modulus of cross-laminated timber
G_{xy}	Shear modulus loaded in-plane in y-direction
G_{xz}	Shear modulus loaded out-of-plane in z-direction
G_{yz}	Shear modulus loaded out-of-plane in z-direction
$M_{\mathrm{R,d,fi}}$	Design value of the resistance moment in fire
$M_{\mathrm{R,fi}}$	Resistance moment in fire
M_{R}	Resistance moment
M_{test}	Moment caused by loading in the fire test
$M_{\mathrm{y,d}}(x)$	Design bending moment about y-direction at the coordinate x
$S_{\mathrm{y,fi}}(z)$	Static moment in fire at the coordinate z
$S_{\mathrm{y}}(z)$	Static moment at the coordinate z
$v_{\mathrm{ij,100°C}}$	Temperature-related reduced poisson's ratio between passive deformation ϵ_{j} and active deformation ϵ_{i} at 100°C
v_{ij}	Poisson's ratio between passive deformation ϵ_{j} and active deformation ϵ_{i}
$V_{\mathrm{z,d}}(x)$	Design shear force in z-direction at the coordinate x

Latin lower-case letters

$\dot{h}_{\mathrm{net,c}}$	Net convective heat flux to the surface of the member in W/m^2 according to EN 1991-1-2
$\dot{h}_{\mathrm{net,r}}$	Net radiative heat flux to the surface of the member in W/m^2 according to EN 1991-1-2
$\dot{h}_{\mathrm{net}}$	Net heat flux to the surface of the member in W/m^2 according to EN 1991-1-2
a	Distance between support and force application according to EN 408
a	Screw spacings
$a_{\mathrm{i,fi}}$	Distance to the centroid of component i from a selected origin in fire
a_{i}	Distance to the centroid of component or fibre i from a selected origin
b	CLT width
$b(z)$	Tributary width at the coordinate z
$b_{\mathrm{ef,fi,sim}}$	Effective width in fire obtained from the simulation (numerical)
$b_{\mathrm{ef,fi}}$	Effective width in fire

$b_{\mathrm{ef,i}}$	Effective width at either side of the rib
$b_{\mathrm{ef,sim}}$	Effective width obtained from the simulation (numerical)
$b_{\mathrm{ef,test}}$	Experimental effective width in fire
b_{ef}	Effective width according to prEN 1995-1-1
$b_{\mathrm{f,i}}$	Clear rib distance
$b_{\mathrm{i,ef}}$	Width of the effective cross-section in fire of component i
b_{i}	Width of component i
b_{l}	Average distance between grooves of the edge bonded laminations
$b_{\mathrm{rib,ef}}$	Rib width of the effective cross-section in fire
$b_{\mathrm{rib,fi}}$	Rib width in fire
b_{rib}	Rib width
c	Specific heat capacity
d_0	Zero-strength layer
$d_{\mathrm{ch,layer,i,sim}}$	Charred depth in CLT layer i of the simulation
d_{ch}	Charred depth
d_{ef}	Effective charred depth
d_{head}	Screw head diameter
$d_{\mathrm{layer,i,sim}}$	Thickness of CLT layer i of the simulation
e_{c}	Distance of the inner force in compression to the neutral axis
e_{t}	Distance of the inner force in tension to the neutral axis
$f_{\mathrm{c,0,d}}$	Design compressive strength parallel to the grain of glued-laminated timber
$f_{\mathrm{c,0,k}}$	Characteristic compressive strength parallel to the grain of glued-laminated timber
$f_{\mathrm{c,0,mean}}$	Mean compressive strength parallel to the grain of glued-laminated timber
$f_{\mathrm{c,x,d}}$	Design compressive strength in-plane of cross-laminated timber
$f_{\mathrm{c,x,k}}$	Characteristic compressive strength in-plane of cross-laminated timber
$f_{\mathrm{c,x,mean}}$	Mean compressive strength in-plane of cross-laminated timber
$f_{\mathrm{d,fi}}$	Design strength value in fire
f_{k}	Characteristic strength value
$f_{\mathrm{m,d,fi}}$	Design tensile bending strength of glued-laminated timber in fire
$f_{\mathrm{m,d}}$	Design bending strength of glued-laminated timber

$f_{m,k}$	Characteristic bending strength of glued-laminated timber
$f_{m,mean}$	Mean bending strength of glued-laminated timber
$f_{m,x,d}$	Design bending strength out-of-plane of cross-laminated timber
$f_{m,x,k}$	Characteristic bending strength out-of-plane of cross-laminated timber
$f_{m,x,mean}$	Mean bending strength out-of-plane of cross-laminated timber
$f_{r,d}$	Design strength for rolling shear out-of-plane of cross-laminated timber
$f_{r,k}$	Characteristic strength for rolling shear out-of-plane of cross-laminated timber
$f_{r,mean}$	Mean strength for rolling shear out-of-plane of cross-laminated timber
$f_{t,0,d,fi}$	Design tensile strength parallel to the grain of glued-laminated timber in fire
$f_{t,0,d}$	Design tensile strength parallel to the grain of glued-laminated timber
$f_{t,0,k}$	Characteristic tensile strength parallel to the grain of glued-laminated timber
$f_{t,0,mean}$	Mean tensile strength parallel to the grain of glued-laminated timber
$f_{t,d,fi}$	Design tensile strength in fire of the glulam rib (parallel to the grain) or the bottom CLT plate (in-plane)
$f_{t,mean}$	Mean tensile strength of the glulam rib (parallel to the grain) or the bottom CLT plate (in-plane)
$f_{t,x,d}$	Design tensile strength in-plane of cross-laminated timber
$f_{t,x,k}$	Characteristic tensile strength in-plane of cross-laminated timber
$f_{t,x,mean}$	Mean tensile strength in-plane of cross-laminated timber
$f_{v,d,fi}$	Design shear strength of glued-laminated timber in fire
$f_{v,d}$	Design shear strength of glued-laminated timber
$f_{v,k}$	Characteristic shear strength of glued-laminated timber
$f_{v,mean}$	Mean shear strength of glued-laminated timber
$f_{v,x,d,fi}$	Design strength for longitudinal shear out-of-plane of cross-laminated timber in fire
$f_{v,x,d}$	Design strength for longitudinal shear out-of-plane of cross-laminated timber
$f_{v,x,k}$	Characteristic strength for longitudinal shear out-of-plane of cross-laminated timber
$f_{v,x,mean}$	Mean strength for longitudinal shear out-of-plane of cross-laminated timber
$g_{d,SW}$	Design value of the self-weight
g_d	Design value of permanent actions
$g_{k,SW}$	Characteristic value of the self-weight

$g_{\mathrm{k,S}}$	Characteristic value of the superimposed action
g_{k}	Characteristic value of permanent actions
h	Total height of cross-section
h_1	Thickness of the single gypsum plasterboard panel
h_2	Thickness of the second gypsum plasterboard panel
$h_{\mathrm{i,ef}}$	Height of the effective cross-section in fire of component i
h_{i}	Height of component i
h_{p}	Thickness of the single panel or the total thickness of multiple panels of the fire protection system
$h_{\mathrm{rib,ef}}$	Rib height of the effective cross-section in fire
h_{rib}	Rib height
$k_{\theta,\mathrm{E}}(\theta_{\mathrm{i}})$	Temperature-dependent reduction factor for the modulus of elasticity depending on the temperature exhibit by fibre i
k_{θ}	Temperature-dependent reduction factor
$k_{\theta,\mathrm{E,c}}$	Temperature-dependent reduction factor for the modulus of elasticity parallel to the grain in compression
$k_{\theta,\mathrm{E,i}}$	Temperature-dependent reduction factor for the modulus of elasticity in i-direction
$k_{\theta,\mathrm{E,t}}$	Temperature-dependent reduction factor for the modulus of elasticity parallel to the grain in tension
$k_{\theta,\mathrm{f,c}}$	Temperature-dependent reduction factor for compressive strength parallel to the grain
$k_{\theta,\mathrm{f,t}}$	Temperature-dependent reduction factor for tensile strength parallel to the grain
$k_{\theta,\mathrm{f,v}}$	Temperature-dependent reduction factor for shear strength
$k_{\theta,\mathrm{G,ij}}$	Temperature-dependent reduction factor for the shear modulus in ij-direction
$k_{\theta,\mathrm{v,ij}}$	Temperature-dependent reduction factor for Poisson's ratio between passive deformation ϵ_{j} and active deformation ϵ_{i}
$k_{100°\mathrm{C,E,c}}$	Temperature-dependent reduction factor at 100°C for the modulus of elasticity parallel to the grain in compression
$k_{100°\mathrm{C,E,i}}$	Temperature-dependent reduction factor at 100°C for the modulus of elasticity in i-direction
$k_{100°\mathrm{C,E,t}}$	Temperature-dependent reduction factor at 100°C for the modulus of elasticity parallel to the grain in tension
$k_{100°\mathrm{C,E,x}}$	Temperature-dependent reduction factor for the modulus of elasticity in x-direction

$k_{100°C,G,ij}$	Temperature-dependent reduction factor at 100°C for the shear modulus in ij-direction
$k_{100°C,v,ij}$	Temperature-dependent reduction factor at 100°C for Poisson's ratio between passive deformation ϵ_j and active deformation ϵ_i
$k_{100°C}$	Temperature-dependent reduction factor at 100°C
$k_{20°C}$	Temperature-dependent reduction factor at 20°C
k_2	Protection factor
$k_{300°C}$	Temperature-dependent reduction factor at 300°C
k_{cr}	Crack factor taking into account the influence of cracks
k_{def}	Deformation factor of timber
k_{fi}	Modification factor for strength and stiffness property for the fire situation
k_h	Depth factor taking into account the effect of member size on bending or tensile strength
$k_{mod,fi}$	Modification factor for fire
k_{mod}	Modification factor taking into account the effect of the duration of load and moisture content
k_n	Conversion factor
k_v	Factor modifying the shear strength for test pieces where the thickness in the grain direction of the sheared area t is less than 50 mm according to EN 14080
l	Span
l_1	Gauge length for the determination of modulus of elasticity or shear modulus
n	Number of CLT layers
$p_{d,fi}$	Design value of the sum of actions in fire
p_d	Design value of the sum of actions
p_k	Characteristic value of the sum of actions
q_d	Design value of a variable action
q_k	Characteristic value of a variable action
q_{pyr}	Endothermic reaction heat during pyrolysis
t	Thickness in the grain direction of the sheared area according to EN 14080
t	Time or time step of simulation
$t_{300°C,layer,i,sim}$	Fall-off time of CLT layer i of the simulation
$t_{300°C,layer,i-1,sim}$	Fall-off time of CLT layer i-1 of the simulation

$t_{300°C}$	Fall-off time of the charred CLT layer defined as the average temperature of 300°C between the CLT layers
t_{ch}	Start time of charring
t_{CL}	Thickness of the CLT plate
$t_{end,sim}$	Duration of simulation
$t_{failure,test}$	Experimental failure time
t_f	Failure time of the fire protection system
t_l	Thickness of the lamination
$t_{prot,0}$	Basic protection time of the fire protection system
$t_{stop,sim}$	Time of simulation stop
t_x	Thickness of the longitudinal CLT layer
t_y	Thickness of the transversal CLT layer
u	Relative slip between CLT plate and glued laminated timber rib
u_L	Relative slip between CLT plate and glued laminated timber rib at the left support
u_R	Relative slip between CLT plate and glued laminated timber rib at the right support
v_{xy}	Poisson's ratio between passive deformation ϵ_y and active deformation ϵ_x
v_{xz}	Poisson's ratio between passive deformation ϵ_z and active deformation ϵ_x
v_{yz}	Poisson's ratio between passive deformation ϵ_z and active deformation ϵ_y
w	Deflection at midspan
w_{loc}	Local deflection at the centre of the gauge length l_1
w_{mean}	Deflection at midspan as mean value
w_m	Bending deflection
w_v	Shear deflection
x	Coordinate parallel to the system's axis
y	Coordinate perpendicular to the system's axis and the cross-section's axis
z	Coordinate perpendicular to the system's axis, parallel to the cross-section's axis
$z_{i,fi}$	Distance of the centroid of component i to the centre of gravity of the effective cross-section in fire
z_i	Distance of the centroid of component or fibre i to the centre of gravity of the composite cross-section

$z_{\mathrm{s,est}}$	Centre of gravity of the estimated system
$z_{\mathrm{s,fi}}$	Centre of gravity in fire of the effective cross-section in fire
$z_{\mathrm{s,max}}$	Centre of gravity of the maximum system
z_{s}	Centre of gravity of the composite cross-section
$z_{\mathrm{t,max}}$	Distance of the centroid of the fibre exhibiting the highest tensile strain to the centre of gravity in fire
c_θ	Temperature-dependent specific heat capacity of the solid material

Greek upper-case letters

Φ	Configuration factor of the exposed surface

Greek lower-case letters

β	Charring rate
β_{CLT}	Charring rate of the CLT plates
$\beta_{\mathrm{layer,i,sim}}$	Charring rate of CLT layer i of the simulation
β_{layer}	Charring rate per CLT layer
$\epsilon_{\mathrm{t,max}}$	Highest tensile strain of the bending resistance
$\epsilon_{\mathrm{x,i}}$	Strain in longitudinal direction of fibre i
$\int \sigma_{\mathrm{x}}(y,z)\,dy\,dz$	Integral of all bending stresses along the thickness t_{CL} and along the width b of the CLT plate
κ	Shear correction factor
$\kappa_{\mathrm{m,max}}$	Bending curvature of the bending resistance
κ_{m}	Bending curvature
λ	Thermal conductivity of the solid material
λ_θ	Temperature-dependent thermal conductivity of the solid material
λ_{x}	Thermal conductivity of the solid material in x-direction
λ_{y}	Thermal conductivity of the solid material in y-direction
λ_{z}	Thermal conductivity of the solid material in z-direction
ρ	Density
$\sigma_{\mathrm{x,fi,i}}$	Stress in longitudinal or x-direction of fibre i in fire
$\sigma_{\mathrm{x,i}}$	Stress in x-direction of fibre i
ε	Strain
α_{c}	Coefficient of heat transfer by convection

β_0	Basic charring rate
β_n	Notional charring rate
ϵ_f	Emissivity of the fire
ϵ_m	Surface emissivity of the member
γ_g	Partial factor for permanent actions
$\gamma_\mathrm{M,fi}$	Partial factor for the fire situation
γ_M	Partial factor for a material property
γ_q	Partial factor for variable actions
ψ_1	Factor for frequent value of a variable action
ρ_θ	Temperature-dependent thermal density of the solid material
$\rho_{20°\mathrm{C}}$	Density at normal temperature of the solid material
ρ_dry	Dry density of the solid material
$\sigma_\mathrm{i,d,fi}(z)$	Design normal stress of component i at the coordinate z in fire
$\sigma_\mathrm{i,d}(x,z)$	Design normal stress of component i at the coordinates x and z
$\sigma_\mathrm{i,d}(z)$	Design normal stress of component i at the coordinate z
$\sigma_\mathrm{i}(z)$	Normal stress of component i at the coordinate z
$\sigma_\mathrm{M,i,d,fi}$	Design normal stress part due to internal bending moment of component i at the coordinate z in fire
$\sigma_\mathrm{M,i,d}$	Design normal stress part due to internal bending moment of component i at the coordinate z
$\sigma_\mathrm{M,i}$	Normal stress part due to internal bending moment of component i at the coordinate z
$\sigma_\mathrm{N,i,d,fi}$	Design normal stress part due to internal normal force of component i at the coordinate z in fire
$\sigma_\mathrm{N,i,d}$	Design normal stress part due to internal normal force of component i at the coordinate z
$\sigma_\mathrm{N,i}$	Normal stress part due to internal normal force of component i at the coordinate z
σ_SB	Stephan Boltzmann constant taken as $5,67 \cdot 10^{-8}\mathrm{W}/(\mathrm{m}^2\mathrm{K}^4)$
$\sigma_\mathrm{x,max}(y,z)$	Maximum bending stress distribution along the thickness of the CLT plate t_CL at rib centre
$\tau_\mathrm{i,d,fi}(z)$	Design shear stress of component i at the coordinate z in fire
$\tau_\mathrm{i,d}(x,z)$	Design shear stress of component i at the coordinates x and z
$\tau_\mathrm{i,d}(z)$	Design shear stress of component i at the coordinate z

$\tau_{\mathrm{i}}(z)$	Shear stress of component i at the coordinate z
θ_{g}	Gas temperature
θ_{m}	Surface temperature
θ_{r}	Effective radiation temperature of the fire environment ($\theta_{\mathrm{r}} = \theta_{\mathrm{g}}$ for fully engulfed members)

Indices

1	Component 'top CLT layer in longitudinal direction'
100	Cross-section of the FE model with an effective width of 100% CLT width
2	Component 'second CLT layer in longitudinal direction'
60	Cross-section of the FE model with an effective width of 60% CLT width
80	Cross-section of the FE model with an effective width of 80% CLT width
bot	At the bottom edge of the glulam rib or at the bottom edge of the bottom CLT plate
c	Compression
COG	Centre of gravity
d	Design value
EC5	Based on Eurocode 5
ef	Effective
est	Estimated
fi	Fire
GL	Glue line
i	Component or fibre i
k	Characteristic value
layer	CLT layer
m	Bending
max	Maximum
mean	Mean value
min	Minimum
r	Rolling shear
rev	Based on the revision of this thesis
rib	Component 'rib'

sim	Obtained form numerical simulation
t	Tension
test	Experimental
top	At the top edge of the CLT plate
tot	Total

Bibliography

Ahn, I.-S. et al. (2004). "Effective flange width provisions for composite steel bridges". In: *Engineering Structures* 26.12, pp. 1843–1851. ISSN: 01410296. DOI: 10.1016/j.engstruct.2004.07.009.

Altenbach, H., J. Altenbach, and R. Rikards (1996). *Einführung in die Mechanik der Laminat- und Sandwichtragwerke: Modellierung und Berechnung von Balken und Platten aus Verbundwerkstoffen; 47 Tabellen*. Stuttgart, Germany: Dt. Verl. für Grundstoffindustrie. ISBN: 3-342-00681-1.

ANSI/APA PRG 320 (2018). *Standard for performance-rated cross-laminated timber*.

ASTM D7247 (2017). *Test method for evaluating the shear strength of adhesive bonds in laminated wood products at elevated temperatures*. DOI: 10.1520/D7247-17.

Augustin, M. and A. Thiel (2017). *Proposal for the determination of the effective width and the verification of ribbed plates*. Research Report hbf 02_2017.

Blomgren, H.-E. et al. (2021). "Development, testing and application of mass timber composite rib floor panels for office buildings". In: *World Conference on Timber Engineering (WCTE) - 11th World Conference on Timber Engineering*. Santiago, Chile, p. 9.

Bodig, J. and B. Jayne (1993). *Mechanics of wood and wood composites*. Reprint ed. Krieger Publishing Company. ISBN: 0-89464-777-6.

Bogensperger, T. (2013). *Darstellung und praxistaugliche Aufbereitung für die Ermittlung mitwirkender Plattenbreiten von BSP-Elementen*. Research Report focus_sts 2.2.3_1.

Bogensperger, T., G. Silly, and G. Schickhofer (2012). *Comparison of methods of approximate verification - Procedures for cross laminated timber*. Graz, Austria.

Brandner, R. et al. (2015). "Scheibenschub von Brettsperrholz - Verifizierung einer Prüfkonfiguration und Parameterstudie". In: *Bautechnik* 92.11, pp. 759–769. ISSN: 09328351.

Brandner, R. et al. (2016). "Cross laminated timber (CLT): Overview and development". In: *European Journal of Wood and Wood Products* 74.3, pp. 331–351. ISSN: 0018-3768. DOI: 10.1007/s00107-015-0999-5.

Brandon, D. and C. Dagenais (2018). *Fire safety challenges of tall wood buildings – Phase 2: Task 5 – Experimental study of delamination of cross laminated timber (CLT) in fire*. Quincy, USA.

Bratulic, K. and M. Augustin (2016). "Screw gluing - Theoretical and experimental study on screw pressure distribution and glue line strength". In: *World Conference on Timber Engineering (WCTE) – Proceedings of the 9th Meeting*. Vienna, Austria.

Bratulic, K., M. Augustin, and G. Schickhofer (2019). "Investigations concerning screw-press gluing of assemblies with CLT". In: *International Network on Timber Engineering Research (INTER) – Proceedings of the 6th Meeting*. Tacoma, Washington.

Brogli, J. (2019). "CLT Rib Panels - Tragverhalten unter Normaltemperatur". Master project thesis. ETH Zürich.

Bühlmann, A. (2014). "Brandverhalten von stirnseitig verklebten Brettsperrholzplatten". Master thesis. ETH Zürich.

CEN/TC 250/SC 5/WG4 N197 (2022). *Meeting Online 2021-09-13 Other Slides*. Tech. rep. Brussels: CEN - CENELEC.

Chen, S. S. et al. (2007). "Proposed effective width criteria for composite bridge girders". In: *Journal of Bridge Engineering* 12.3, pp. 325–338. ISSN: 1084-0702, 1943-5592. DOI: 10.1061/(ASCE)1084-0702(2007)12:3(325).

Chen, Y. and F. Lam (2013). "Bending performance of box-based cross-laminated timber systems". In: *Journal of Structural Engineering* 139.12, p. 04013006. ISSN: 0733-9445, 1943-541X. DOI: 10.1061/(ASCE)ST.1943-541X.0000786.

Chen, Z. et al. (2020). "A temperature-dependent plastic-damage constitutive model used for numerical simulation of wood-based materials and connections". In: *Journal of Structural Engineering* 146.3, p. 04019225. ISSN: 0733-9445, 1943-541X. DOI: 10.1061/(ASCE)ST.1943-541X.0002524.

Chiewanichakorn, M. et al. (2004). "Effective flange width definition for steel–concrete composite bridge girder". In: *Journal of Structural Engineering* 130.12, pp. 2016–2031. ISSN: 0733-9445, 1943-541X. DOI: 10.1061/(ASCE)0733-9445(2004)130:12(2016).

Chwalla, E. (1936). "Die Formeln zur Berechnung der voll mittragenden Breite dünner Gurt- und Rippenplatten". In: *Bautechnik* 10, pp. 73–78. ISSN: 09328351.

Clauss, S. (2011). "Structure-property relationships of one-component moisture-curing polyurethane adhesives under thermal load". ETH Zurich. DOI: 10.3929/ETHZ-A-007142066.

Dagenais, C. et al. (2021). "Improved fire performance of cross-laminated timber". In: *World Conference on Timber Engineering (WCTE) - 11th World Conference on Timber Engineering*. Santiago, Chile, p. 10.

Dassault Systemes (2013). *Abaqus FEA (version 6.13-2) [computer program]*. Dassault Systemes.

Davalos, J. F. and H. A. Salim (1993). "Effective flange width for stress–laminated T–system timber bridges". In: *Journal of Structural Engineering* 119.3, pp. 938–953. DOI: 10.1061/(ASCE)0733-9445(1993)119:3(938).

Dias, A., J. Schänzlin, and P. Dietsch (2018). *Design of timber-concrete composite structures - A State-of-the-Art report by COST Action FP1402 / WG 4*. Shaker Verlag GmbH. ISBN: 978-3-8440-6145-1.

Dietsch, P. et al. (2018). "Eurocode 5:2022 - Einführung in die neuen Abschnitte Brettsperrholz Und Verstärkungen". In: *Karlsruher Tage 2018 – Holzbau – Forschung für die Praxis*. Karlsruhe, Germany: KIT Scientific Publishing. ISBN: 978-3-7315-0827-4.

Drysdale, D. (2011). *An introduction to fire dynamics*. 3rd ed. Chichester West Sussex: Wiley. ISBN: 978-0-470-31903-1.

Ebner, G. (2018). "Rippen, die den Holzbau schlank halten, BSP-Werk in Schweden im Testbetrieb - Neuheit: Rippen-Elemente". In: *Holzkurier* BSP Special.11.

Ehrenberg, C. von (2020). "CLT Rib Panels - Simulation der Tragfähigkeit im Brandfall". Master thesis. ETH Zürich.

Ehrhart, T. et al. (2015). "Rolling shear properties of some European timber species with focus on cross laminated timber (CLT): Test configuration and parameter study". In: *International Network on Timber Engineering Research (INTER) – Proceedings of the 2nd Meeting*. Šibenik, Croatia. DOI: 10.3929/ETHZ-A-010548168.

EN 1363-1 (2012). *Fire resistance tests - Part 1: General requirements*. Brussels.

— (2020). *Fire resistance tests - Part 1: General requirements*. Brussels.

EN 1365-2 (2014). *Fire resistance tests for loadbearing elements - Part 2: Floors and roofs*. Brussels.

EN 14080 (2013). *Timber structures – Glued laminated timber and solid timber – Requirements*. Brussels.

EN 15425 (2017). *Adhesives – One component polyurethane (PUR) for load-bearing timber structures – Classification and performance requirements*. Brussels.

EN 16351 (2021). *Timber structures – Cross laminated timber – Requirements*. Brussels.

EN 17224 (2019). *Determination of compressive shear strength of wood adhesives at elevated temperatures*. Brussels.

EN 1990 (2002). *EN 1990:2002/A1:2005/AC:2010, Eurocode - Basis of structural design*. Brussels.

EN 1991-1-2 (2002). *EN 1991-1-2:2002, Eurocode 1: Actions on structures – Part 1-2: General actions – Actions on structures exposed to fire*. Brussels.

EN 1992-1-1 (2004). *EN 1992-1-1:2004/AC:2010, Eurocode 2: Design of concrete structures - Part 1-1: General rules and rules for buildings*. Brussels.

EN 1993-1-5 (2006). *EN 1993-1-5:2006/AC:2009, Eurocode 3: Design of steel structures - Part 1-5: Plated structural elements*. Brussels.

EN 1994-1-1 (2004). *EN 1994-1-1:2004/AC:2009, Eurocode 4: Design of composite steel and concrete structures - Part 1-1: General rules and rules for buildings*. Brussels.

EN 1995-1-1 (2004). *EN 1995-1-1:2004/AC:2006/A1:2008/A2:2014, Eurocode 5: Design of timber structures – Part 1-1: General – Common rules and rules for buildings*. Brussels.

EN 1995-1-2 (2004). *EN 1995-1-2:2004/AC:2006/AC:2009, Eurocode 5: Design of timber structures – Part 1-2: General – Structural fire design*. Brussels.

EN 338 (2003). *Structural timber – Strength classes*. Brussels.

EN 408 (2012). *Timber structures - Structural timber and glued laminated timber - Determination of some physical and mechanical properties*. Brussels.

EN 520 (2009). *Gypsum plasterboards – Definitions, requirements and test methods*. Brussels.

ENV 1995-1-2 (1997). *EN 1995-1-2:1997, Eurocode 5: Design of timber structures – Part 1-2: General rules – Structural fire design*. Brussels.

ETA-11/0190 (2018). *Würth self-tapping screws - Self-tapping screws for use in timber constructions*.

ETA-14/0349 (2019). *CLT – Cross Laminated Timber by Stora Enso'*.

ETA-17/0911 (2018). *CLT Rib Panels by Stora Enso - Prefabricated wood-based loadbearing stressed skin panels'*.

ETA-20/0893 (2020). *Stora Enso CLT Rib Panels - Prefabricated wood-based loadbearing stressed skin panels'*.

Eurofins Expert Services Oy (2019a). *Test Report EUFI29-19002767: Fire resistance test on a wooden floor construction made of CLT ribbed slabs*.

— (2019b). *Test Report EUFI29-19002768: Fire resistance test on a wooden floor construction made of CLT ribbed slabs*.

— (2019c). *Test Report EUFI29-19002770: Fire resistance test on a wooden floor construction made of CLT ribbed slabs*.

— (2019d). *Test Report EUFI29-19002771: Fire resistance test on a wooden floor construction made of CLT ribbed slabs*.

Fahrni, R. (2021). "Reliability-based code calibration for timber in fire". Doctoral thesis. ETH Zürich.

Fahrni, R., M. Klippel, and A. Frangi (2021). *Fire safety of cross-laminated timber*.

Fahrni, R. et al. (2018). "Correct temperature measurements in fire exposed wood". In: *World Conference on Timber Engineering (WCTE) – Proceedings of the 10th Meeting*. Seoul, South Korea.

FSITB (2010). *Fire Safety in Timber Buildings. Technical Guideline for Europe*. SP Report 2010:19. SP Technical Research Institute of Sweden. ISBN: 978-91-86319-60-1.

Fischer, J. (2019). "CLT Rib Panels - Thermal and mechanical simulation of a T-cross-section". Master thesis. ETH Zürich.

Frangi, A. (2001). "Brandverhalten von Holz-Beton-Verbunddecken". Doctoral thesis. ETH Zürich. DOI: 10.3929/ETHZ-A-004228944.

Frangi, A. and M. Fontana (2000). *Versuche zum Tragverhalten von Holz-Beton- Verbunddecken bei Raumtemperatur und Normbrandbedingungen.*

Frangi, A., M. Fontana, and A. Mischler (2004). "Shear behaviour of bond lines in glued laminated timber beams at high temperatures". In: *Wood Science and Technology* 38.2, pp. 119–126. DOI: 10.1007/s00226-004-0223-y.

Frangi, A. et al. (2008). "Fire behaviour of cross-laminated solid timber panels". In: *Fire Safety Science* 9, pp. 1279–1290. ISSN: 18174299. DOI: 10.3801/IAFSS.FSS.9-1279.

Frangi, A. et al. (2009). "Experimental analysis of cross-laminated timber panels in fire". In: *Fire Safety Journal* 44.8, pp. 1078–1087. ISSN: 03797112. DOI: 10.1016/j.firesaf.2009.07.007.

Frangi, A. et al. (2012). "Mechanical behaviour of finger joints at elevated temperatures". In: *Wood Science and Technology* 46.5, pp. 793–812. ISSN: 0043-7719, 1432-5225. DOI: 10.1007/s00226-011-0444-9.

Franssen, J.-M. and T. Gernay (2017). "Modeling structures in fire with SAFIR: Theoretical background and capabilities". In: *Journal of Structural Fire Engineering* 8.3, pp. 300–323. ISSN: 2040-2317. DOI: 10.1108/JSFE-07-2016-0010.

Fredlund, B. (1988). "A model for heat and mass transfer in timber structures during fire - A theoretical, numerical and experimental study." Doctoral thesis. Lund, Sweden: Lund University.

Garcia-Castillo, E., I. Paya-Zaforteza, and A. Hospitaler (2021). "Analysis of the fire resistance of timber jack arch flooring systems used in historical buildings". In: *Engineering Structures* 243, p. 112679. ISSN: 01410296. DOI: 10.1016/j.engstruct.2021.112679.

Gaspar, F., H. Cruz, and A. Gomes (2018). "Evaluation of glue Line shear strength of laminated timber structures using block and core type specimens". In: *European Journal of Wood and Wood Products* 76.2, pp. 413–425. DOI: 10.1007/s00107-017-1217-4.

Gerhards, C.C. (1982). "Effect of moisture content and temperature on the mechanical properties of wood: An analysis of immediate effects". In: *Wood and Fiber* 14, p. 34.

Gilun, A. and J. Meronk (2006). "Stress-laminated timber T-beam and Box-beam bridges". Master thesis. Chalmers University of Technology.

Girkmann, K. (1963). *Flächentragwerke - Einführung in die Elastostatik der Scheiben, Platten, Schalen und Faltwerke.* 6th ed. Springer Vienna. ISBN: 978-3-7091-8097-6. DOI: 10.1007/978-3-7091-8096-9.

Glos, P. and D. Henrici (1990). *Festigkeit von Bauholz bei hohen Temperaturen.* 87505, p. 83.

Gu, M. (2017). "Strength and serviceability performances of southern yellow pine cross-laminated timber (CLT) and CLT-glulam composite beam". Doctoral thesis. Clemson University.

Gundelwein, H., M. Grosse, and K. Rautenstrauch (2002). "Ein Beitrag zur Bemessung von Rippenplatten aus MERK-Dickholz". In: *Bautechnik* 79.11, pp. 737–743. ISSN: 09328351. DOI: 10.1002/bate.200205320.

Hodel, P. (2021). "CLT Rib Panels - Simulation der Tragfähigkeit im Brandfall". Master thesis. ETH Zürich.

Hofmann, V. (2022). "Analyse der raumabschließenden Funktion von Holztafelelementen mit biogenen Dämmstoffen mittels additiven Verfahrens unter Herleitung temperaturabhängiger Materialkennwerte". Doctoral thesis. Technical University Munich.

ISO 834-1 (1999). *Fire-resistance tests – Elements of building construction – Part 1: General requirements*.

Jacquier, N. (2015). *Bending tests on glulam-CLT beams connected with double-sided punched metal plate fasteners and inclined screws*. ISBN: 978-91-7583-212-8.

Jacquier, N and U.A. Girhammar (2015). "Evaluation of bending tests on composite glulam–CLT beams connected with double-sided punched metal plates and inclined screws". In: *Construction and Building Materials* 95, pp. 762–773. ISSN: 09500618. DOI: 10.1016/j.conbuildmat.2015.07.137.

Jans, N. (2013). "Modellierung der Abbrandrate von Holzbauteilen unter Naturbrandbedingungen". Master thesis. ETH Zürich.

Janssens, M. (1994). "Thermo-physical properties for wood pyrolysis models". In: *Pacific Timber Engineering Conference*. Vol. 1994. Gold Coast, Australia.

JCSS (2006). "Part III: Resistance models. Properties of timber". In: *JCSS Probabilistic Model Code*. Joint Committee on Structural Safety, p. 16. ISBN: 978-3-909386-79-6.

Kairi, M. et al. (1999). *Screw gluing KERTO-LVL structures with polyurethane*. Ed. by Helsinki University of Technology, Laboratory of Wood Technology. Espoo, Finland.

Kipfer, J. (2020). "CLT Rib Panels - Thermal simulation of two case studies". Master thesis. ETH Zürich.

Kleinhenz, M., A. Just, and A. Frangi (2021a). "Experimental analysis of cross-laminated timber rib panels at normal temperature and in fire". In: *Engineering Structures* 246, p. 113091. ISSN: 01410296. DOI: 10.1016/j.engstruct.2021.113091.

— (2021b). "Temperature-dependent thermal properties for cross-laminated timber exposed to standard fire". In: *International Network on Timber Engineering Research (INTER) – Proceedings of the 6th Meeting*. Online.

Kleinhenz, M. et al. (2021). "The composite action of cross-laminated timber rib panels at elevated temperatures". In: *AOSFST 2021 – 12th Asia-Oceania Symposium on Fire Science and Technology*. Brisbane, Australia: The University of Queensland.

Klippel, M. (2014). "Fire safety of bonded structural timber elements". Doctoral thesis. ETH Zürich. DOI: 10.3929/ETHZ-A-010171655.

Klippel, M. and J. Schmid (2017). "Design of cross-laminated timber in fire". In: *Structural Engineering International* 27.2, pp. 224–230. DOI: 10.2749/101686617X14881932436096.

Kumpenza, C. et al. (2018). "Measuring Poisson's ratio: Mechanical characterization of spruce wood by means of non-contact optical gauging techniques". In: *Wood Science and Technology* 52.6, pp. 1451–1471. ISSN: 1432-5225. DOI: 10.1007/s00226-018-1045-7.

Källsner, B. and J. König (2000). "Thermal and mechanical properties of timber and some other materials used in light timber frame construction". In: *CIB W18 Timber Structures - Meeting 33*. Delft, Netherlands, pp. 33–16–3.

König, J. (2005). "Structural fire design according to Eurocode 5 – design rules and their background". In: *Fire and Materials* 29.3, 147–163. DOI: 10.1002/fam.873.

König, J. and L. Walleij (1999). *One-dimensional charring of timber exposed to standard and parametric fires in initially unprotected and post-protected situations*. Rapport I 9908029.

— (2000). *Timber frame assemblies exposed to standard and parametric fires - Part 2: A Design model for standard fire exposure*. Rapport I 0001001.

Lamberti, M. (2019). "CLT Rib Panels - Parameterstudie zum Tragverhalten unter Normaltemperatur". Master project thesis. ETH Zürich.

Masoudnia, R., A. Hashemi, and P. Quenneville (2017). "Effective flange width of a CLT slab in timber composite beams". In: *International Network on Timber Engineering Research (INTER) – Proceedings of the 4th Meeting*. Kyoto, Japan.

— (2018). "Predicting the effective flange width of a CLT slab in timber composite beams". In: *Journal of Structural Engineering* 144.7, p. 04018084. ISSN: 0733-9445, 1943-541X. DOI: 10.1061/(ASCE)ST.1943-541X.0001979.

McNamee, R. et al. (2021). "Enclosure fire dynamics with a cross-laminated timber ceiling". In: *Fire and Materials* 45.7, pp. 847–857. ISSN: 0308-0501, 1099-1018. DOI: 10.1002/fam.2904.

Mehaffey, J. R., P. Cuerrier, and G. Carisse (1994). "A model for predicting heat transfer through gypsum-board/wood-stud walls exposed to fire". In: *Fire and Materials* 18.5, pp. 297–305. ISSN: 0308-0501. DOI: 10.1002/fam.810180505.

Mestek, P. (2011). "Punktgestützte Flächentragwerke aus Brettsperrholz (BSP) - Schubbemessung unter Berücksichtigung von Schubverstärkungen". Doctoral thesis. Technical University Munich.

Mindeguia, J.-C. et al. (2020). "Thermo-mechanical behaviour of cross-laminated timber slabs under standard and natural fires". In: *Fire and Materials*, fam.2938. ISSN: 0308-0501, 1099-1018. DOI: 10.1002/fam.2938.

Mäger, K.N. et al. (2021). "Influence of adhesives on fire resistance of wooden I-joists". In: *World Conference on Timber Engineering (WCTE) - 11th World Conference on Timber Engineering*. Santiago, Chile, p. 8.

Neuhaus, F.-H. (1981). *Elastizitätszahlen von Fichtenholz in Abhängigkeit von der Holzfeuchtigkeit*. Ed. by Institut für konstruktiven Ingenieurbau. Vol. Mitteilung Nr. 81-8. Technisch-Wissenschaftliche Mitteilungen. Bochum, Germany: Ruhr-Universität Bochum.

Palma, P. (2016). "Fire behaviour of timber connections". Doctoral thesis. ETH Zürich. DOI: 10.3929/ETHZ-A-010836621.

prEN 1363-1 (2018). *Fire resistance tests - Part 1: General requirements*. Tech. rep. Brussels: European Committee for Standardization (CEN).

prEN 16351 (2018). *Timber structures – Cross laminated timber – Requirements*. Tech. rep. Brussels: European Committee for Standardization (CEN).

prEN 1995-1-1 (2021). *CEN/TC 250/SC 5 N1489 - Consolidated draft prEN 1995-1-1 for informal enquiry*. Tech. rep. Brussels: CEN - CENELEC.

prEN 1995-1-1 first draft (2016). *CEN/TC 250/SC 5 N571 - Working draft of design of CLT in a revised Eurocode 5-1-1*. Tech. rep. Brussels: CEN - CENELEC.

prEN 1995-1-2 (2021). *CEN/TC 250/SC 5/WG 4 N193 - Consolidated draft prEN 1995-1-2 for informal enquiry*. Tech. rep. Brussels: CEN - CENELEC.

Python Software Foundation (2015). *Python (version 2.7.11) [programming language]*. Python Software Foundation. URL: https://www.python.org/.

RISE Fire Research (2022). *FIRENWOOD. Model scale charring tests of CLT (to be published)*.

Roberts, A.F. (1970). "A review of kinetics data for the pyrolysis of wood and related substances". In: *Combustion and Flame* 14.2, pp. 261–272. ISSN: 00102180. DOI: 10.1016/S0010-2180(70)80037-2.

— (1971). "The heat of reaction during the pyrolysis of wood". In: *Combustion and Flame* 17.1, pp. 79–86. ISSN: 0010-2180. DOI: 10.1016/S0010-2180(71)80141-4.

Schickhofer, G. et al. (2010). *BSPhandbuch: Holz-Massivbauweise in Brettsperrholz - Nachweise auf Basis des neuen europäischen Normenkonzepts*. 2. revised ed. Verl. der Techn. Univ. ISBN: 978-3-85125-109-8.

Schleifer, V. (2009). "Zum Verhalten von raumabschliessenden mehrschichtigen Holzbauteilen im Brandfall". Doctoral thesis. ETH Zürich. DOI: 10.3929/ethz-a-005771863.

Schmid, J. and A. Frangi (2021). "Structural timber in compartment fires – The timber charring and heat storage model". In: *Open Engineering* 11(1), pp. 435–452. DOI: 10.3929/ethz-b-000475521.

Schmid, J., J. König, and J. Köhler (2010). "Fire-exposed cross-laminated timber - Modelling and tests". In: *World Conference on Timber Engineering (WCTE) - 5th World Conference on Timber Engineering*. Riva del Garda, Trentino, Italy.

Schmid, J. et al. (2018). "Simulation of the fire resistance of cross-laminated timber (CLT)". In: *Fire Technology* 54.5, pp. 1113–1148. DOI: 10.1007/s10694-018-0728-9.

Schmid, M. (2001). "Verhalten von auf Schub beanspruchten BSH-Klebstoffen bei hohen Temperaturen". Diploma thesis. ETH Zurich.

Schänzlin, J. (2018). "Eurocode 5:2022 - Zur Bemessung von Holz-Beton-Verbunddecken". In: *Karlsruher Tage 2018 – Holzbau – Forschung für die Praxis*. Karlsruhe, Germany: KIT Scientific Publishing. ISBN: 978-3-7315-0827-4.

Shi, D. et al. (2022). "Thermo-mechanical analysis on shear behavior of grooved connectors for glulam-concrete composite beams under fire". In: *Fire Safety Journal* 130, p. 103594. ISSN: 03797112. DOI: 10.1016/j.firesaf.2022.103594.

Silly, G. (2010). "Numerische Studien zur Drill- und Schubsteifigkeit von Brettsperrholz (BSP)". Diploma thesis. Technical University of Graz.

Stora Enso (2018). *CLT Rib Panels - Structural Design Manual*.

— (2020). *Declaration of Performance - Stora Enso CLT – Cross Laminated Timber'*.

— (2021). *Loadbearing floor fire tests on CLT elements - carried out at CSI S.p.a. fire laboratory in Bollate, Italy. Unpublished data*.

— (2022). *Declaration of Performance - Stora Enso CLT Rib Panels'*.

Taylor, S. E. et al. (2001). "Field investigation of stress-laminated T-Beam and Box-beam timber bridges". In: *2001 Sacramento, CA July 29-August 1,2001*. American Society of Agricultural and Biological Engineers. DOI: 10.13031/2013.7440.

Thiel, A. et al. (2014). *Mitwirkende Breite bei Plattenbalken aus BSH und BSP - Kurzfassung und Anwendungsbeispiele, Report Focus_sts 1.3.3_1*. Ed. by holz.bau forschungs gmbh and TU Graz.

Thomas, G. C. (1997). *Fire resistance of light timber framed walls and floors*. 97/7. Christchurch, New Zealand.

Timoshenko, S. P. (1940). *Strength of materials - Part II Advanced theory and problems*. 2nd ed. D. Van Nostrand Company, inc.

Timoshenko, S. P. and J. N. Goodier (1951). *Theory of elasticity*. 2nd ed. Engineering Societies Monographs. Auckland, New Zealand: McGraw-Hill. ISBN: 0-07-085805-5.

University of Liège (2016). *DIAMOND (Version 1.5.2.0)*. University of Liège. URL: https://www.uee.uliege.be/cms/c_4016387/en/safir-resources.

VTT Expert Services LTD (2017). *Test Report VTT-S-03969-17: Bending tests of CLT Rib Panels*.

Wallner-Novak, M., J. Koppelhuber, and K. Pock (2014). *Cross-laminated timber structural design - Basic design and engineering principles according to Eurocode*. proHolz Information. Vienna, Austria: proHolz Austria. ISBN: 978-3-902926-03-6.

Wiesner, F. (2019). "Structural behaviour of cross-laminated timber elements in fires". Doctoral thesis. University of Edinburgh.

Winter, S., H. Kreuzinger, and P. Mestek (2008). *Flächen aus Brettstapeln, Brettsperrholz und Verbundkonstruktionen*. Holzbau der Zukunft 15. Fraunhofer IRB Verl. ISBN: 978-3-8167-7875-2.

Yeh, B. and R. Brooks (2006). "Evaluation of adhesive performance at elevated temperatures for engineered wood products". In: *World Conference on Timber Engineering (WCTE) – Proceedings of the 5th Meeting*. Tacoma, Washington.

Young, S.A. and P. Clancy (2001). "Compression mechanical properties of wood at temperatures simulating fire conditions". In: *Fire and Materials* 25.3, pp. 83–93. ISSN: 0308-0501, 1099-1018. DOI: 10.1002/fam.759.

Zelinka, S.L. et al. (2018). "Performance of wood adhesives for cross-laminated timber under elevated temperature". In: *World Conference on Timber Engineering (WCTE) – Proceedings of the 10th Meeting*. Seoul, South Korea.

Zelinka, S.L. et al. (2019). "Small scale tests on the performance of adhesives used in cross laminated timber (CLT) at elevated temperatures". In: *International Journal of Adhesion and Adhesives* 95, p. 102436. ISSN: 01437496. DOI: 10.1016/j.ijadhadh.2019.102436.

A. Parametric study results of the extreme cases 'thin layers, 3-layered'

Figures A.1-A.5 present the numerical results of the thermo-mechanical simulations for each extreme case of group 1 'thin layers, 3-layered' of the parametric study, discussed in section 4.9.3. Figures A.1-A.5b2 include the performance criterion for failure of the loadbearing capacity as limit value for the amount of the deflection according to prEN 1363-1. Figures A.1-A.5c2 include the values for the estimated effective widths at normal temperature according to prEN 1995-1-1.

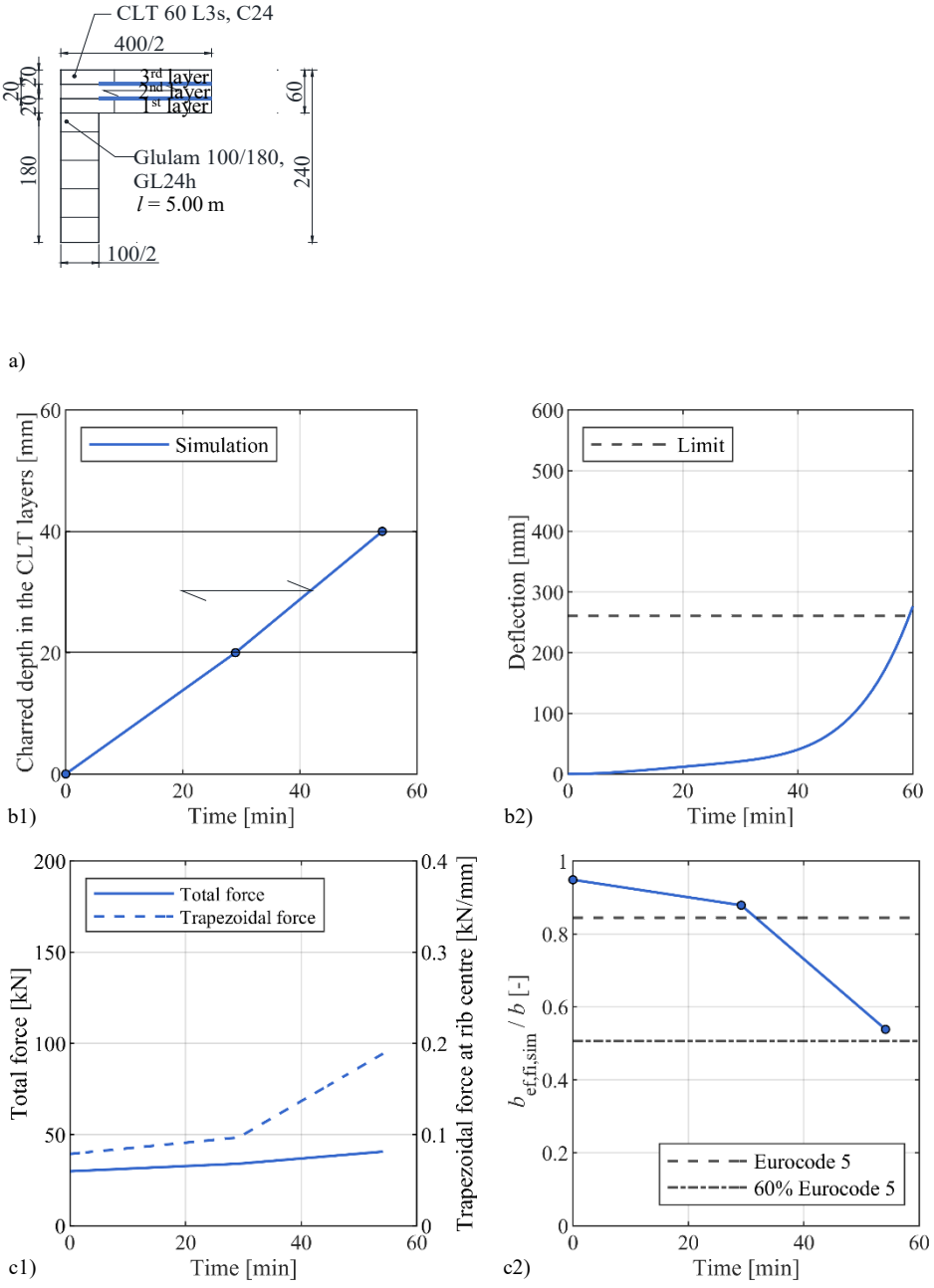

Figure A.1. Parametric study - Numerical results over time of the extreme case 1b: a) Cross-section; b1) Charred depth in CLT layers; b2) Deflection compared to the performance criterion according to prEN 1363-1; c1) Total force and trapezoidal force at rib centre in fire; c2) Ratio of effective width in fire to CLT width $b_{\mathrm{ef,fi,sim}}/b$ related to a limit value based on prEN 1995-1-1 (Eurocode 5).

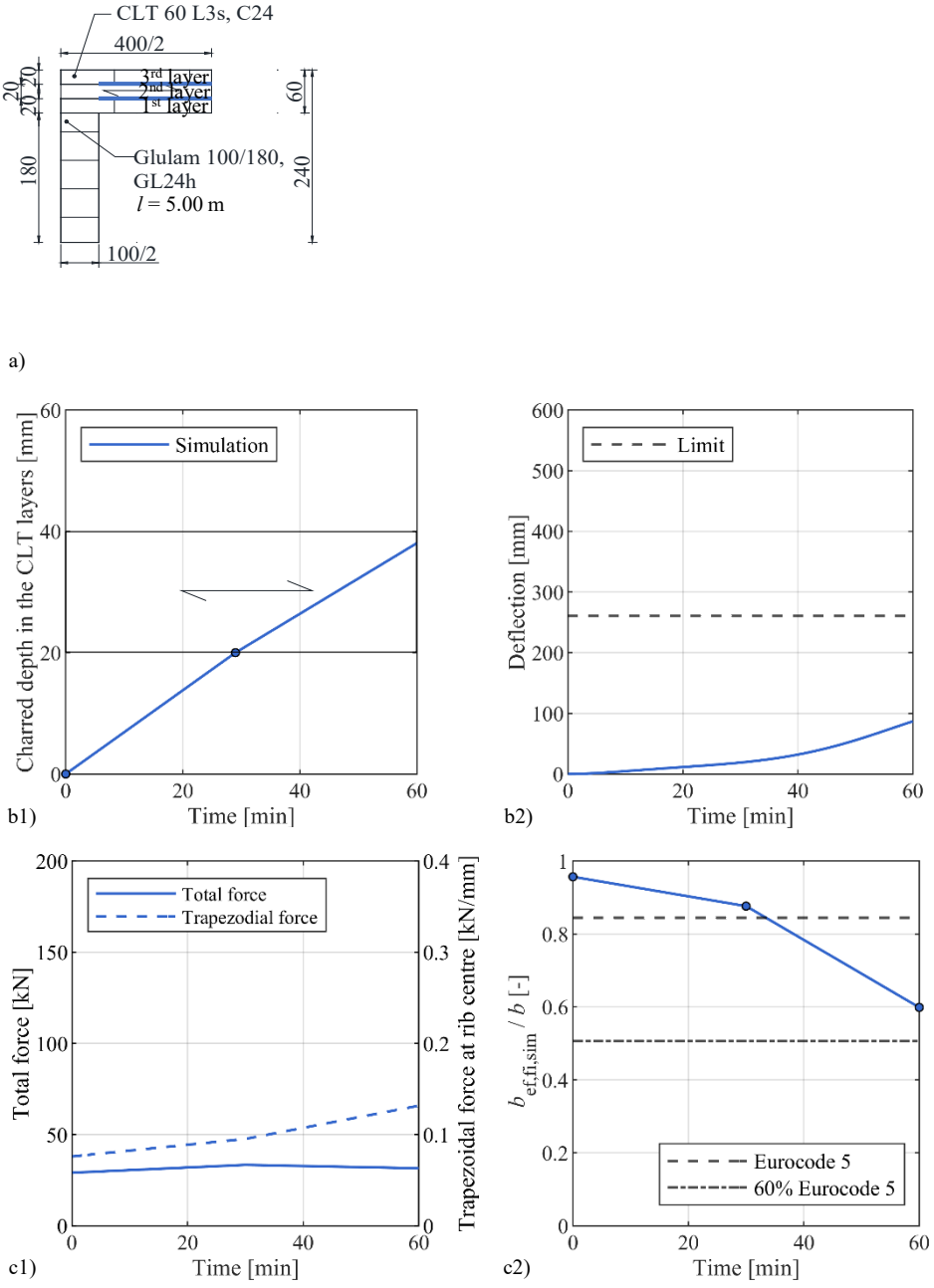

Figure A.2. Parametric study - Numerical results over time of the extreme case 7 (no fall-off): a) Cross-section; b1) Charred depth in CLT layers; b2) Deflection compared to the performance criterion according to prEN 1363-1; c1) Total force and trapezoidal force at rib centre in fire; c2) Ratio of effective width in fire to CLT width $b_{\mathrm{ef,fi,sim}}/b$ related to a limit value based on prEN 1995-1-1 (Eurocode 5).

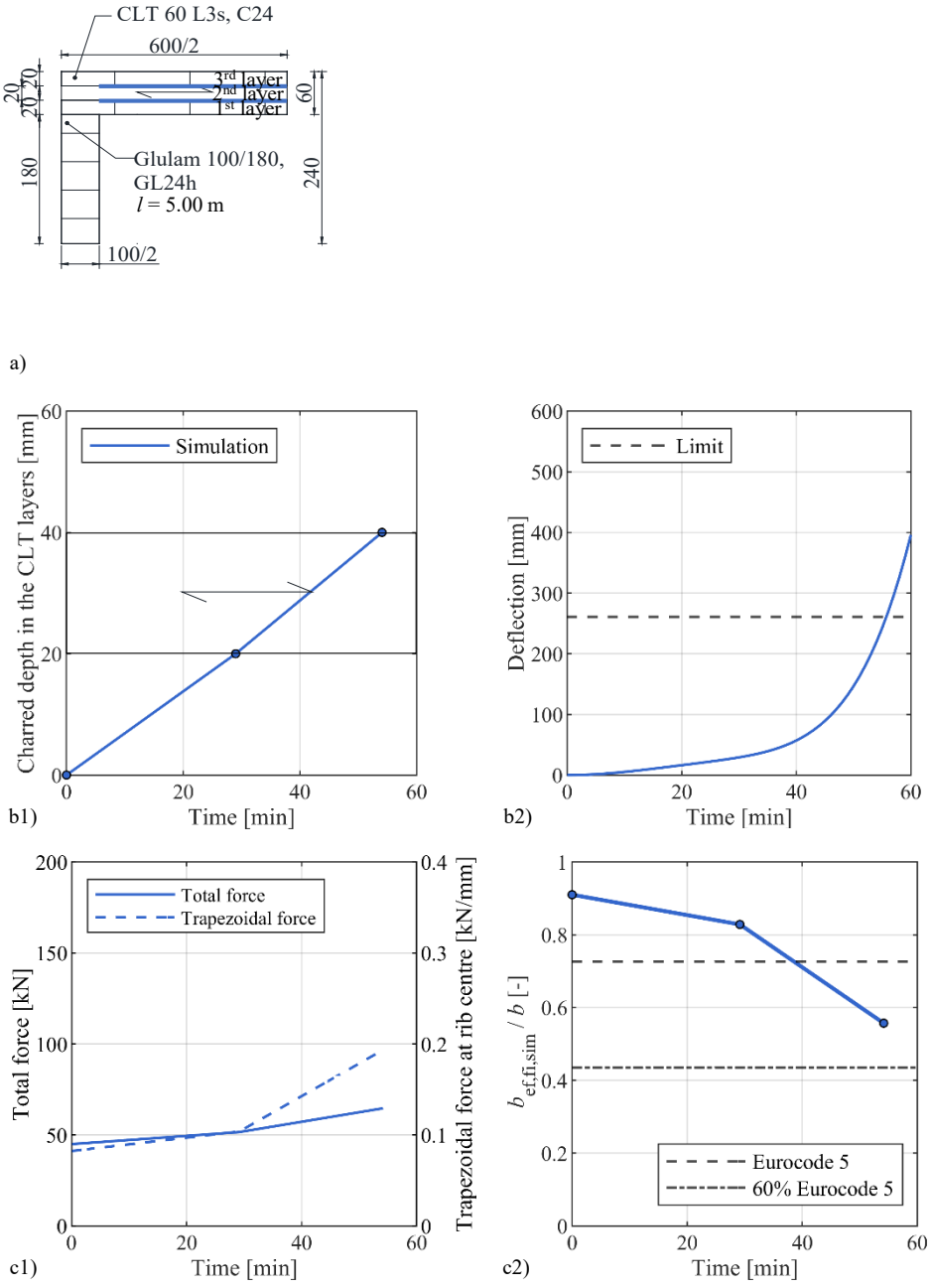

Figure A.3. Parametric study - Numerical results over time of the extreme case 2b: a) Cross-section; b1) Charred depth in CLT layers; b2) Deflection compared to the performance criterion according to prEN 1363-1; c1) Total force and trapezoidal force at rib centre in fire; c2) Ratio of effective width in fire to CLT width $b_{\mathrm{ef,fi,sim}}/b$ related to a limit value based on prEN 1995-1-1 (Eurocode 5).

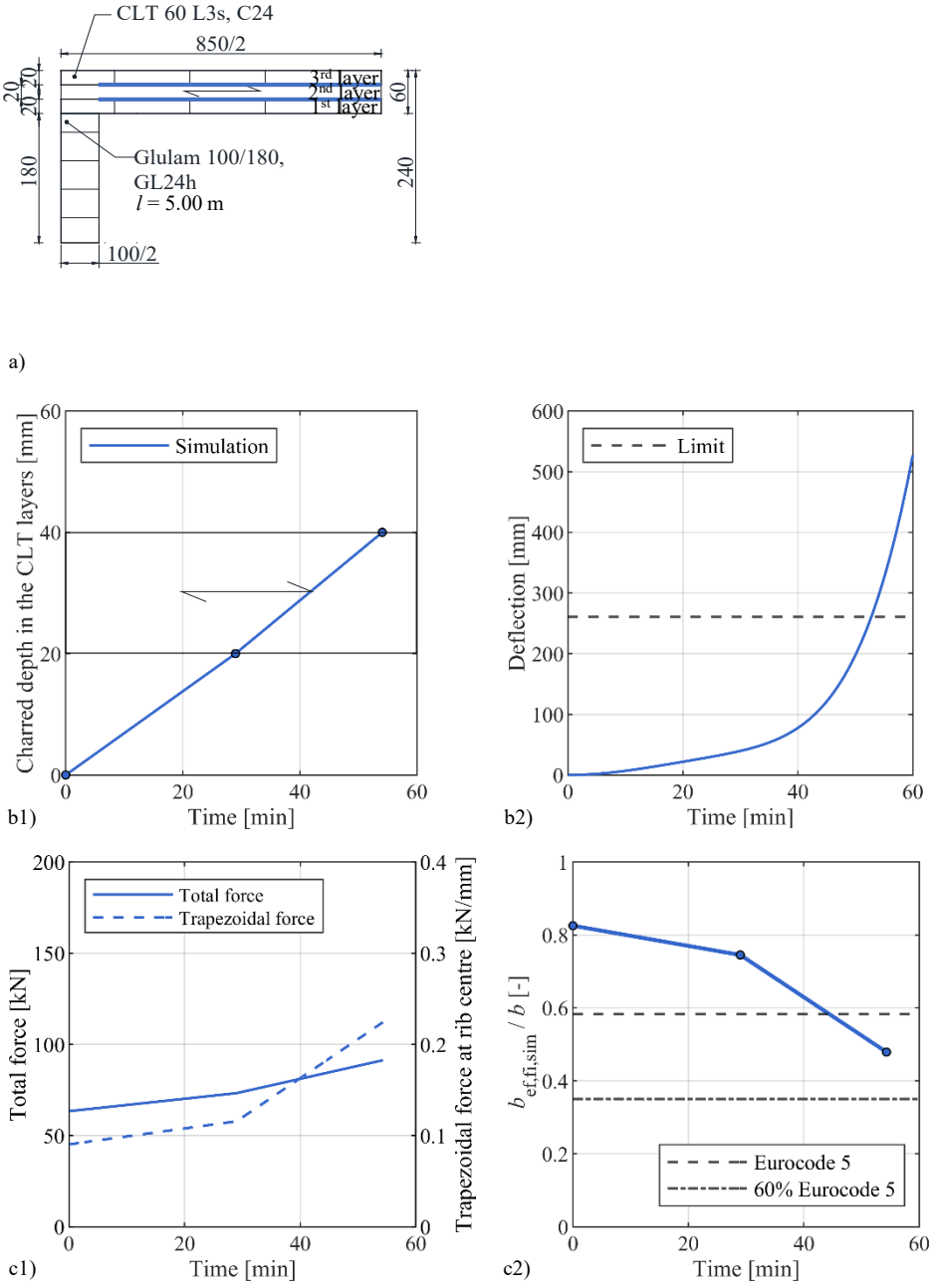

Figure A.4. Parametric study - Numerical results over time of the extreme case 5b: a) Cross-section; b1) Charred depth in CLT layers; b2) Deflection compared to the performance criterion according to prEN 1363-1; c1) Total force and trapezoidal force at rib centre in fire; c2) Ratio of effective width in fire to CLT width $b_{\mathrm{ef,fi,sim}}/b$ related to a limit value based on prEN 1995-1-1 (Eurocode 5).

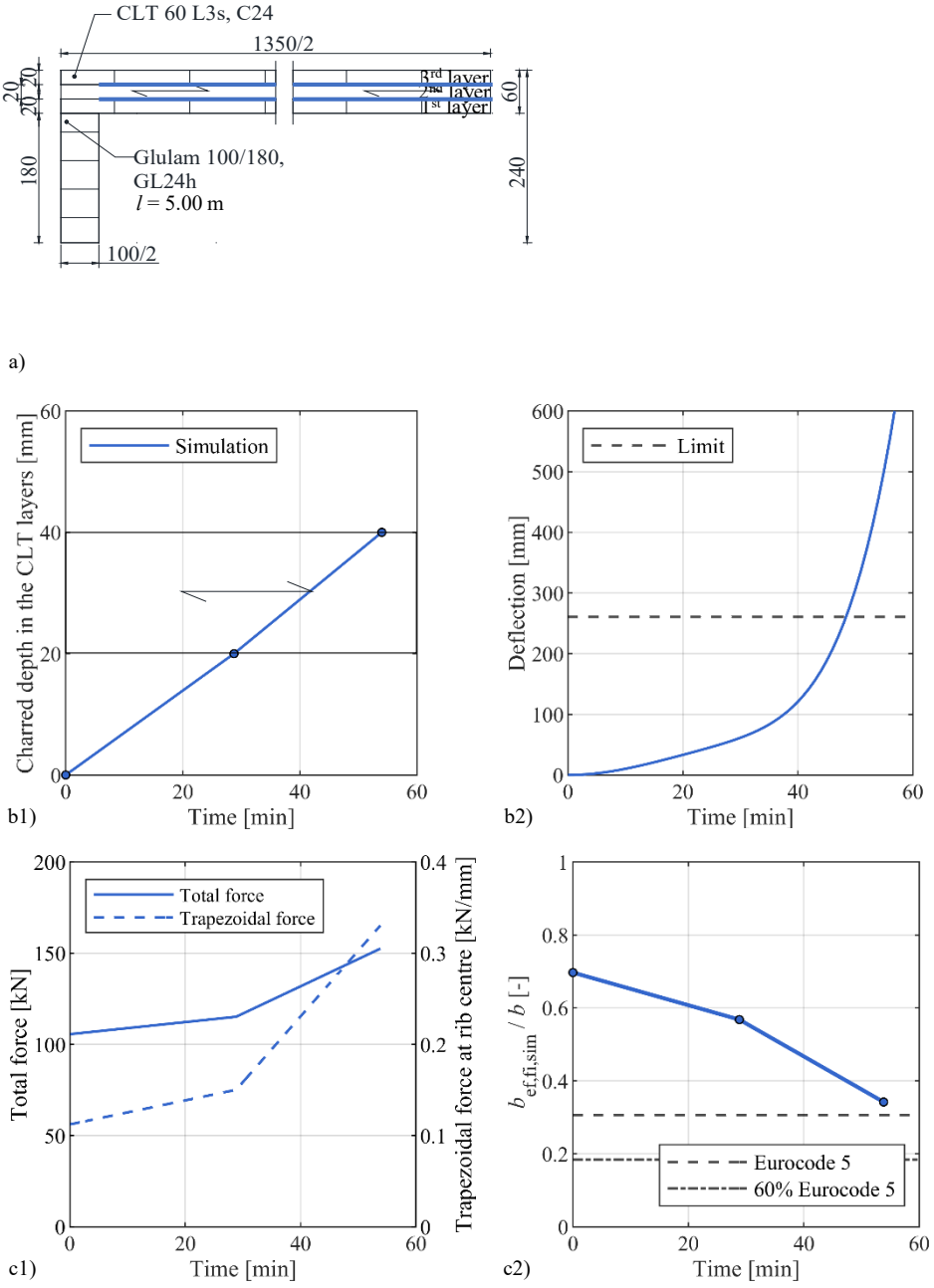

Figure A.5. Parametric study - Numerical results over time of the extreme case 3b: a) Cross-section; b1) Charred depth in CLT layers; b2) Deflection compared to the performance criterion according to prEN 1363-1; c1) Total force and trapezoidal force at rib centre in fire; c2) Ratio of effective width in fire to CLT width $b_{\mathrm{ef,fi,sim}}/b$ related to a limit value based on prEN 1995-1-1 (Eurocode 5).

B. Parametric study results of the extreme cases 'thin layers, 5-layered'

Figures B.1-B.4 present the numerical results of the thermo-mechanical simulations for each extreme case of group 2 'thin layers, 5-layered' of the parametric study, discussed in section 4.9.3. Figures B.1-B.4b2 include the performance criterion for failure of the loadbearing capacity as limit value for the amount of the deflection according to prEN 1363-1. Figures B.1-B.4c2 include the values for the estimated effective widths at normal temperature according to prEN 1995-1-1.

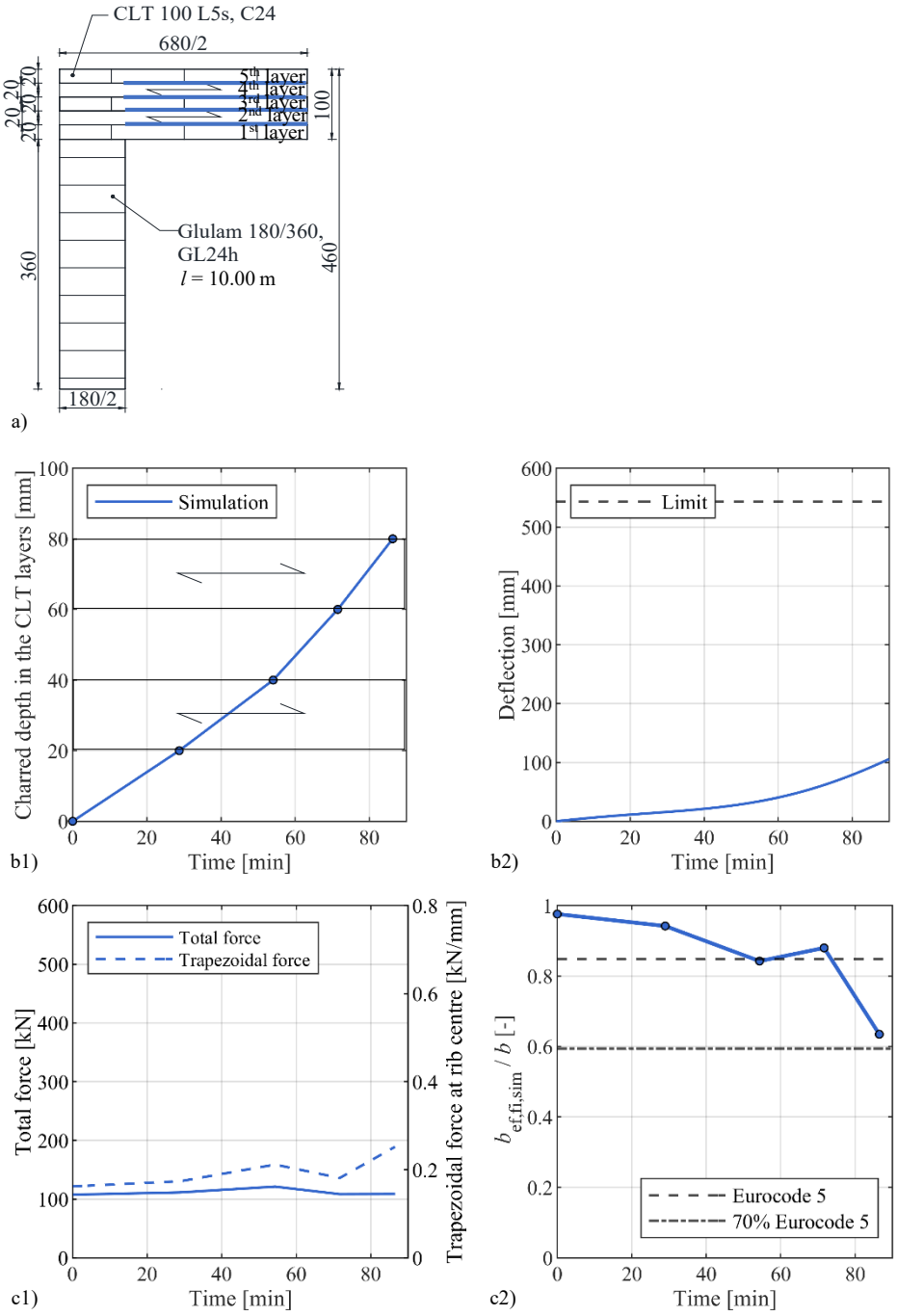

Figure B.1. Parametric study - Numerical results over time of the extreme case 1: a) Cross-section; b1) Charred depth in CLT layers; b2) Deflection compared to the performance criterion according to prEN 1363-1; c1) Total force and trapezoidal force at rib centre in fire; c2) Ratio of effective width in fire to CLT width $b_{\mathrm{ef,fi,sim}}/b$ related to a limit value based on prEN 1995-1-1 (Eurocode 5).

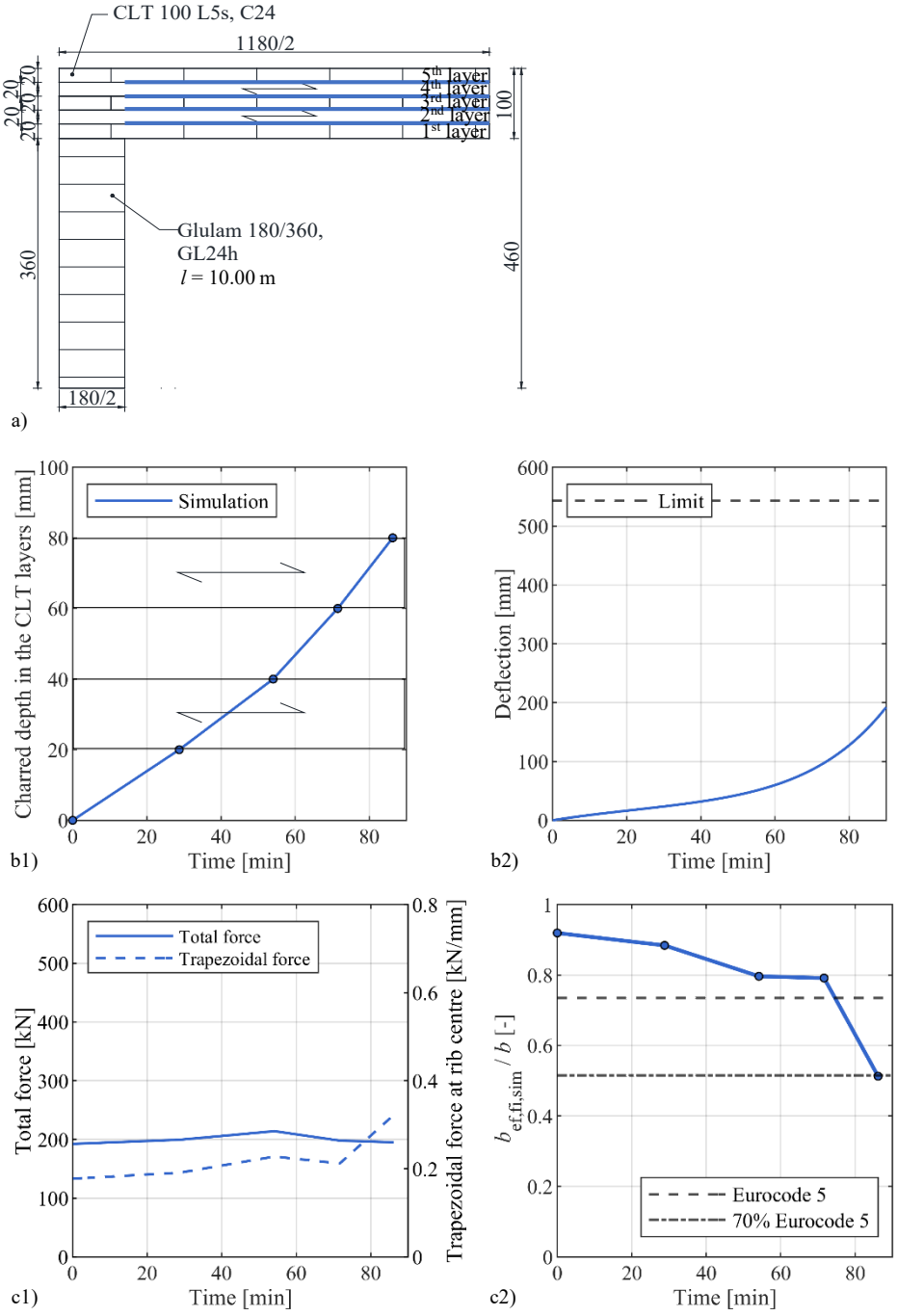

Figure B.2. Parametric study - Numerical results over time of the extreme case 2: a) Cross-section; b1) Charred depth in CLT layers; b2) Deflection compared to the performance criterion according to prEN 1363-1; c1) Total force and trapezoidal force at rib centre in fire; c2) Ratio of effective width in fire to CLT width $b_{\mathrm{ef,fi,sim}}/b$ related to a limit value based on prEN 1995-1-1 (Eurocode 5).

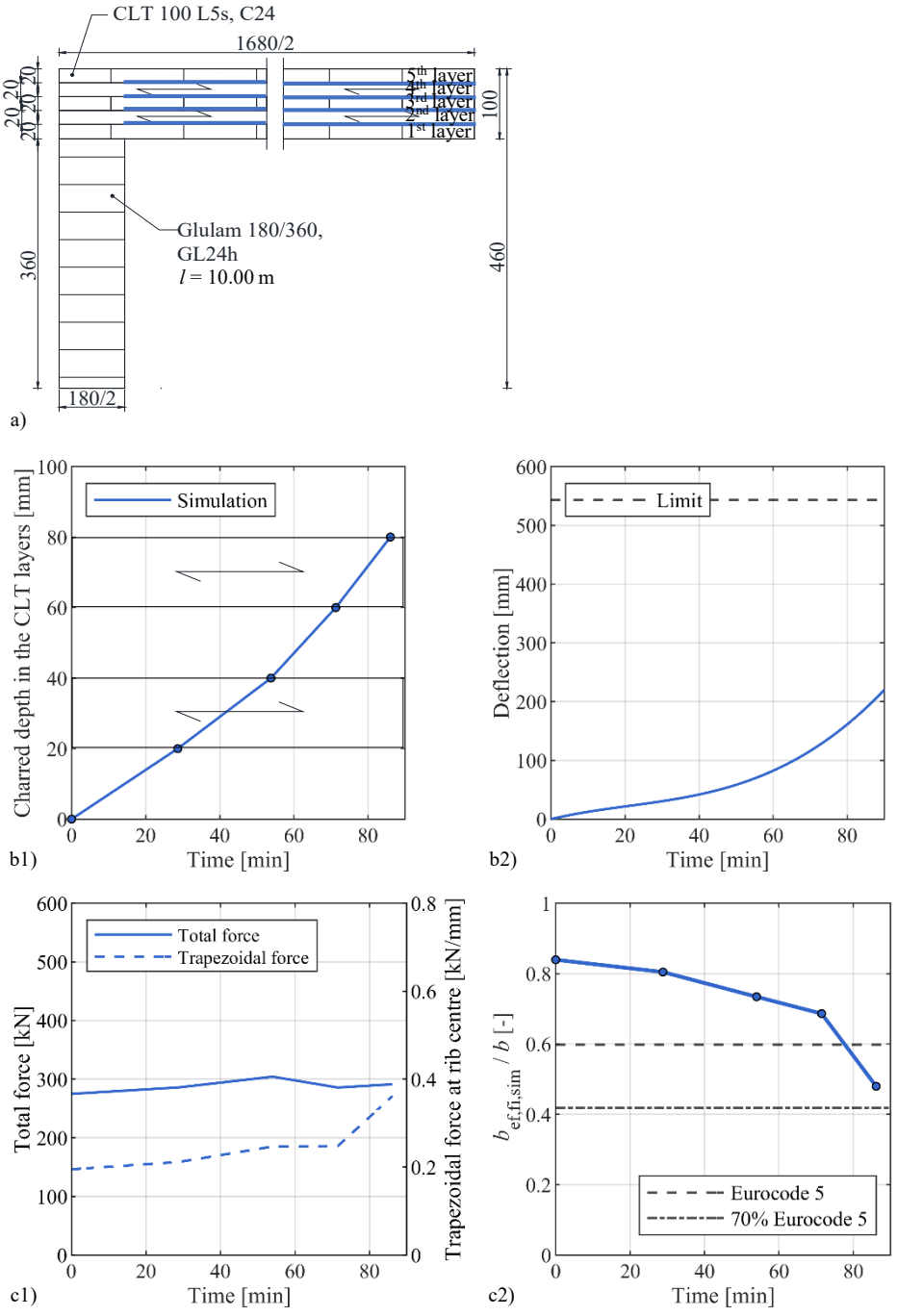

Figure B.3. Parametric study - Numerical results over time of the extreme case 5: a) Cross-section; b1) Charred depth in CLT layers; b2) Deflection compared to the performance criterion according to prEN 1363-1; c1) Total force and trapezoidal force at rib centre in fire; c2) Ratio of effective width in fire to CLT width $b_{\mathrm{ef,fi,sim}}/b$ related to a limit value based on prEN 1995-1-1 (Eurocode 5).

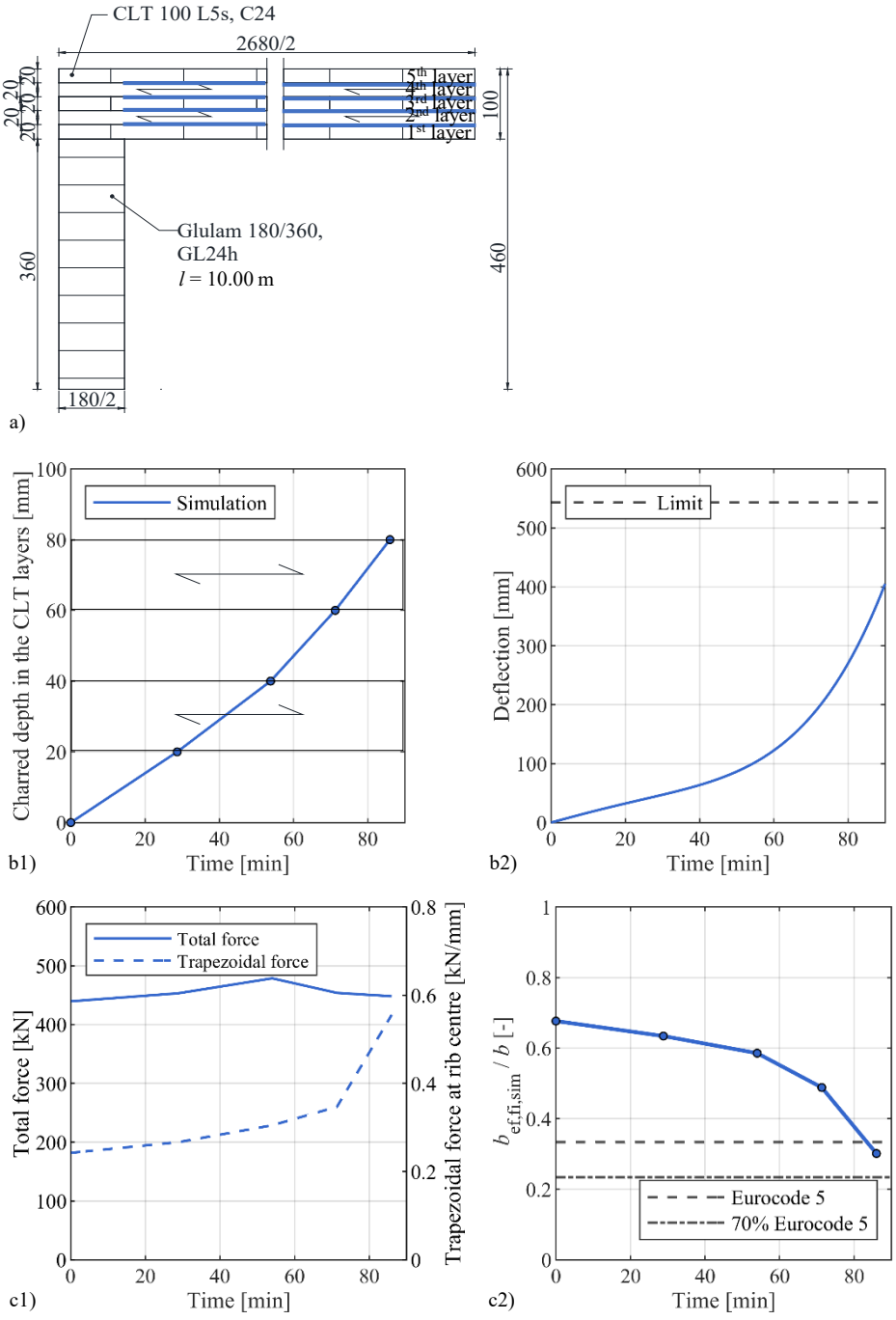

Figure B.4. Parametric study - Numerical results over time of the extreme case 3: a) Cross-section; b1) Charred depth in CLT layers; b2) Deflection compared to the performance criterion according to prEN 1363-1; c1) Total force and trapezoidal force at rib centre in fire; c2) Ratio of effective width in fire to CLT width $b_{\mathrm{ef,fi,sim}}/b$ related to a limit value based on prEN 1995-1-1 (Eurocode 5).

C. Parametric study results of the extreme cases 'thick layers, 3-layered'

Figures C.1 and C.2 present the numerical results of the thermo-mechanical simulations for each extreme case of group 3 'thick layers, 3-layered' of the parametric study, discussed in section 4.9.3. Figures C.1 and C.2b2 include the performance criterion for failure of the loadbearing capacity as limit value for the amount of the deflection according to prEN 1363-1. Figures C.1 and C.2c2 include the values for the estimated effective widths at normal temperature according to prEN 1995-1-1.

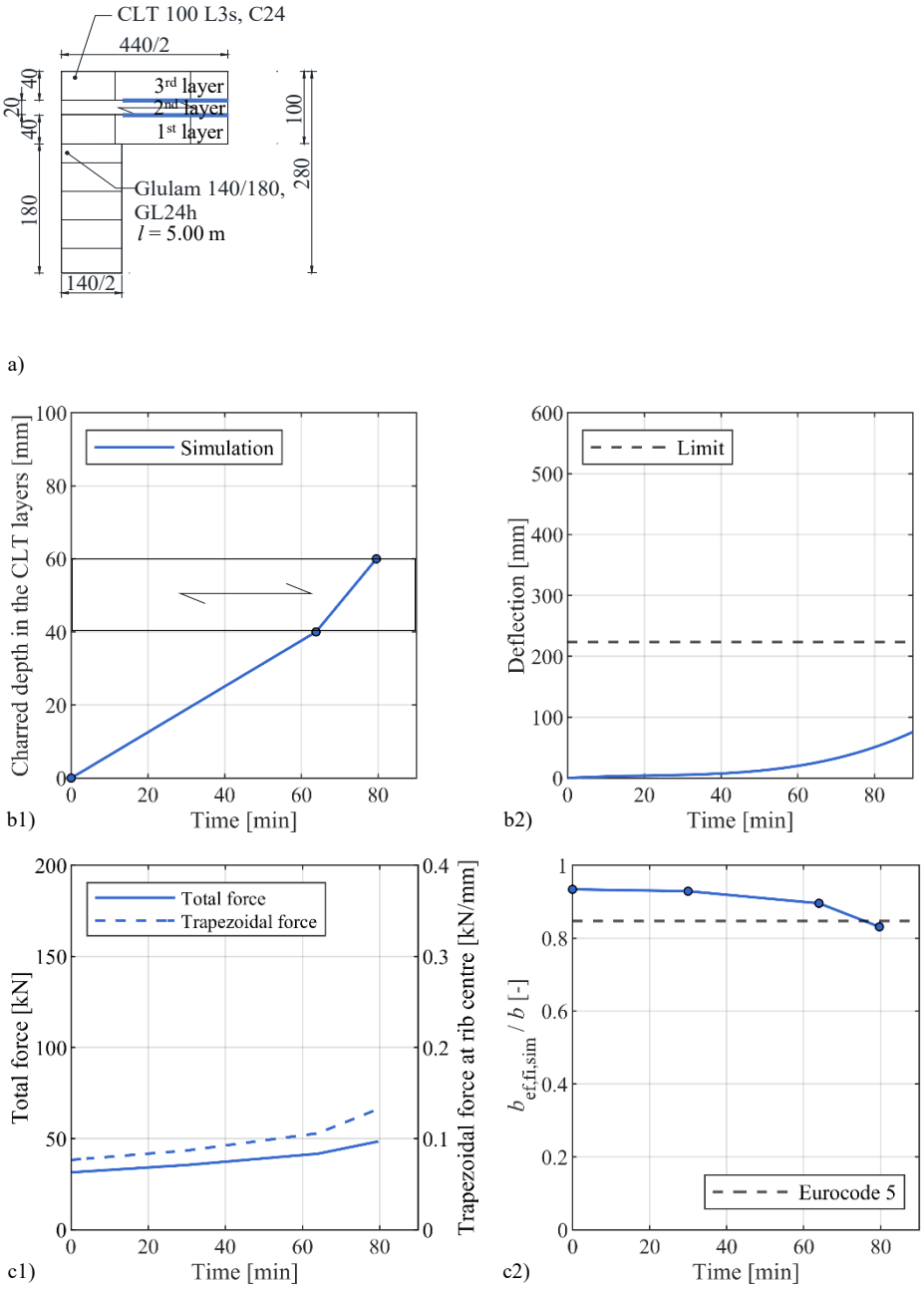

Figure C.1. Parametric study - Numerical results over time of the extreme case 6: a) Cross-section; b1) Charred depth in CLT layers; b2) Deflection compared to the performance criterion according to prEN 1363-1; c1) Total force and trapezoidal force at rib centre in fire; c2) Ratio of effective width in fire to CLT width $b_{\mathrm{ef,fi,sim}}/b$ related to a limit value based on prEN 1995-1-1 (Eurocode 5).

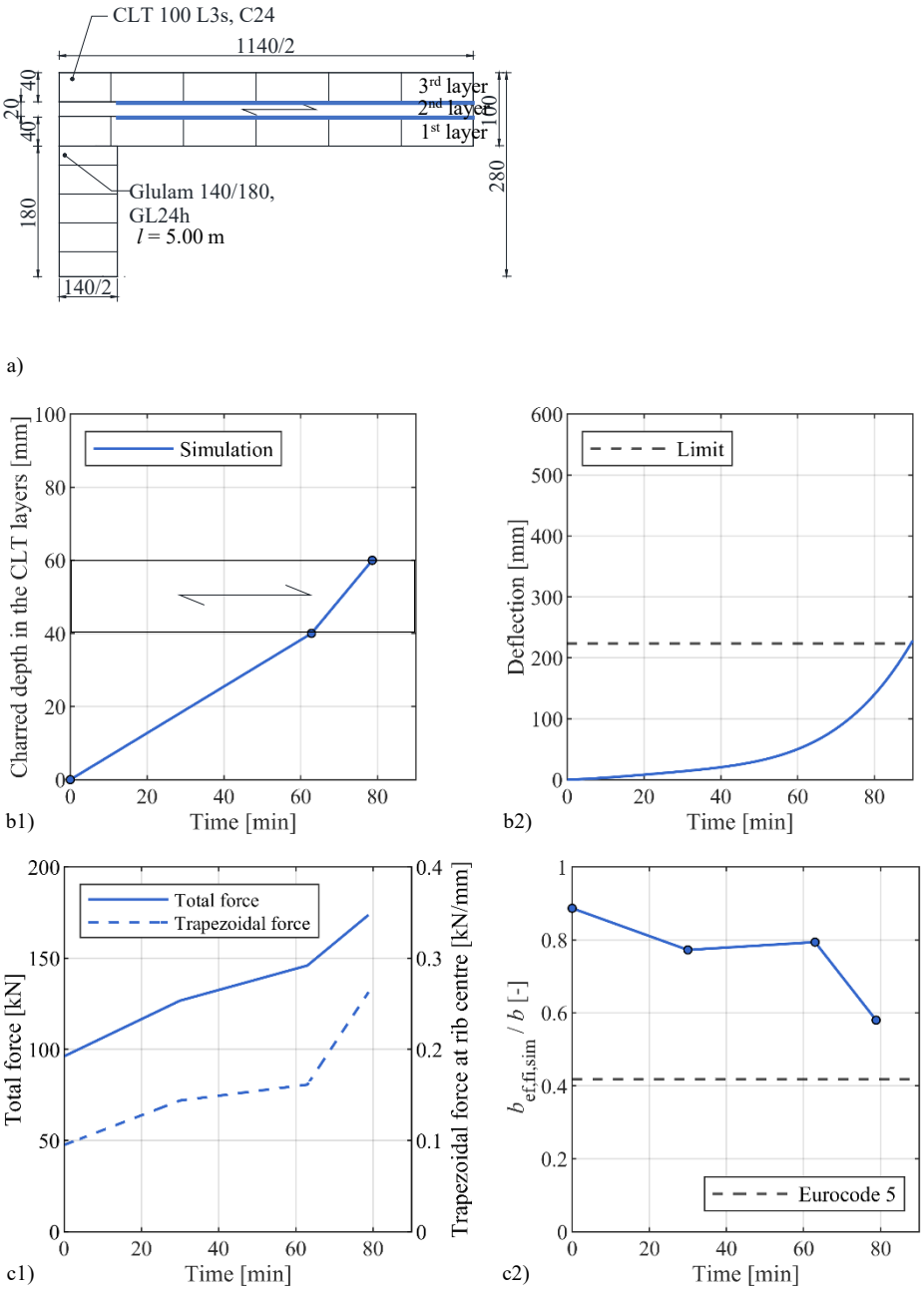

Figure C.2. Parametric study - Numerical results over time of the extreme case 4: a) Cross-section; b1) Charred depth in CLT layers; b2) Deflection compared to the performance criterion according to prEN 1363-1; c1) Total force and trapezoidal force at rib centre in fire; c2) Ratio of effective width in fire to CLT width $b_{\mathrm{ef,fi,sim}}/b$ related to a limit value based on prEN 1995-1-1 (Eurocode 5).

List of publications

Kleinhenz, M., A. Just, and A. Frangi (2022). "The structural behaviour of cross-laminated timber rib panels in fire". In: *SiF 2022 - 12th International Conference on Structures in Fire*. Hong Kong: The Hong Kong Polytechnic University.

Kleinhenz, M., A. Frangi, and A. Just (2022). "The effective width of cross-laminated timber rib panels in fire". In: *International Network on Timber Engineering Research (INTER) – Proceedings of the 7th Meeting*. Bad Aibling, Germany.

Kleinhenz, M., M. Sterley, A. Just, and A. Frangi (2021). "The composite action of cross-laminated timber rib panels at elevated temperatures". In: *AOSFST 2021 – 12th Asia-Oceania Symposium on Fire Science and Technology*. Brisbane, Australia: The University of Queensland.

Kleinhenz, M., A. Just, and A. Frangi (2021). "Temperature-dependent thermal properties for cross-laminated timber exposed to standard fire". In: *International Network on Timber Engineering Research (INTER) – Proceedings of the 6th Meeting*. Online.

Kleinhenz, M., A. Just, and A. Frangi (2021). "Experimental analysis of cross-laminated timber rib panels at normal temperature and in fire". In: *Engineering Structures* 246, p. 113091. issn: 01410296. doi: 10.1016/j.engstruct.2021.113091.

Kleinhenz, M., and A. Frangi (2020). "CLT-Rippendecken im Brandfall – erste Versuchsreihe inkl. Referenzversuchen". In: *8. Doktorandenkolloquium „Holzbau Forschung + Praxis" (DoKo 2020), March 5-6, 2020*. Stuttgart, Germany: Universität Stuttgart.